Karlsruhe Institute of Technology

IceScint:
A Scintillation Detector Array for the IceCube Surface Enhancement

To receive the academic degree of a

Doctor of Natural Sciences

from the KIT Faculty of Physics
of the Karlsruhe Institute of Technology (KIT)

approved
Dissertation

by
Thomas Huber
from Regensburg

Karlsruhe Institute of Technology, KIT
Deutsches Elektronen-Synchrotron, DESY

Referee Prof. Dr. Marc Weber, KIT-IPE

Co-Referee Prof. Dr. Günter Quast, KIT-ETP

Supervisor Dr. Andreas Haungs, KIT-IKP

2nd Supervisor Dr. Timo Karg, DESY in Zeuthen

Day of the oral exam: 17. July 2020

IceScint:
Ein Szintillationsdetektor-Feld für die Oberflächen-Erweiterung von IceCube

Zur Erlangung des akademischen Grades eines

Doktors der Naturwissenschaften

von der KIT Fakultät Physik
des Karlsruher Instituts für Technologie (KIT)

genehmigte
Dissertation

von
Thomas Huber
aus Regensburg

Karlsruher Institut für Technologie, KIT
Deutsches Elektronen-Synchrotron, DESY

Referent Prof. Dr. Marc Weber, KIT-IPE

Koreferent Prof. Dr. Günter Quast, KIT-ETP

Betreuer Dr. Andreas Haungs, KIT-IAP

2. Betreuer Dr. Timo Karg, DESY in Zeuthen

Tag der mündlichen Prüfung: 17. Juli 2020

IceScint:

A Scintillation Detector Array for the IceCube IceTop Enhancement

The IceCube Collaboration will enhance the surface instrumentation of the IceCube Neutrino Observatory (IceTop) with scintillation detectors (IceScint). This thesis deals with the research and development, the deployment, the commissioning and the characterization phase of the first IceScint station. In addition, the science case, prospects of the enhancement and first air-shower measurements with IceScint will be discussed.

The planned full array out of these detectors will increase the veto capabilities for high energy astrophysical and cosmogenic neutrino search of IceCube. In addition, it will considerably improve the capabilities of cosmic-ray measurements in the 100 TeV - 1 EeV energy range. Furthermore, it will serve as a research and development program for a possible future large-scale surface array of the IceCube-Gen2 program. Three prototype stations with 7 scintillation detectors each have been developed within this thesis, where one of them were deployed at the South Pole in January 2018. The other stations are deployed as test array at KIT and as cold temperature cross calibration station at the Physical Science Lab (PSL) in Madison, respectively.

Each scintillation detector features 1.5 m^2 of plastic scintillators and wavelength-shifting fibers which are read out by Silicon Photomultipliers (SiPMs). These solid-state photosensors are similar in detection efficiency compared to classical photomultiplier tubes, but have considerable advantages like robustness and low-voltage operation. One disadvantage comes with the large temperature dependency in its operation. To ensure a stable gain, a temperature and SiPM bias voltage control loop was developed and works well at the South Pole IceScint station and ensures a uniformly performing detector array. Substantial understanding of SiPMs could be won by comparing the IceScint signal behavior with extended laboratory cross-checks. A newly developed SiPM readout module, IceARM, transfers the signal waveforms to the IceTAXI DAQ. IceARM is now also used for Outreach experiments.

In the frame of this thesis it could be shown that the developed full chain of the IceScint system (plastic scintillator, wavelength shifting fiber, SiPM readout, IceARM as analog electronic and IceTAXI as DAQ) is a working concept to be capable in measuring cosmic-ray air-shower events under extreme environmental conditions like given at the South Pole. The operation of the first station at the South Pole has proven that, e.g., the direction of incident air showers are reconstructed accurately.

The deployed scintillator stations show that it fulfills the requirements of a surface instrumentation upgrade of IceTop and paved the way for the full enhancement of IceTop including radio antennas. With this thesis, the baseline for the planned deployment of 32 stations at the South Pole, each with 8 IceScint detectors and 3 radio antennas as the new surface detector array of the IceCube Neutrino Observatory was created.

IceScint:

Ein Szintillationsdetektor-Feld für die Oberflächen-Erweiterung von IceCube

Die IceCube Kollaboration wird das Oberflächenexperiment des IceCube Neutrino Observatoriums (IceTop) mit Szintillationsdetektoren (IceScint) erweitern. Diese Arbeit befasst sich mit der Forschung und Entwicklung, der Installation, der Inbetriebnahme und der Charakterisierungsphase der ersten IceScint Station. Darüber hinaus werden der naturwissenschaftliche Hintergrund, die physikalischen Möglichkeiten dieser Erweiterung und erste Luftschauer-Messungen mit IceScint diskutiert.

Ein vollständiges Array aus diesen Detektoren wird die Vetomöglichkeiten für die Suche nach hochenergetischen astrophysikalischen und kosmogenen Neutrinos von IceCube erhöhen. Zusätzlich wird es die Möglichkeiten zur Vermessung der kosmischen Strahlung im Energiebereich von 100 TeV-1 EeV erheblich verbessern. Darüber hinaus wird es als Forschungs- und Entwicklungsprogramm für ein mögliches zukünftiges großflächiges Oberflächen-Array des IceCube-Gen2 Observatoriums dienen. Im Rahmen dieser Arbeit wurden 3 Prototyp-Stationen mit je 7 Szintillationsdetektoren entwickelt und gebaut, von denen eine Station im Januar 2018 am Südpol installiert wurde. Die anderen beiden Stationen sind als Testanordnung am KIT und als Kalibrierungsstation für tiefe Temperaturen am Physical Science Lab (PSL) in Madison eingesetzt.

Jeder Detektor verfügt über 1,5 m^2 Plastikszintillatoren mit wellenlängenschiebende Lichtleitern, die von Silicon-Photomultipliern (SiPMs) ausgelesen werden. Diese auf Festkörperphysik basierenden Photosensoren sind in der Detektionseffizienz zum Beispiel den klassischen Photomultiplierröhren ähnlich, haben aber wesentliche Vorteile, wie eine robustere Bauweise und niedrigere Betriebsspannungen. Ein Nachteil ergibt sich aus der hohen Temperaturabhängigkeit der Effizienz. Um eine stabile Verstärkung zu gewährleisten wurde eine Temperatur- und SiPM-Vorspannungs Regelschleife entwickelt, die an der IceScint Station am Südpol funktioniert und ein homogen operierendes Detektorarray gewährleistet. Ein substantielles Verständnis der SiPMs konnte durch den Vergleich des IceScint Signalverhaltens mit erweiterten Laborvergleichsuntersuchungen gewonnen werden. Ein neu entwickeltes SiPM-Auslesemodul, IceARM, moduliert und überträgt die Signalformen an die IceTAXI Datenerfassung. Das IceARM Modul wird mittlerweile auch für Outreach Experimente und Studentenpraktika verwendet.

Im Rahmen dieser Arbeit konnte gezeigt werden, dass die entwickelte Signalkette des IceScint-Systems (Szintillatormaterial, wellenlängenschiebende Lichtleiter, SiPM Auslese, IceARM als analoge Elektronik und IceTAXI als Datenerfassung) ein funktionierendes Konzept ist, um kosmische Luftschauer unter extremen Umweltbedingungen, wie am Südpol gegeben, zu vermessen. Der Betrieb der ersten Station am Südpol hat bewiesen, dass beispielsweise die Herkunftsrichtung einfallender Luftschauer sehr akkurat rekonstruiert werden kann.

Die installierten IceScint Stationen zeigen, dass sie die physikalischen Anforderungen einer Oberflächenerweiterung von IceTop erfüllen und der Weg für die vollständige Erweiterung einschließlich zusätzlichen Radioantennen von IceTop damit geebnet ist. Mit dieser Arbeit wurde die Grundlage geschaffen für die am Südpol geplante Installation von 32 Stationen mit je 8 IceScint Detektoren und 3 Radioantennen als neues Oberflächen-Detektorfeld des IceCube Neutrino Observatoriums.

Contents

1 Introduction

The first sign of the existence of cosmic rays was discovered by Theodor Wulf in 1910 when he climbed the Eiffel Tower with an electrometer [1, 2]. After more precise measurements by Victor Hess [3] through balloon flights up to an altitude of five kilometres, the existence of cosmic rays was verified and further experimental methods were devised.

The collision of a high-energy cosmic ray particle with the atmosphere releases new hadronic, muonic and electromagnetic particles. These particles collide again with atomic nuclei in the atmosphere or decay and generate more particles until the energy of the primary particle is released. These resulting particles propagate towards the Earth's surface and are called extensive air-showers. The discovery of extensive air-showers is shown in Figure 1.1. It displays the results of three different measurement setups, measuring the rate of coincidences with Geiger counters compared to the distance between one reference Geiger counter. The lesser rate at larger distances indicates higher primary energies with lower flux.

The detection of this air showers allows us to make conclusions about the primary particle. As the cosmic ray particle flux decreases rapidly at high energies, the direct measurement of high-energy cosmic particles is not possible via balloon or satellite experiments. Hence, a large detector surface is required in order to achieve the highest possible statistics of events. A large instrumented area allows us the research of cosmic rays to obtain new scientific insights about the otherwise inaccessible reaches of the Universe.

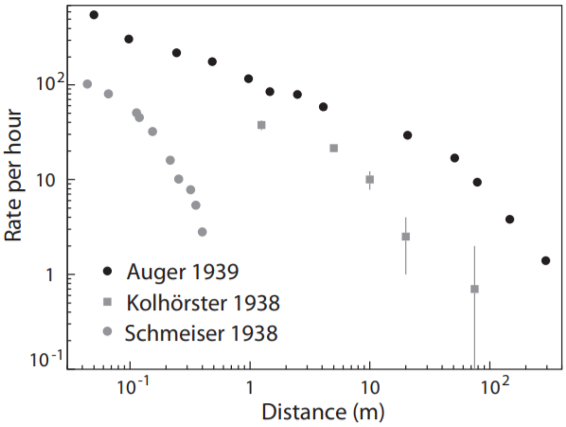

Figure 1.1: The discovery of extensive air-showers: Decoherence curves of 3 different measurement setups, measured with Geiger counters separated up to 300 m distance [4]. The measurement was only possible by the design, deployment and operation of a first particle detector array.

Measuring these extensive air-showers for the detection of UHECRs[1] is used in large-scale experiments like the Pierre Auger Observatory in Argentina [5] and for very high energy cosmic rays [2] one part of the IceCube Observatory [6] at the geographical South Pole. The IceCube Observatory is a cubic-kilometer Cherenkov telescope deployed at the South Pole that detects neutrinos of all flavors with energies from tens of GeV to several PeV. The perpetual ice at the South Pole represents an almost ideal detector volume, which is why the IceCube Observatory was built at the South Pole. The observatory provided first measurements of the flux of high-energy astrophysical neutrinos, opening a new window to the non-thermal universe. For measuring extensive air-showers in the PeV To EeV range with this observatory, the IceTop surface detector array, consisting of ice Cherenkov tanks as particle detector, was deployed.

An additional array of surface detectors, like scintillators, allows an improved (cross) calibration of the in-ice detector and IceTop by measuring in coincidence air showers and muons. A scintillator array in the size of IceTop is able to detect air showers with a primary energy from 100 TeV to EeV. The higher density of detectors at the IceTop surface will allow accurate reconstruction of air showers for energies lower than IceTop alone can do, means the energy range of the knee in the cosmic ray spectrum will be finally covered.

This thesis deals with the technological realisation of the enhancement of IceTop with scintillators (IceScint) and its data acquisition and gives prospects of the capabilities of the design of one whole scintillator station. The thesis is structured as follows.

An introduction describes the basic terms and definitions in astroparticle physics with focus on the latest discoveries and on detection techniques (Chapter 2). Afterwards, the IceCube Observatory will be explained and the prospect of the discovery possibilities offered by future extensions like IceCube Upgrade and a possible IceCube-Gen2 facility (Chapter 3). In Chapter 4 an introduction of the planned IceTop surface enhancement and its components, which is currently in prototyping status, is given. The IceScint detector system that has been developed within this work will be explained in Chapter 5 by an overview of the single components of the system. In Chapter 6 the production, test measurements and calibration results of IceScint can be found. The actual deployment and the first measurements at the South Pole are explained in Chapter 7. In Chapter 8 we discuss the calibration and commissioning of the deployed IceScint station. The description of the detector performance after months at the South Pole and the capabilities of the IceScint station are placed in Chapter 9. Finally, in Chapter 10, the use of the developed IceScint electronics for teaching and outreach is briefly discussed.

---

[1] Ultra high-energy cosmic rays $> 10^{18}$eV

[2] $> 10^{14}$eV

2 Cosmic rays

In this chapter a brief introduction to the physics of cosmic rays (CRs) and the by there CRs induced extensive air-showers will be given. In addition, a choice of detection techniques of extensive air-showers, with focus on scintillation detectors like developed for this thesis, will be described.Since a rather detailed and historical introduction has already been given my preceding Bachelor's [2] and Master's these [7], only certain latest developments and discoveries and associated new questions will be explained in more detail.

Even more than hundred years after the discovery of cosmic rays, numerous important key questions remain unanswered. For example related to the sources, the acceleration mechanisms and the composition of ultra-high energy cosmic rays (UHECR) [4].

Cosmic rays consists mainly of ionised atomic nuclei [8] (Table 2.1 shows composition for low energies). The composition of UHECRs is still much less known and several experiments, like the Pierre-Auger Observatory, approaching to determine the composition of cosmic rays beyond an energy of 10^{19} eV.

Protons	85%
Helium nuclei	12%
Nuclei with $Z \geq 3$	1-2%
Electrons	1-2%
Photons	0,1%

Table 2.1: Distribution of elements in cosmic rays around a primary energy of 10^{12} eV [8]

2.1 Energy spectra

The flux of cosmic rays (Figure 2.2), i.e. the number of detected particles $\mathrm{d}N$ reaching the Earth per energy area $\mathrm{d}E$, surface $\mathrm{d}A$, time $\mathrm{d}t$ and solid angle $\mathrm{d}\Omega$, can be described as a function of energy, using a power law [9]:

$$\phi_{(E)} = \frac{\mathrm{d}N}{\mathrm{d}E \cdot \mathrm{d}A \cdot \mathrm{d}\Omega \cdot \mathrm{d}t} = \phi_0 \cdot E^{-\gamma}. \tag{2.1.1}$$

The energy spectrum of comic rays has been studied with many different experiments. Figure 2.2 shows the flux of cosmic rays over energy. All of these primary particles are charged and can be deflected by magnetic fields and thus lose most of their directional information on their way to Earth. The flux of the high-energy cosmic rays of individual components is energy-dependent relative to each other. For a better visualization the flux is multiplied by $E^{2.5}$.

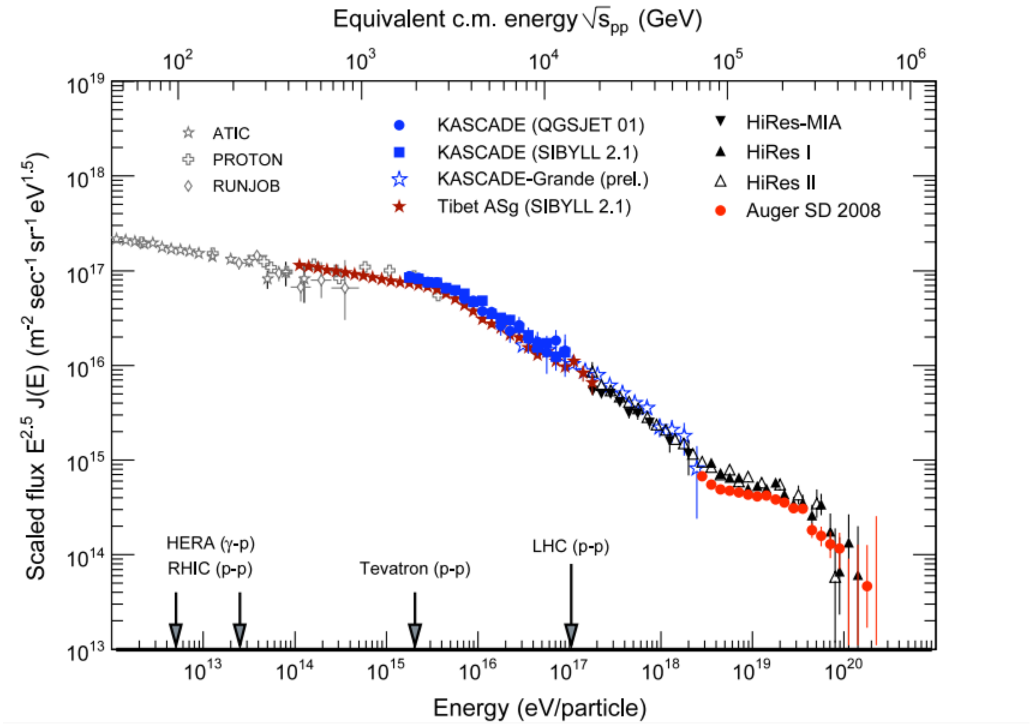

Figure 2.1: Galactic and extragalactic energy spectrum of cosmic rays multiplied with $E^{2.5}$. In this scaling the “knee” at 10^{15} eV and the “ankle” at 10^{18} eV is easy to see [10].

What is particularly interesting on this spectrum is the change in the gradient at about $4 \cdot 10^{15}$ eV from y = -2.7 To y = -3.1, the so-called "knee", and the flattening at 10^{18} eV, the "ankle". The knee is due to the decrease in the particle flux of light elements. With regard to the flattening at 10^{18} eV, the dip model (e^+e^- generation by protons) and the transition between the galactic and extragalactic origin of cosmic rays come into consideration. With regard to the sharp drop at $5 \cdot 10^{19}$ eV , missing accelerator sources or the GZK effect[1] [11], i.e. the interaction of cosmic rays with the cosmic microwave background radiation, are currently under discussion as explanation [10].

Shortly after cosmic background radiation was discovered, Greisen, Zatsepin and Kuz‘min simultaneously calculated that the background-radiation photons decelerate cosmic particles within a particular path. For example, high-energy protons interact (at above $5 \cdot 10^{19}$ eV) with the cosmic background-radiation photons, thereby producing a Δ^+ resonance, which decays into pions, and lose energy in this process:

$$p + \gamma \rightarrow \Delta^+ \rightarrow p + \pi^0,\ n + \pi^+. \tag{2.1.2}$$

This effect allows protons with more than an energy of 10^{20} eV to decelerate to less than 10^{20} eV within a distance of 100 Mpc. The rate at $E = 10^{20}$ eV corresponds to one particle per square kilometre per century. The latest IceCube IceTop result of compositions and its systematic uncertainties are one motivation for this thesis.

There is a variety of methods for detecting cosmic rays. For low-energy particles, the

---

[1] Greisen, Zatsepin, Kuzmin

fluxes are high enough to be observed directly with balloon and satellite experiments using relatively small detectors. For particles with high energies, large-area detector arrays or large detector volumes are necessary. The challenge for cosmic ray experiments is to expose a detection area which is as large as possible to measure a significant amount of secondary particles of cosmic rays, called extensive air showers (EAS). Observing cosmic rays via the EAS channel will be explained later in this Chapter.

2.2 Multi-Messenger astroparticle physics

With the multi detection of several astroparticle physics messengers like high-energy neutrinos, gamma rays and cosmic rays, the era of multi-messenger astroparticlephysics started. The IceCube observatory set up an real time alert [12] for high energetic neutrino signals, detected at the South Pole. Since neutrinos are uncharged and have close to zero mass and are only weakly interacting, the quality as "smoking gun" signatures for point sources of (extra)galactic point sources is exceptional.

The IceCube Observatory (Chapter 3) detected September 2017 a high-energy neutrino with around 209 TeV and sent an alert (Figure 2.2) to a network of worldwide distributed astroparticle physics and optical astronomy observatories. The arrival direction points to a known blazar (TXS 0506+056).

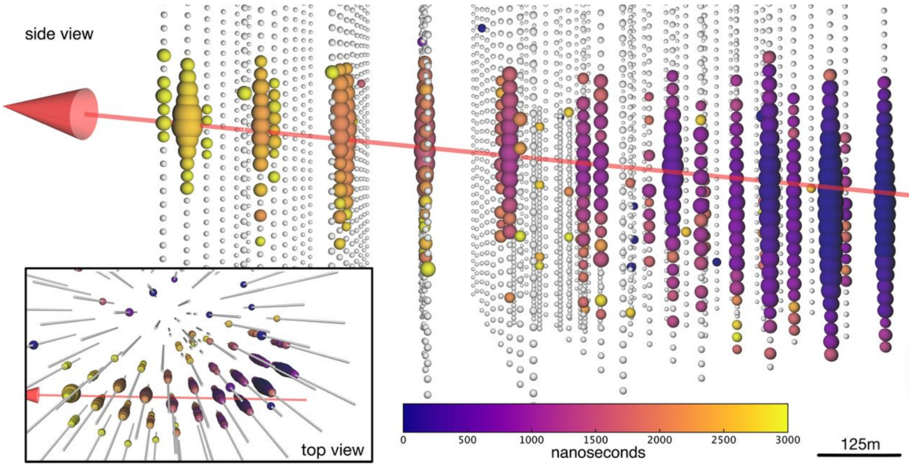

Figure 2.2: The muon Cherenkov track, initiated by a high-energy neutrino, seen by the IceCube observatory [13]. The white dots represent the in-ice photosensors, the size the charge deposit seen by the photosensors and the color code the signal-over-threshold trigger time. The event length was around 3000ns, which leads to a good determination of the arrival direction of the origin of the high-energy neutrino. The IceCube Observatory detection techniques are described in more details in Chapter 3.

Follow-up studies (Figure 2.3) by more than 10 of worldwide observatories showed that, for the first time, it was possible to identify a distant galaxy as a source of high-energy neutrinos [13] by detecting gamma rays from the same source.

Theoretical models and simulations suggest an acceleration mechanism which, next to high-energy neutrinos, can produce high-energy gamma rays. The discovery of a coincident signature of this blazar, consisting of high-energy neutrinos and gamma rays,

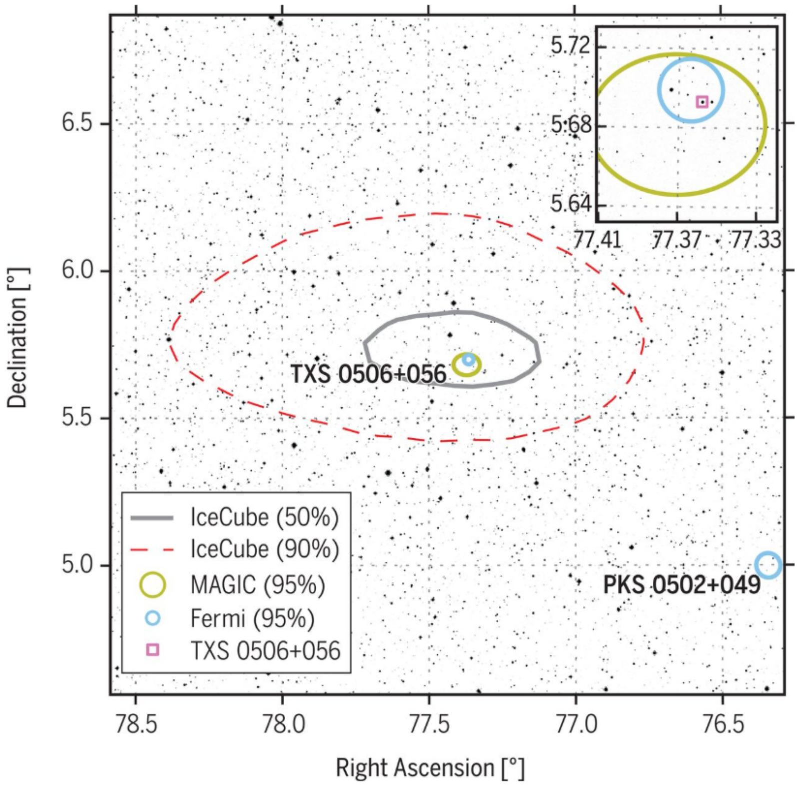

Figure 2.3: Multimessenger observation of the blazar TXS 0506+056 [13]. The 50% and 90% containment region is dashed and solid "circled". The yellow and blue region is the 95% containment gamma ray detection by the Fermi free-flyer and the MAGIC gamma ray telescope at La Palma.

might confirm that blazars can be the source of high-energy neutrinos.

2.3 Extensive air-showers and its muon production

High-energy particles are detected by ground experiments using air showers due to the low flux of cosmic rays at high energies (Figure 2.1). An extensive air-shower (EAS) is shown schematically in Figure 2.4.

Air showers develop when incident cosmic-ray particles interact with particles in the Earth's atmosphere. Depending on their energy, they either interact with other particles, decay into other particles, or loose energy by Bremsstrahlung. A distinction is made between different shower components, the muonic component with neutrinos, the hadronic and the electromagnetic components.

In hadronic interactions, pions ($\frac{\text{Pions}}{\text{Kaons}} = \frac{9}{1}$) and the three charge states (0, +, -) are nearly produced with the same rate, so that one third feeds into the electromagnetic component. Charged pions can, however, generate further pions through strong interaction with particles of the atmosphere. Most of the energy is thus deposited in the electromagnetic component. Electrons and positrons are the most common particles in an air shower. First, the number of electrons and positrons increases with the depth of the shower. Due

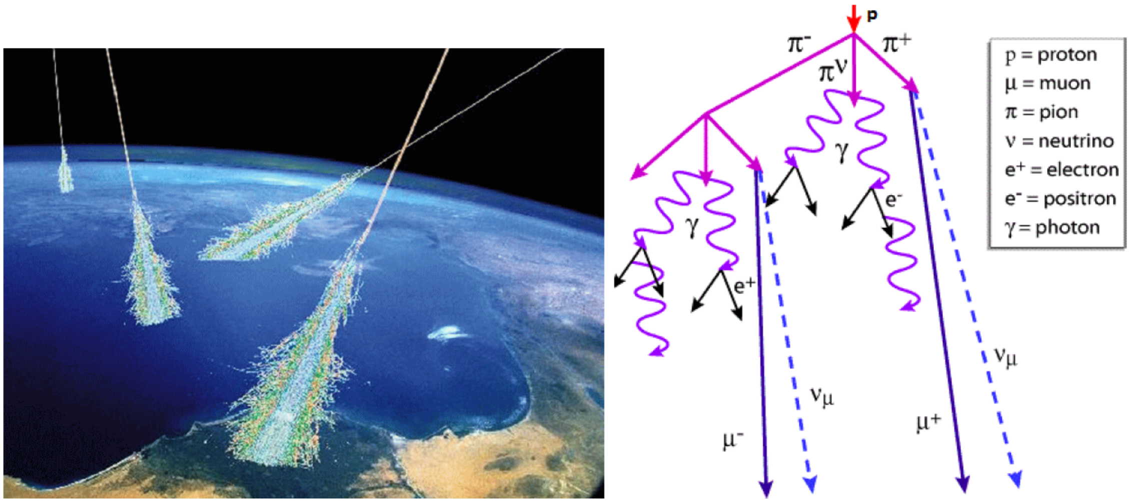

Figure 2.4: Left: Illustration of air showers, induced by cosmic rays. A large instrumented area is necessary to detect cosmic rays with high energies due to their low flux. Right: Sketch of a particle cascade with its hadronic, muonic and electromagnetic component [7].

to absorptive processes such as ionization, Compton scattering and the photo effect, particle production decreases exponentially after a shower maximum. An estimation of the shower maximum of the electromagnetic component can be done by using the Heitler model [14].

Photons, electrons, positrons and muons are carrying the majority of the EAS energy to the ground. In Figure 2.5 the number and energy density ($x_G = \frac{E_i}{E_G}$) of photons, electrons, positrons and muons for EAS, with different primary particle energy, at 5000 m altitude is shown. EAS induced by gamma rays showing the observed dominance of photons as well as the occasional generation of muons and even the occasional energetic dominance at the bottom of muons. In proton-induced cosmic ray air-showers, most of the incoming energy is typically in the form of muons [15]. For both primary particle types, large fluctuations are to be expected at these energies, since only a few particles reach the ground.

The peak of the energy distribution in relation to the number per logarithmic energy interval is 6 MeV for photons, 20 MeV for electrons and 2-3 GeV for muons. In terms of total energy per logarithmic interval, the peak is 150 MeV for photons, 600 MeV for electrons, and 30-40 GeV for muons. The shape of these distributions is similar for air showers caused by primary particles with different energies [15].

In the atmosphere high-energy primary nuclei interacts with atmospheric ones, which produces pions and kaons. These particles decay into muons through the following mechanisms [16]:

$$\pi^- \longrightarrow \mu^- + \bar{\nu_\mu} \tag{2.3.3}$$

$$K^- \longrightarrow \mu^- + \bar{\nu_\mu} \tag{2.3.4}$$

Since the muon is not a stable particle, it decays with a half-life of 2.2 μs into following

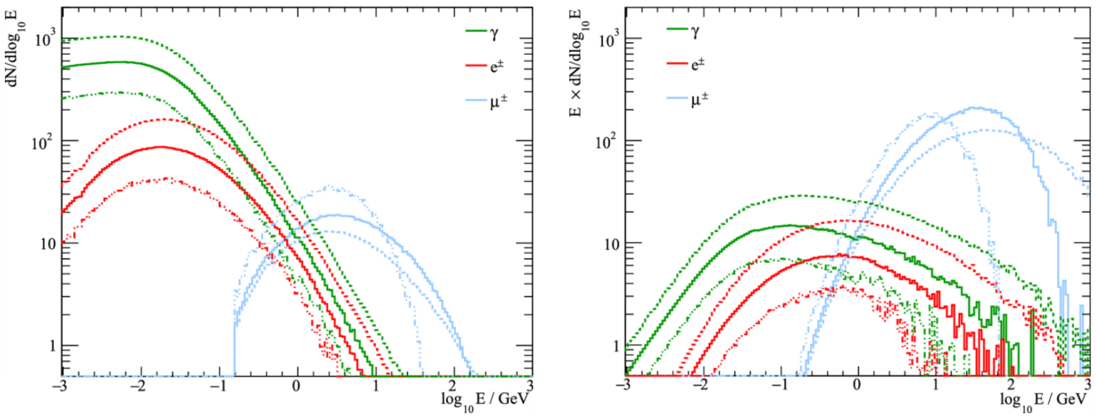

Figure 2.5: Number density (left) and energy density (right) distributions of particles near the ground at an altitude of 5000 m for vertical showers triggered by primary protons at three different energies. Solid lines correspond to 1 TeV primary energy, dashed lines to 10 TeV and dashed-dotted lines to 100 GeV. The distributions of the 10 TeV primary proton were reduced by a factor of ten, while the 100 GeV curves were multiplied by a factor of ten [15].

particles:

$$\mu^- \longrightarrow e^- + \bar{\nu}_e + \nu_\mu \tag{2.3.5}$$

Compared to the electron the mass of the muon is over 200 times higher. Due to this heavy mass the muon has a high penetration power. The high-energetic muons from air-showers are able to travel to sea level due to their relativistic speeds and can be measured with different detectors, like described in the next Section.

2.4 Detection techniques

In this section a selection of the worldwide most deployed detector systems for air showers will be introduced. After a short explanation schematics of the detector principles are following, including a reference for obtaining more information about the detection channel. A special focus will be set on the scintillation detectors, since they are used for this thesis (Chapter 2.3.1).

Cherenkov detectors

In a collision with an air molecule, charged particles are generated whose velocity is lower than the vacuum speed of light, but higher than the medium speed of light in the atmosphere. These particles emit Cherenkov light in the ultraviolet range, which can be seen as an optical analogue to the shock wave of a supersonic aircraft. This radiation was first observed in 1934 by Pavel Cherenkov. By filling a smaller, light-tight tank with as example water, the cherenkov light can be detected with photomultiplier tube. The Pierre Auger Observatory is using this instrumentation for around 1600 surface detectors with a diameter of 4 m each. In addition, the IceCube observatory also uses this type of detector for cosmic ray studies and as a veto detector for atmospheric muons (IceTop). If

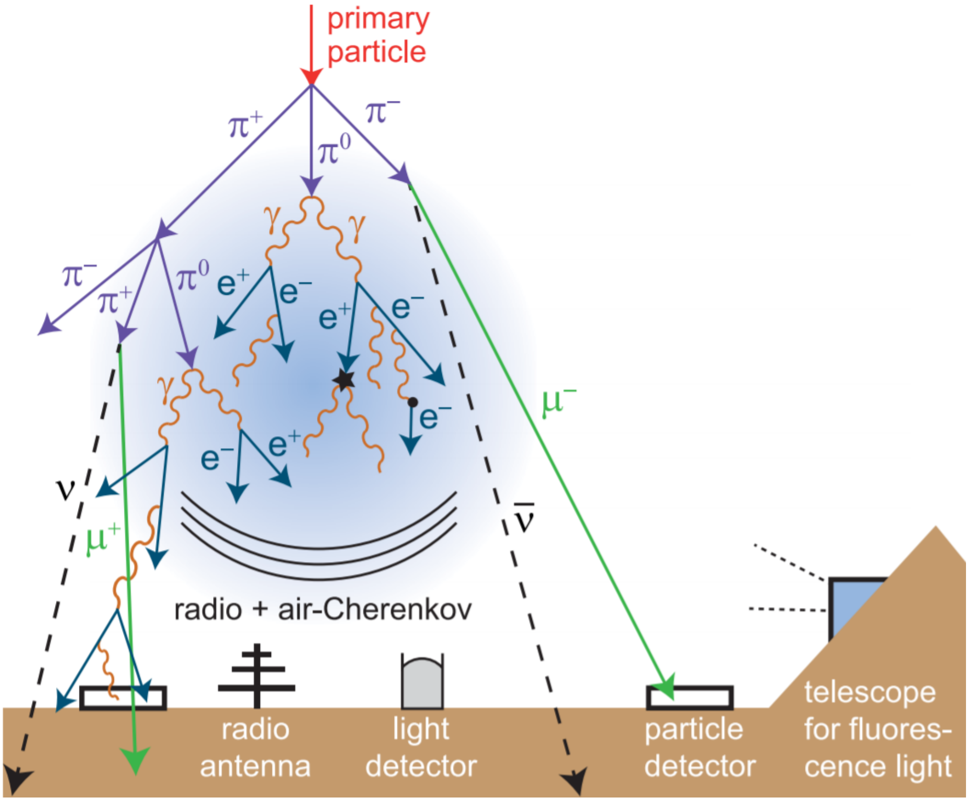

Figure 2.6: A selection of different experimental methods to obtain information about an extensive air-shower and therefore about the primary cosmic ray particle. Shown are particle detectors like scintillators, radio antennas and direct or indirect light detection cameras [17].

the detector volume is larger, the instrument can be used as a telescope, by recording the development of the cherenkov cone. This technique, used by the IceCube Observatory to detect astrophysical Neutrinos due to the weakly interaction with ice molecules, will be described in Chapter 3 in more detail.

Fluorescence cameras

The extensive air-shower is emitting isotropically fluorescence light along the shower axis mainly by the excitation of nitrogen molecules in the atmosphere (Figure 2.6). At the end of the cascade of the extensive air-shower, the particles have lost much energy as a result of collisions that at further collisions nitrogen molecules are excited to emit ultraviolet radiation. The different excitation states of nitrogen, for example, generate a characteristic spectrum which can be detected with UV-sensitive cameras. The radiation is emitted isotropically along the shower axis and is used to measure the longitudinal development of the shower. A fluorescence camera consists of one or more mirrors (Figure 2.8). In the case of several mirrors, these are aligned in different directions in order to achieve the largest possible field of view. The larger the actual mirror, the greater the number of photons that hit it, i.e. the greater the sensitivity of the camera. The mirror

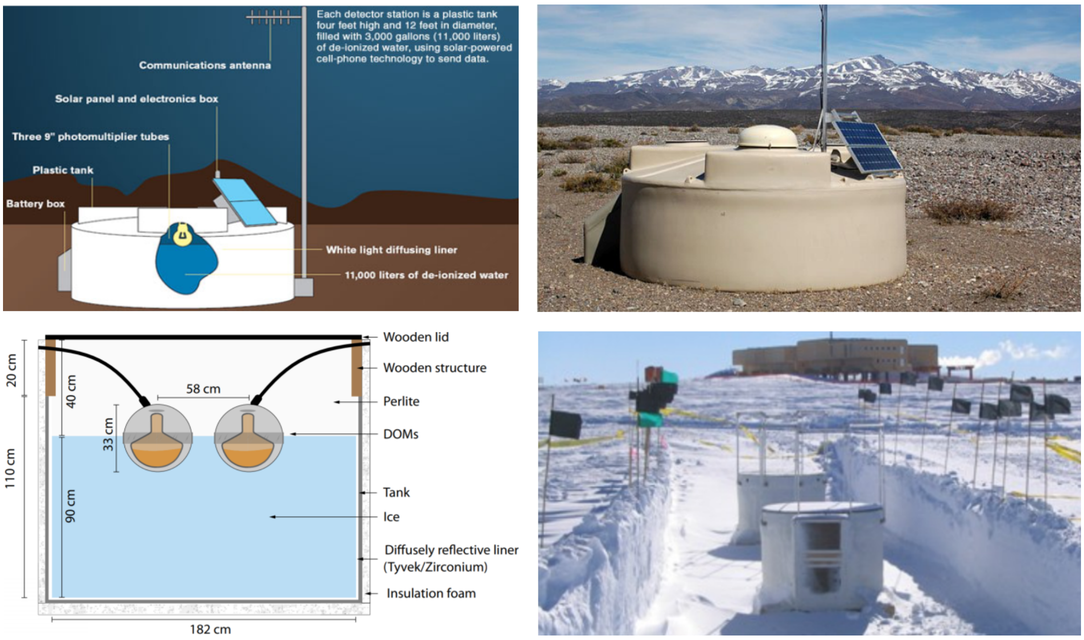

Figure 2.7: Top left and right: The water Cherenkov tanks of the Pierre Auger Observatory, located in the Mendoza region, Argentinia. The tanks are filled with 11,000 liters of de-ionized water, painted inside with a white light reflecting and diffusing layer and a read out with three photomultiplier tubes. The data is transmitted via a communications antenna which is using cell-phone technology. Bottom left and right: The same working principle is used by the surface array of IceCube at the South Pole, IceTop. Instead of water the tanks are filled with ice and are read out with 2 digital optical modules (DOMs), which are also deployed in-ice. The signal is transferred via a cable connection to a central DAQ, the IceCube Lab. [18, 19].

is curved that the reflected photons hit a camera of photomultipliers through which the photons are counted. The fluorescence cameras of the Pierre Auger Observatory or the Silicon Elementary Cell Addon (SiECA) are an example for measuring this channel of observation of extensive air-showers.

Radio antennas

A rather new approach to detect the electromagnetic channel of air showers are radio antennas. Due to mainly two effects, the Askaryan effect, in which a shower of particles in a material coherently emits radio frequency energy, and the geomagnetic emission, where the source of the radio emission is the geomagnetic induced separation of electrons and positrons in the air shower [17]. Most of the antennas are designed to receive radio signals in the 60-400 MHz band region since in this range the best signal-to-noise ratio coherence is given. As example, radio antennas are deployed at the Tunka region of Russia (Tunka-Rex) and is foreseen at the South Pole as further surface enhancement of IceTop. A description of the antennas used for the South Pole surface follows in Chapter 4 and can be found in [21].

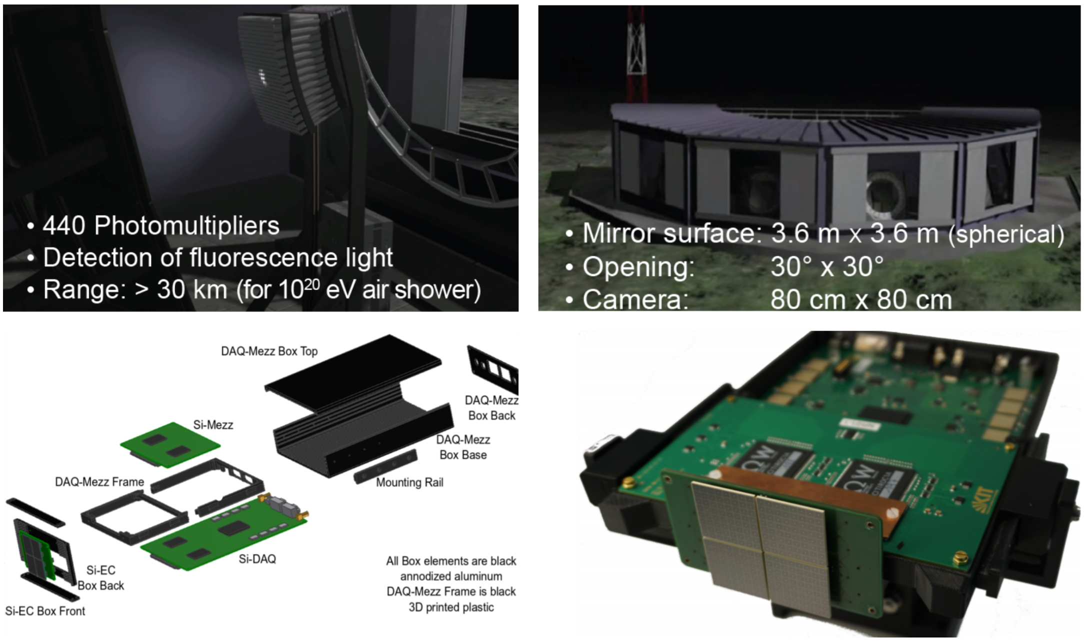

Figure 2.8: Top left and right: The Fluorescence detector (FD) of the Pierre Auger Observatory. Several mirrors are aligned in different directions and collect photons from the electromagnetic component of air showers excited ultraviolet radiation 2.6. The mirrors are curved in a way that the photons are guided to a focal point where a 440 photomultiplier tubes (PMTs) are placed. Bottom left and right: The Silicon Elementary Cell Addon (SiECA) camera. This camera is designed to be an extension to the EUSO pathfinder experiments to compare the baseline design of the EUSO camera, which is using PMTs with Silicon Photomultiplier (SiPMs). The EUSO collaboration foresees to measure fluorescence light by observing the atmosphere from space. For this, several pathfinder experiments like EUSO-TA, EUSO-SPB or Mini-EUSO are ongoing [19, 20].

Working principle of scintillation detectors

If a charged particle travels through matter, it loses kinetic energy and the particle can be deflected from its origin direction. For charged heavy particles, as example muons, these effects are primarily due to inelastic collisions with atomic electrons of the target material. A quantum mechanical description of how this energy loss relates to its relevant quantities is mathematically represented by the Bethe-Bloch formula, which describes the stopping power of a material for incident particles:

$$\left\langle -\frac{dE}{dx}\right\rangle = \left(0.307\frac{MeV}{g}cm^2\right) z^2\frac{Z}{A}\frac{1}{\beta^2}\left[\frac{1}{2}\ln\left(\frac{2m_ec^2\beta^2\gamma^2W_{max}}{I^2}\right)-\beta^2-\frac{\delta\left(\beta\gamma\right)}{2}\right] \tag{2.4.6}$$

where

$$W_{max} = \frac{2m_ec^2\beta^2\gamma^2}{1+2\gamma m_e\,/\,M+\left(\frac{m_e}{M}\right)^2} \tag{2.4.7}$$

describes the maximum energy transfer at a single collision and the term $\delta\left(\beta\gamma\right)$ adds the density effect correction to ionization energy loss. The charge and the mass of the

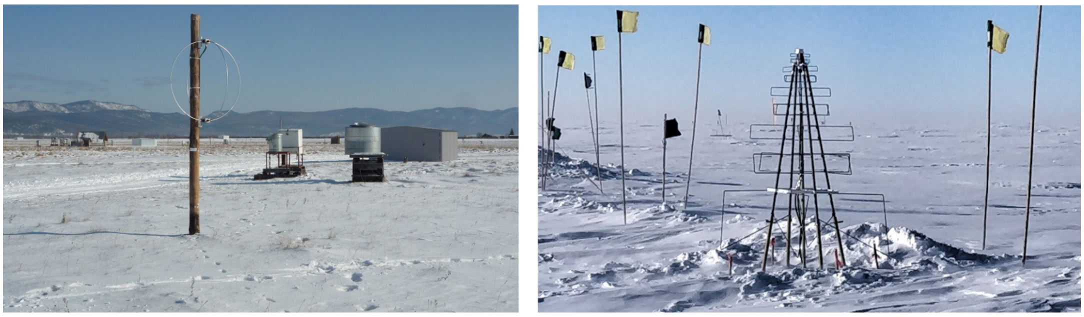

Figure 2.9: Left: Picture of the radio antenna of Tunka-Rex. The experiment is placed in the Tunka region of Russia. The 63 radio antenna stations measure the electromagnetic component of air showers in the 60-80 MHz band. Right: One of two deployed radio antennas at the South Pole. A more detailed description of the detection method can be found in Chapter 4: [17, 22].

incident particle is z and M. Z the charge of the medium and A its atomic mass. The mean excitation energy of the medium is described with I.

For low energies and momenta $\frac{dE}{dx}$ decreases like $\frac{I}{\beta^2}$ up to a minimum value which is reached around $\beta\gamma \approx 3 - 3.5$ (Figure 2.10). Particles in this kinematic region are called "minimum ionizing particles" (MIPs). These are the main effect detected by a scintillation detector for extensive air-showers.

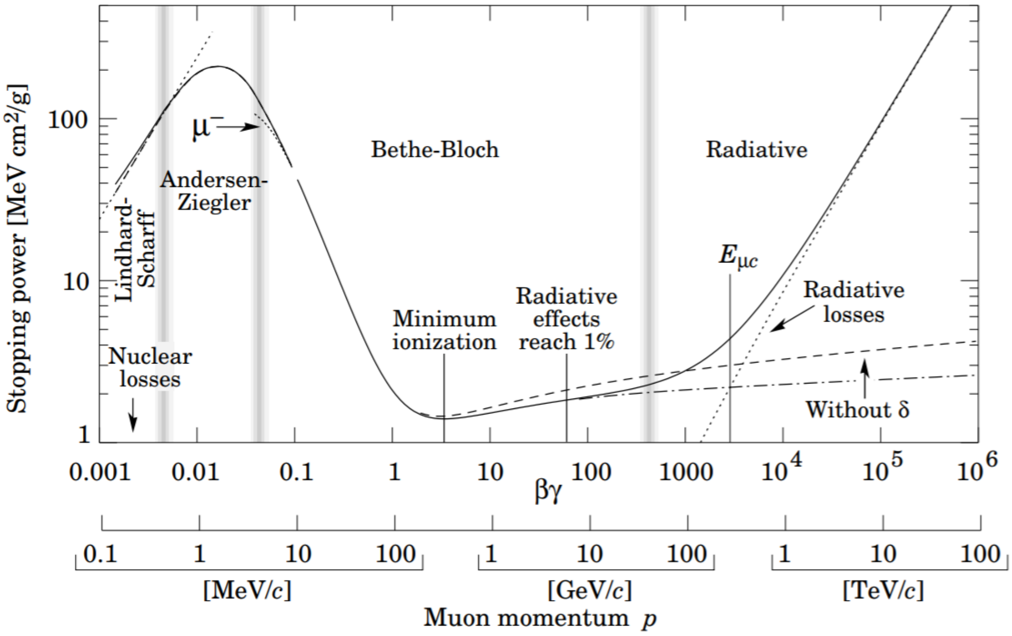

Figure 2.10: Bethe Bloch formula for muons, describing the stopping power $\left\langle -\frac{dE}{dx} \right\rangle$ of muons in a medium. The minimum ionizing region can be found at $\beta\gamma \approx 3 - 3.5$ [23].

The AGASA (Akeno Giant Air Shower Array) collaboration used a scintillation detector array to measure extensive air showers. The detectors were placed over an area of

100 km^2, 111 detectors in total, each with a 1 m^2 and 5 cm^2 thick scintillation material [24]. With Monte Carlo simulations the energy deposit of electrons and muons (Figure 2.11) in the scintillation material was simulated.

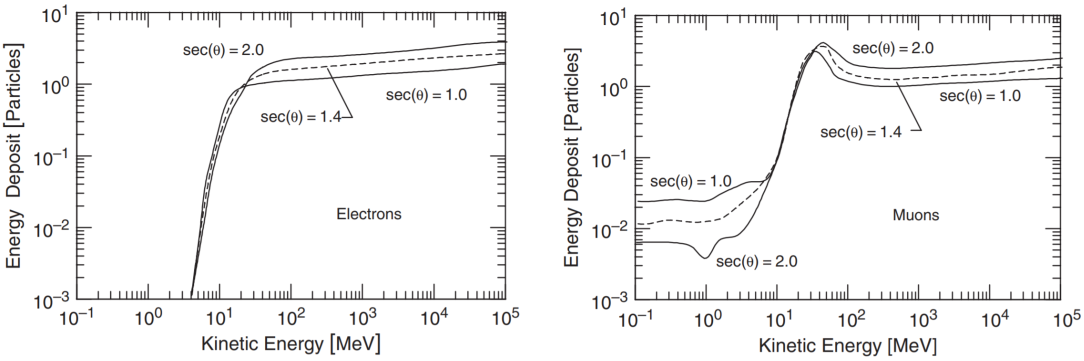

Figure 2.11: Simulated distribution of energy deposit in a standard AGASA type scintillation detector by electrons and muons incident at different zenith angles sec(θ). The energy deposit is converted to a particle number, using the standard pulse height produced by a single vertical equivalent muon (VEM) in the detector. [25].

As one example, this simulation shows that the main contribution of particles with a signal in the scintillation detector is from muons and high energetic electrons above 5 MeV. Since it is the lowest threshold energy, most of the detected particles are MIPs, visible in the charge histograms which are shown in the next chapters (Figure 2.10).

To detect the muonic component and high-energetic electrons from air showers, scintillation detectors can be used.

The scintillation effect in general results in the production of a pulse of photons, with material- and doping depending emission wavelengths, after a material is hit by a charged particle or by radiation. Two commonly used type of scintillators, organic ones and inorganic crystals, can be used. The scintillation mechanism differs between these two types.

The working principle of organic, in specific organic plastic scintillators [26] will be explained, since this type of material is used within developing the scintillation detectors.

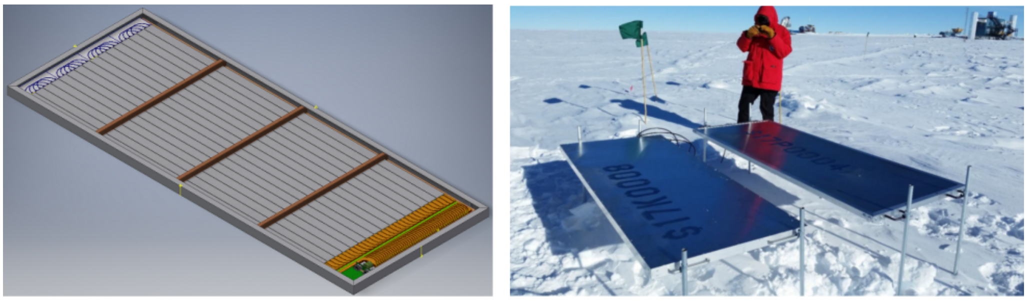

Figure 2.12: Left: The designed IceScint scintillation detector for this thesis. The scintillator bars (grey) are connected via wavelength-shifting optical fibers (green) and collect the produced photons to a readout electronic inside of the detector housing (green). A more detailed explanation will be given in later chapters. Right: One station of the deployed prototype scintillator array at the South Pole [27].

Organic scintillators are hydrocarbons containing ring compounds of the benzene type. Responsible for the scintillation process are de-localized valence electrons, which are not assigned to a certain atom within the molecule but "molecular π-orbitals". Typically these are electrons which circulate within a benzene ring. The default state is a singlet (S_0) (Figure 2.13, left). The excited singlet states (S_1, S_2, S_3) as well as the triplet states (T_0, T_1, T_2) are in terms of the energy level located above S_0. In addition, each state has a fine structure which corresponds to the various oscillating modes of the molecule.

The kinetic energy from a charged particle is absorbed by the scintillator material and excites the electron into different excited states. The singlet states with electron spin equal to 0 are named S_1, S_2, S_3 (Figure 2.13, left). For organic scintillators the energy level as example S_0 and S_1 is between $\sim$ 3 eV to 4 eV. Each of the single states are subdivided into a bunch of sub states with a finer structure. This is due to the different degrees of freedom, i.e. which of the translating or vibration eigenstates of the molecule are excited. The typical spacing of the sub states is 0.15 eV.

After excitation by ionization, the molecule undergoes excitation to e S_{10} e.g.. The state decays radiatively to sub-levels of the ground state. An excited triple state can't decay to ground due to angular momentum selection rules, which results in delayed fluorescence and phosphorescence light.

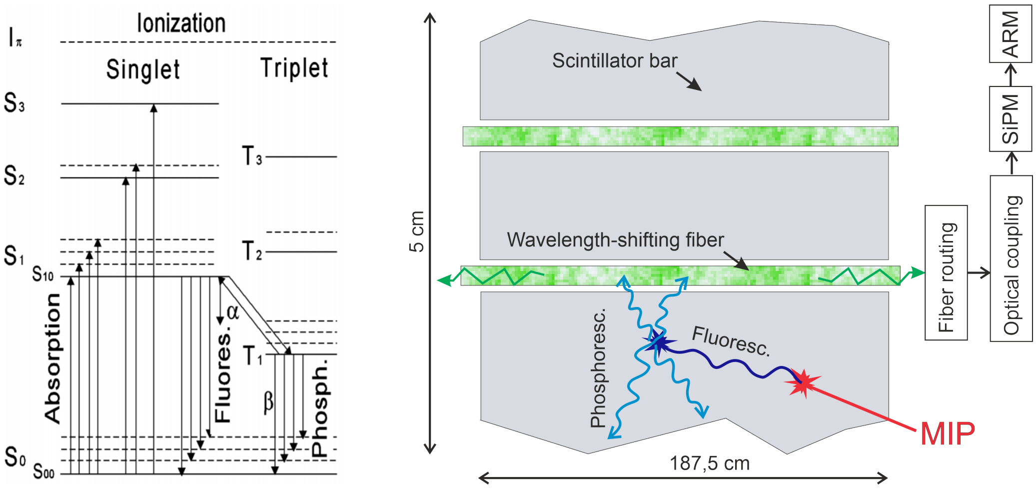

Figure 2.13: Left: Photon production in plastic scintillators. After excitation by ionization, the molecule undergoes vibrational relaxation to as example S_{10}. The state decays radiatively to sub-levels of the ground state. An excited triple state can't decay to ground due to angular momentum selection rules, which results in delayed fluorescence and phosphorescence light [25]. Right: Schematic section of the used scintillator bars for the detectors. The extruded plastic scintillator material includes 2 holes for the wavelength-shifting fiber. The scintillator material is coated with a layer of high reflective TiO2. The emitted photons are routed to an optical coupling which transports the collected photons to a SiPM, read out by an electronic inside of the detector (Chapter 5).

After the absorption of a photon, light with a larger or at least the same wavelength is emitted within a few nanoseconds. This fluorescence process is described by the Stokes shift [28] (Figure 2.14). Some energy is lost by non-radiative processes like transformation in translation energy [29]. Therefore it leads towards longer wavelengths, so in less energy $\left(E = \hbar \cdot f = \hbar \cdot \frac{c}{\lambda}\right)$. Two different emissions of photons are possible. In the first case it is called Stokes displacement and in the second case resonance fluorescence [30] . There is one exception to the stokes rule: The two-photon fluorescence.

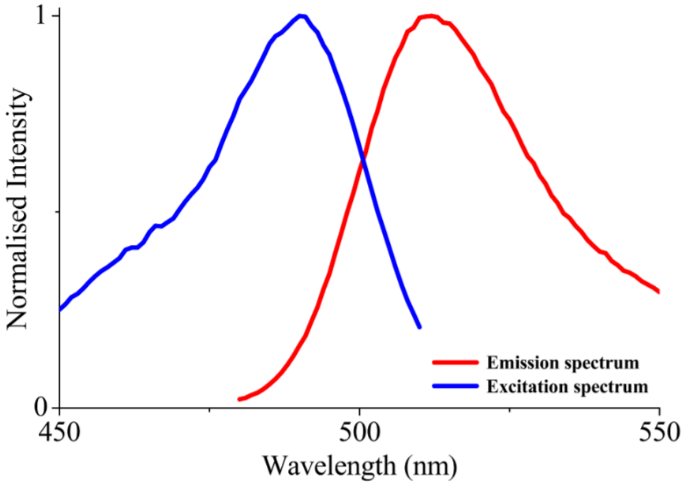

Figure 2.14: Example of the excitation and emission spectrum of a organic scintillator material. Some energy is lost by non-radiative processes like transformation in translation energy. Therefore it leads towards longer wavelengths, so in less energy. The Stokes shift is best visible in the shift of the peak wavelength of the spectra. [29]

Here two photons are absorbed and the wavelength of the emitted photon is greater than or equal to half the wavelength of the absorbed photons. The phosphorescence emission is similar to fluorescence, but the excited electrons come either directly or after loss of part of their excitation energy into a meta-stable energy state. The return to the ground state under photon emission is therefore delayed, up to a millisecond timescale. The for this thesis used plastic scintillator material, produced by a Fermilab extruder facility, is described in Chapter 5.2.

A single scintillator can provide information about the charge deposit and the time of arrival of the MIP. Furthermore it can be used for local coincidences with other detectors nearby (Chapter 8). With an array of scintillators, additional information like the shower axis and the energy of the shower can be measured (Chapter 9). In addition, the scintillator array can provide a trigger information for several other experiments like radio antennas deployed in between or next the scintillator array (Chapter 4).

3 The IceCube Observatory

The IceCube Neutrino Observatory is a cubic-kilometer Cherenkov telescope deployed at the South Pole that detects neutrinos of all flavors with energies from tens of GeV to several PeV. The observatory provided first measurements of the flux of high-energy astrophysical neutrinos, opening a new window to the non-thermal universe. IceCube is instrumented with 5160 digital optical modules (DOMs). Each DOM contains one large area photomultiplier tube and electronics for a local digitization of the charge deposit and the waveform of the signal over the set threshold.

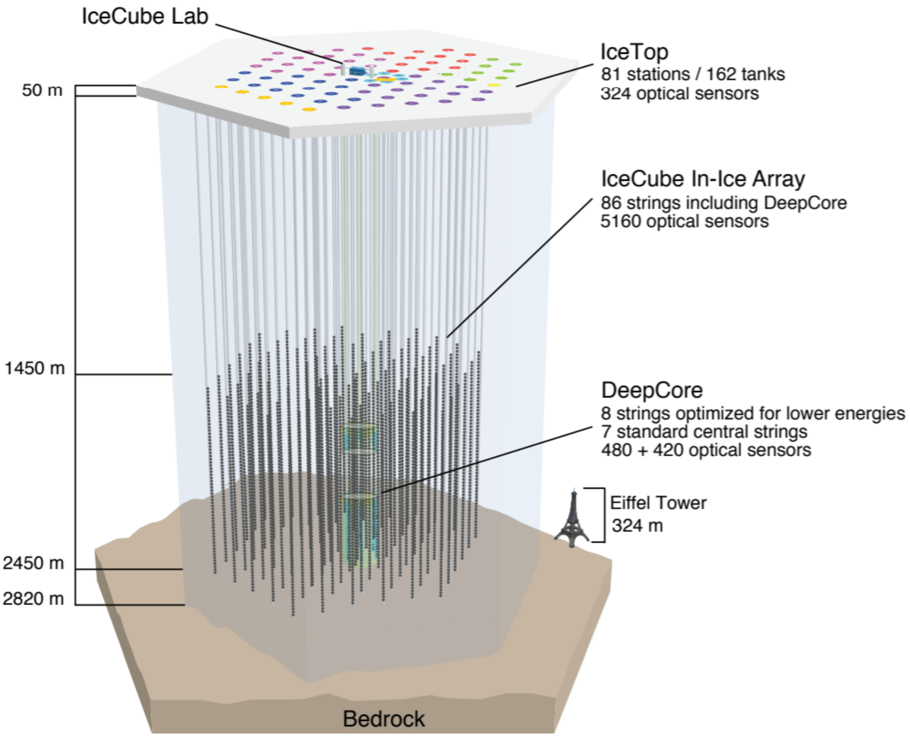

Figure 3.1: Illustration of the IceCube observatory at the South Pole. Sketched is the IceCube Lab as central DAQ, the IceTop surface array, the 86 strings with DOMs and the additonal DeepCore strings with smaller spacing. [6]

These DOMs are arranged in 86 strings, each buried in the ice (Figure 3.1). The DOMs are placed at a instrumented depth between 1450 m and 2450 m to increase the signal-to-noise ratio between neutrino signatures and atmospheric muons. The spacing between the drilled holes for the strings is approximately 90 m. This design allows neutrinos with energies above 100 GeV to be detected.

In addition, the DeepCore extension was deployed. DeepCore consists of the same DOMs, but the surface spacing and the string spacing between single DOMs at one string is lower of the 8 additional strings. This extension allows the IceCube observatory to measure low energy neutrinos of 50 GeV.

Detection technique

Neutrinos from galactic and extragalactic sources are not deflected by magnetic fields on their way through the universe due to their charge neutrality and their very small cross section and are only absorbed to a very small extent.

At the IceCube observatory, an incoming neutrino can not be detected directly, but is detected by the secondary particles produced by weak interaction (Figure 3.2) with the atomic nuclei of the ice molecules. Weak interactions can be divided in charged and neutral current. In hadronic neutrino interaction it can be divided into two classes, depending on if the neutrino continues on its way (neutral current, NC) or if a charged lepton (e, μ, τ) appears (charged current, CC). They differ in the exchanged weak boson, $W^{\pm}$ for NC and Z_0 for CC.

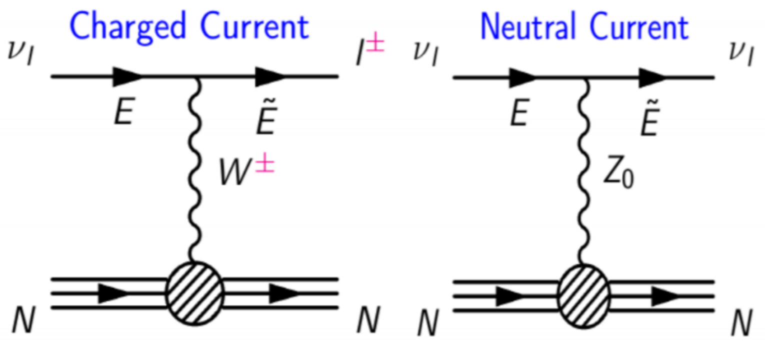

Figure 3.2: Feynman diagrams for charged current and neutral current neutrino interactions with a nucleon. They differ in the exchanged weak boson and the outgoing lepton (charged current) or neutrino (neutral current) [31].

The in-ice detection technique is for the water- or ice Cherenkov detectors based on the Cherenkov effect (Chapter 2). Unlike the small volume water- or ice detectors, which are detecting a signal of as example a muon and calculating locally the charge deposit and therefore the energy of the particle emitting cherenkov light, the same effect can used in large-scale Cherenkov detectors to reconstruct a arrival direction of the particle.

If a neutrino interacts with an atomic nucleus of the detector material, a charged particle is formed which moves in the medium with a faster speed as the light speed in the medium. Since a charged particle radiates photons when traversing a medium, if its velocity is larger than the local phase velocity of light in the material. The light is emitted

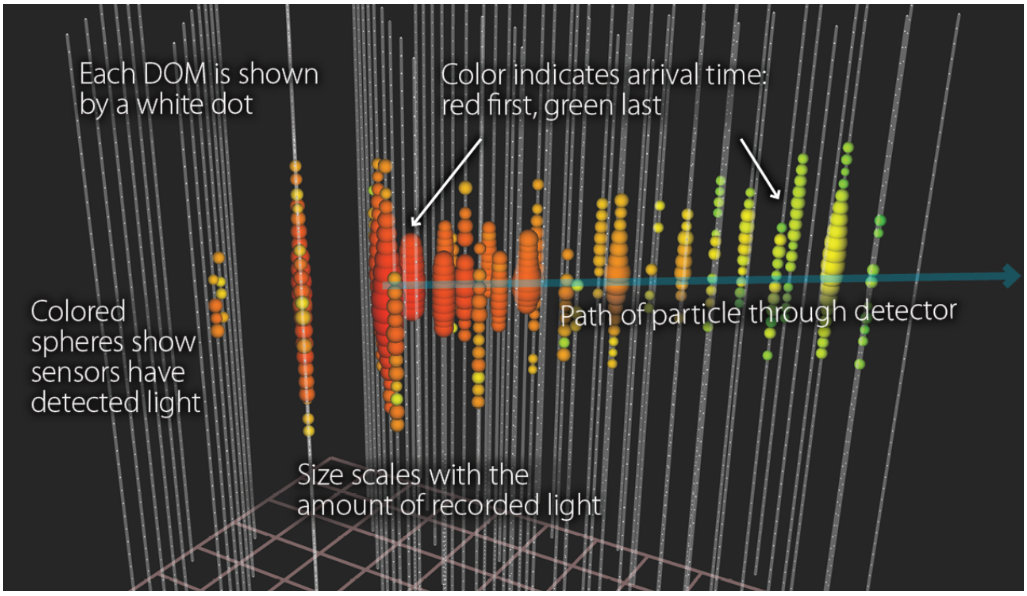

Figure 3.3: Example event of a detected muon trace at IceCube in-ice detector Each dot is a DOM. The color code indicates the trigger- and therefore the arrival time of the photons. The size of the colored dots scales with the charge deposit at the DOM [32].

in a characteristic (Cherenkov-) cone with an specific opening angle [6], which depends on the velocity of the particle and the index of refraction. IceCube uses glacial ice as a Cherenkov medium for the detection of secondary charged particles produced by neutrino interactions with the Earth. The resulting cone can be reconstructed with the in-ice DOMs.

In Figure 3.4 the signal shapes of the in-ice detector, depending on the flavor of the neutrino, is shown. All three Lepton flavors can be detected with the in-ice detector, but muons are particularly suitable for good directional or trace reconstruction of initially neutrino. Myons generate long traces in the detector (3.4) because they have a relatively high mass ($105.66\ \frac{\mathrm{MeV}}{\mathrm{c}^2}$ compared to $0.511\ \frac{\mathrm{MeV}}{\mathrm{c}^2}$ for electrons [35]) and a long lifetime. Electrons, on the other hand, are almost directly reabsorbed, since they are interact more strongly with the atoms. Tau leptons induce in the detector a very bright, but also very short cascades. Due to their high mass, they decay quickly and therefore have only a short trace. By decay of the tauon to a muon or electron the detector is seeing, as long as the decay process happens in the detector volume, a “double-bang” (3.4).

3.1 IceTop

IceTop is located almost on the edge of the surface and consists of 162 tanks (Figure 3.5, right) filled with ice. These are also instrumented with DOMs and were mainly installed to detect air shower using the Cherenkov effect and to serve as veto detectors for the in-

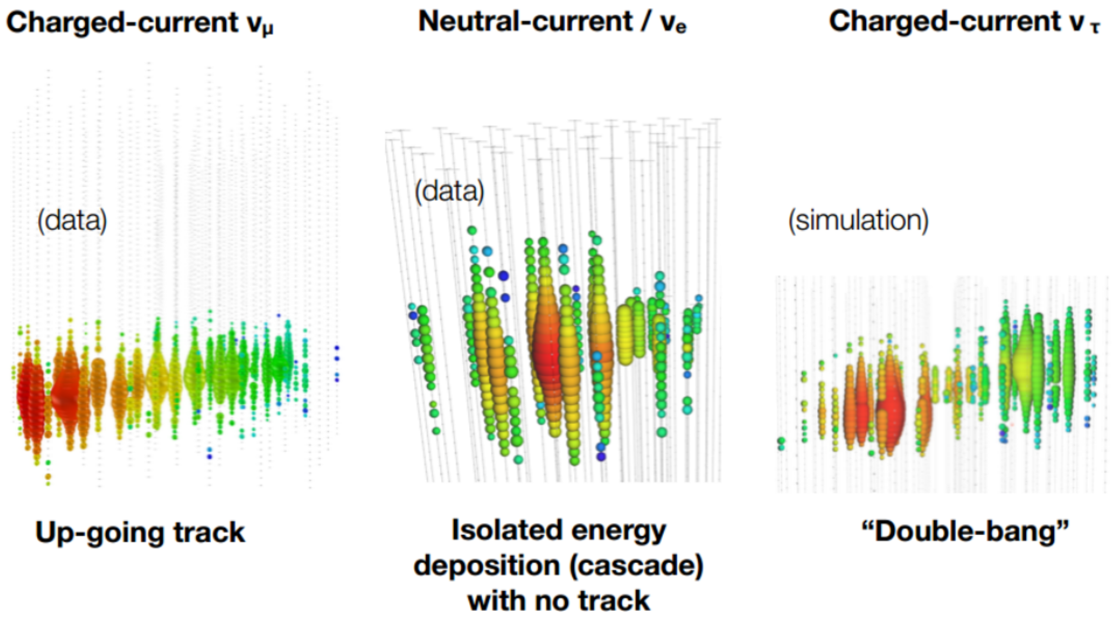

Figure 3.4: Signals shapes of the in the in-ice detector, depending on the leptonic flavor of the neutrino interacting with the ice molecule. A muon neutrino is starting a track (left) which can be used to reconstruct the arrival direction of the neutrino. The electron neutrino is visible as a isolated energy deposition, like a "bang" (center). By decay from the tau neutrino to a muon or electron neutrino the detector is seeing a "double-bang". [33]. The track signal and the isolated energy deposition are real data, the tau neutrino signal is, in this Figure, a simulated one. An atmospheric tau neutrino might have been seen in the analysis of 3 years of recorded data with the DeepCore sub-array [34].

ice to distinguish neutrino induced events and cosmic muons. IceTop is divided into 81 stations, which have the same layout as the in-ice strings (Figure 3.5, left).

The individual stations consist of two tanks at a distance of 10m. Each of these tanks is equipped with two different DOMs. They differ in the gain of the PMT signals on the DOM main board to increase the dynamic range of a tank. The air shower energy resolution of the IceTop array is in the PeV to EeV region.

In Figure 3.6 (left) a typical waveform of a DOM in an IceTop tank is shown. The pulse shape is determined by the tank properties and the readout electronics and follows the typical PMT increasing and decreasing flank. By integrating these signals, a charge histogram follows (Figure 3.6, right).

Several fit functions have been applied to illustrate the structure of the whole histogram (black fit). In this case, the background signals (red) have their peak at low charges of around 30 photo electrons (PE) and the VEM [1] peak (green) can be found at 134 PE.

---

[1] vertical muon equivalent

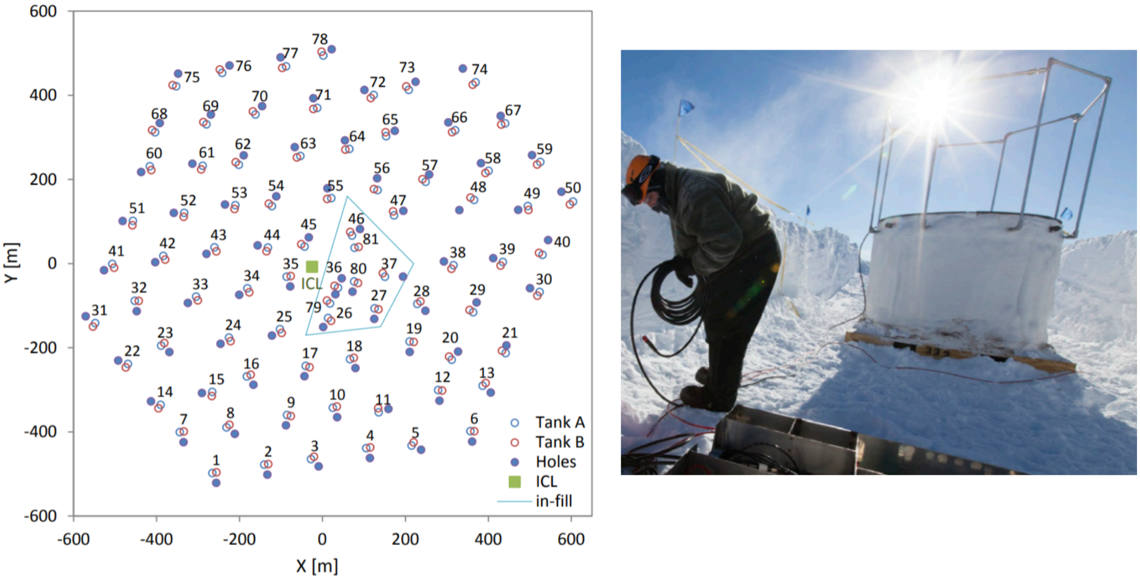

Figure 3.5: Left: The positioning of the IceTop stations with 2 tanks each (empty circles) in relation to the in ice strings location (filled circles). For logistics reason and less trenching the IceTop stations are close to the string locations [18]. Right: Picture of one IceTop tank during deployment. Today all IceTop tanks are fully covered and hidden by snow [36].

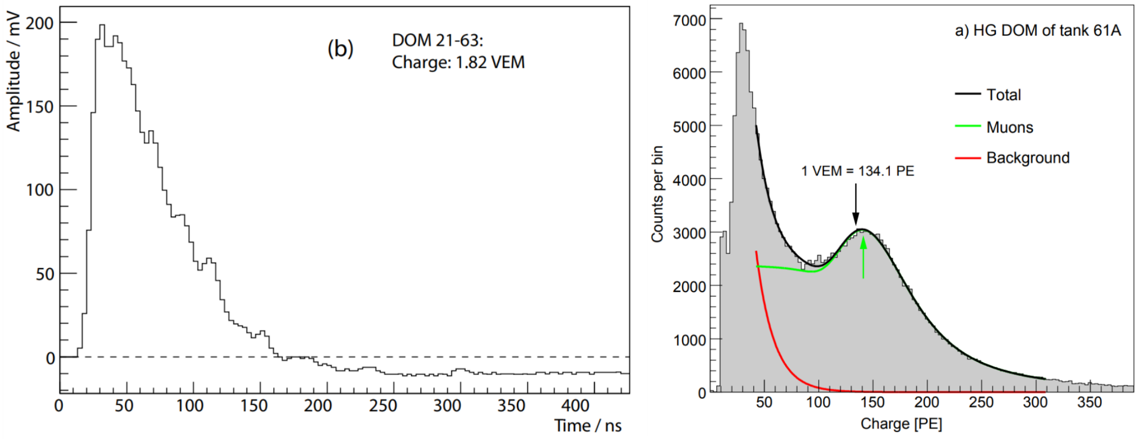

Figure 3.6: Left: Waveform of one DOM (21-63) of an IceTop tank. Like typical PMT signals, it has a steep rise and an exponential tail [36]. Right: Typical charge histogram normalized to PE, integrated from the High-Gain DOM signals in tank 61A. The VEM peak is visible at around 134 PE [36].

3.2 IceCube Upgrade

The IceCube collaboration foresees to increase the amount of deployed strings starting at the South Pole deployment season 2022/23 in order to enhance the capabilities of the

IceCube Observatory. Studies have shown that a deployment of new strings in the geographical region of the DeepCore array increases the capabilities of measurements the most. As example, DeepCore, which was deployed to measure low energy astrophysical neutrinos, will be improved by an additional new array of strings in order to lower the threshold for low energy neutrinos even more [37]. Due to the geometrical density of the array, IceCube will be the most sensitive experiment down to energies of 10 GeV for determining mixing parameters of neutrino oscillation like $\sin^2(\Theta_{23})$ and Δm^2_{32} (Figure 3.7) from the standard neutrino oscillation formula for as example the oscillation between muon neutrinos and tau neutrinos:

$$P_{\nu_\mu \to \nu_\tau} = \sum_{j,k} U_{\mu j} U^*_{\tau,j} U^*_{\mu,k} U_{\tau,k} \cdot e^{\left(i\frac{\Delta m^2_{j,k} \cdot L}{2E_\nu}\right)} \tag{3.2.1}$$

where U describes the PMNS [2] matrix, $\Delta m^2_{j,k} = m^2_j - m^2_k$ the mass-squared splittings, E_ν the neutrino energy and L the oscillation baseline. For, e.g, the new, observables $\sin^2(\Theta_{23})$ and Δm^2_{32}, distinguishable (Figure 3.7) with the IceCube upgrade, following 2-flavor approximation of the survival probability of a muon neutrino can be made [38]:

$$P_{\nu_\mu \to \nu_\mu} = 1 - \sin^2(2\Theta_{23}) \sin^2(1.27 \cdot \Delta m^2_{32} \frac{L}{E_\nu}) \tag{3.2.2}$$

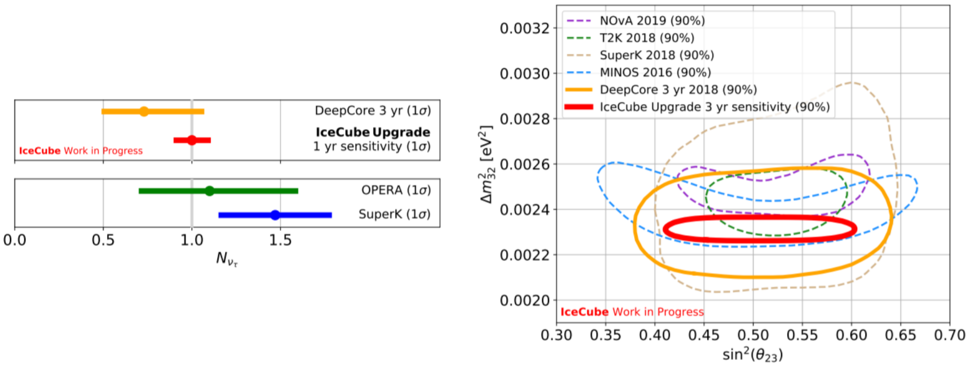

Figure 3.7: Left: 68% sensitivity of the IceCube Upgrade on ν_τ normalization value assuming a true value of 1 with 1 year observation. Also shown are the current best fit values of ν_τ normalization from OPERA and Super-Kamiokande. Right: The predicted performance of the IceCube Upgrade on the measurements of $\sin^2(\Theta_{23})$ and Δm^2_{32} assumes 3 years of lifetime. Also shown are the 90% confidence contours in the $\sin^2(\Theta_{23})$ and Δm^2_{32} plane in comparison with the ones of the most sensitive experiments [37].

The IceCube upgrade contains the drilling of 7 additional holes and therefore 7 new strings (Figure 3.8) will be deployed. This strings are equipped with different new DOM designs and several calibration devices like UV-flashers and acoustic sensors.

The, in this thesis used and calibrated, surface “fieldhub” DAQ, which contains among others the IceTAXI system, is a proof of design of the infrastructure in development for the IceCube Upgrade (Chapter 4).

---

[2] Pontecorvo-MakiNakagawa-Sakata

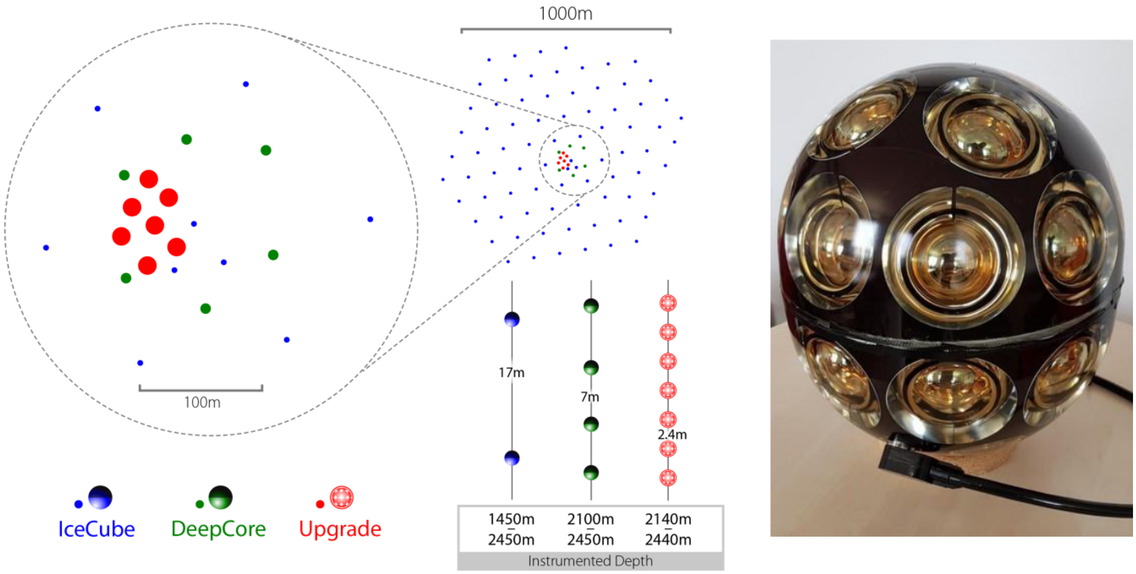

Figure 3.8: Left: Schematic of the IceCube upgrade. Next to the existing IceCube and DeepCore strings (blue and green) the new position of the 7 new drilled holes at the South Pole is marked. Next to a closer spacing between the strings the strings itself are denser instrumented compared to IceCube or DeepCore. Right: One of the three different new developed DOMs. Pictured is the "mDOM", with 24 PMTs mounted to one module each [32]

While the IceCube Upgrade will open new measurement channels for neutrino physics and astroparticle physics in general, it will also serve as research and development and benchmark of the in-ice instrumentation for a proposed new facility, the IceCube-Gen2 Observatory. In parallel also the surface array will be enhanced.

3.3 IceCube-Gen2 Observatory

The IceCube Collaboration foresees to increase the present surface and in-ice instrumentation by a factor of 10, so 10 km^3 instrumented volume instead of 1 km^3 [39], dedicated to the high-energy astrophysical neutrinos in the PeV range. It will offer significantly improved sensitivity at both high and low energies. This proposed new astroparticle detector facility is called IceCube-Gen2. This facility can be divided into two deployment sections, the In-Ice and the surface instrumentation.

In-Ice instrumentation:

In first case studies the in-ice array aims for increasing the amount of detected high-energy astrophysical neutrinos and a better angular resolution of its origin. To achieve this, approximately 120 strings are to be deployed and have a larger spacing with ~240 m instead of ~90 m of the current IceCube setup [40].

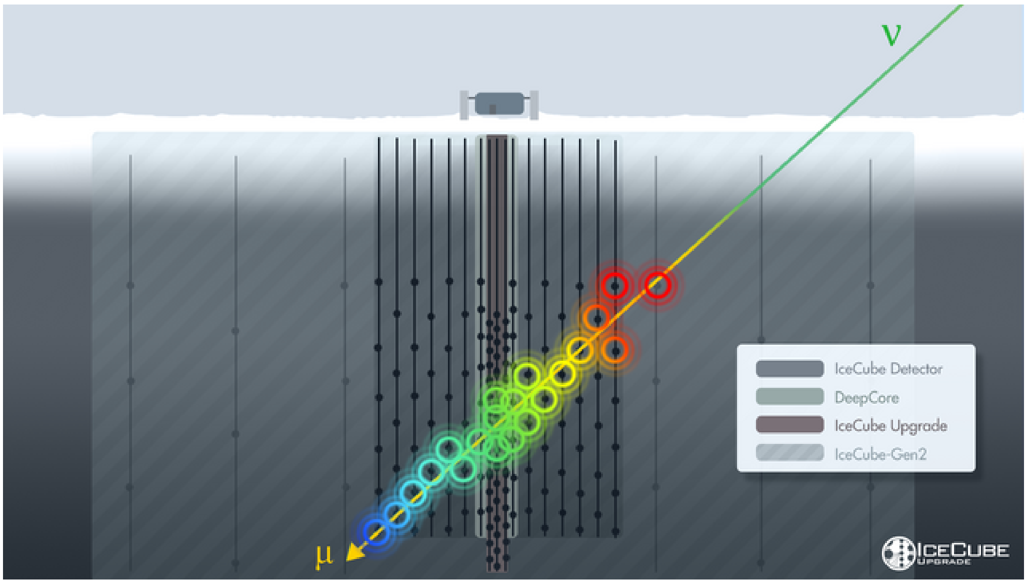

Figure 3.9: Illustration of a possible IceCube-Gen2 facility with focus on the In-Ice instrumentation. The IceCube-Gen2 strings volume is colored in light gray. Visible is the larger spacing between the strings. This allows to detect and reconstruct high energy muon traces and increases the possibility to determine “double-bang”signatures of tau-neutrinos. In addition, a muon-neutrino detection signature is sketched [32].

Surface instrumentation:

In Figure 3.10 a proposed layout of IceCube-Gen2 is illustrated. Visible in red is the actual IceCube, which is extended in red with additional in-ice DOM-strings. This “bird view” shows the proposed surface enhancements in green and blue, too. It should consists of cosmic ray array, realized as example with scintillators and radio antennas. Currently under discussion is whether the new surface array should cover an area as shown in this sketch or only be distributed over the area of the new DOM-Strings to be installed.

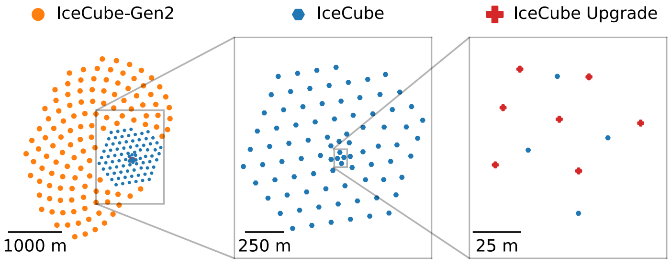

Figure 3.10: Sketch of a proposed IceCube-Gen2 layout, compared to IceCube and the IceCube Upgrade. The markers are illustrating the position of the strings of IceCube (blue), the to be deployed strings of IceCube Upgrade (red) and the new strings of a possible IceCube-Gen2 Observatory (orange). For the surface design, one station per string position is foreseen [39].

Expected performance of IceCube-Gen2:

One aspect of the expected performance and the increased discovery potential of IceCube-Gen2, with deployment parameters and dimensions like described in this Subchapter, can be seen in Figure 3.11. The focus is set on the improved reconstruction of events in terms of the decreased angle reconstruction uncertainty and the possibility to determine the behaviour of the flux of high energetic neutrinos. The median angular distance between the true muon direction and the reconstructed one is due to the larger instrumented area and therefore more sensors which can contribute to parametrize the arrival direction of the muon lowered. Since the IceCube-Gen2 DOM systems, like described in Chapter 3.1, are developed for an improved charge deposit determination and the increased amount of deployed DOMs at all, it can be expected that a high-energetic neutrino-like event, for example sketched in Figure 3.9, allows IceCube-Gen2 to dismantle the behavior of the flux of neutrinos in the UHECR region.

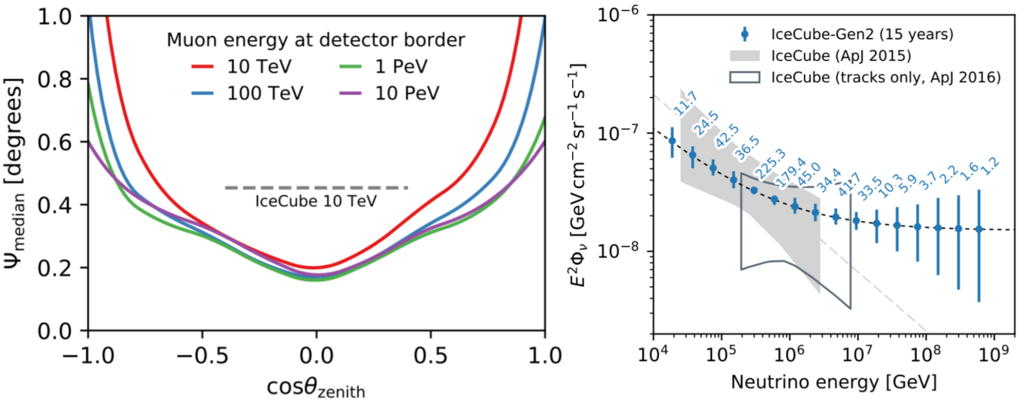

Figure 3.11: Left: Decrease of the zenith angle uncertainty of muons with IceCube-Gen2. It shows the median angular distance between the true muon direction and the reconstructed one at different muon energies. For comparison the median angular uncertainty of the IceCube observatory is shown. Right: Expected flux of high-energy diffuse neutrinos measured with IceCube-Gen2 after 15 years in operation compared with the actual IceCube observatory. The dotted line represents a superposition of different (E^{-2} and $E^{-2.5}$) components of the flux, which is compatible to the all-channel (low threshold) and muon only (high threshold) component analysis. Gen2 would allow to distinguish between the low energy spectrum (grey dashed line) and the high threshold UHECR spectrum that continues at higher energies (at around $10^{5.5}$GeV) [40].

In addition to a new and geometrically extended in-ice upgrade at IceCube-Gen2, it is foreseen to instrument the surface of the South Pole with different, but combined detector systems. The first scintillator station (Chapter 4) is also a prototype for a large-scale surface array of IceCube-Gen2.

4 The IceCube IceTop surface enhancement

In this Chapter a short introduction of the planned IceTop surface enhancement, which is currently in prototyping status, is given. Next to the scintillator array station, the topic of this thesis, a brief overview of the plans for additional radio antennas and an imaging Cherenkov telescope will be shown. Furthermore, a sum up of the science case of this enhanced surface instrumentation will be given.

4.1 IceScint

IceTop examines the cosmic-ray sky by investigating the muonic and electromagnetic component of air showers. More detailed measurements are needed to understand the astrophysics of the high-energy cosmic-ray sky. In addition, the need to mitigate the impact of snow accumulation on the existing IceTop tanks is necessary. Like the IceTop tanks, scintillators are sensitive to electromagnetic particles and muons from extensive air-showers. However, the measurable signal is differently compared by the muonic and electromagnetic air-shower components and therefore will provide complementary in function. The total charge deposit in each scintillation detector, measured in calibrated units of MIPs, is used to reconstruct the energy deposits of the air-shower particles into the scintillation detector. This can be obtained by fitting the MIP peak from the charge spectra.

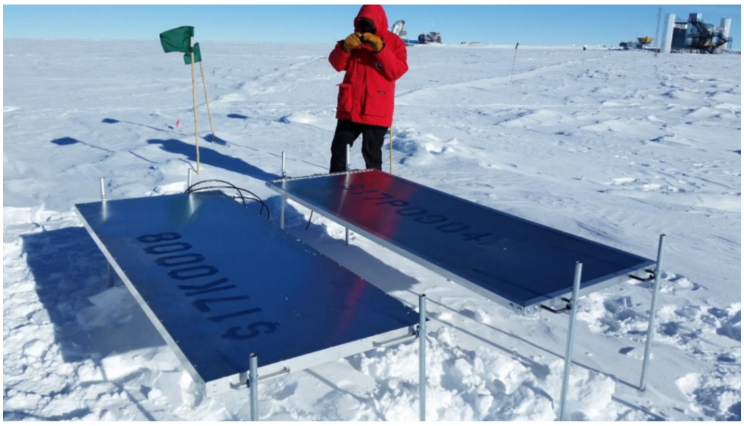

Figure 4.1: One detector position of the first IceScint station at the South Pole, deployed in season 2017/18.

The original concept for the new IceScint scintillator array was to extend the existing surface of IceTop with 37 stations homogeneously-spaced, each station comprising seven scintillators, aligned in an hexagonal shape, communicating with a central DAQ (Figure 4.2), like the IceScint prototype station developed within this thesis for the 2017/18 deployment season.

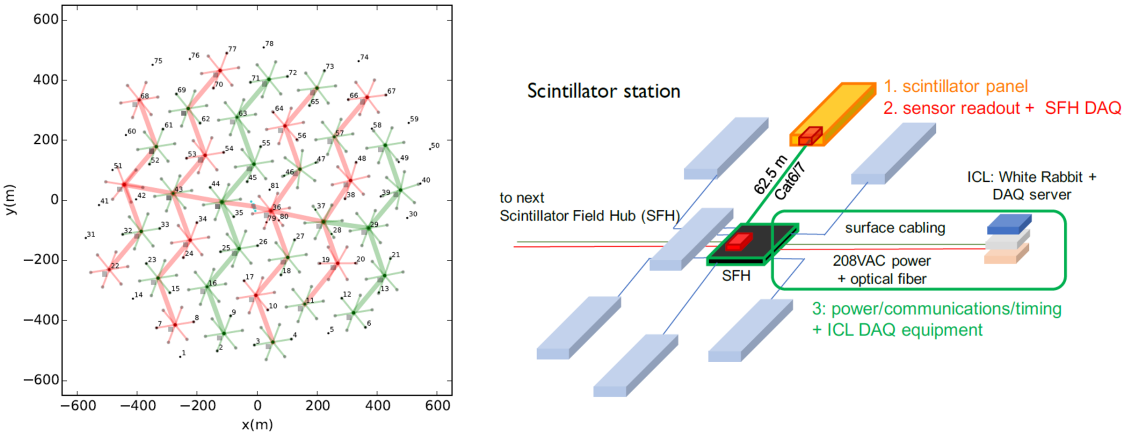

Figure 4.2: Left: Proposed deployment map of the 37 scintillator stations as enhancement of the IceTop array, as planned in 2018. Each number points to an existing IceTop station. The hexagon shaped forms denotes the proposed scintillator station with its seven scintillaton detectors. The red and green lines showing a possible and effective cable trenching plan. Right: Sketch of one of the 37 planned scintillator stations. Seven scintillation detectors are connected to a central surface field hub (SFH), which includes the DAQ, the power suppy and timing and communication via a white rabbit (WR) node. The WR node communicates with the central IceCube DAQ at the IceCube Lab (ICL). In 2019 the layout of the proposed deployment map and the layout of one station changed and can be found in [41] and [42].

Details about the scintillation detectors and its DAQ are discussed the following chapters.

4.2 Radio antennas

As described in Chapter 2, another window to measure a component of air showers is its electromagnetic footprint in the MHz region. Therefore, it is planned to deploy radio antennas at the South Pole in order to achieve a hybrid detector array with scintillators and radio antennas. For this, in the season 2018/19 two first radio antennas were installed by a KIT group inside of the 2017/18 deployed IceScint station and are read out by "Radio-TAXI", a derivative of IceTAXI (Figure 4.3, left). The distance between the DAQ and the antennas is approximately 35 m. For prototyping purposes in terms of snow accumulation and mechanical stability, two different antenna heights were deployed.

The design of the antenna was developed by the SKA collaboration [43]. The key feature of this logarithmic antenna design is the possibility to receive signals in the high MHz region with a high bandwidth and a good suppression of upgoing (e.g. at the surface reflecting) radio signals. Each antenna has two polarization channels which can be read out by a low noise amplifier (LNA), attached on the top of the antenna. First measurements at the KIT hybrid array, the calibration process and measurements from the

South Pole can be found in [41].

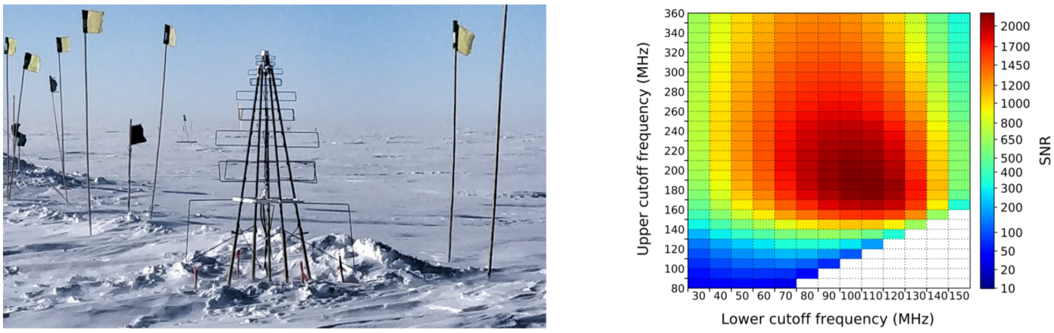

Figure 4.3: Left: Picture of a deployed prototype antenna at the South Pole in the IceCube season 2018/19 . Visible is the logarithmic antenna design in order to receive a higher frequency range [21]. Right: By extending the frequency band of measurement to higher frequencies than those used by current radio air shower arrays will improve the capabilities of radio measurement at the South Pole. Visible is the in a 2D-heatmap the expected optimal frequency region for the detection of PeV gamma rays from the galactic center [44].

It could be shown that, by using antennas with a frequency band in the 100 to 200 MHz region (Figure 4.3, right), the energy threshold is lowered to a value so that PeV gamma rays (PeVatrons) from the galactic center are detectable ([44], Chapter 4.4). The galactic center region is a complex and energetic region for all observable wavelengths. Plenty of experiments are targeting the galactic center, trying to observe as example dark matter, like the H.E.S.S. observatory [45]. In addition, H.E.S.S. measurements suggests a continuous injection of cosmic rays and that the super massive black hole Sagittarius A* is a hadronic cosmic-ray accelerator. The injection spectrum should reach up to 1 PeV and the detection of a signal, as example with radio antennas at the South Pole, would be the first proof of a existence of PeVatrons in the galactic center [46]. Each IceScint (hybrid) station will have 3 antennas included, e.g. ~100 antennas will be deployed. Radio antennas are sensitive to inclined showers [47]. This is important as the galactic center is always visible at 62° zenith from IceCube.

4.3 IceACT

Next to particle detectors and radio antennas, prototype studies and prototype deployments of an air-cherenkov telescope (IceACT) are ongoing since 5 years at the South Pole. IceACT contains a focal surface with 61 6 mm² SiPMs, which are used for the imaging of the air-shower emitted UV-light. The refractive optics allows a field-of-view of 12°. IceACT consists of a 0.5 m diameter Fresnel lens and Winston cones directly mounted to the photosensitive area of the SiPM in order to increase the effective area of the focal surface.

Within this thesis a, for prototyping purposes, a trigger board for IceTAXI was developed and tested [1] one week at the KIT hybrid array. The purpose of the trigger board is to enhance the capabilities of IceTAXI to give an external trigger from IceScint and radio

---

[1] with colleagues from RWTH Aachen and FAU Nürnberg-Erlangen and DESY Zeuthen

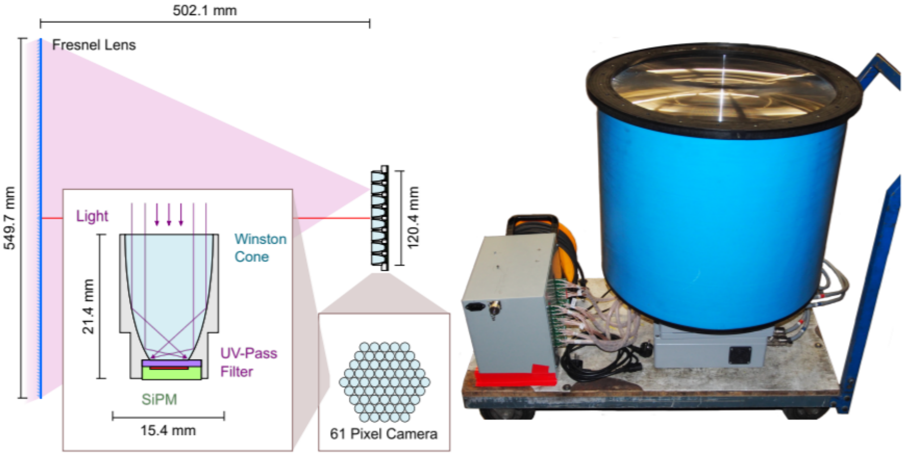

Figure 4.4: Left: Sketch of the imaging process of UV light. The Fresnel lens focuses the photon to a focal surface. The focal surface contains 61 SiPMs, with an UV-Pass filter layer and glued at the photosensitive area of the SiPM in order to increase the effective area. Right: Photo of the IceACT device. The blue tube contains the Fresnel lens and the focal surface, including and Winston cones on top of each SiPM [48].

antennas to the IceACT camera and, opposite side, to receive a trigger from the camera (Figure 4.5).

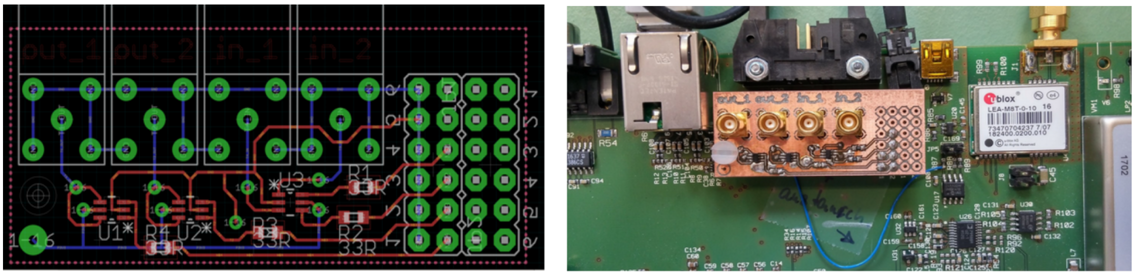

Figure 4.5: Left: Printed circuit board (front and rear) of the developed IceTAXI trigger board for IceACT. Right: Prototype of the triggerboard attached to IceTAXI. It transforms the TAXI trigger (LVDS pulses) to a trigger out with LVTTL pulses with a 3 V level. The board provides two trigger inputs from IceACT to IceTAXI and two different trigger outputs. One signal-over-threshold trigger is used for self-triggering the IceTAXI scintillator system and a second trigger output with the possibility to choose the coincidence level of the scintillator array system for the trigger out.

4.4 Science case of the surface enhancement

The surface enhancement, consisting of an array of scintillation detectors, radio antennas and imaging air Cherenkov telescopes will help to improve the astroparticle measurements by installing new detection techniques which add new observation channels to the existing observatory. The scientific gain of the surface enhancement is briefly outlined in the following and is discussed in more detail in [49] and [47].

IceScint:

The IceTop tanks were initially installed at the level of the snow surface, but snow dunes bury the IceTop tanks under a layer of snow that weakens the electromagnetic component. The thickness of this shielding changes over time. The consideration of this shielding is an important factor for the correct reconstruction of the extensive air-showers. Although initially deployed at the level of the snow surface, drifting snow buries the IceTop tanks under a layer of matter which attenuates the electromagnetic component and the snow thickness changes slowly over time (Figure 4.6). at the area of IceTop. It is shown that the snow accumulation of the IceTop tanks is not homogeneous and differs already a couple of years after deployment up to 1.8 m.

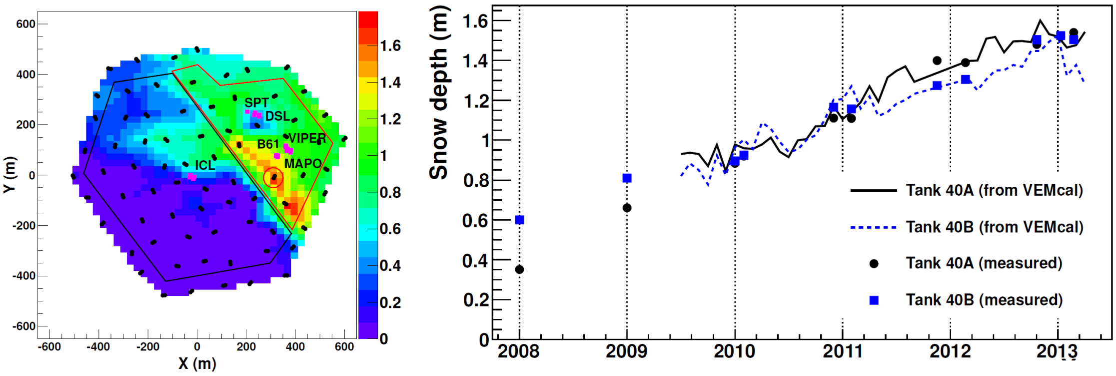

Figure 4.6: Left: Snow accumulation of the IceTop tanks in 2010. The black paired dots are showing the IceTop tank positions and the color code indicates the amount of snow above the tank. Already in the year 2010 a difference of the IceTop tank snow coverage of about 1.8 m between the tanks were found. Right: Snow depth of the IceTop tanks 40A (dotted) and 40B (squared) from deployment 2008 and till 2013. The solid and dashed lines shows the indirect snow depth reconstruction by using the simulation framework VEMcal of IceCube [50].

The IceScint array will elevate and provide a reference measurement of the behavior of the air-shower reconstruction versus the influence of the attenuation of snow as shielding of the electromagnetic component.

This will provide an empirical model to include in the event reconstruction and reduce the possible biases on reconstructed energy, thereby decreasing the systematic by snow accumulation. If the attenuation length is determined with an accuracy of 0.05 m, the systematic uncertainty in the spectrum for 2016 will be reduced by around 4% [50].

An additional array of surface detectors, like scintillators, allows an improved (cross) calibration of the in-ice detector and IceTop by measuring in coincidence air showers and muons. For calibration of single IceScint scintillators and single IceTop tanks, the first IceScint prototype array was deployed in way that it provides an overlap with IceTop tanks (Chapter 7). As example, the signal transmission timing difference between an IceTop tank and the ICL and a scintillator and the ICL can be examined. In addition the charge deposit distribution in the tank compared to the distribution in a scintillator can be determined.

Since most of the signals of the scintillators result from high energetic electrons, an additional advantage will be an improved possibility to distinguish between the muon and electron contribution of the signals in IceTop detectors, like the "AugerPrime" called upgrade of the Pierre Auger Observatory. This ratio information can be used to enhance the mass of the primary cosmic rays determination.

Therefore, the scintillator upgrade will improve the capabilities for studying cosmic rays. Combining IceScint, IceTop, and in-ice measurements will increase the accuracy and the energy range for cosmic-ray energy and mass composition measurements. It is capable to significantly lower the detection threshold for cosmic rays and to detect vertical air showers with primary energy greater than 0.6 PeV (assuming primaries are protons) to 0.95 PeV (assuming they are iron nuclei) [42]. The higher density of detectors will allow accurate reconstruction of air showers for energies below 1 PeV, means the energy range of the knee in the cosmic-ray spectrum will be fully covered [49]. Although not occupying a larger area, the new detectors will allow to analyze cosmic-ray data where the core lands outside the IceCube footprint [49].

The scintillator upgrade will improve the measurement of different air shower components:

- Improvement of the understanding of hadronic interaction physics by opening a new detector channel and thus of the muon background for the neutrino measurements [49].
- Opens the window for a larger energy range and a expended phase space for the gamma-ray detection of sources.
- Disentanglement of the relative contribution of electromagnetic and muonic shower components in individual air showers because of the different response of the two components in IceTop tanks in scintillators. The electron-muon-ratio provides a strong parameter for the determination of the mass composition of cosmic rays [49].

Thus, the scintillator array will improve the cosmic-ray and gamma-ray search performance of IceCube.

By adding scintillators with a similar coverage as IceTop, the energy threshold at which the muon veto becomes efficient at a 10^4 to 10^5 rejection factor is estimated to be lower by a factor of two [49]. The energy threshold for vetoing the muon background to astrophysical neutrinos in IceCube will be reduced [49].

In addition, the scope of the enhancement of the IceTop array with scintillators, it includes R&D towards a larger surface detector in the scope of IceCube-Gen2 (Chapter 3). A higher quality of the multi-messenger capabilities will be reached by adding another independent shower detection technique like radio antennas

Radio antennas

The surface enhancement consisting of scintillators and radio antennas will improve air shower measurements. The total accuracy is increased, also the sky coverage (Figure 4.7) and the detection threshold is lowered [47]. Advantages of the radio upgrade are:

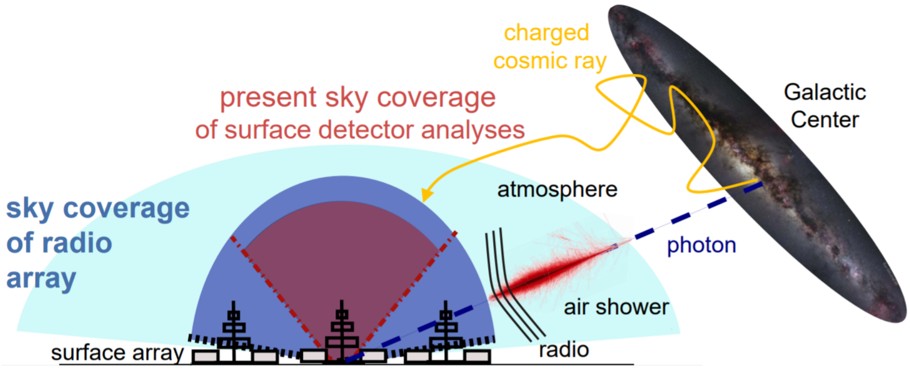

Figure 4.7: Schematic of a radio extension of the IceCube surface array. The radio array will improve the accuracy and extend the field of view to lower elevations. In addition to cosmic-ray measurements, the radio array can search for photons of PeV energy from the Galactic Center due to the geographical location of IceCube since the galactic center is visible all over the year [47] (modified).

- More precise measurements of the size and depth of the electromagnetic shower component at the shower maximum are possible. This helps to perform a better composition measurement and helps to test hadronic interaction models.
- Due to the lower systematic uncertainties of the radio technique compared to surface particle detection, the surface antenna array will increase the per-event precision and the absolute accuracy in the reconstruction. Hence, by such a radio antenna array the energy scale of IceTop can be compared to other cosmic-ray experiments with a radio extension.
- Radio antennas increase the sky coverage for more inclined showers, which leads to an improved search for PeV photons. In this way, also the sensitivity for anisotropy studies is improved [47].
- Gamma-ray induced showers emit a slightly stronger radio signal than showers initiated by cosmic-ray nuclei and contain an order of magnitude fewer muons. Thus, the combination of radio and muon detectors is ideal to search for photons.

Due to the large radio footprint of inclined showers, a radio surface array could veto very inclined events, even if the shower core is far outside of the array.

In addition, a radio surface array will serve as an R&D area for next generation projects, like IceCube-Gen2. In particular, surface antennas could be used to eliminate cosmic ray transients and anthropogenic backgrounds to a future in-ice radio detector of UHE astrophysical and/or cosmogenic neutrinos.

With the enhancement of the existing IceTop by an instrumentation of the surface with the in this Chapter explained scintillators, radio antennas and air-cherenkov telescopes, it will increase the overall accuracy of the IceCube Observatory and enables in a broad way new prospects in astroparticle physics, new scientific explorations in the era of multi-messenger astrophysics will be possible and it will enable new discovery potentials for a whole series of remaining open questions in fundamental science.

5 IceScint detector and IceTAXI DAQ

In this chapter the IceScint detector system that has been developed for the IceTop enhancement will be explained by going through the single components of the system. The research and development was driven by the aim of having a modular design in and during the prototyping phase, as much open in experimental, technical and financial aspects as necessary for a final design review. During a dedicated kickoff meeting an agreement was reached on following key aspects for a first prototype of IceScint:

- A light-tight, light-weight and stable mechanical housing based on certificated and exportable plywood or aluminum.

- A detector baseline design based on scintillator bars [26] with wavelength shifting fibers [51] collecting and focusing the emitted photons. The fiber type, placement of fibers inside the bars, and routing of the fibers to the optical sensor has to be optimized for sensitivity and uniformity with a baseline design of the scintillators of the Pierre Auger Observatory for the AugerPrime SSD upgrade. Due to the smaller detection area and the replacement of classical photomultiplier tubes with SiPMs compared to the AugerPrime scintillation detectors, several major adjustments of the routing and scintillator bar placement have to be developed.

- A fiber-to-sensor coupling that is easy to produce, very durable and optimized for the sensitive area of 6 x 6 mm^2 of the used SiPM photo sensors [52].

- A modular Analog Readout Module (IceARM) controlling and monitoring the SiPM, its Gain, temperature change compensation and allowing a calibration and an easy commissioning of the scintillator panels in the laboratory and at the South Pole.

- An eight-channel Field Hub DAQ based on a readout board developed for the TAXI project [53] that allows different trigger options, nanosecond-precision time stamping of incoming detector pulses, and recording of the photo sensor waveforms. The waveforms can either be charge-integrated online by a FPGA [54] or be stored (or transferred) for calibration and debugging purposes.

All mechanical and electronic designs were developed to be generic to some degree to ensure the potential to be optimized according to, at this stage not yet fully defined, scientific requirements and to operation experience in the laboratory and at the South Pole. After an IceCube Collaboration internal review in May 2017 of the first scintillator prototype (with a wooden housing) some suggested improvements were considered and have been implemented in the research, development and production of more than 3 IceScint stations with 7 detectors each.

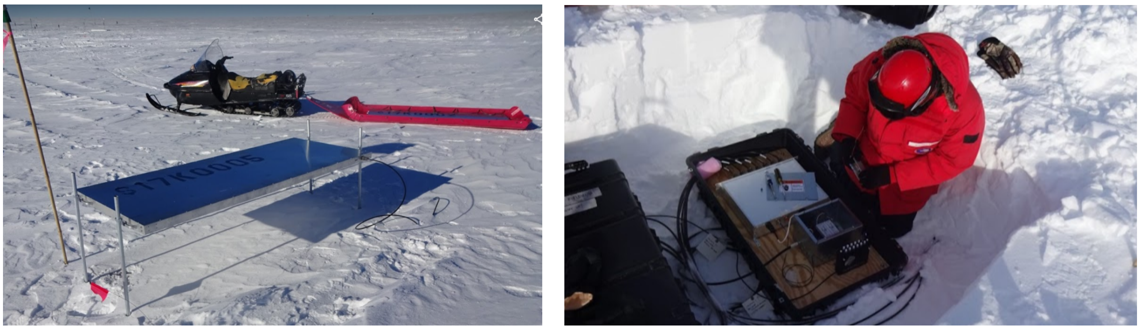

Figure 5.1: Pictures of the IceScint enhancement major components of the IceTop array at a glance. Left: One IceScint detector position at poles to prevent an early snow coverage of the detector surface and in the background the most suitable method to transport the detectors to the deployment position for each station. Right: The Fieldhub for the readout of the IceScint detectors (and radio antennas). Visible is the black fiberglass housing and inside, mounted on a wooden plate, the IceTAXI DAQ, the power supply and the White Rabbit switch for communication with the ICL.

This Chapter focuses on the design of these 3 IceScint stations, since they were deployed at different locations, namely at KIT as a hybrid test array, in the cooling chambers of the Physical Science Lab (PSL) at Madison (Chapter 7) and at the South Pole (Chapter 8).

To show the development efforts and measurements necessary for the three successfully operating IceScint stations, the first scintillator prototype with a wooden housing is also briefly presented within this Chapter.

5.1 IceScint detector components

After a brief overview of the IceScint detector and its DAQ system (Figure 5.1 shows the system at a glance) the detector components will be explained.

5.1.1 General overview and timeline

Figure 5.2 shows the basic working principle of the IceScint scintillation detectors as deployed in the IceCube season 2017/2018. The key components are shown as flowchart and the actual implementation beyond the flowchart with photos of the components. To measure charged particles by the scintillation detector technique, some material which reacts with charged particles like muons or high energetic electrons is necessary to obtain a first information (actual the hit itself by a particle, amount of energy deposit, timing), a optical routing to a photo sensor (SiPM) to get the decentralized information focused on a small area. A coupling between the small area with the light yield and the SiPM, a readout electronic which transfers the light yield information into an electronic signal which can be modified and processed (IceARM) and a central DAQ (IceTAXI) to digitize and transfer the detector information to the main data processing center (IceCube Lab) is involved in this whole readout and data pipeline chain.

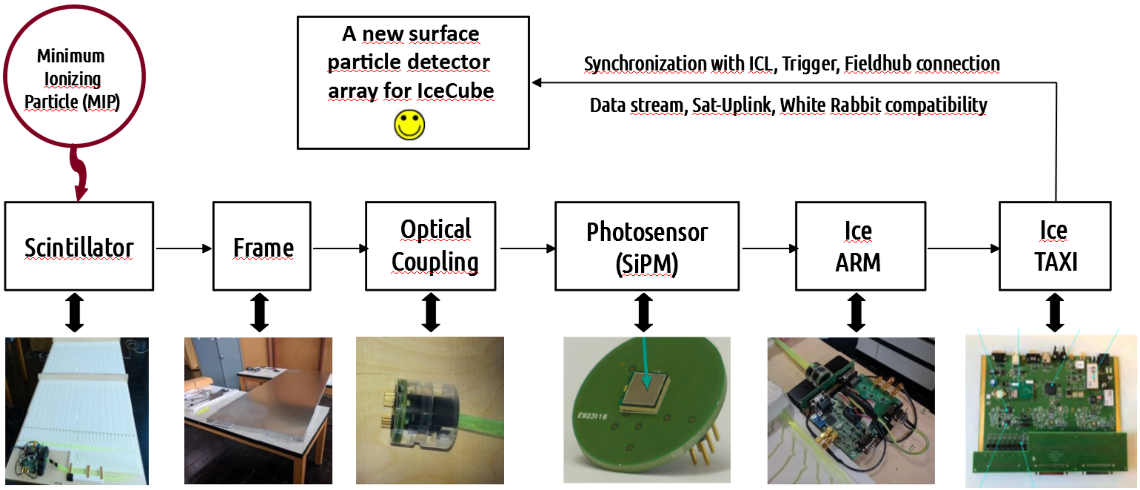

Figure 5.2: Overview of the measurement system of the first IceScint scintillation detector units and the DAQ of the first prototype station. The measurement method, roughly from ionizing particles to a photon yield to a measurable voltage to an analyzable detector array data is displayed. The scintillator is getting excited by ionizing particles, mostly with a origin in extensive air-showers, and emits photons in the UV range. This photons are collected by wavelength shifting fibers and transmitted via a routing and an optical coupling to a SiPM. The sensor is read out and amplified already inside of the detector and the analog data is transferred differential to a field hub DAQ, IceTAXI.

In order to give a brief chronological proceeding of the surface enhancement, Figure 5.3 shows an experimentally focused timeline of the actual realization of enhancing the IceCube surface with new detector systems. Next to the part described in this work, a timeline shows the following seasons of upgrading the first prototype station (2018/2019 and 2019/2020).

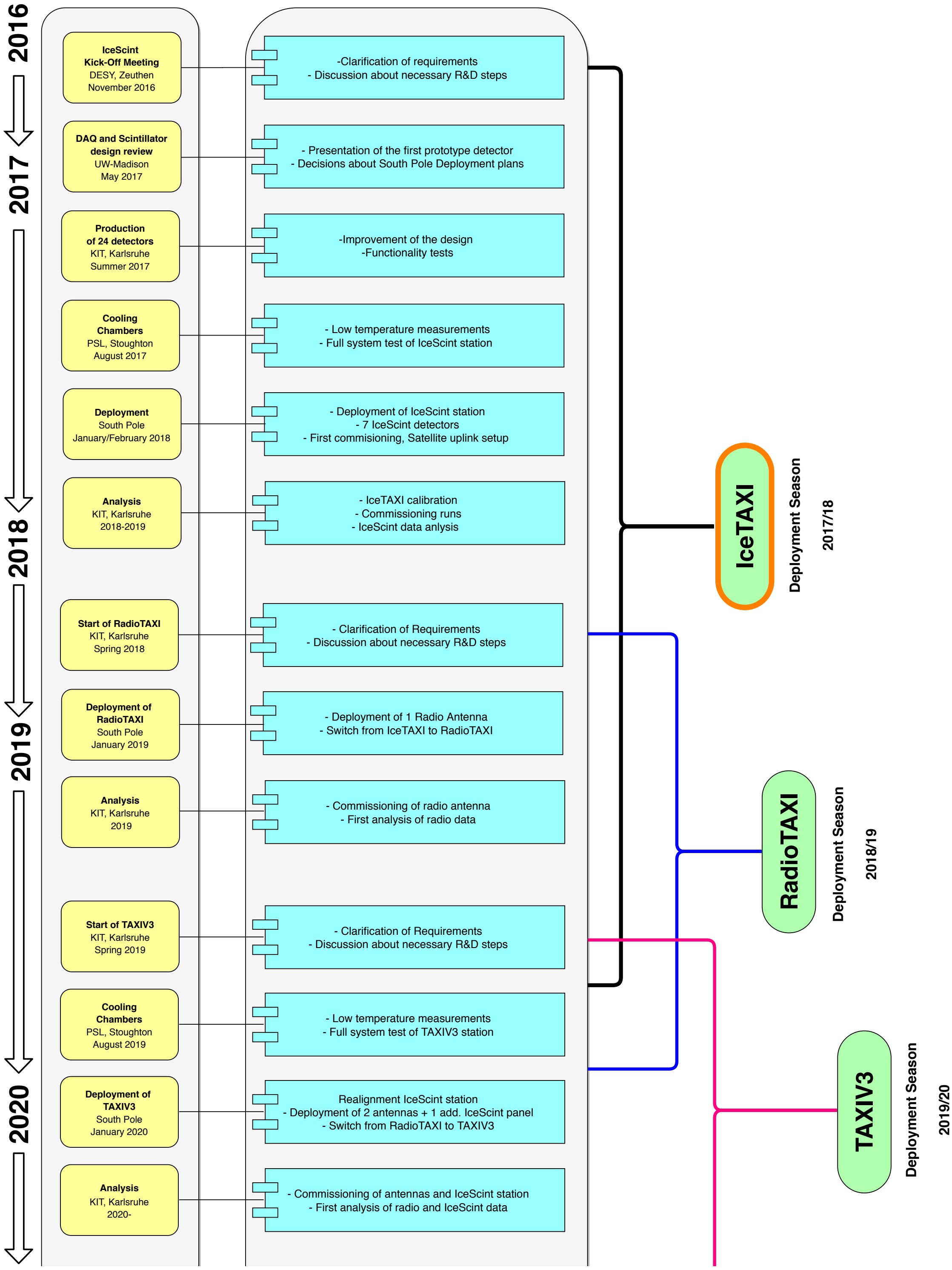

Figure 5.3: Timeline of the IceCube IceTop enhancement, including the radio antenna addon (2018/19; RadioTAXI) and the combination of the uDAQ system with the IceTAXI system (2019/20; TAXIV3). This work is marked in orange.

Table 5.1: Basic parameters of the first wooden prototype detector of IceScint.

Dimensions	$2\,320 \times 1\,000 \times 103\text{mm}^3$
Total weight	$\approx$ 48kg
Number of Fermilab bars	16
Length of Fermilab bars	1 875mm
Sensitive area	1.5m^2
Optical fiber type	1 mm ϕ Kuraray Y-11(300)

Table 5.2: Basic parameters of the aluminum IceScint detector design which was used for the series production of over 3 stations with 7 detectors each.

Dimensions	$2235 \times 885 \times 50\text{mm}^3$
Total weight	$\approx$ 41kg
Number of scintillator bars	16
Length of scintillator bars	1 875mm
Sensitive area for MIPs	1.5m^2
Optical fiber type	1 mm ϕ Kuraray Y-11(300)

5.1.2 Mechanical frames and detector housing

For the IceScint first prototype detector (Table 5.1), a wooden housing was build and afterwards for the series production an advanced and improved aluminum frame was developed and used.

The design decisions for the aluminum frame for the series production can be found later in this Chapter. The basic parameters, to compare it with the first wooden prototype detector, are listed in Table 5.2.

In total one wooden prototype and 24 aluminum IceScint housings (and detectors) have been produced during Spring and Summer 2017. The quality assurance protocols of the production are stored on a dedicated server. These protocols lists, among others the bar code of each scintillator bar, the amount of fiber, the series numbers of the fiber rolls, the series number of the ARM electronic, the installed SiPM, linked pictures of the installed electronics and connectors and, if there were any, noticeable details are noted in there protocols.

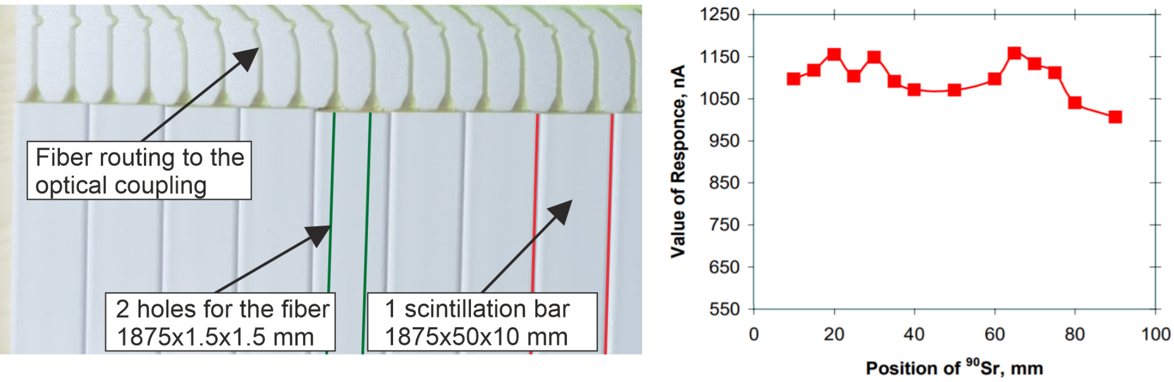

Figure 5.4: Left: Picture of the Fermilab scintillating bars and the Kuraray optical wavelength shifting fiber, installed in one IceScint detector. Red lined one of the scintillating bars and green lined the position of the two holes per bar are highlighted. The fiber and its routing is visible in the top left corner. Right: Current response in nA vs the width (100 mm) of one fermilab bar with two holes, read out with a PMT [26]. The muon tower calibration measurements of the IceScint detectors confirmed the variation of the response (Chapter 6).

5.1.3 Scintillation material and optical fiber

Each panel comprises 16 extruded plastic scintillator bars, produced by the Fermilab extruder facility [26]. These plastic scintillator bars are made of polystyrene with doping of 1% PPO and 0.03% POPOP and coated with a 0.250 mm thick layer of TiO2 reflector. Y-11(300) wavelength shifting fiber[1] [51] are routed and looped back through the holes of the bars, resulting in a bundle of 32 fiber ends which are coupled and readout by a SiPM.

The scintillating bars and the fiber are highlighted in Figure 5.4, left. The current response of an example measurement with a Fermilab bar with 10 mm width and two holes, read out with a PMT, is shown on the right side of the figure. The spatial resolution was obtained by the usage of a radioactive source (^{90}Sr). The muon tower calibration measurements of the IceScint detectors confirmed the same variation of the measured current response, respectively the pulse width, over the scintillator width (Chapter 6).

The detector is shown in Figures 4.1 and 5.15. It comprises 16 Fermilab scintillator bars of 1.875 m length and 5 cm width, resulting in a sensitive area for ionizing particles of 1.5 m². Each bar is read out with two wavelength-shifting fibers. The fiber routing is supported by Styrofoam plates and the 32 fibers are bundled in a cookie. The basic parameters of the mechanical panel design are listed in Table 5.2.

To increase the light yield and to optimize the detector efficiency and uniformity of a detector system with Fermilab bars and Kuraray fibers several tests were performed [55]. It turned out that a coupling of 4 Fermilab bars with 2 holes for optical fibers each, forming one unit, leads to the best results (Figure 6.37). This coupling optimizes the ratio between the bending radius, and therefore the loss of light due to reflection in the fiber and the light yield. In addition, the fiber alignment fixed with routing sockets, shown in Figure 5.13 and 5.15, ensures a uniform detector by adjusting the bending radius and

---

[1] produced by Kuraray Co. Ltd.

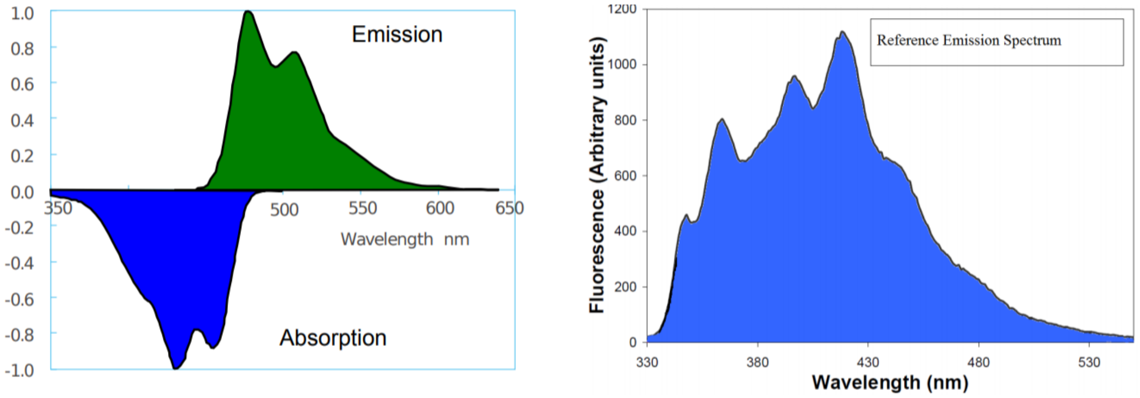

Figure 5.5: Left: Emission and absorption spectra of the chosen Kuraray "Y11" wavelength shifting optical fiber. Right: Reference emission spectrum of the chosen extruded scintillator out of the Fermilab extruder facility [56].

therefore the reflexion coefficient.

The size of the detector was chosen to consist of 16 bars since 32 fibers of 1 mm diameter are the maximal number to ensure a full visibility by the 6x6 mm^2 SiPM with optical cement coupling (Chapter 6).

5.1.4 Light shielding

Compared to as example imaging SiPM cameras like SiECA (Chapter 2) the relatively low light outcome of scintillator bars and the given sensitivity of SiPMs, a photon shielding, surrounding the detector system, is necessary to avoid a contamination of the SiPMs with external light. In addition, it ensures that every collected photon by the SiPM has its origin in the scintillator bars due to the transformation from the interaction of ionizing particles into UV photons. For first prototype testing and for the first wooden detector prototype, a simple black foil was used. After performing temperature tests with heating up and cooling cycles, it turned out that not every foil is suitable for South Pole conditions. For example, the black foil from the KASCADE experiment, where a rest was still stored in the warehouse, increases the brittleness of the material at low temperatures under mechanical stress to such an extent that the foil broke at several places. Material science studies on the elastometric tensor have shown [57] that this kind of plastic is getting too stiff at low temperatures even without mechanical stress. These studies led to additional efforts to identify a black foil suitable for the environmental conditions at the South Pole.

A black foil, serving as photon shielding, needs to fulfill following key aspects for the IceScint detectors:

- High-density polyethylene (PE) to ensure enough flexibility at low temperatures to prevent brittleness. In addition, due to the high-density of PE $\geqslant 0.941\frac{g}{cm^3}$ the probability to get cracks during production of the scintillators is lowered and a denser material increases the photon reflection index, too.

- Preventing damage to internal electronics from electrostatic discharges (ESD) by any build-up electrostatic charge, caused as example by rubbing the foil during assembly of the detectors or at transport movements, by using a high-impedance ($\geq 10^3\Omega$) foil.
- At least 150 my thickness [2] of the foil in order to increase the photon shielding and prevent leakage.
- At least a half tube foil to speed up the production process of the IceScint detectors and to reduce the probability of foil cracks occurring during the production process and shipment.
- The foil must be at least two times (half tube) 1.1 m wide to cover the whole IceScint detector interior.
- At least a total length of the black tube foil roll of 70 m to produce the developed IceScint detectors at least up to 3 stations with 7 detectors each.

It was found that, for the first IceScint stations, a black tube foil which is used for building oil pipelines fits the requirements. The company NWO GmbH sent us the required foil.

After 2 years in operation, it can be concluded that the black tube foil fulfilled the requirement with respect of the production process, the intactness during shipping and stable and light tightness during measurements at the South Pole, as shown in Chapter 9.

5.1.5 Silicon Photomultipliers (SiPMs)

For the readout of the optical fiber, Silicon Photomultipliers (SiPMs) are used. This new kind of low light-yield photo detectors have several advantages compared to classical photomultiplier tubes (PMTs) and its photoelectron gain is based on several thousands APDs (Avalanche Photo Diode) connected in parallel.

Compared to normal photodiodes APDs contain an additional p-doped layer, called multiplication zone. This layer changes the charge distribution in a way that a high electric field strength is created. This area is defined as avalanche layer (Figure 5.6, left). When an appropriate reverse voltage is applied to the PN-junction, the electrons are accelerated due to the electric field to the N^+-doped layer. A PN-junction is the basic building block of many semiconductor devices like diodes and transistors. It can be made by joining or diffusing together differently doped semiconductor materials. If the applied voltage is high enough, the kinetic energy will be transformed to additional electron-hole pairs. This multiplication effect (e.g. the avalanche) leads to a measurable current even for a single photon.

For charge histograms obtained from SiPM waveforms (Chapter 6) with small charge deposition, "fingers" of single photoelectrons (PE) can be seen, analogous to photomulitpliers. This designation does not quite correspond to the functionality of a SiPM. In contrast to PMTs, where a photoelectron is released from the cathode by an incoming photon due to the photoelectric effect and is accelerated and multiplied via dynodes, SiPMs create, accelerate and multiply an electron-hole pair. However, since the result is similar to

---

[2] 150 my = ~ 1.37 mm

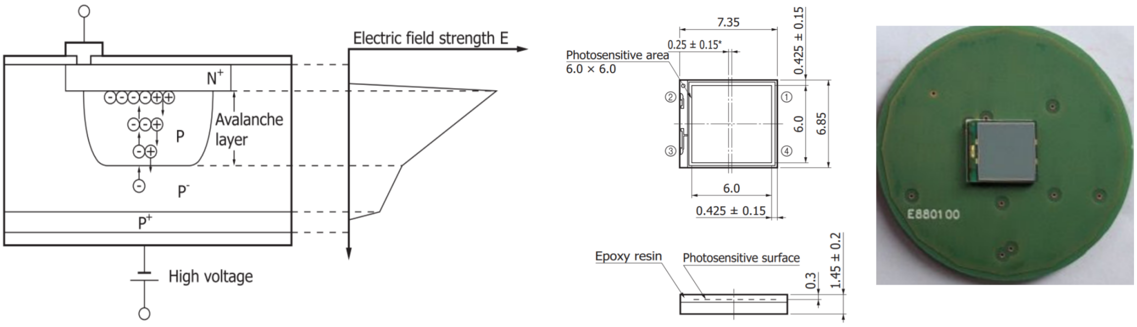

Figure 5.6: Left and center: Working principle of a SiPM, shown at a single APD. The different doped layers are changing the charge distribution in a way that with an applied reserve voltage a high electric field strength is created. By the creation of a electron-hole pair the electric field accelerates the charges and the kinetic energy is transformed into additional electron-hole pars. This multiplication effect leads to a gain which is high enough to detected single photons with one APD cell [7]. Right: Picture of the used SiPM, soldered on the Cookie board for the IceScint detectors. The front side of the board, with the SiPM, is coupled via optical cement to the fiber readout of the scintillator bars and the back side to the analog readout electronic (IceARM).

that of finger spectra, for example, the term "PE" for peaks has also been accepted in the literature. For SiPMs one could read "PE" as “Photoelectron Equivalent”.

In addition to the key features of low-level light photo sensors, the photo detection efficiency (PDE) and the gain, SiPMs have several advantages like a more robust design, more cost effective and a operation voltage below the high-voltage region compared to PMTs. Furthermore, the bias voltage and the noise rates as the dark counts (Figure 5.7) or the cross talk probability and afterpulses decreases with temperature, e.g. improves the sensors performance at South Pole’s thermal conditions. A detailed description of the working technique, the performance and the noise creating contributions to the signal shape of SiPMs for in specific astroparticle physics purposes can be found in great detail in my master thesis [7] and more compacted in reference [58].

For the first series of IceScint detectors, SiPMs[3] with a trough-silicone via (TSV) technology are used, produced by Hamamatsu Photonics [52]. This technology enables to pass completely through the silicon waver and decreases the dead space between neighbored avalanche layers of the photosensitive APDs compared to wire-bond anode and cathode output drastically. Given that the anode and cathode are wired out of the side of the SiPM (Figure 5.6), an asymmetrical allocation of the photosensitive area results, which had to be taken into account for development of the optical coupling between the optical fiber bundle and the SiPM (Chapter 6).

The following arguments for the SiPM, focused on the possible experimental data output of deployed IceScint detectors at the South Pole were, considered:

- This SiPM with TSV technique for SiPMs available in two different configurations[4]. The difference is the pitch value of the SiPM, e.g. the size of one APD cell ($50\mu m$ or $25\mu m$) which leads, since the photosensitive area of $6mm^2$ is fixed, to different

---

[3] TSV-MPPC S13360-6050PE

[4] S13360-6050PE and S13360-6025PE

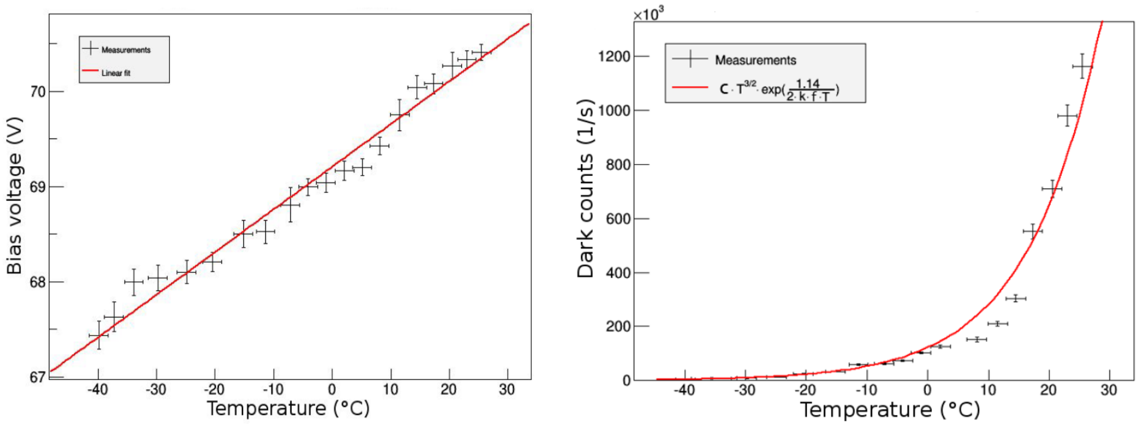

Figure 5.7: Example measurements of the behavior of the bias voltage and the dark count rate at changes of the ambient temperature of the used SiPMs [52] for IceScint, measured with SPOCK at KIT. At low temperatures, the necessary bias voltage for operating SiPMs decreases linear and the dark count rate of SiPMs declines exponentially. The fit parameters can be found in [7].

amount of APD cells at the SiPM. For the $50\mu m$ pitch version, there are 14400 APD cells on the SiPM and for the $25\mu m$ pitch version a total amount of 65000 APD cells. A direct consequence of this difference is the dynamic range with respect to how many photons can be seen and resolved at a discrete time. Each APD can detect, with the boundary condition of an idealistic SiPM with 100% PDE and 0% noise effects, one photon at one time. For dissolving different amounts of energy deposits by MIPs into the detector, the larger the interval of the dynamic range thus defined, the greater the number of resolvable energy depositions from the detector system that can be measured. I.e, this perspective suggests the choice of SiPMs with a larger number of APDs.

- Since a geometrically dimensioned smaller APD cell also has a smaller avalanche region, the maximum charge generated is lower. This means, seen as an equivalent circuit, a quenching resistor drops the voltage after a certain time, e.g. the capacity of an APD cell is smaller. This means that the APD cell is again sensitive for the next photon after a shorter period of time, because less charge has to flow off during the decreasing flank until the baseline is reached again. This shortens the dead time of the SiPM and allows a better time resolution of the air shower front.

- Measured with SPOCK[5] and in accordance with the datasheet [52], a SiPM with smaller APD cells size is a few percent less effective regarding the photo detection efficiency at a discrete wavelength. Since it was measured with the first wooden prototype of the IceScint detectors that we have a very good signal-to-noise ratio (~$75 \frac{SPE}{MIP}$, Chapter 6.8), which meets the set requirements more than fourfold and equals to a high light yield due to the detector design and in specific the optical coupling, it es reasonable to choose the SiPM series with smaller APD cell size. In

---

[5] Single Photon Calibration Stand at KIT

Table 5.3: Example summary measurement of the SiPM calibration results for the Hamamatsu S13360-6050PE measured with SPOCK. These measurements were done for each SiPM which is installed in an IceScint detector.

	Result	Stat. error	Sys. error
Breakdown voltage	51.66 V	0.27 V	3%
Gain	$1.18 \cdot 10^6$	$0.05 \cdot 10^6$	$0.05 \cdot 10^6$
PDE	37.49 %	0.32 %	1.6 %
Darkcount rate	3.17 MHz	0.09 MHz	0.14 MHz
Crosstalk Prob.	11.03%	0.50%	0.02%

addition, the IceTAXI DAQ it increases the dynamic range regarding the amount of resolvable charge values.

- An argument for the choice of the 50 um pitch SiPMs is that the baseline design of TAXI was actually developed for PMT signals. The larger amplitude of 50 um pitch SiPMs leads to more PMT-like signals. However, in test measurements at KIT and DESY Zeuthen, it was ensured that the used IceTAXI system can also process SiPMs with 25 um pitch.

In conclusion, it was decided to use the $25\mu m$ SiPM series from Hamamatsu Photonics since the scientific output of the measurements possible with the IceScint Array is expected to be the highest when choosing this type of SiPM. The calibration process of all used SiPM for IceScint and its prototypes is described in detail in Chapter 6. Table 5.3 gives an overview of the result of an representative SiPM measurement before the SiPM is installed into the IceScint detector.

These measurements have been made with photon bundles $(2 - 15\frac{\gamma}{\text{pulse}})$ of a wavelength of $(423{\pm}8)$nm and an over voltage of 3V. In addition to SiPM calibration measurements, further measurements of the linearity of the used SiPM, effects of dust and dirt on the photosensitive area of the SiPM were also by with the SPOCK measurement setup and are presented in Chapter 6.

5.1.6 IceScint detector readout system

For the IceScint array prototype, a new analog readout system of the SiPMs of the Scintillators, IceARM (Analog Readout Module) was developed within this thesis. Figure 5.8 shows the first CAD outline of IceARM. Since the development of the scintillators, the development of the DAQ (IceTAXI), the adjustments of SiPM signal processing and the full system test calibration of IceScint had to take place simultaneously, IceARM was designed as modular as technically and financially feasible in order to have as many options as possible to react to subsequent measurement results and limitations of other components of the system. This flexibility of the analog SiPM readout electronics has benefited

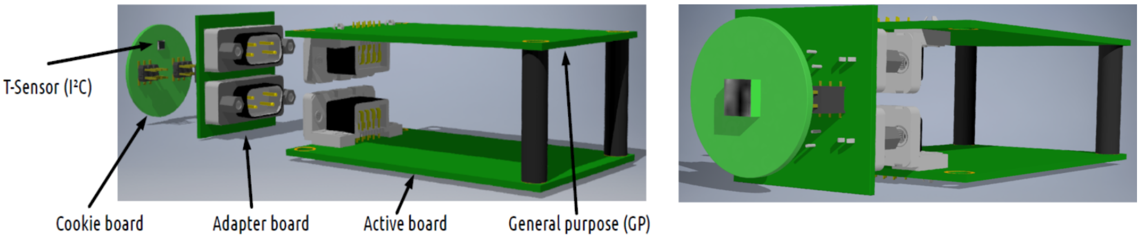

Figure 5.8: First CAD version of the Analog Readout Module IceARM. Visible are the Cookie board with the SiPM, the Readout (active) board, the Adapter board for communication with the GP-Board and the major connectors (9-Pol D-Sub and 6-Pol SAMTEC male and female) between the different modules of IceARM.

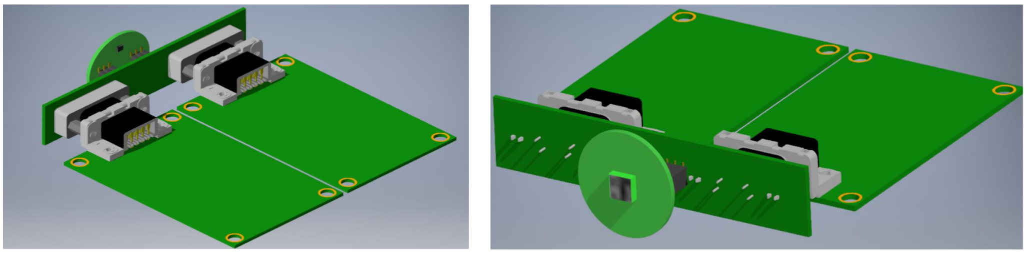

Figure 5.9: Second CAD version of the Analog Readout Module IceARM. The major change is the reduction of the height of IceARM in order to achieve a, after the first wooden prototype, halved total detector height. This additional R&D efforts enabled to ship twice as much IceScint detectors per transport crate to the South Pole. To achieve this, a new adapter board was developed. By this, the absolute detector housing height changes from 100 mm to 50 mm.

several other experiments, mostly located in student teaching and outreach experiments (Chapter 10).

In special calibration runs, the discriminator threshold of the IceTAXI board can be lowered to $\ll$ 1MIP so that a high-statistics sample of low-charge pulses can be collected with a ring sampler. It has to be shown in the full system configuration that the single photo electron "fingers" in such a charge spectrum can be resolved and the charge of one photoelectron can be extracted from the difference between two fingers (Chapter 6), therefore different Op-Amp gain level circuits are embedded. If required, full waveforms can be transferred for debugging purposes (Chapter 8).

After a first IceCube internal review of the IceScint design, it was decided to put additional R&D efforts into IceARM (Figure 5.9). The requirements of the IceScint detector housing changed to a total geometrical height from 100 mm to max. 50 mm in order to ship more detectors per transport crate to the South Pole. One of the limiting factors in the absolute detector height was the first designed (and built) IceARM. By changing the PCBs and the alignment of the several modules of IceARM it was possible to reduce the total height of the detectors to below the required 50 mm.

A more detailed description of IceARM and its parts can be found later in this chapter. The R&D thoughts and the performed calibration measurements can be found in the following chapter.

Pin	Taxi	Taxi Remark
A	P24V	
B	P24V_Return	
C	RS485_P	
D	RS486_N	
E	NC	
F	NC	
G	ANA_P	
H	ANA_N	
J	Shield	
K	Shield	
L	Shield	
M	Shield	

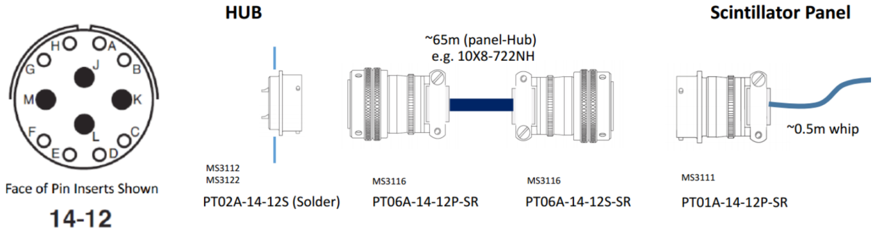

Figure 5.10: Left and center: Pin alignment table and connector positioning of the pins for the connection between the detectors and IceTAXI. Right: CAD of the decided connection system. Both connectors, which of course are outside of the detectors and the IceTAXI housing and therefore exposed to the weather conditions at the South Pole, are military standard, developed and produced by Amphenol Co. Ltd. The screw head visible at each end of the cable and, rotated by 180 degrees to provide a tight connection, the second thread are part of the cable protection.

Figure 5.11: Left: Picture of the used Amphenol Co. Ltd. PT-Series connectors. This military standard is widely used for several experiments in Antarctica and was recommended by IceCube. Right: The IceTAXI frame with 8 connected IceScint detectors in the SPOCK lab for hodoscope measurements. It shows the male and female part of the Amphenol connectos, including the stiff Cat 7 cable from Draka Co. Ltd.

5.1.7 External and internal detector cabling

Amphenol PT-series, PT02A-14-125 (male) and SP02A-14-125 (female) [59] connectors will be used as connection between the IceScint detectors and IceTAXI (Figure 5.11). This military standard connectors are, following the datasheet, only allowed by manufacturer side for operation down to -55°C but are long-term proven for South Pole conditions by several experiments.

In addition, the bayonet coupling system of the PT-series ensures an easy and fail safe deployment of IceScint at the South Pole, since it is only possible to connect the 14-pin plug (Figure 5.10) in only one possible pin-to-pin assignment and the locking technology allows a haptic feedback to ensure that the connection between cable and socket has electrical contact and is mechanically fixed. The chosen connector alloy ensures a long UV light resistance, which is of special interest as the IceScint detectors are mostly mounted on poles an the South Pole surface.

For the external transmission of data and the control of the detectors by the central DAQ, IceTAXI, Cat 7 cables are used. Since the Cat 7 standard offers next to a global shield to reduce noise by external sources, an additional individual shielding for two pairs of signal cables. Hence, this type of cable is particularly suitable, as it provides extra protection for the differential detector signal for both high- and low gain SiPM readout. Suitable and tested for South Pole conditions are Draka Co. Ltd. UC900 with 23 AWG[6] solid copper conductors and a PE jacket (Figure 5.11). Four of the cable pairs are used. One for 24 V DC power supply, two for transmission of the SiPM analog signal in High-Gain and Low-Gain and one for the RS485 serial connection for detector control and monitoring. A strain relief for the connector is installed at each cable end to prevent damage to the wires or the shielding during installation.

5.1.8 White Rabbit Timing

The surface field hub houses next to IceTAXI a White Rabbit [60] timing distribution and communications system via fiber link to the IceCube Computing Lab ICL. In it's original configuration, the time synchronization of the (Ice)TAXI board is achieved via GPS. The 1 PPS pulse and time string from a GPS module[7] are processed in the FPGA. It is foreseen to replace the GPS timing with White Rabbit. It was chosen to synchronize different surface enhancement stations, including scintillators, cameras and radio antennas, as well as to cross-check the air-shower particles signals with the existing IceTop experiment. The White Rabbit project is a flexible and modular real-time Ethernet based network for universal data transfer and synchronization. It can synchronize up to 1000 network nodes with less than one nanosecond accuracy over optical fiber lengths up to 10 kilometers and enables deterministic delivery of messages of different priority.

To achieve synchronization in nanoseconds, White Rabbit uses Synchronous Ethernet (SyncE). A bidirectional exchange of the synchronization messages of the timing protocol enables a precise adjustment of the clock phase and offset. The connection delay is known from hardware time stamps and the calculation of the delay asymmetry. Verification of the GPS timing distribution via White Rabbit was realized using coincident events between IceTop and the scintillators and its commissioning measurements can be found in Chapter 8.

In addition, next to an open source hardware-, firmware- and software pool for developing electronic boards for own needs and specific synchronization tools, several (future) large-scale particle and astroparticle experiments like FAIR and CTA will use the white rabbit timing protocol that ensures a long-term community driven support and a existing knowledge base in future. The 1 PPS signal and IRIG-B signal from the WR-LEN will be utilized. Existing FPGA test-I/O pins on the IceTAXI board are used to establish the physical connection to the WR-LEN.

---

[6] American Wire Gauge

[7] U-blox LEA-M8T

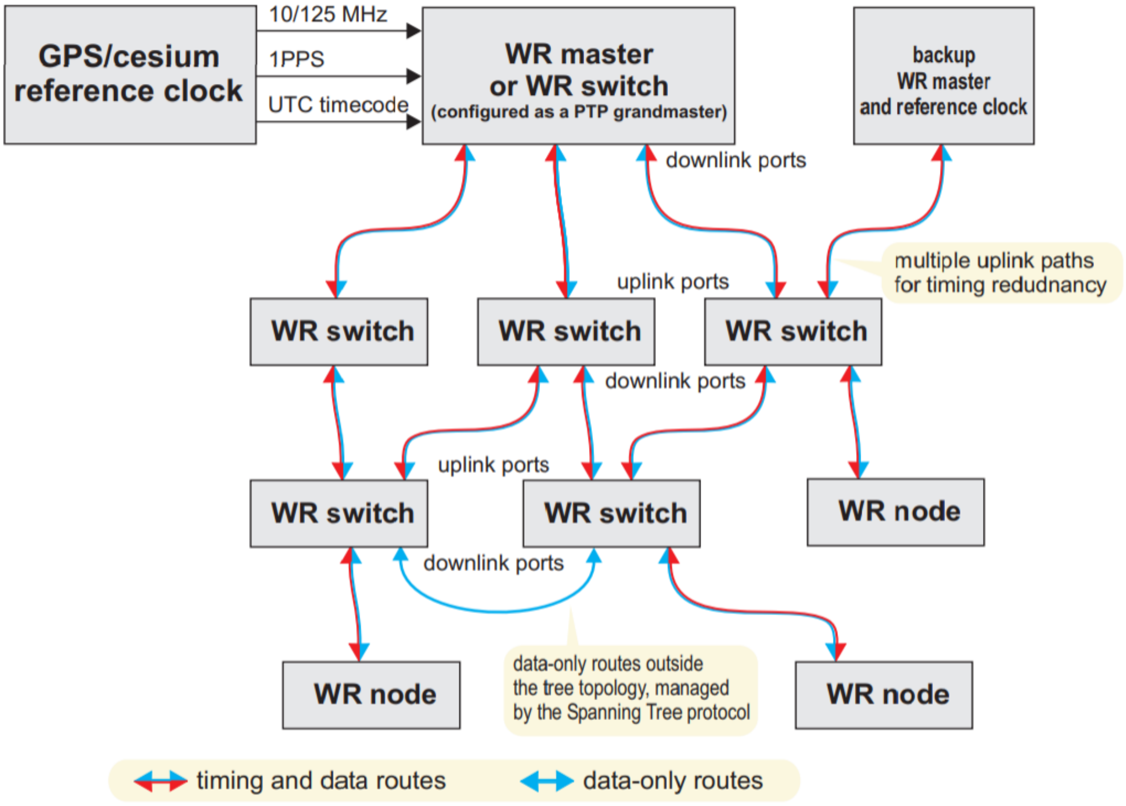

Figure 5.12: A sketch of a white rabbit timing network. An external clock like GPS or a reference clock provides the overall time stamp and frecency and sends both to an WR master which forwards it to WR switches and WR nodes like scintillators, sensors and data storage systems [60]. In addition, the system can be build in multiple redundancy, means the protocol provides the the possibility to automatically switch on backup WR master or backup reference clock devices.

5.2 First prototype detector

One of the first steps was to develop a prototype detector which fulfills the defined requirements for an IceScint detector and to show the technical readiness of a SiPM readout of the Fermilab scintillator bars in combination with a wavelength-shifting optical fiber routing and the resulting bundle. Figure 5.13 shows the CAD of the whole detector, including the wooden housing, the scintillator bars, the routing and the position of the first IceARM version. The wood was already chosen to be exportable to the U.S. and to New Zealand, since special conditions for the import of organic material is regulated in New Zealand and Antarctica.

Figure 5.14 shows the designed connector panel. For evaluation purposes, special focus was placed on obtaining as many connections as possible to all individual modules from the first IceARM version in order to test them under real conditions, i.e. the detection of ionizing particles using scintillator bars.

To keep the scintillator bars at position, e.g. during transport to the South Pole, a wooden clamp system was developed, visible in Figure 5.15, left. Since this system has

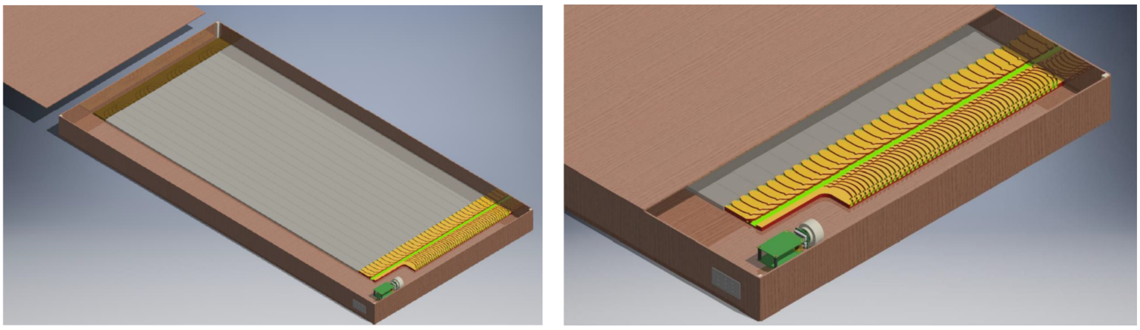

Figure 5.13: Left: CAD of the developed wooden prototype scintillation detector. Right: Zoom-in on the fiber routing, optical coupling and readout electronic. The detector design and its components are described in more detail at the final design of the deployed detectors.

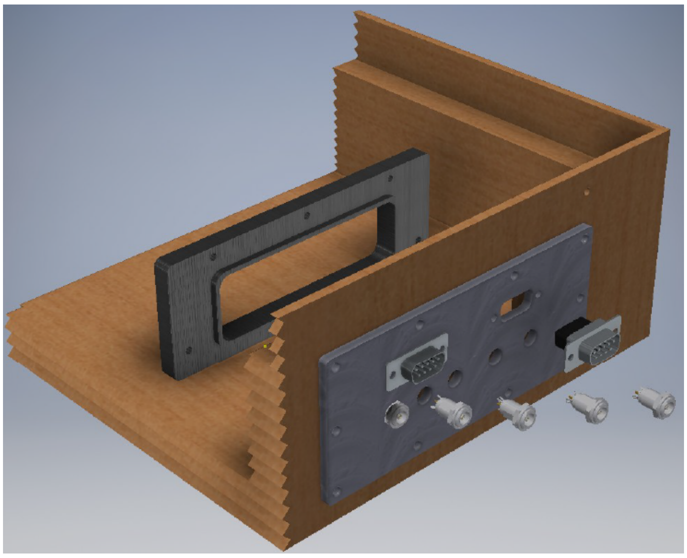

Figure 5.14: CAD of the designed connector panel for the wooden prototype detector. Special focus was placed on obtaining as many connections as possible to all individual modules from the first IceARM version in order to test them under real conditions, i.e. under the detection of ionizing particles using scintillator bars.

Figure 5.15: Left: Picture of the assembled wooden prototype detector. Visible are the scintillator bars, the fiber routing and the fibers connected to the optical coupling of the cookie board. Three wooden clamps keep the scintillator bars in position. The detector design and its components are described in more detail at the final design of the deployed detectors. Right: "Hello World" photo of the first SiPM peak induced by a MIP, hitting a scintillator bar, read out with an oscilloscope and therefore demonstrating the readiness of the detector system.

been retained for the final detector design for the first series production, it is described in more detail in the next section. Figure 5.15, right, shows the very first "hello World" signal of a MIP, hitting the detector and transformed into a waveform with a SiPM peak, demonstrating the readiness of the detector system of all major components.

5.3 Detector design for the first 3 stations

The detector design in general was driven with a focus on a low-cost, fast to produce and high static load design. For the housing, the detector should be as stable as possible, but also as lightweight as technically feasible, in order to reduce the high shipping costs to the South Pole. It was taken into consideration to use as much standard parts in stock as possible with a minimum of parts or unusual components critical in purchasing or crafting.

The decision of the change from wooden to aluminum housing is based on several considerations.

FEM[8] simulations (with different materials and material thicknesses) with Autodesk Inventor have shown that a higher load-bearing capacity as for a wooden housing can be achieved by a combination of aluminum u-profiles and a plywood plate supporting the detector - with a weight saving of more than 33%. The stability was validated with a short trial construction.

---

[8] Finite element method

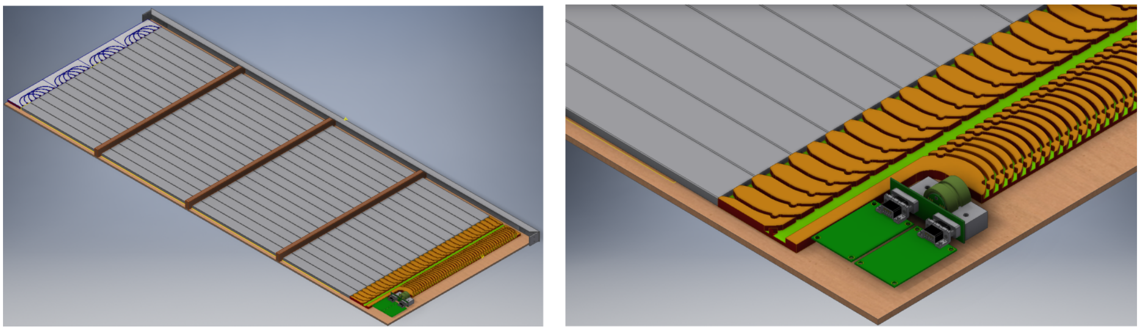

Figure 5.16: Left: Developed CAD for the IceScint detectors. The top plate and parts of the housing are removed in that view to enable a look inside of the detector. Both sides of the fiber routing are visible, the scintillator bars, the wooden clamps and the place of the IcARM electronic, including the cookie and its holder. Right: Close view of the fiber routing, the Cookie and IceARM. The small “nose” at each beginning of the routing, next to the scintillator bars has been added to further reduce the probability of fiber "jumping out" of the routing. The routing and the IceARM dimensions are matched to each other to design the detector no longer than necessary.

By taking the housing from a system of aluminum U-profiles instead of a wooden housing that has to be manufactured individually, a faster and less production error prone detector system is achieved, since a large part of the housing consists of standard components with dimensional tolerances defined by the manufacturer of the U-profiles.

In addition, the wooden frame for the cover of the detector is omitted, which, in addition to adapting the boards for the readout electronics, allows a reduction from 100mm to 50mm of the overall height. Since it is planned to keep the IceScint array free of snow for as long as practically feasible, all detectors are mounted on poles (Chapter 7). This implies that the detectors are annually exposed to the high UV radiation at the South Pole for half a year. A detector housing made of wood, i.e. organic material, ages and may become brittle in the long term. Finally, there is a very practical reason not to use wood for the housing. Most of the cargo to the South Pole goes via Christchurch in New Zealand, which has very strict import regulations [61] for the handling of organic materials, even if the material used is plywood.

Figure 5.16 shows the developed CAD for the IceScint scintillation detector, as produced and calibrated for 24 detectors. The top plate and other parts of the housing are removed in the figure in order to show the parts of the detector itself.

In terms of the transportability and durability, the flat and rectangular design of the detectors, the packing and shipping can be easily done by stacking the detectors, pictured in Figure 5.17, left. The wooden cargo crates (right) were designed to ensure a space effective transportability. The bottom side of one detector is protected from scratching during shipment by small wooden beams with the top side of the next detector.

The detectors can be mounted on an elevated support, designed to keep position at the typical South Pole wind and weather conditions. In addition, all parts of the detectors inside are fixed by several solutions like with wooden clamps for the scintillation bars (Figure 5.16). After almost 2 years of operation, the detectors are still at deployment position and no measurement showed an evidence of a major performance loss due to, as example, moving bars, broken fiber or changes in the signal shape (Chapters 7 and 8).

Figure 5.17: Left: Shown is the space saving transport possibility via a stacking of the IceScint detectors. The bottom side of one detector is protected from scratching during shipment by small wooden beams with the top side of the next detector. Right: One of the constructed transport crates for shipping. There is room for 8 detectors in each transport crate.

The production plan was to split the process into three major parts. One group can work on building the detector itself, another one can produce in parallel the aluminum housing and afterwards both modules can be combined by the usage of using a black tube film as photon shielding between the scintillation detector itself and the housing. The IceARM electronic can be prewired and mounted on its holder by another group (Chapter 6).

Major design decisions for the IceScint detectors are explained and discussed in Chapter 6. Some primary CADs, technical drawings and parts lists can be found in the attachment. In addition, a bill of materials for the installation of IceARM in the IceScint detec-

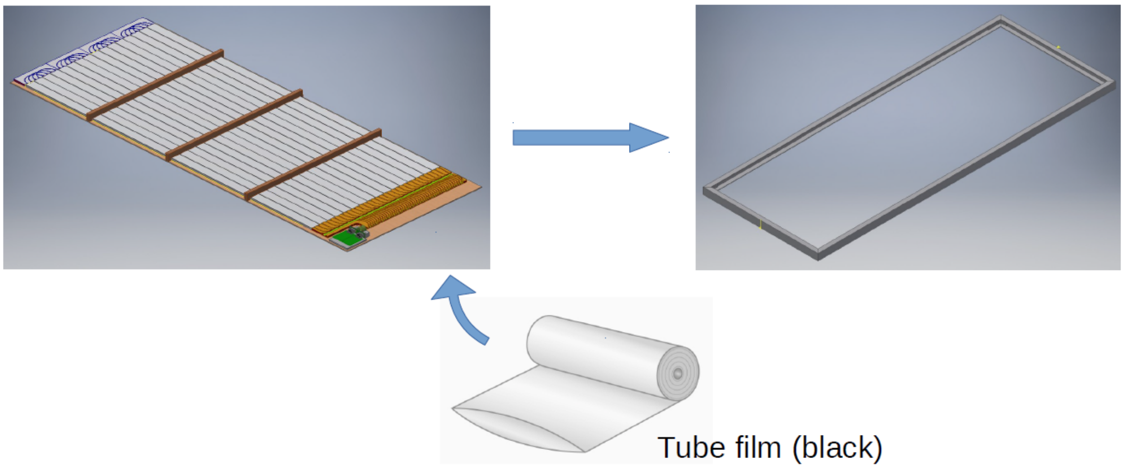

Figure 5.18: Simplified production procedure of one IceScint detector. The design concept was driven to separate the IceScint detector major components into sub-production items. Three major parts, the detector itself, the aluminum housing and the read out electronic can be assembled and prewired independently from each other. The coverage of the detector with the black tube film finishes the detector assembly and combines the aluminum housing with the detector itself.

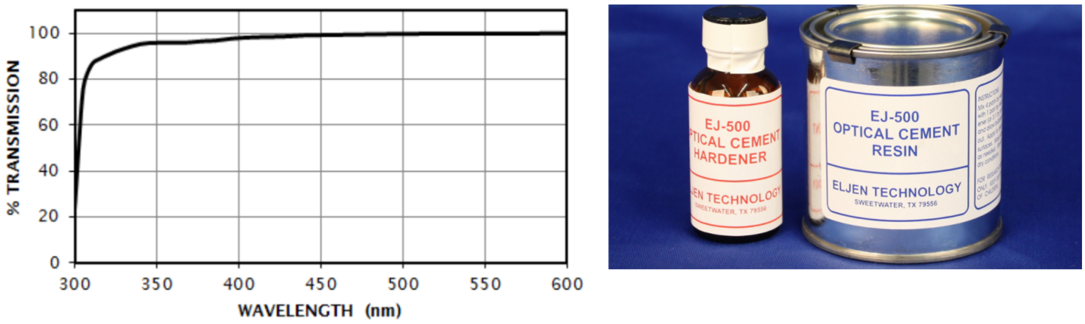

Figure 5.19: Left: Transmission probability versus the wavelength of the photons of the used optical cement [63]. The mean emission wavelength of the optical fiber is approximately 480 nm. Right: Picture of the components for the optical cement (hardener and the resin).

tors can be found in the attachment. Since it would go beyond the scope of the thesis to include all developed CAD, technical drawings, assembly instructions, test measurements and everything else that is required for the later successful production of the first IceScint stations, only some of them are shown in the Appendix. The complete documentation is available at the IKP, will be used as a basis for the IceScint mass production and can be inquired at the institute. It includes also has the entire "Autodesk Inventor" CAD model, including the analysis methods applied prior to production of the first three IceScint stations, such as static stability estimation via Finite Element Method.

5.4 Optical Coupling between fibers and SiPM

The optical fibers are collected into a cookie. The fiber ends are cut and heated on a hot glass plate which turned out to result in less light loss compared to cutting and polishing [62]. The cookie is then glued into a PMMA (Polymethyl methacrylate) coupler. The SiPM, mounted on a PCB ("Cookie Board"), is also glued to the coupler: The 1 mm gap between the SiPM and the fiber ends is bubble-free filled with two-component optical cement, EJ-500[9] [63]. EJ-500 is a clear and colorless epoxy based glue with a refractive index of 1.57. It is ideal for an optical connection of plastic scintillators and acrylic (PMMA) light guides like the used fibers for the IceScint detectors [63]. This optical cement has a certain degree of flexibility and is therefore suitable for the optical bonding of the mentioned plastics to form a glass window between the optical fiber and the SiPM as used in the Cookie system.

The optical cement is fully cured at 20 °C room temperature after 60 minutes. The mixed cement takes 3-4 hours to set and 24 hours to harden. For the production of the first stations we took these manufacturer's specifications into account and timed many other production steps at this curing time.

The two-component mixed and hardened optical glue was cooled with liquid nitrogen for 2 hours to -90°C. No changes, macerations or cracks were visible. In addition, the fully assembled Cookie including the Cookie Board were cooled down to -70°C for

---

[9] Eljen Technology

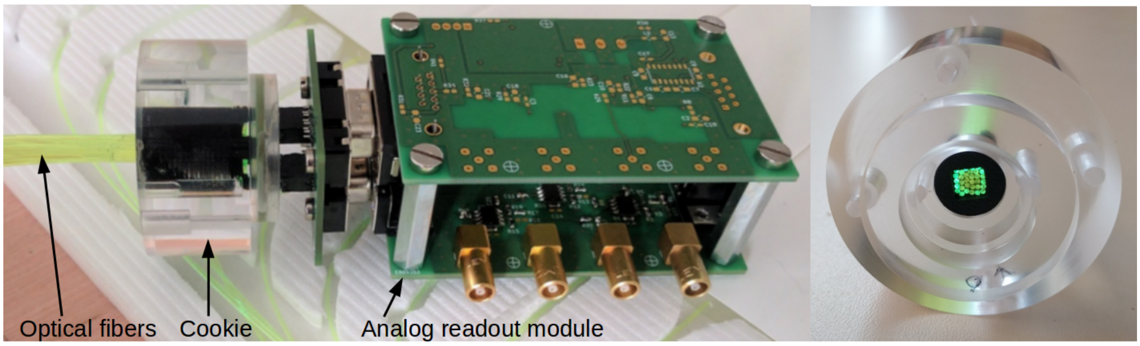

Figure 5.20: Left: Complete optical system of the first wooden prototype to ensure high light yield and detector uniformity. Right: Optical connection to the SiPM, the "cookie".

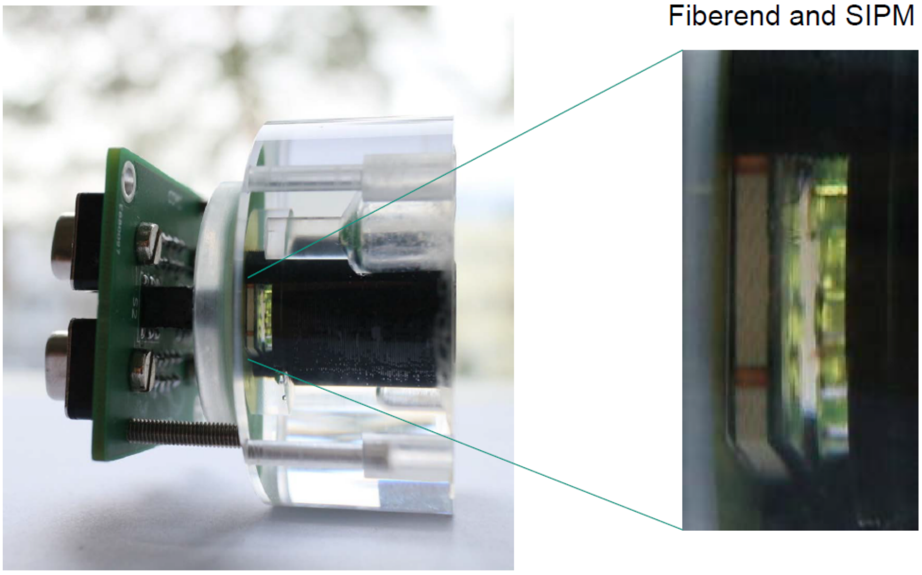

Figure 5.21: Optical coupling with SiPM attached. The 1 mm gap filled with optical cement ensures that all pixels of the SiPM can be triggered. This optimizes the linearity and the dynamic range and is explained in more detail in the next section.

several days. No visible changes or cracks were visible. The fully, including the SiPM, assembled Cookie was calibrated with SPOCK (Chapter 6) to ensure the same optical behavior like before the cooling cycles.

Figure 5.20 shows the optical fibers and the cookie board glued together with the cookie. The dimensions of the cookie are 50 mm diameter and 25 mm length. For the final design, a cookie with a smaller diameter was developed in order to decrease the height of the total detector from 10 cm to 5 cm.

In Fig. 5.21 the connection between the fiber bundle and the SiPM is shown. The 1 m m gap is filled with optical glue and no optical impurities are visible. In summary, the most important points are:

- Fibers are cut and heated. Tests with different shortening methods (cut, polished, not treated) show that this process results in the best transmission coefficient there with less reflection due as example quenching the outer layer film of the fiber by cutting into the light guide part of the fiber.
- New inner part of the Cookie, 3D-printed, to align the 32 fibers in a square and to provide a socket for the SiPM to align the Cookie Board with the cookie and therefore the fiber bundle.
- The cookie is 100% solid, filled up with optical glue which was tested for low temperatures stability. The fully solid optical connection ensures robustness to environmental conditions and increases the long-term stability of the optical connection.
- A 1 mm gap between the end of the fibers and the SiPM photosensitive area allows illumination of every pixel and thus increases the dynamic range (Chapter 6) as for the 45° opening at the end of the fiber.
- The production process, which was optimized that no air bubbles are trapped in the glue between the fibers and the SiPM.

More details about the optical coupling and its design decisions and changes between the first prototype and the first IceScint production are given in the next section.

5.5 Analog Readout Module (ARM)

The general development idea of the Analog Readout Module (ARM) was to make it as cost-effective, modular, and flexible as possible. The ARM consists of four parts: the Cookie Board, the Adapter Board, the Readout Board, and the General Purpose Board.

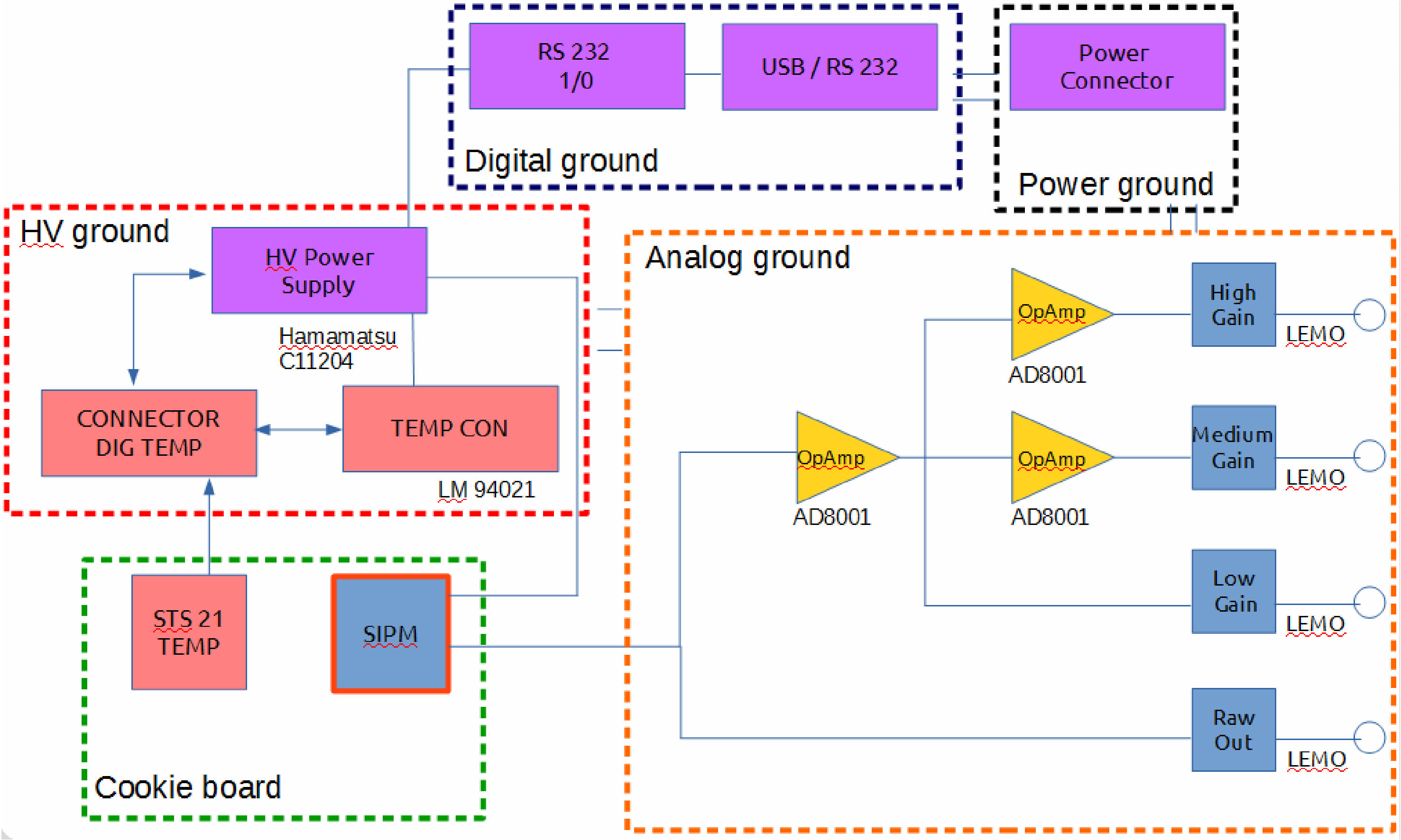

Figure 5.22: Simplified IceARM block diagram with amplifier chain for lab tests, based on the different ground levels at IceARM. The SiPM, soldered to the cookie board (botton left), is read out by the readout board (right) and can be amplified in with three different gain levels, depending on the processing purpose of the SiPM pulses e.g. scintillator readout, calibration, single photo electron finger charge spectra. To stabilize the gain of the SiPM, a temperature sensor is placed next to the SiPM to adjust the gain in real time with a developed temperature-gain-biasvoltage control loop. The Hamamatsu power supply (top left) can be controlled via a RS232 interface and, for easier handling, ajdusted to the USB standard for laptops or desktop PCs (top right).

Figure 5.22 shows a simplified block diagram of the ARM. The temperature-bias voltage control loop is implemented between the analog temperature sensor and the Hamamatsu power supply [64]. In addition, a digital temperature sensor on the Cookie Board can be used for an external control loop. To use a different position and model of temperature sensor a connector is placed on the Readout Board. The SiPM signal can be readout with four different outputs with different amplification. The high gain is used to resolve the single photon finger spectrum of the SiPM for calibration (Chapter 6), the mid- and low gain can be used for the readout of any scintillation detector with fiber readout.

Figure 5.24 shows three different parts of the first IceARM electronic. A focus was set on the different in and outgoing connections of IceARM. For the in-field measurements of IceScint, not all of the connectors needed to be soldered (e.g. three different gain levels or two different temperature sensors). For the first prototyping and for calibrating proceedings (Chapter 6), however, all of the connectors were used highlighted in the figure.

In Figure 5.23 the full IceARM assembly is shown. To read out the temperature and control the power supply an UART is used. For this first prototype we have a flexible design to test different options which need to be defined and fixed for mass production. E.g., the interfacing IC, the D-Sub connectors and its footprint were chosen to change quickly between RS232 and USB interface. A short listing of the key features of each board follows.

Cookie Board

- Easily adaptable to different SiPMs (versions and manufactures). PCBs were made for the Hamamatsu S13360 series. Footprints for new Cookie Boards for the $6 \times 6\text{mm}^2$ SiPMs of SenSL or KETEK have been made, since at the R&D time of the IceARM electronic it was not sure what kind of SiPM fits best to the system.
- Analog and digital temperature sensors are on the backside of the PCB. The idea was to use the analog one for an onboard temperature control loop via the Hamamatsu power supply and the digital one to inform the Field Hub DAQ about the temperature at the scintillator. It turned out (Chapter 6) that transferring the temperature values and controlling the gain via IceTAXI gives the best results for the prototype array.
- The accurate positioning of the SiPM to the optical connection was possible at KIT-IPE[10]. A 3D-printed holder to arrange the SiPM correctly in series production is have been developed.

Adapter Board

- The board is mainly mechanical stability and allow the Cookie Board with the SiPM to be mounted inside the cookie.
- Used to screw the Cookie Board via the Adapter Board to the optical coupling which leads to a more stable, transport resistant mechanical connection.
- In addition, used to connect the Readout Board with the General Purpose Board.

---

[10] Institute for Data Processing and Electronics

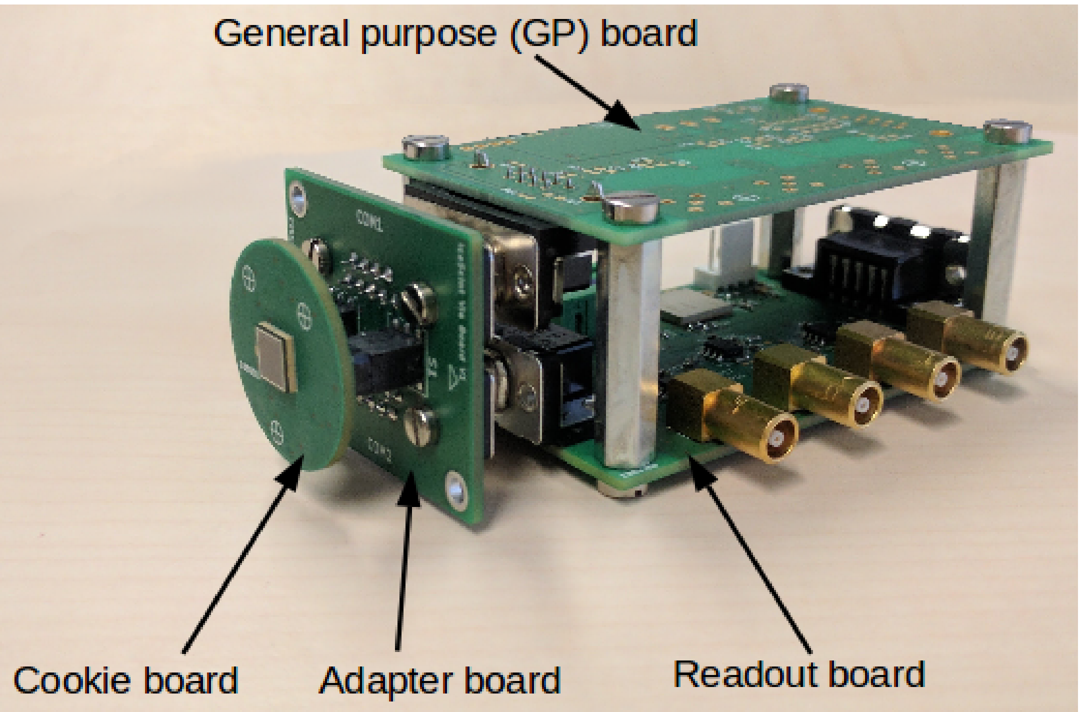

Figure 5.23: The complete first IceARM assembly as developed for the wooden prototype detector. The Cookie board with the SiPM, the adapter board which is connecting the general purpose board and the readout board are visible. For the IceScint series production, so with aluminum housing, the total height of IceARM was reduced by changing the adapter board in a way that it connects the cookie board, the readout board and the general purpose board next to each other, instead of, as pictured, stacked to each other. More details in the change of the alignments of the IceARM parts can be found in Chapter 6.

Readout Board

- A Hamamatsu C11204-02 power supply is used [64]. Key features are the wide output voltage range (40 V to 90 V); the low ripple noise and the finely adjustable resolution in 1.8 mV steps. A Python based script has been written to monitor and control the power supply (com3.py). The temperature-bias voltage control loop has been implemented and is working with the analog temperature sensor (Chapter 8).

- Three different pre-amplifiers ($\times 1$, $\times 5$, $\times 10$). The $\times 5$ one is used for scintillator readout and measuring MIPs, the $\times 10$ is used in order to resolve more precisely the SPE fingers and to calibrate the SiPM with SPOCK. Both measurements can be done at the South Pole simultaneously. The number of amplification stages and therefore the amount of signal outputs can be reduced to only two (high-gain for SPE calibration, low-gain for scintillator readout) to reduce costs after the final design is fixed.

- Four different ground shieldings prevent electronic noise entering into the high frequency SiPM signal, explained in Chapter 6.

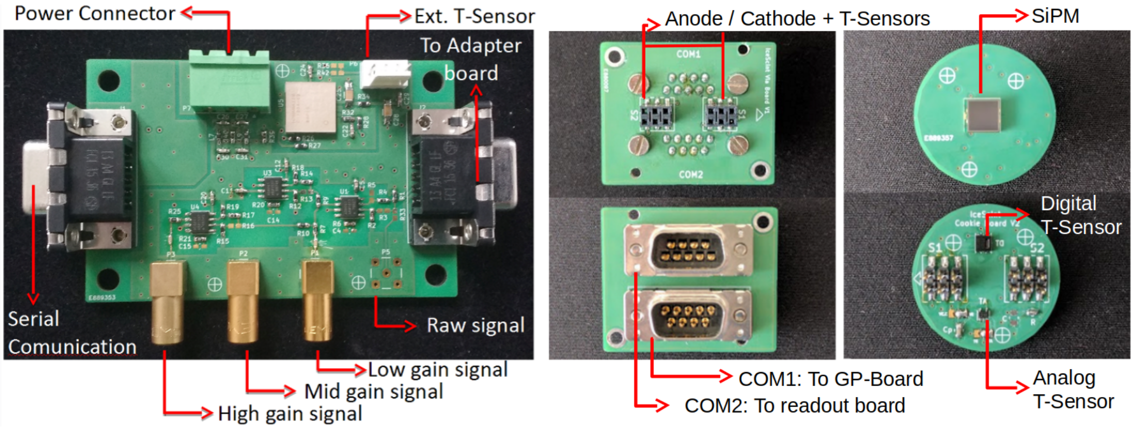

Figure 5.24: Left: The 4-layered readout board. Reading out and amplifying the SiPM signal, implementing the temperature control loop and the SiPM power supply, as well as communication with the power supply. Center: Adapter Board for mechanical stability, to make ARM modular and flexible and to connect the Readout Board with the Cookie Board. In addition, it is used to mechanically mount the optical coupler to the ARM. Right: Cookie Board with the SiPM on the front side. The analog and digital temperature sensors are at the backside. Only six electrical connections needed, the other six are connectors for mechanical stability.

- Only ±5V supply voltage is needed to operate the Hamamatsu power supply.
- Analog and, as option, digital[11] temperature readout has been implemented for reading out a digital or analog temperature sensor placed on the Cookie board.
- Possibility to connect an additional external temperature sensor for as example measuring the ambient temperature inside of the IceScint detectors.
- The SiPM gain tuning of the detectors is done via the RS485 connection from the IceTAXI board to the Hamamatsu power supply [64]. The Hamamatsu power supply is directly connected to a temperature sensor and has its own control loop, that can be written from the TAXI board via the RS485 connection. The SiPM temperature, voltage, and current are monitored via a RS485 connection.

General Purpose Board

- Contains line drivers to transmit the analog signal from the scintillator panel to the Field Hub.
- Contains a microcontroller for slow control (temperature, voltage, and current monitoring and control) that is connected to the Field Hub DAQ via a RS485 connection.
- The signal will be shaped and amplified on the ARM General Purpose Board. The analog signal will be transmitted as a differential signal from the scintillator panel to the TAXI board.

---

[11] I²C protocol

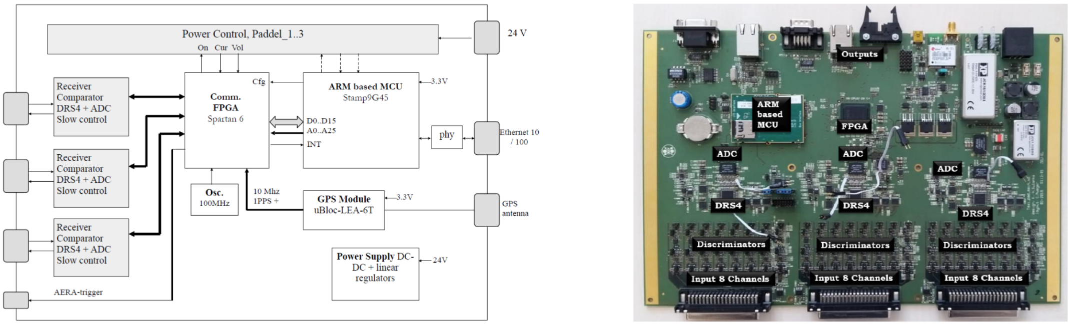

Figure 5.25: Left: The schematic of the original TAXI board with 24 analog input channels in three blocks of eight channels each. Right: Image of a fully assembled TAXI board. Visible are the three blocks with 8 input channels each. The Input channels are at the bottom and the output channels at the top of the picture. The modified TAXI (IceTAXI) can be found enlarged in the next figures.

All parts of the IceARM electronics are explained in more detail in the next (R&D) Chapter and part of the calibration measurements can be found in Chapter 8.

Temperature performance of IceARM The standard components (resistors, capacitors, ...) of the ARM were chosen to operate at low temperatures, according to the data sheets of the manufacturer. The full IceARM device has been tested at $-70°$C in the temperature chamber for 4.5 days as part of the calibration measurements of the analog and digital temperature sensors, including the glued Cookie Board inside the optical coupler and the SiPM. A dark count spectrum at $-70°$C was obtained. No problems occurred with the op-amps, the SiPM, the connectors, or other parts of IceARM. In addition, the Hamamatsu power supply was tested at $-70°$C separately. The measurements are shown in Chapter 6 in more detail.

5.6 IceTAXI Data acquisition

The data acquisition is based on a readout board that was developed for the TAXI project [53]. Within this thesis and in co-operation with DESY Zeuthen the TAXI board was modified to fulfill the requirements for reading out SiPM signals, to control via a serial interface the operation parameters and work at environmental South Pole conditions. In order to characterize and calibrate the deployed IceTAXI, the DAQ parameters like the ADC calibration parameters or the discriminator threshold values were measured (Chapter 8).

The original TAXI board (Figure 5.25) supports 24 analog input channels in three blocks of eight channels each.

The output from the individual discriminators are interfaced with serial-input parallel-output (SIPO) Serializer Deserializer (SerDes) blocks in a FPGA [54] with a 8:1 ratio at 950 MHz. The subsequent 8-bit parallel output is then recorded at 118.75 MHz. In addition, input waveforms are recorded with a ring sampler (DRS4 [65]) and the integrated charge can determined online in the FPGA.

A slightly modified version of the board, IceTAXI, with only one block of eight channels in use was developed within this thesis (Figure 5.26).

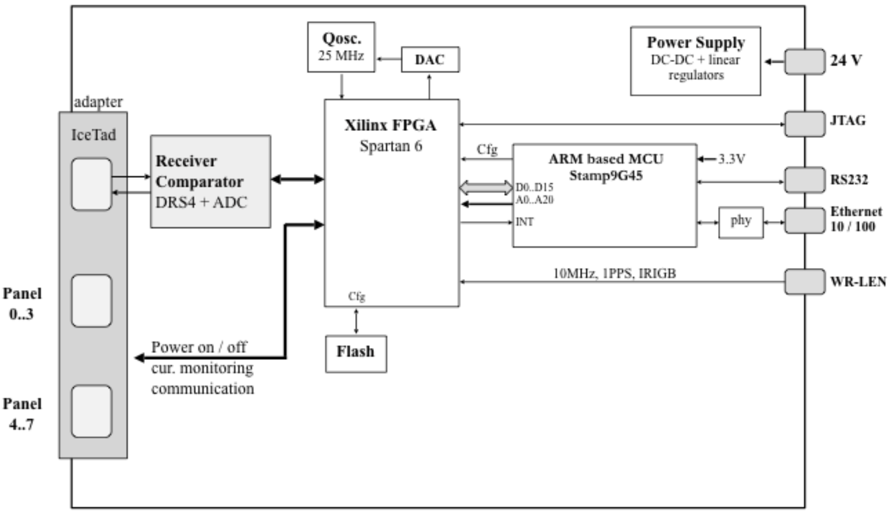

Figure 5.26: The schematic of the modified TAXI board for scintillators with SiPM readout for deployment at the South Pole, IceTAXI. The key features are an onboard Linux system to control IceTAXI, embedded in an ARM MCU via SD-card, an FPGA for controlling the input channels and enabling a nanosecond time resolution and 2 mounted DRS4 chips for sampling the incoming SiPM waveforms with up to 5 GS/s at two different gain levels simultaneously.

Since the array consists of 7 detectors, The remaining channel was used for electronic and environmental noise measurements. Each channel is discriminated and the leading and trailing edge of the discriminator output are timestamped in an FPGA with a nanosecond time precision.

Therefore, two different operational modes are possible. In the first one, IceTAXI works in a way that the charge deposit by air-shower particles which induces a photomultiplier peak is integrated on site of IceTAXI and only the resulting charge value and a timestamp is transferred. In the other operational mode the input waveform, which is sampled and recorded by the DRS4 and triggered by a signal-over-threshold system, can be transferred to the ICL and analyzed offline. This mode was also used to characterize the IceTAXI system (Chapter 8).

The TAXI board consists of an FPGA chip combined with a microcontroller with an embedded Linux system as shown in Figure 5.26, optimized for the detection of charged air-shower particles. All of the differential input signals into the board are offset adjusted and split into two paths: One to a comparator with a variable threshold and the other one to a Domino Ring Sampler chip (DRS4) [65]. Once discriminated, the output pulses are passed to the FPGA [54] where configurable trigger conditions are applied. On a fulfilled trigger condition the DRS4 chip is 'frozen' at a suitable time to digitize the waveform from all the IceScint detectors at once and converted by a 14-bit low power ADC (LTM9007-14) [67]. This features a simultaneously sampling of 8 input channels and a Signal-to-Noise rate of 73 dB. The pulse time information and the charge-integrated or

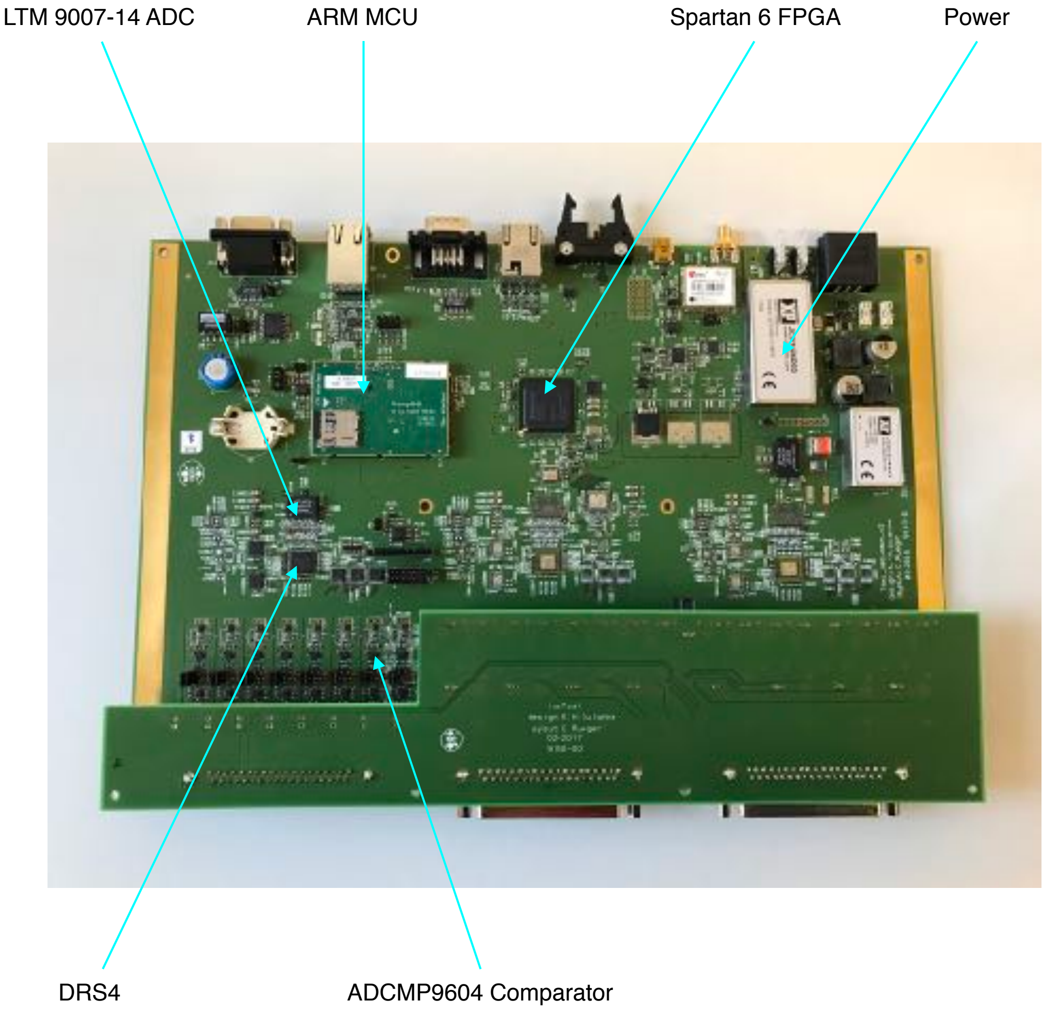

Figure 5.27: Photo of the IceTAXI board, as used for readout of the scintillators in the South Pole Season 2018. Only two blocks are mounted since the IceScint station consists of 7 scintillation detectors. One DRS4 is in charge for sampling SiPM signals in Low-Gain mode, the other for the High-Gain readout. The remaining channel at each block without a detector connected was used for electronic and environmental noise measurements and for estimating the crippling noise which was subtracted at the signal channels. The IceTAD board (See Chapter 5.6.1) can be seen on the bottom of the photo, placed one layer above the IceTAXI mainboard [66].

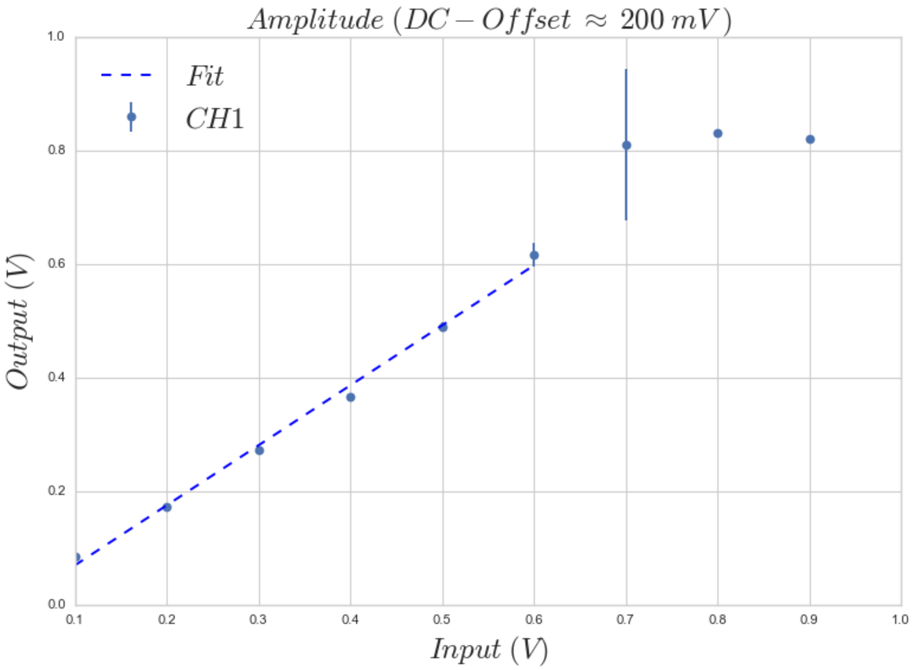

Figure 5.28: Saturation and small signal non-linearity with 200 mV DC offset [69]

full waveform are then transferred to a micro-controller unit (Stamp9G45 from TasKit GmbH) running Linux [68]. It handles the data formatting and transmission to the IceCube DAQ via an 100 Mbit Ethernet interface.

The relatively easy reconfiguration of the TAXI board was possible as different iterations of the board have already been in use for cosmic ray air shower detection at a small test array in Zeuthen and to study muon rates along a passage from northern Germany to Neumayer Station at Antarctica. Trigger configuration, debugging and other firmware and software updates can be performed remotely via the embedded Linux system on IceTAXI.

The DRS4 chip has an input range of Δ =1 V and a low integral non-linearity (0.5×10^{-3} at the 1 V range). Together along with the ADC (± 1 LSB[12]) results in a slight non-linearity. This very small non-linearity and the saturation of the DRS4 chip after offset and gain correction is shown in Fig. 5.28.

For testing the analog signal transmission and digitization of IceTAXI itself, a pulse generator connected to the IceTAXI Board was used to verify the working principle of the DRS4 and 14-bit LTM9007-14 low power ADC [67]. The charge spectrum in Fig. 5.29 illustrates a 20ns long 400mV and 200mV pulse. We expect 80pC and 40pC of charge respectively for these measurements and anticipate improving the calibration in the future.

To test the analog signal transmission from the IceScint detector to the IceTAXI the differential transmission of a SiPM signal via 100 m has been demonstrated during the R&D phase at DESY Zeuthen. The DC power for the differential line-driver was supplied over

---

[12] Least Significant Bit

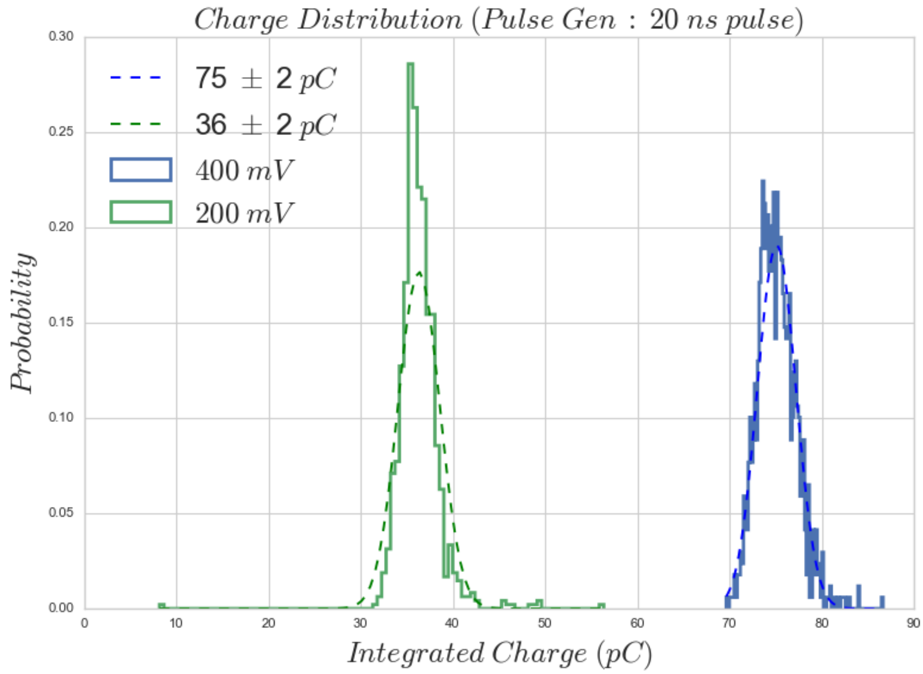

Figure 5.29: Charge distribution with 200mV (green) and 400mV (blue) pulses (both 20ns wide) using a pulse generator [69].

another pair in the same cable to check for interferences, which were not observed. The General Purpose Board, as part of the IceARM, that contains the signal shaping and is part of the amplification chain, was tested at DESY Zeuthen, too, before it was shipped to KIT for additional tests using the first assembled IceScint wooden prototype detector.

In summary, the key features of the IceTAXI are [53]

- An accurate and tuneable 25 MHz oscillator (HC49US Series, ECS Co. Ltd., [70]) that is pulse aligned to an external GPS or White Rabbit PPS signal. In circumstances where the White Rabbit or GPS signal acquisition is not possible, accurate timing is still possible with this oscillator. For the IceScint array, the White Rabbit system is used to align to the pulse [71].
- The ADA4932-1 [72] from Analog Devices GmbH is a high speed, low offset and low noise voltage-feedback op-amp with adjustable gain that can be adjusted depending on need. The offset is set via an 8-bit micro power octal DAC (DAC088S085, National Semiconductor) enabling optimal usage of the available dynamic range.
- The Analog Devices' ADCMP604 [73] comparators are very fast and low-noise that enables discrimination without the need for a lot of calibration.
- A Xilinx Spartan 6 (XC6SLX45) FPGA [54] provides input Serializer/Deserializer blocks that are implemented along with input delay blocks allowing the board to easily achieve nanosecond timing resolution.

- The board features a ARM MCU (Stamp9G45 [68]) equipped with a 16-bit parallel bus which has already been proven to be reliable and versatile and is in use in experiments such as H.E.S.S. (High Energy Spectroscopic System), XFEL (X-ray Free Electron Laser) and the digital trigger for CTA (Cherenkov Telescope Array).

- A DRS4 chip is operated at 2.5 V, and around 1 Gigasamples per second which is adjustable (up to 5 GS/s) and eight channels with selectable region of interest of up to 1024 storage cells. These waveforms are then digitized with a 14-bit low-power ADC (LTM9007-14, [67]) from Linear Technology.

- A targeted trigger rate of 0.5-1 kHz per IceScint detector has to be handled. The major factor contributing to the dead time is the digitization of the DRS4 output (Chapter 8). While the DRS4 can be written to at 1 GHz/Sample, the readout is limited to about 30 MHz, leading to a deadtime of up to 35μs to read out the entire 1024 sampling cells (Chapter 8). If necessary this can be reduced by selecting a smaller region of interest. In addition, it can be cascaded with the other two DRS4 chips in order to increase the trace, like done for the next version of IceTAXI with additional radio antenna readout (Chapter 4).
  To minimize data loss the readout strategy will be to wait for the maximum allowable time after a single-panel trigger before the DRS4 content is frozen and read out. This way possible correlated signals from the same air shower in the other six IceScint detectors will be in the 1 μs long readout window. Leading and trailing edge times of discriminator crossings occurring during the DRS4 readout deadtime is still recorded.

The TAXI board requires 24V DC for operation. The average power consumption of the stand-alone IceTAXI board during operation is 7 W. The average power consumption of the IceTAXI board with seven IceScint detectors connected during operation is approximately 10 W. The Stamp9G45 ARM CPU on the IceTAXI board provides a 100 Mb Ethernet interface on a RJ45 connector. The data will be formatted and transferred from the CPU[13]. This guarantees large flexibility and an easy adaption to IceCube requirements and further integration in more detail into the IceCube data format system.

5.6.1 Interface with the SiPM readout system

The original TAXI was mainly developed to read out detectors built with PMTs. Among others, to fulfill the other requirements of SiPMs compared to PMTs (Chapter 6), in cooperation with Karl-Heinz Sulanke (DESY) an adapter board, IceTAD (Figure 5.30), was developed. In addition it allows the half-duplex communication between the readout electronic in the IceScint scintillators and therefore enables a serial communication to control the detectors. This board is placed over the signal input section of the IceTAXI board (Figure 5.27).

---

[13] Stamp9G45 ARM

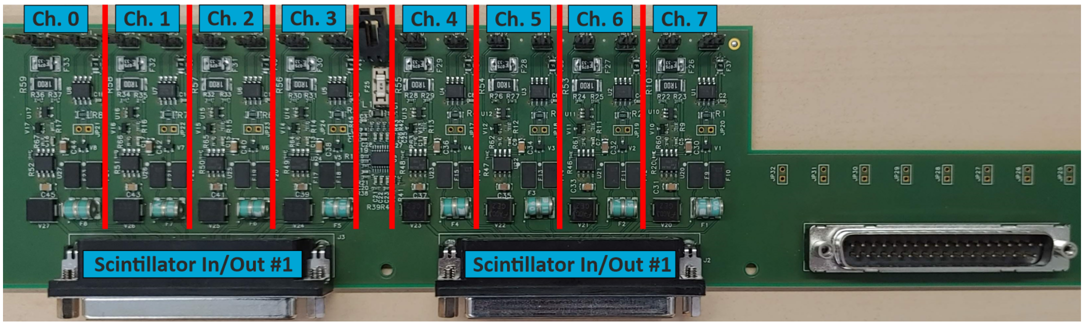

Figure 5.30: Picture of the IceTAD board as new interface for the IceScint detectors and the IceTAXI board.

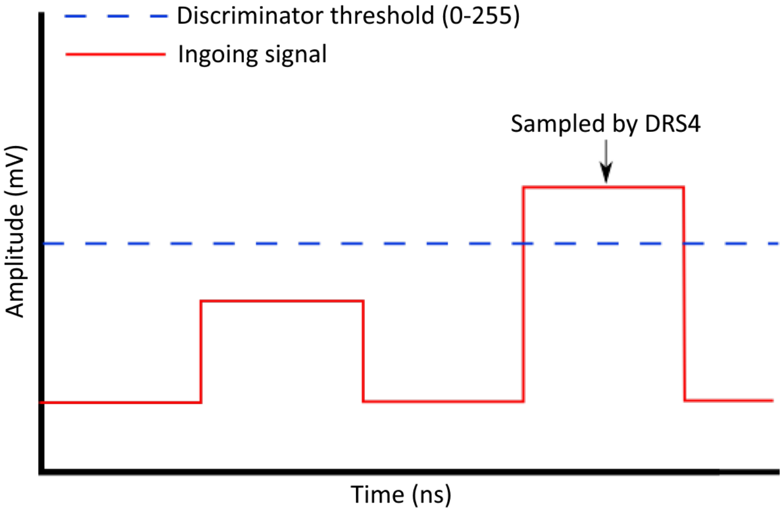

Figure 5.31: Schematic of the IceTAXI trigger technique. The incoming signal needs to have higher amplitudes which exceeds the set discriminator threshold, which is variable between 0-255 decimal values which equals to threshold voltages in the mV region (Chapter 8). The set discriminator level is sketched in dashed lines and the pulses as solid red line. The, in terms of timing, first pulse (right) is going to pass the threshold, the second one will not be recognized by the following IceTAXI subsystems.

5.6.2 IceTAXI trigger system

The trigger of the IceTAXI system for the IceScint station is a signal-over-threshold technique (Figure 5.31). The ingoing signal must have a higher amplitude value as the set discriminator threshold. This discriminator value can be set between 0 and 255 decimal values in one decimal steps. If the, in calibration measurements well defined pulses and in normal measurements SiPM peaks, signal passes this threshold, the DRS4 will sample the signal and the following IceTAXI subsystems will process the signal. The transformation from the decimal discriminator values to voltages is described in Chapter 8.

In Figure 5.26 it is seen that the discriminators are placed directly after the IceTad board, this entails at the beginning of the input side of the IceTAXI board. The calibration measurements performed to transform the threshold levels (0 - 255) for each of the 8 input

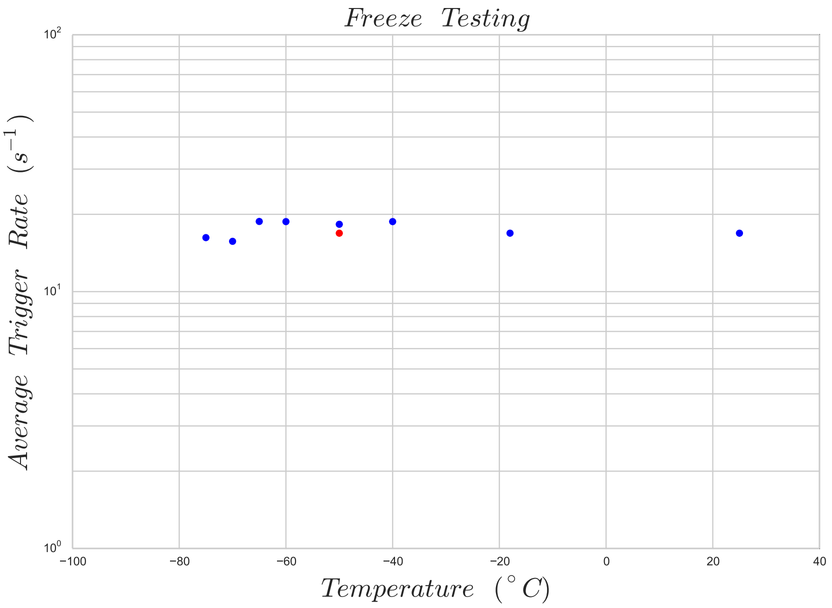

Figure 5.32: The IceTAXI board tested in a freezer down to −75°C [69]

channels in a voltage can be found in Chapter 8. A cable pair on the IceScint connection is integrated to inject electric pulses from the IceTAXI onboard FPGA into IceARM. Measurements of the pulse time of the returning pulse with the TAXI board will allow us to determine the pulse round-trip time and to derive the cable delay (Chapter 8). The RS485 signal cable pair will be used for this in a special time-calibration operation mode.

The behavior of the trigger rate at the IceTAXI board has also been tested in a freezer down to −75°C with a cold reboot performed at −50°C. This test was conducted by searching for coincident muons in a scintillator hodoscope set up. No irregularities were observed as seen in Fig. 5.32.

5.6.3 Adjustments to SiPM waveforms processing

Since SiPMs have a significant higher dark count rate in the MHz region, compared to photomultiplier (Chapter 6), the signal transfer and the cabling were chosen to fulfill a sufficient shielding. To minimize additional interference noise from other experiments and generally the environment at the South Pole, the SiPM signals are transferred double ended instead of single ended (Figure 5.26).

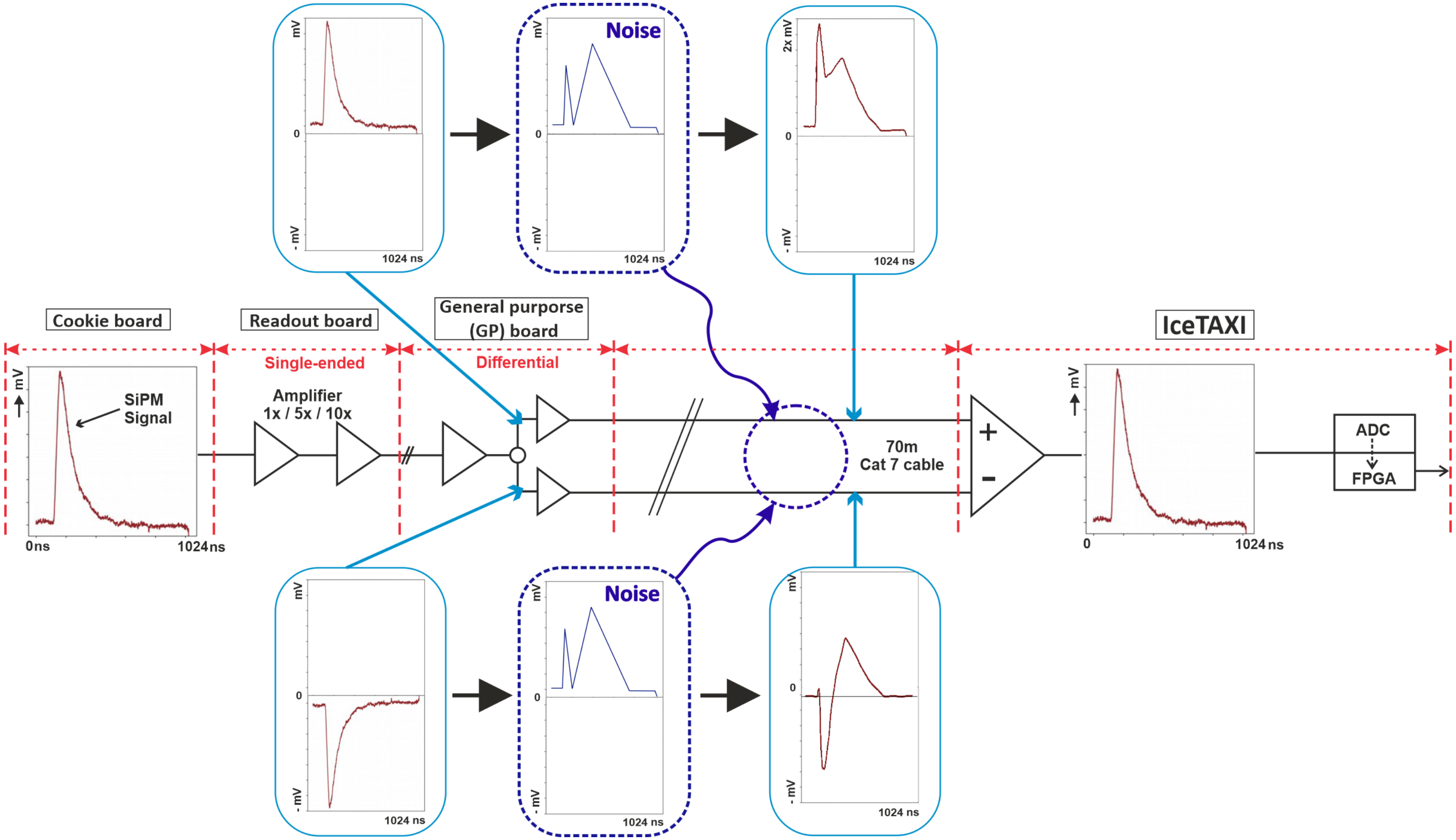

Figure 5.33: Sketch of the analog SiPM waveform transmission between IceARM and IceTAXI. The SiPM signal is transfered via an Adapter board to the Readout board. After a first signal modulation, the GP board modulize the signal double-ended (differential) to finaly substract EM noise which radiates into the 70m cable between the detectors and the DAQ.

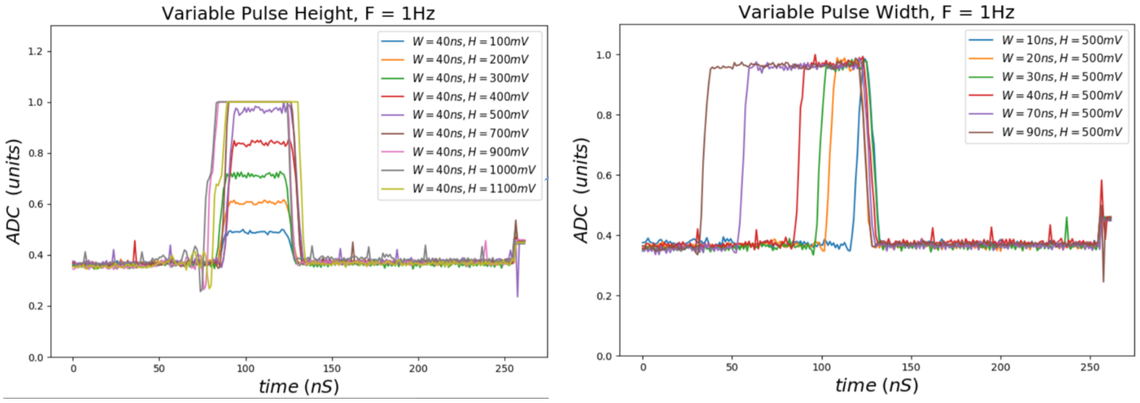

Figure 5.34: Left and Right: Ingoing rectangular pulse to IceTAXI, generated at a frequency generator and sampled with the DRS4 chip, sent via the IceTAXI EventReceiver to a desktop PC. Left: Variation in the pulse amplitude. The dynamic range of 1 V can be seen. Right: Change of the pulse width. The trigger was set to the decreasing edge. The offset to 0 V can be moved in other voltage regions (like at this measurement to $U = 400mV$).

The single ended analog SiPM signal is transferred via an Adapter board to the Readout board. The signal can be (at South Pole deployment) via Op-Amps amplified around 1.1 (Low-Gain) times and 9 (High-Gain) times (see Chapter 6 for exact measurements of the total gain of the IceScint system) and in the Laboratory amplified by a factor of 5.

Figure 5.34 shows the use of the DRS4 sampling of IceTAXI to obtain the waveform of the signal in order to debug and calibrate the IceScint detector readout. It is shown the waveform sampling of a rectangular signal from a signal generator input. It shows the variation of the amplitude of the signal (left) and the change of the pulse width (right). The amplitude variation shows the dynamic range of the DRS4 chip of ΔU=1 V. Pulses higher than 1 V are in saturation and can not be sampled correctly.

From these shown measurement it is clear that sampling waveforms is a great advantage for calibrating and debugging a DAQ and detector system.

This feature of IceTAXI was used for the commissioning of the first IceScint station installed at the South Pole (Chapters 7 and 8). For example, by this mode, the ADC, discriminator threshold, trigger and gain calibration of the IceTAXI DAQ system itself could be validated (Chapter 6).

6 IceScint detector production, tests and calibration

In this Chapter, the research and development phase for the detectors and the DAQ as well as the resulting test and calibration measurements of the individual parts required to ensure that the detector system operates at the South Pole conditions and to correctly interpret the first measurement results of the commissioning runs are explained. Since the first adjustments and improvements after the first scintillator review changed some parts of the IceScint detector, in this Chapter only the measurements and calibration of the finally deployed version of the IceScint station will be shown. This Chapter focuses on showcasing the developed and used calibration devices and test setups used for the first stations of the IceScint array which will be useful and applied for further development, production and calibration for the full IceScint array.

6.1 First test devices for SiPM and fiber couplings

In the initial stages of this thesis many R&D efforts were necessary to meet fundamental design decisions. To achieve the required 1.5 m^2 ionizing particles sensitive area per scintillator, the interconnected components and their constraints throughout the whole detector system are tied to the number of optical fiber ends up to the size of the photosensitive SiPM area. Several items had to be considered and balanced:

- the photosensitive area of largest SiPM available (Hamamatsu S13360-6050PE, [52]) 6 mm^2) with a one channel readout of the single APDs,
- the amount of the chosen 1 mm^2 optical fiber in terms of photons loss at the SiPM surface,
- the routing of the fiber with as small reflexional loss of photons [51] and the bending radius of the fiber,
- the uniformity of the whole detector regarding a constant bending radius of the fiber,
- the amount of scintillator bars for the detector, which is coupled with the amount of fiber for the detector.

CADs and printed prototype mounts (Figure 6.1) were developed for this purpose. For a 6 mm^2 photosensitive area of a SiPM, the maximum amount of 1 mm^2 fiber is 36. This indicates, illustrated in Figure 6.1, that there is little space between two fibers and between a fiber and the edges of the photosensitive area. This maximum number of fiber would have caused some difficulties in production, most likely less light yield to the SiPM and less uniformity of the single IceScint detector. As there is no dimensional

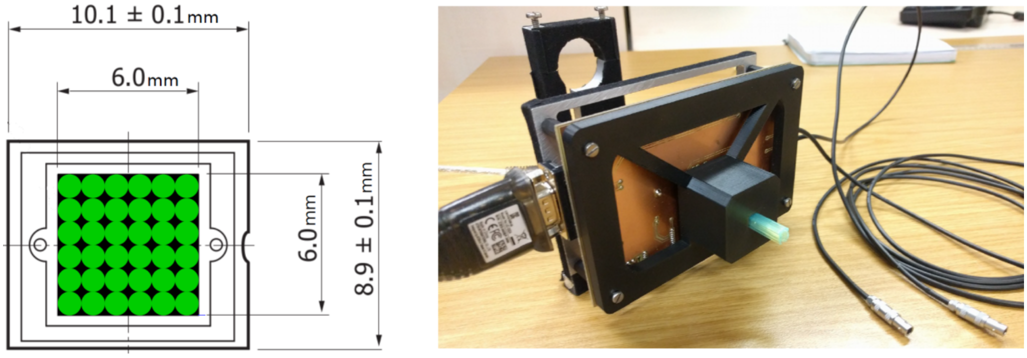

Figure 6.1: Left: Simulation of the wavelength shifting fiber with 1 mm diameter placed on the photosensitive surface of the chosen Hamamatsu SiPM series. The black area indicates the photosensitive area of the SiPM and the green dots the fiber. As visible at the picture, the maximum fiber size is 36 fibers. Due to the loss of photons, not enough gap space for the optical cement and major changes necessary in the routing of the fiber with the scintillation bars, a design was developed with 32s fiber at the SiPM. Right: A first test device with a handmade double sided readout board. The board (cooper plate) includes the SiPM readout electronic, an RS232 COM interface and pins for the Anode and Cathode of the SIPM. The black 3D printed structure at the front of the picture was to test the option to place 36s fiber at the SiPM. The cables can be seen as green reflecting cut bundle in the holder. The SiPM soldered to the test board is located on the other side of the bundle.

tolerance available in this configuration with 36 fiber, there would always be a potential risk of damaging the outer sheathing of the fiber (Chapter 5) due to friction inside of the Cookie during the production. In addition, there would also be limited space for the optical cement to completely seal the optical coupling, i.e. the Cookie. Therefore the 32 fiber design was chosen which leads to a length of 1,875 m length of the scintillator bars. For setting a limitation for the maximal bending radius of the fiber, measurements by the manufacturer of the optical fiber were used. Figure 6.2 shows the loss of photons by the bending loss vs the bending diameter of the optical fiber. Visible are two different curves (dotted and squared) for two different sheathings of the fiber. For the IceScint detectors the decision to use the "S type" sheathing. At a bending diameter larger than 5 cm there is a significant increase of a loss of photons due to the bending which equals to cracking the fiber core. The routing was accurately developed in such a way that a larger bending diameter than 10cm is not exceeded.

Summing up the considerations in this subchapter, the ideal combination of the individual components, so the amount of scintillator bars, the amount of wavelength shifting fiber and the photosensitive SiPM area with $6\,\mathrm{mm}^2$ and as given detector requirement for the ionizing particle sensitive detector area of $1.5\,\mathrm{m}^2$. In Table 6.1 the necessary additional amount for the fiber routing and the coupling to the SiPM is considered.

6.2 Analog Readout Module (IceARM)

After the changes of the IceARM from the first wooden IceScint prototype detector to the first series production of 24 detectors, explained in Chapter 5, the geometrical dimensions

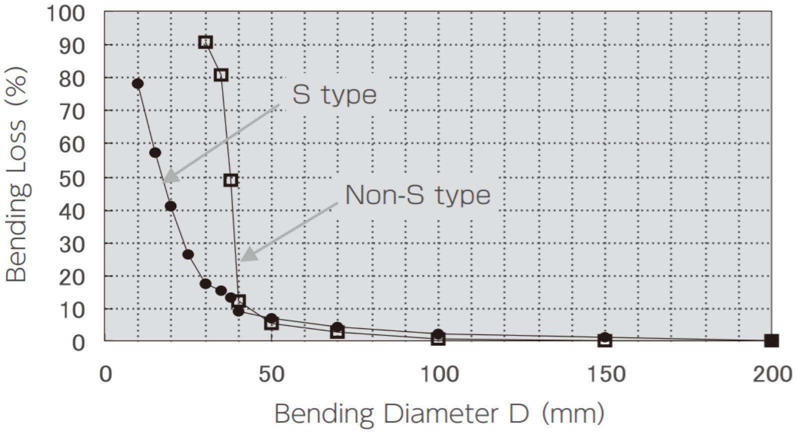

Figure 6.2: Bending loss vs. the bending diameter of the used optical fiber (dotted, "S Type"). The rapid increase of bending loss is due to cracking of the fiber core [51].

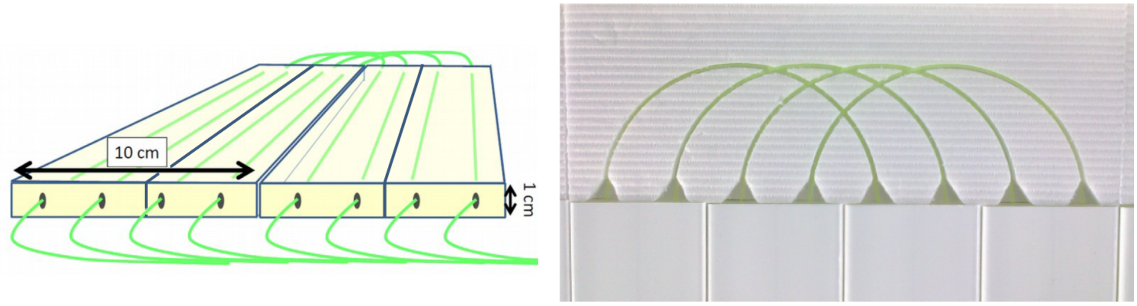

Figure 6.3: Left: Sketch of the chosen coupling system between the scintillator bars and the optical fiber. The coupling decision was, among others, driven by reducing the amount of reflected photons due to the bending loss of the fiber. Right: Picture of the routing of the used four-bars coupling. The milled form keeps the bending radius constant and ensures an uniform detector area, sensitive for ionizing particles.

of the whole IceARM electronic, inside the IceScint detectors, is defined to

$$\begin{aligned} \text{Length} &= 150\text{ mm}; 5.90\text{ inch} \\ \text{Width} &= 110\text{ mm}; 4.33\text{ inch} \\ \text{Height} &= 28\text{ mm}\,; 1.2\text{ inch}. \end{aligned}$$

Figure 6.4 shows the fully assembled IceARM, installed into one IceScint detector. The major testing and calibration procedures are described later in this Chapter.

6.2.1 Readout board

In Figure 6.5 the design of the final readout board is shown. It features the bias voltage for the SiPM and for an analog and digital temperature sensor at the cookie board, three different SiPM amplifications (1x, 5x, 10x), a Hamamatsu power supply and LC-circuits as high-pass filter for the SiPM signal. The cookie board is connected via the adapter board to the readout board.

Table 6.1: Combination of the individual detector components for the achievement of a sensitive detector area of 1.5 m^2. For the optical fiber the additional length for the routing and SiPM coupling is taken into account.

Scintillator bars (length)	1.875m
Scintillator bars (amount)	#16
Optical fiber (length each)	$\sim$ 6m
Optical fiber (length in total)	$\sim$ 96m
Optical fiber ends (amount)	#32
SiPM photosensitive area	$6mm^2$
IceScint detector area	$1.5m^2$
IceScint detector volume	$0.015m^3$

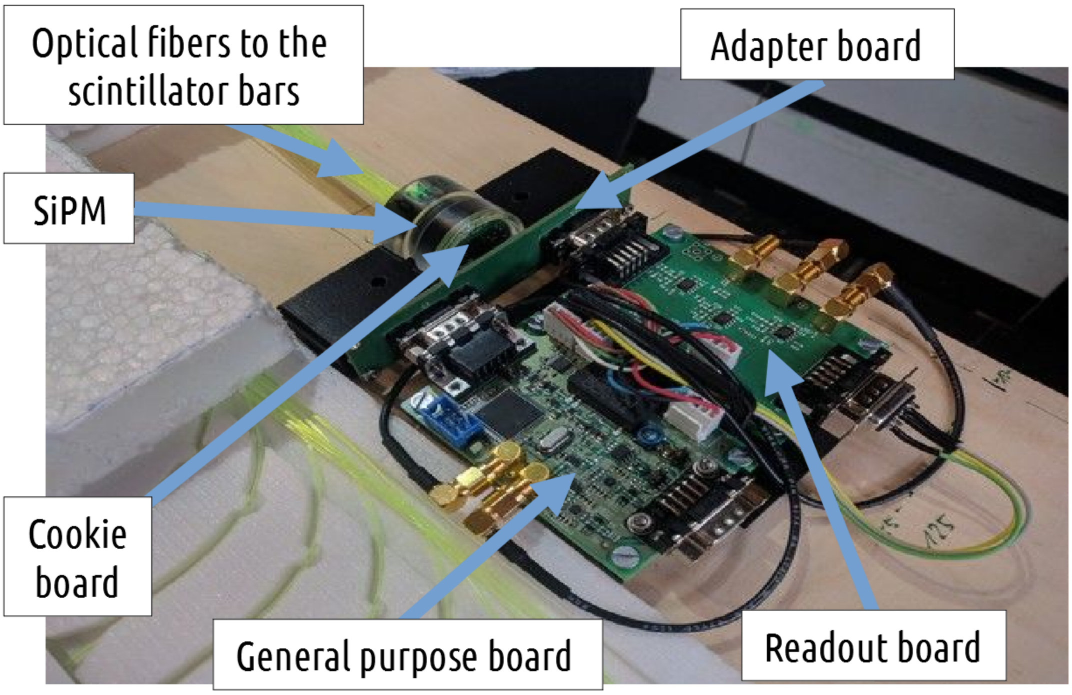

Figure 6.4: Photo of the fully assembled, tested, calibrated and into one IceScint detector installed IceARM. Visible are all four developed boards, the optical coupling, part of the developed 3D printed fixtures and the optical fiber bundle, routed from the scintillator bars.

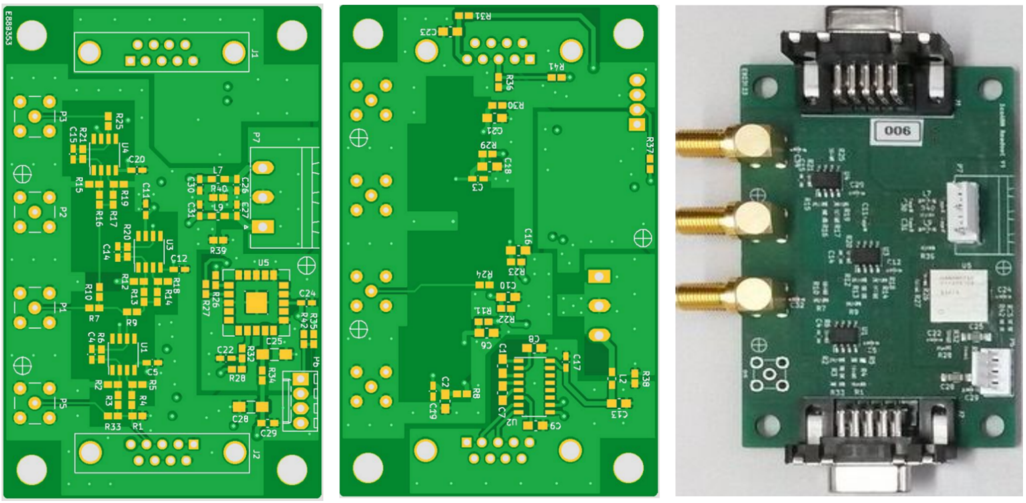

Figure 6.5: PCB front- (left) and backside (center) and photo (right) of the developed IceScint readout board.

The readout board is transferring the SiPM signal (with different gain levels simultaneously) analog single ended to the GP-board. The monitoring info of the Hamamatsu Power supply and the slow-mode control of the SiPM parameters is communicated via a RS232 interface. The temperature values, after the decision to use an analog temperature sensor, is transferred analog to the GP-board. The GP-board finally communicates via double-ended differential (SiPM signal in High- and Low Gain) and RS485 (slow-mode control read and write, "smcrw") with the IceTAXI station of the full IceScint array.

6.2.2 Adapter board

As there were many uncertain factors for the first season of using IceScint at the South Pole, e.g., what are the tasks of the electronics or which experimental and electro-technical parameters are important and may need to be modified, care was taken to design IceARM as modular and flexible as possible. The adapter board (Figure 6.6), although it is only a passive connection card, plays a major role in these considerations. Finally, it was used to connect the Cookie board with the SiPM to the readout board and in combination with the GP board to give IceARM additional mechanical stability via the connectors. The connection lines between the two D-Sub connectors was not needed for the first IceScint detectors of the first three stations, but are later in use for additional SiPM readouts (Chapter 10).

6.2.3 Cookie board

To connect the optical fiber to the SiPM and for the front-end readout of the signal, the cookie board was developed. In addition, this cookie board provides a footprint for a temperature sensor, installable close to the SiPM, to stabilize the SiPM gain via a temperature bias-voltage control loop (Chapter 8).

The photosensitive area of the used SiPM (Figure 6.7) is geometrical asymmetric due to

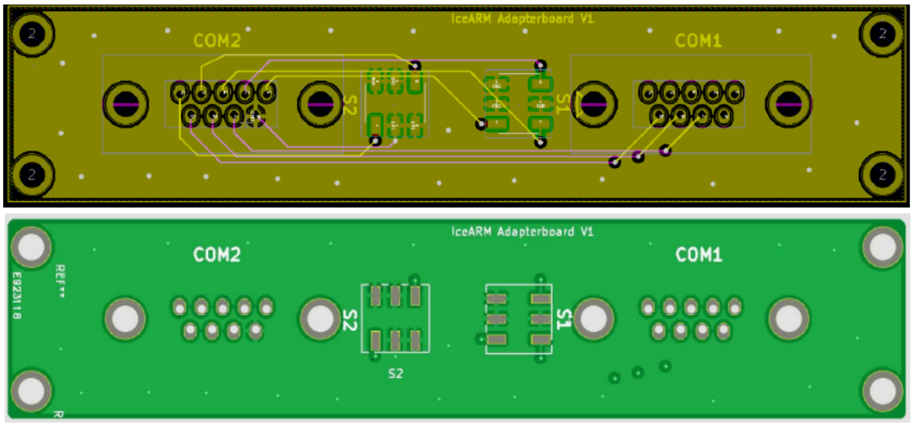

Figure 6.6: Routing (top) and PCB (bottom) of the adapter board. It is used to enable for the first series of IceScint detectors a modular, flexible design. For the first 3 stations of IceScint, the adapter is used to connect the cookie board with the readout board.

the inlet of the anode and cathode at one side. In order to in increase the dynamic range regarding the total amount of the 64.000 Avalanche Photo-diodes (APDs) at the SiPM, the footprint positioning was calculated and has been incorporated into the printed circuit board design in a way that the photons which are emitted by the optical fiber have a chance to hit and trigger all of the APDs. Figure 6.8 shows the dimension and the front and back side of the cookie board. The round board design was chosen to provide an easy connection with the optical coupling (e.g. the cookie). On the front side, the design paid attention to having as few components and vias as possible to provide the optical cement with the largest possible bonding surface. To simplify the positioning of the SiPM and as a "fail safe" feature for manual control of the pick and place machine, the position of the 6x6 mm^2 SiPM was marked in white on the front side. SAMTEC connectors [74] were used for the rear side. Actually 6 connection pins, i.e. one SAMTEC connector, would be enough (anode/cathode SiPM, 4x temperature sensor readout), but the number of connectors was doubled to give the whole IceARM module additional mechanical stability.

6.2.4 General purpose board

The general purpose board (Figure 6.9) was mainly developed by DESY Zeuthen in order to ensure a stable and not error-prone communication and control between the readout board and the IceTAXI DAQ. It contains line drivers to transmit the analog signal from the scintillator panel to the FieldHub and a micro-controller for slow control (temperature, SiPM bias voltage, and current monitoring and control) that is connected to the IceTAXI DAQ via a RS485 interface. The communication with the Hamamatsu power supply onboard the readout board and therefore the SiPM parameter adjustments is done via a RS232 interface. The SiPM signal is modified from single-ended to differential for both, high- and low-gain SiPM readout and transferred to IceTAXI (Chapter 5.3).

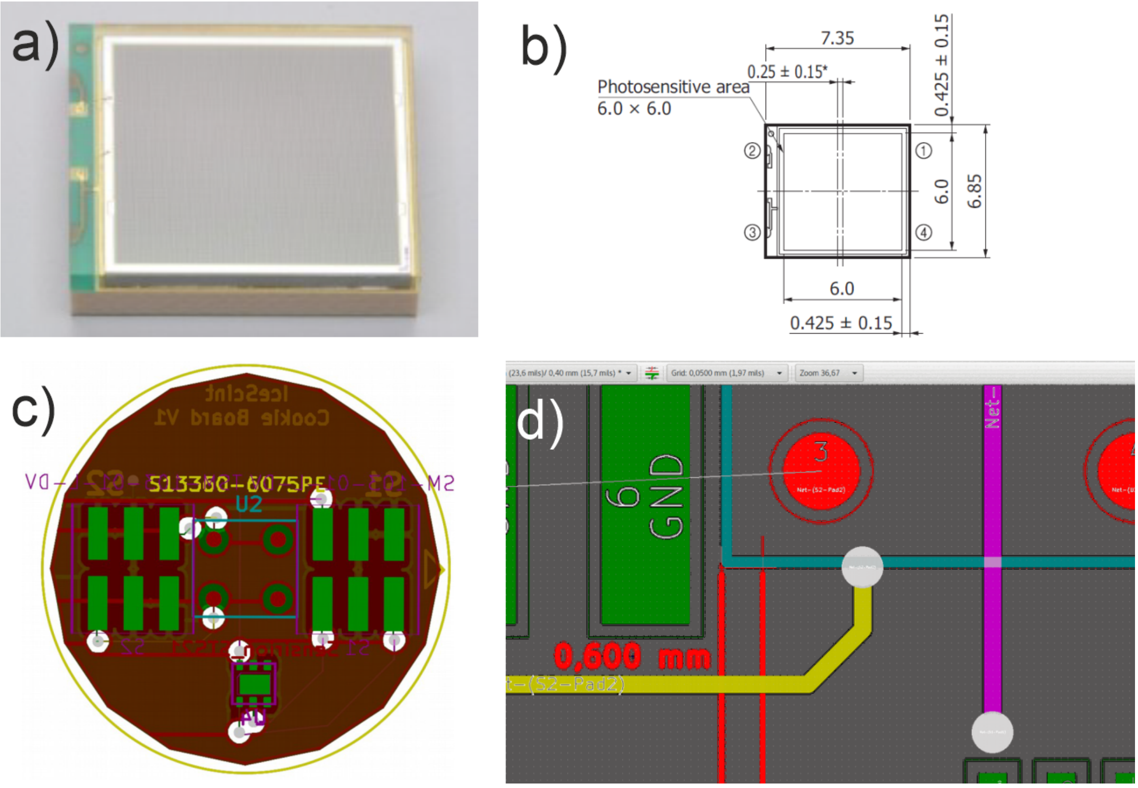

Figure 6.7: The photosensitive area of the used SiPM from Hamamatsu is not symmetric compared to both symmetric axis of the whole chip (a). Since the Cookie and the fiber routing is symmetric and fits to the outer dimensions of the cookie board, the board was developed within this thesis to ensure that as much photon as possible are hitting the photosensitive area. (c) Shows the PCB of the cookie board and in (d) it is zoomed into the asymmetric design of the soldering points of the SiPM at the cookie board due to the SiPMs asymmetrical placement of the photosensitive area on its wafer.

6.2.5 3D printed parts for IceARM

For some major parts of the IceScint detectors, 3D printed structures where developed and produced and some of them will are shown in this Subchapter. The filament for the 3D printer in ABS[1], a thermoplastic polymer, is used. A major disadvantage of ABS is its minor long-term resistance to UV light. The polymer becomes brittle and loses its fracture resistance. However, as the 3D printed components are used only inside the detector, therefore inside the black tube foil, they are only exposed to some UV light during production.

As described in Chapter 6.4 and in [57] measurements and performance tests for low temperature stability, even under mechanical stress, have been made and have shown that the used 3D printed material is suitable for South Pole conditions.

For the key parts shown in Figure 6.10 of the detector readout, the analog readout of the optical fiber and its optical coupling with IceARM, several 3D printed parts have been developed.

---

[1] Acrylonitrile butadiene styrene

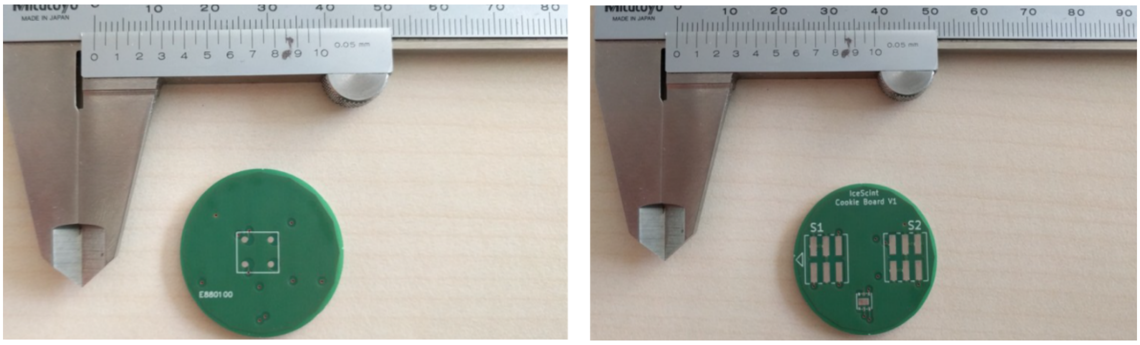

Figure 6.8: The cookie board. Left: The front side of the board. To ensure an optimal glueing result with the cookie, the optical cement and the fiber, the surface of the board is as blank as possible. The white lined squared area is the position of the SiPM. Due to the asymmetric SiPM the ideal footprint of the SiPM was marked in order to make the soldering of the boards easier. Two of the soldering contacts at the front side are for the anode and cathode of the SiPM, the remaining two contacts are for mechanical stability. Right: Backside of the Cookie board. The soldering contacts “S1” and “S2” are connecting via the adapter board the SiPM and the temperature sensor (small footprint bottom centred of the board) with the readout board and provide an option to route it directly to the General Purpose board.

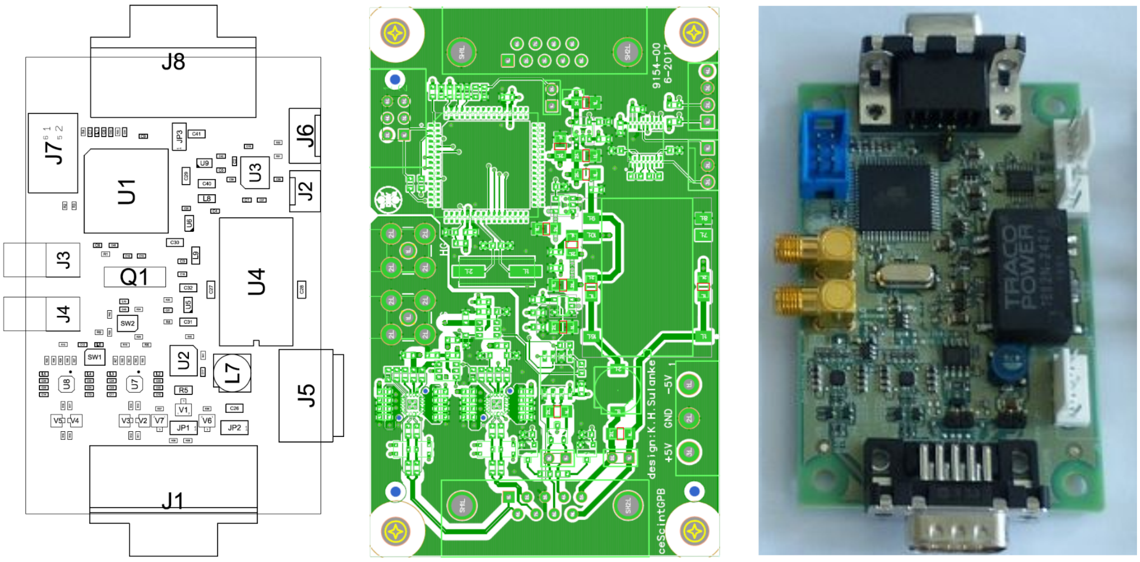

Figure 6.9: Part numbering, PCB and picture of the GP-board. As a main feature it serves as intersection between the readout board of IceARM and the IceTAXI DAQ. It receives two (high- and low gain) analog SiPM signals and modulates it into a double-ended differential signal to subtract emitted noise at the South Pole which can be interfere with the SiPM signal during the 70m cable between the IceScint detectors and the central IceTAXI DAQ. In addition it communicates with the SiPM control by the Hamamatsu power supply via a RS232.

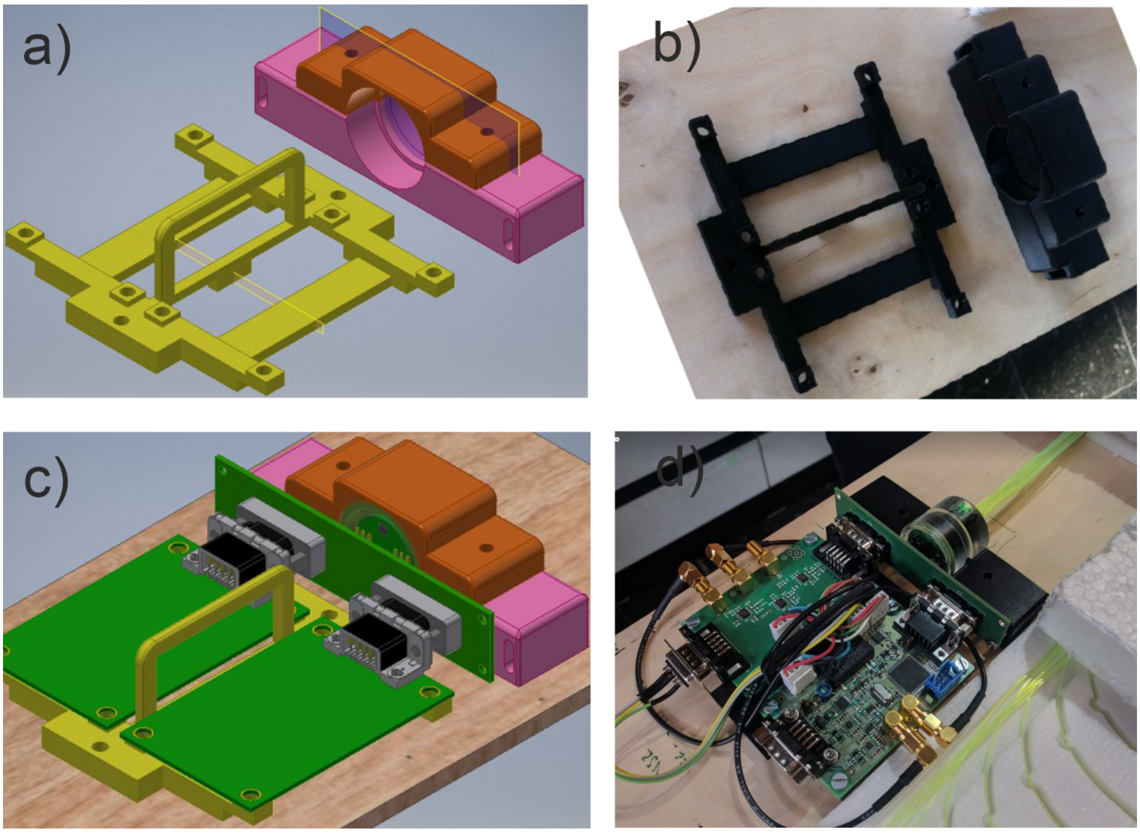

Figure 6.10: CADs and pictures of the developed mechanical multi purpose structures used in the IceScint detectors. a) CAD of the whole setup for the fiber readout. It includes the two 3D printed parts of the cookie holder (orange, pink) and the fixture of the IceARM (yellow). Picture b) shows the blank 3D printed parts. c) CAD of IceARM including the Cookie assembled and attached to the 3D printed parts. Picture d) shows the full IceARM including the optical coupling and the fiber bundle. Alle parts in this pictures are screwed together and connected to the wooden ground plate.

A simplified IceARM CAD model was designed[2] to speed up the development process. The requirements for the fixture of the electronics and the optical coupling are followed:

- The mount must protect IceARM in all three degrees of clearance from possible impacts on the detector housing during transport, deployment and from strong winds.
- In order to increase the production speed of the detectors, it is reasonable to design the mounting kit so that IceARM can be completely assembled and pre-wired independently of the rest of the detector.
- Since there are no wooden clamps and no other denser material than polystyrene between the top and bottom plate, a form of " step protection" should be located near IceARM. This was realized by the bracket between the Readout Board and the

---

[2] in Autodesk Inventor

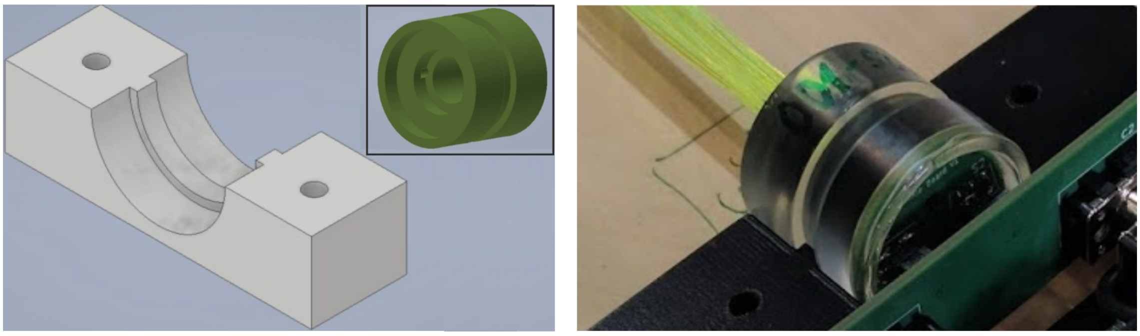

Figure 6.11: CADs and picture of the developed cookie holder and the modified cookie (top middle, not in scale). This mount keeps the cookie in position at possible impacts on the detector housing during transport, deployment and from strong winds. The additional stepping in the 3D printed holder in combination with the modified Cookie adds additional safety for the optical cement connection, e.g. against fracture of the cement.

GP Board. In addition, the height of the cookie holder (next point) was adjusted so that it is almost form-fitting with the absolute internal dimensions of the detector.

- The cookie is cylindrical for (fast) manufacturing reasons and to simplify the detector installation. This means that if the position of the detector, including the fiber, were to change, the cookie would twist axially or roll away. This was achieved by an additional two-stage mounting for the cookie (Figure 6.11).
- In addition to the optical cement that connects the fiber to the SiPM, the mounting of IceARM, the cookie and the tangential degree of freedom could be connected to each other for the safety of the connection, e.g. against fracture of the cement. This was achieved by an additional stepping in the cookie holder and a later machined grooved slot in the cookie (Figure 6.11).

6.3 Characteristics and function tests of the electronics

For pre-prototyping purposes and for the first IceScint detectors, several function tests, characteristics and calibration of the whole IceARM electronics and IceTAXI DAQ have been performed. For the purpose of clarity and in consideration of the full functionality of the first IceScint Station at the South Pole, not each individual measurement of the electronics will be discussed here. For each part of IceARM and of IceTAXI, a test routine and inspection checklist was created together with students, which provide fundamentally checks for all parts of the 24 IceScint detectors. This ensured that the detectors and DAQ were fully operational before being shipped to the South Pole (or other places such as Madison, the IceCube headquarter). Figure 6.12 and Figure 6.13 show, as an example, a test routine for measuring the stability of the Op-Amp gain of the readout board over various pulse lengths. Two additional functional test measurements (overall gain of the readout board and functional test of the temperature sensor) can be found in the attachment. The characterization and calibration for IceTAXI is given in Chapter 8.

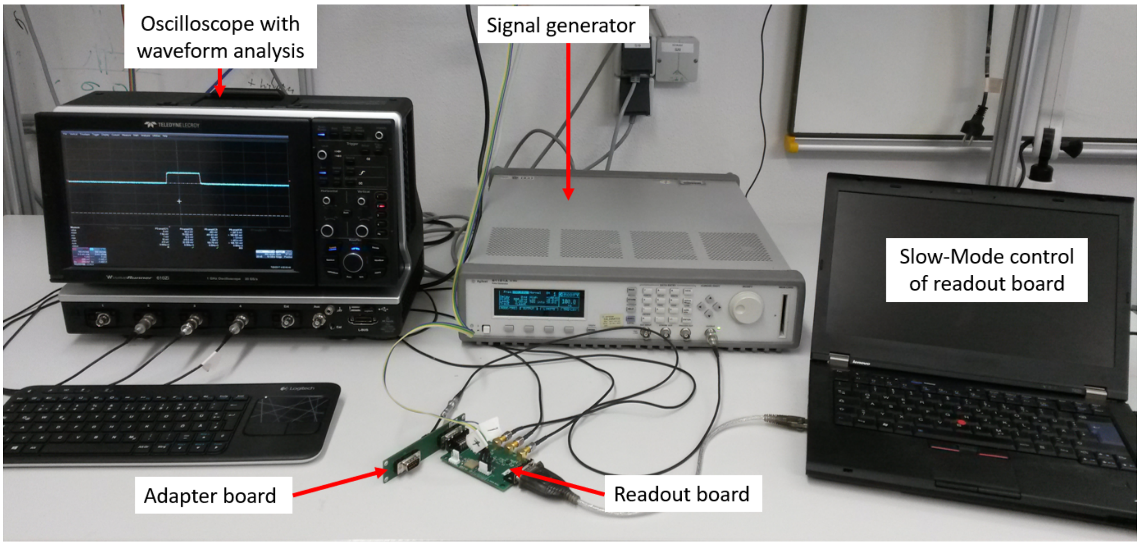

Figure 6.12: Exemplary shown is the test routine setup for the readout board to measure the stability of the Op-Amp gain over various pulse lengths, which were selected of nanoseconds intervals in which the whole SiPM pulse, e.g. the increasing edge and the falling edge, fits in. This stability was checked, next to many other test routine measurements, for every IceARM before the installation into the IceScint detector.

The main component to slow-mode control the readout board, read out the temperature and configure the SiPM on the cookie board, the python script of my master thesis [7] was enhanced to fulfil the new requirements for scintillator based front-end readout and control. A RS232 interface, since it is the easiest way to slow-mode control IceARM via the IceTAXI DAQ, is used and, for test and calibration purposes, transformed via an adapter into a more common USB interface. The software source code can be found in the Appendix. A choice of the most important control commands is listed here:

- `getOutputVoltage(self)`: "Query the voltage currently on supply output."
- `getOutputCurrent(self)`: "Query the measured output current."
- `getTemperature(self)`: "Query the measured output voltage."
- `getTemperatureCorrectionFactor(self)`: “Query the set correction gradient $\left(\frac{mV}{K}\right)$”. See Chapter 6.7 for details
- `setTemperatureCorrectionFactor(self, dT1_s, dT2_s, dT1, dT2, tb)`: “For enabling the temperature control loop (via the power supply)to set the gradients for the control loop”
- `getStatus(self)`: “Query an overview of set key parameters like SiPM voltage on/off, overcurrent protection on/off, t-sensor connected yes/no, set SiPM bias voltage, ...”
- `setHighVoltageOutput(self, on)`: "Switch the high voltage output on and off."
- `setTemperatureCompensationMode(self, on)`: "Enable and disable temperature compensation mode."

- `resetPowersupply(self)`: "Reset power supply to default settings."
- `setReferenceVoltage(self, voltage)`: "Set the reference voltage (V)."
- `getMonitoringInfo(self)`: "Get all measured and set parameters (e.g.: display “everything”)"
- `setOverCurrentProtection(self, on)`: "Set Over Current Protection Function to protect the power supply and the SiPM"
- `help(self)`: "Most important and self-explaining"

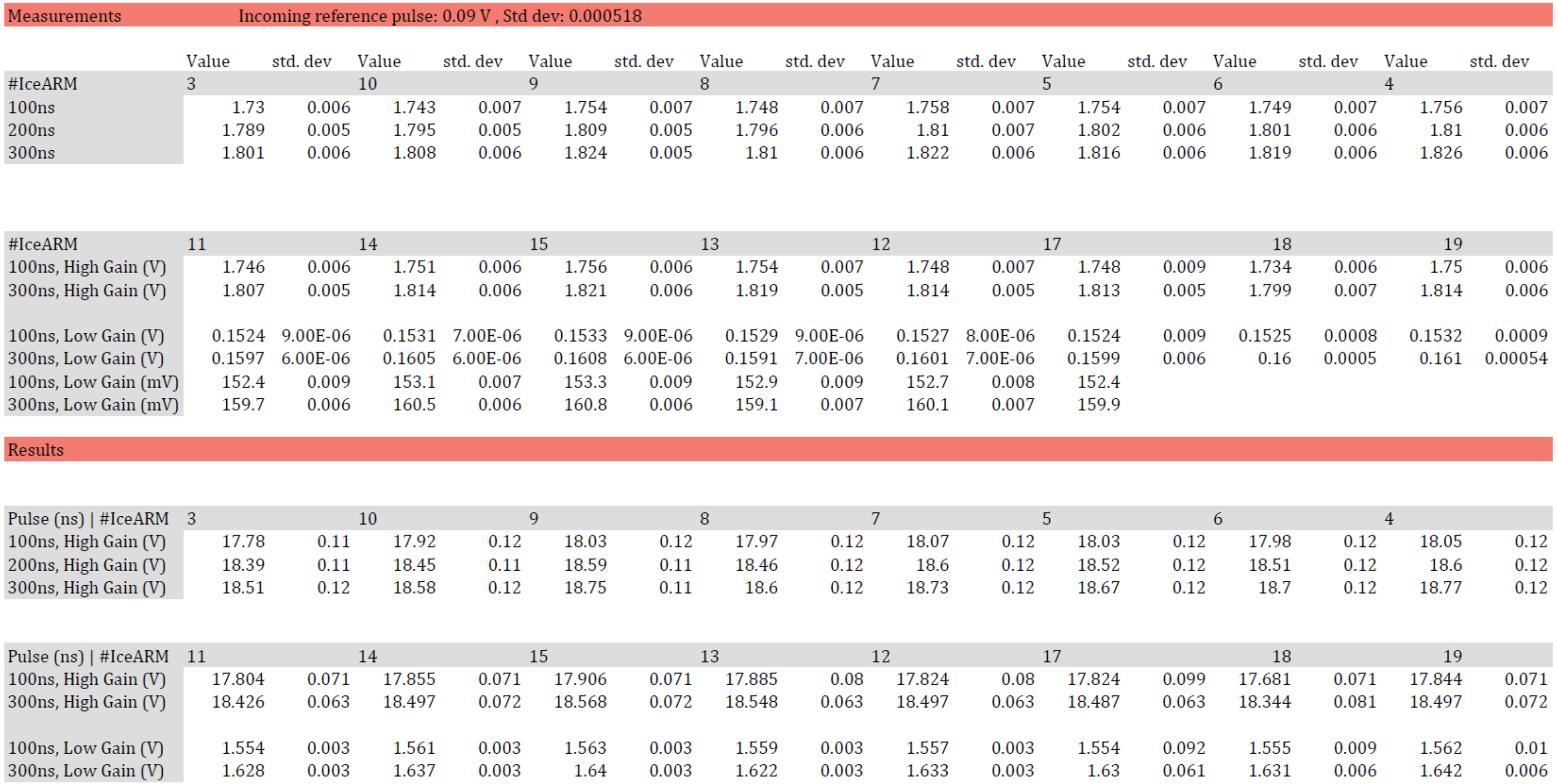

Measurements Incoming reference pulse: 0.09 V , Std dev: 0.000518

	Value	std. dev	Value	std. dev	Value	std. dev	Value	std. dev	Value	std. dev	Value	std. dev	Value	std. dev	Value	std. dev
#IceARM	3		10		9		8		7		5		6		4	
100ns	1.73	0.006	1.743	0.007	1.754	0.007	1.748	0.007	1.758	0.007	1.754	0.007	1.749	0.007	1.756	0.007
200ns	1.789	0.005	1.795	0.005	1.809	0.005	1.796	0.006	1.81	0.007	1.802	0.006	1.801	0.006	1.81	0.006
300ns	1.801	0.006	1.808	0.006	1.824	0.005	1.81	0.006	1.822	0.006	1.816	0.006	1.819	0.006	1.826	0.006

#IceARM	11		14		15		13		12		17		18		19	
100ns, High Gain (V)	1.746	0.006	1.751	0.006	1.756	0.006	1.754	0.007	1.748	0.007	1.748	0.009	1.734	0.006	1.75	0.006
300ns, High Gain (V)	1.807	0.005	1.814	0.006	1.821	0.006	1.819	0.005	1.814	0.005	1.813	0.005	1.799	0.007	1.814	0.006
100ns, Low Gain (V)	0.1524	9.00E-06	0.1531	7.00E-06	0.1533	9.00E-06	0.1529	9.00E-06	0.1527	8.00E-06	0.1524	0.009	0.1525	0.0008	0.1532	0.0009
300ns, Low Gain (V)	0.1597	6.00E-06	0.1605	6.00E-06	0.1608	6.00E-06	0.1591	7.00E-06	0.1601	7.00E-06	0.1599	0.006	0.16	0.0005	0.161	0.00054
100ns, Low Gain (mV)	152.4	0.009	153.1	0.007	153.3	0.009	152.9	0.009	152.7	0.008	152.4					
300ns, Low Gain (mV)	159.7	0.006	160.5	0.006	160.8	0.006	159.1	0.007	160.1	0.007	159.9					

Results

Pulse (ns) | #IceARM	3		10		9		8		7		5		6		4	
100ns, High Gain (V)	17.78	0.11	17.92	0.12	18.03	0.12	17.97	0.12	18.07	0.12	18.03	0.12	17.98	0.12	18.05	0.12
200ns, High Gain (V)	18.39	0.11	18.45	0.11	18.59	0.11	18.46	0.12	18.6	0.12	18.52	0.12	18.51	0.12	18.6	0.12
300ns, High Gain (V)	18.51	0.12	18.58	0.12	18.75	0.11	18.6	0.12	18.73	0.12	18.67	0.12	18.7	0.12	18.77	0.12

Pulse (ns) | #IceARM	11		14		15		13		12		17		18		19	
100ns, High Gain (V)	17.804	0.071	17.855	0.071	17.906	0.071	17.885	0.08	17.824	0.08	17.824	0.099	17.681	0.071	17.844	0.071
300ns, High Gain (V)	18.426	0.063	18.497	0.072	18.568	0.072	18.548	0.063	18.497	0.063	18.487	0.063	18.344	0.081	18.497	0.072
100ns, Low Gain (V)	1.554	0.003	1.561	0.003	1.563	0.003	1.559	0.003	1.557	0.003	1.554	0.092	1.555	0.009	1.562	0.01
300ns, Low Gain (V)	1.628	0.003	1.637	0.003	1.64	0.003	1.622	0.003	1.633	0.003	1.63	0.061	1.631	0.006	1.642	0.006

Figure 6.13: Example of one IceARM test protocol and characterization before installing into the IceScint detectors. Shown is the Op-Amp stability over different incoming pulse widths at the two set operation modes of the IceScint detectors, High Gain and Low Gain. In general, all IceARMs have been tested for functionality at low temperatures and all sensors and ICs and Op-Amps have been tested and calibrated.

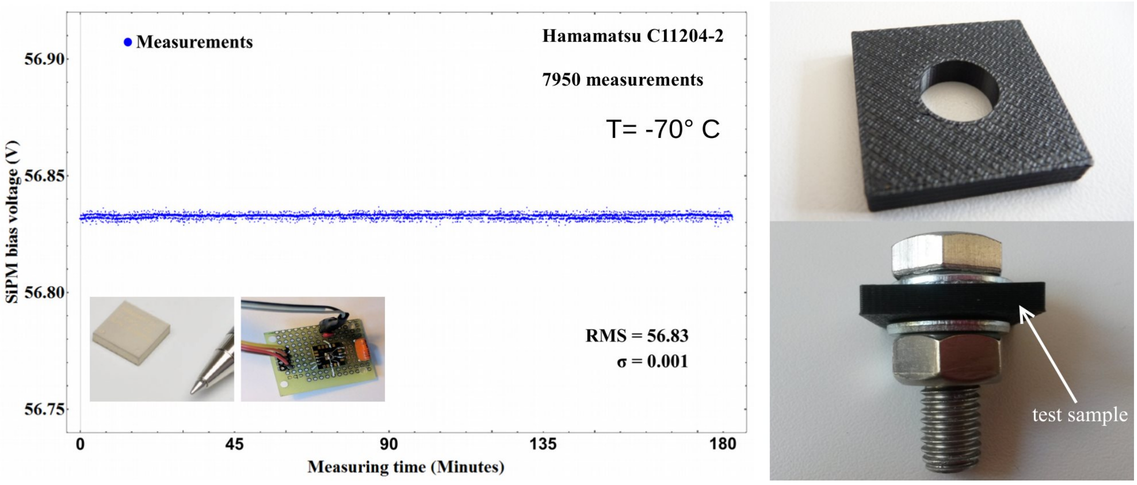

Figure 6.14: Left: Behavior of the SiPM operation voltage provided by the used power supply at −70°C over time. The power supply [64] is constantly and stably working. Bottom left: Power supply and a pen tip for scale. Next to it the soldered test board to investigate the power supply independently. Right: 3D-printed material test sample to investigate the behavior under mechanical stress.

To ensure a possible and stable readout of the IceARMs inside the panels by IceTAXI, therefore the opposite side of the readout chain, every physical channel (e.g. military connector) was connected with every fully assembled IceARM, before it was installed into the IceScint detectors and connected to the SiPM via the Cookie- and Adapter board. At the SiPM signal input of the Readout board a pulse generator was connected and reference rectangular pulses have been sent via the whole readout chain to IceTAXI. This measurement principle was used to calibrate the ADCs of IceTAXI, too and is described in more detail in Chapter 8.

In summary, great care has been taken to ensure that every single electronic component of IceARM has been tested and calibrated for functionality for the IceScint detectors. Only after all boards have operated within the tolerance range of the deviations found in the data sheets, and have therefore shown full functionality, the complete IceARM modules were installed in the IceScint detectors and finally lightproof sealed with black tube foil.

6.4 Temperature tests of the components

To investigate the behavior of the components at temperatures down to −70°C a programmable temperature chamber (Vötsch VT 7021 [75]) is available at KIT.

Several temperature tests of the components were performed. To test the 3D-printed material (Acrylonitrile butadiene styrene, ABS), which is used in the additional inner photon shielding and inside the cookie to route the fibers and arrange the SiPM, test samples were produced (Figure 6.14). The samples are tightened with a torque wrench at different torques (22 Nm to 32 Nm) to investigate the behavior under mechanical stress and were stored for 24 hours at −70°C. Without storing at −70°C, one sample breaks at room temperature at 31 Nm, one at 32 Nm and two of the samples (23 Nm and 27 Nm) show bright lines in the material. The cooled down samples with torques between 22 Nm and 30 Nm did not break or get cracks. Now, after nearly 2 years of operation of the first IceScint station, the detectors are still operating and no indication was found yet that there is any thermal or mechanical fatigue in the 3D printing components.

A main component of the analog readout module is the thumbnail-sized Hamamatsu power supply C11204-02. A circuit board was produced to investigate the behavior of the power supply at $-70°$C, independently of ARM. It was constantly biasing for five days at $-70°$C. There is very low variation at the outgoing SiPM bias voltage (Figure 6.14). It was shut down and kept at $-70°$C for 25 hours and restarted again twice. This "cold start" works [57]. As with the 3D printing materials, no change could be found in the detector signals during continuous operation of the power supply at low temperatures.

The full ARM device has been tested at $-70°$C in the temperature chamber for 4.5 days as part of the calibration measurements of the analog and digital temperature sensors, including the glued cookie board inside the cookie and the SiPM. A dark count spectrum at $-70°$C was obtained with an oscilloscope to investigate the behavior of the whole module at low temperatures (Figure 6.23).

6.5 Characteristics of the SiPMs with SPOCK

The SiPM calibration measurements are performed in the Single Photon Calibration Stand at KIT (SPOCK) (Figure 6.16, left) [76]. The calibration stand consists of a light-tight wooden black box in which the measurement setup is placed. For calibration measurements, pulsed LEDs of various wavelengths between 371 nm and 423 nm can be used. During my bachelor thesis [2] I developed the light source of SPOCK. Initially the SPOCK test stand was built for the calibration of the Multi-Anode Photomultiplier (MAPMTs, Chapter 2) and part of the sensor module of the EUSO project. More details about the modification of SPOCK to distinguish the efficiency of each SiPM and its optimal operational parameters used for, among others, IceScint can be found in my master thesis [7].

The pulsed LED is attached to an entrance port of an integrating sphere [3] (Figure 6.15) which works as a splitter and diffuser of the incoming photons of the LED. One exit port of the integrating sphere [77] houses a NIST-calibrated photo diode [4] with which the optical power inside of the integrating sphere can be measured precisely [2]. The UV-light from the LED-array is diffusely reflected inside the integrating sphere. The sphere's inside is made of PTFE [5] which reflects 98% of UV-light in the region of 300-430 nm. The sphere is working as a beam splitter and a diffuser. The number of photons N can be calculated via the measurement of the number of photons inside the sphere. This is done by placing a calibrated photodiode at the collimator exit. As a result the number of emitted photons N is known. By measuring the amount of detected photons N_{SiPM} of the SiPM the ratio $\frac{N_{SiPM}}{N}$ corresponds to the photo detection efficiency of the SiPM at this wavelength, the set bias voltage and the ambient temperature. A more detailed description can be found in [76].

A collimator is attached to the second exit port of the integrating sphere to reduce the

---

[3] Labsphere 3P-GPS-053-SL

[4] OSI Opto-electronics UV-100

[5] Polytetrafluoretylene

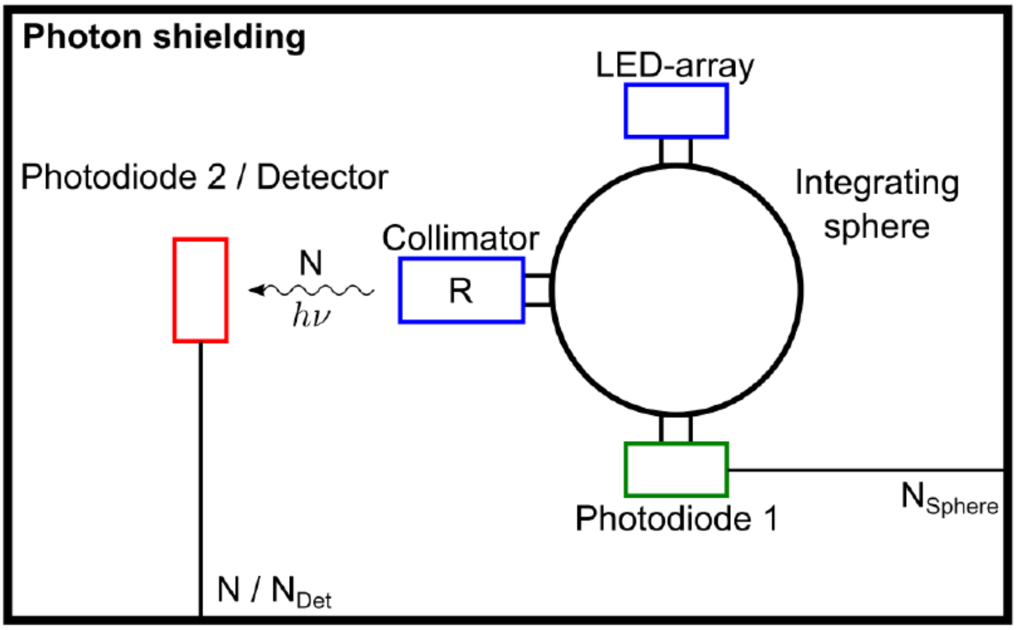

Figure 6.15: Single Photon Calibration Stand at KIT (SPOCK), edited from [76]. This setup has been used to characterize each SiPM which was afterwards glued with an optical cement into the IceScint detectors to read out the optical fibers which are routing the scintillation bars. A optical cable connects the light source (LED-Array) to the integrating sphere and a Collimator is directly connected to one of the outputs of the integrating sphere. On the second exit port is a calibrated photo diode mounted in order to measure and control the photon flux. The SiPM is located directly in front of the collimator opening. The functions and sequence of the individual components are explained in the corresponding text.

outgoing optical power by a factor of about 10^{-6}. With this optical setup, light pulses down to one photon per pulse can be send to the SiPM which has to be calibrated. Because of the low gain of the photodiode and the strong collimator reduction, the whole LED-array is set to continuously emit light. The collimator factor R only depends on the collimator geometry and is measured very precisely with both photodiodes. The number of photons N can be calculated via the measurements of the number of photons inside the sphere. As a result the number of emitted photons N is known. By measuring the amount of detected photons N_{SiPM} of the SiPM the ratio $\frac{N_{SiPM}}{N}$ corresponds to the detection efficiency of the SiPM at this wavelength and temperature [7]

For the calibration of SiPMS, the positive SiPM signals are inverted and guided to a Queued Analog-to-Digital Converter (QADC). The QADC measures the charge of the incoming signal during an adjustable gate time which is synchronized with the pulse time of the LED. By sending light pulses containing several photons per pulse to the SiPM and measuring the charge of the resulting SiPM signals, a finger spectrum can be recorded like it can be seen in Figure 6.18. The pedestal peak as well as the first and the second photo-electron (p.e.) peaks are visible. To illustrate the step between the photon pulse and the integrated voltage in terms of ADC values for the charge deposit, Figure 6.17 can be considered. It shows the test setup inside of SPOCK which consists

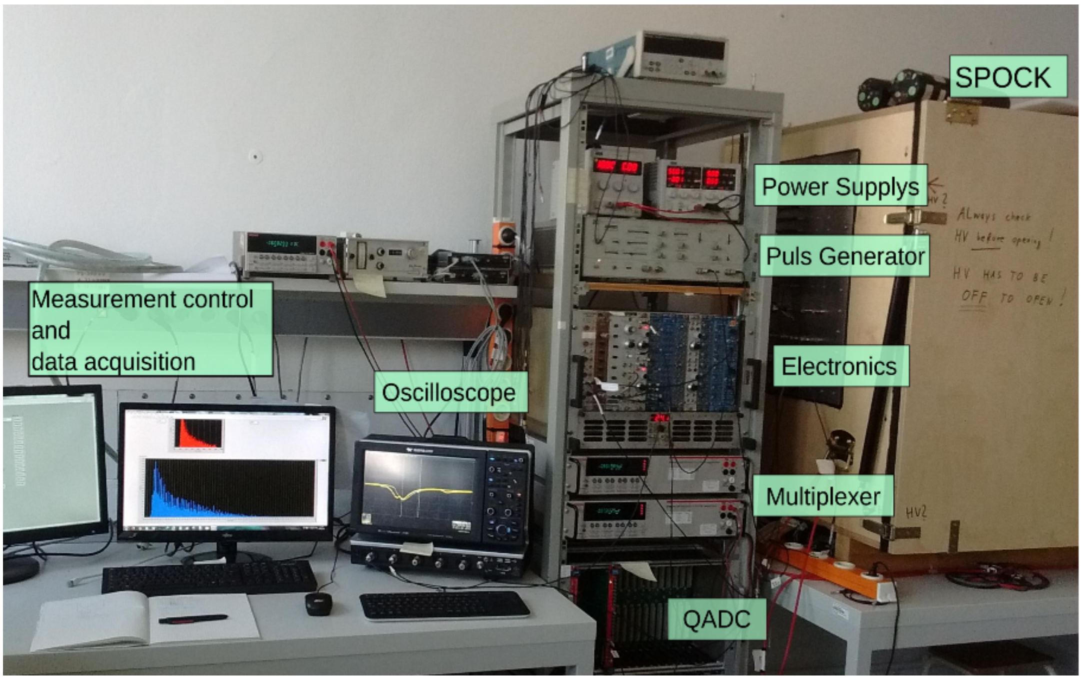

Figure 6.16: Single Photon Calibration Stand at KIT (SPOCK). This setup has been used to characterize each SiPMs, soldered on the cookie boards, which were glued into the IceScint detectors. With the SPOCK setup it is possible to emit close to single photons per pulse with an uniform scattering at different wavelengths, depending on the sensitive wavelength range of the photosensor to be calibrated.

of the integrating sphere with the LED array (Figure 6.15) and the cookie board with the SiPM on it.

The readout is done via an oscilloscope. In yellow the photon gates are visible and in the colored persistence mode the response of the SiPM. It shows the typical sharp increasing flank and the exponential drop down to the baseline in a nice manner. Uniform SiPM responses and less dark counts and crosstalk is visible which enables a correct integration behavior of the QADCs, resulting in single photo electron (SPE) charge spectra (Figure 6.18) and its analysis (Figure 6.19 and following).

The positive SiPM signal is inverted via the linear fan-in/fan-out and the inverted signal is sent to the QADC. The calibrated QADC converts the voltage of the SiPM input signal into a charge stage or QADC channel respectively. This channels are divided into a higher and a lower charge range. Since the charge does not exceed 100 pC for SiPM signals, even with the highest Op-Amp amplification of IceARM, only the lower measuring range up to 100 pC is of interest. The QADC is connected to the DAQ computer via USB cable, where the QADC signals are read out with a Labview program and a charge respectively ADC spectra can be obtained (Figure 6.18).

By measuring finger spectra at different over voltages and dark spectra during which no light pulses have been emitted to the SiPM, information about the breakdown voltage, the gain, the photo detection efficiency (PDE) (Figure 6.19), the dark count rate, and the crosstalk probability (Figure 6.20) can be obtained by an automated calibration procedure with the SPOCK setup [7]. The characterization with SPOCK and IceARM was made for

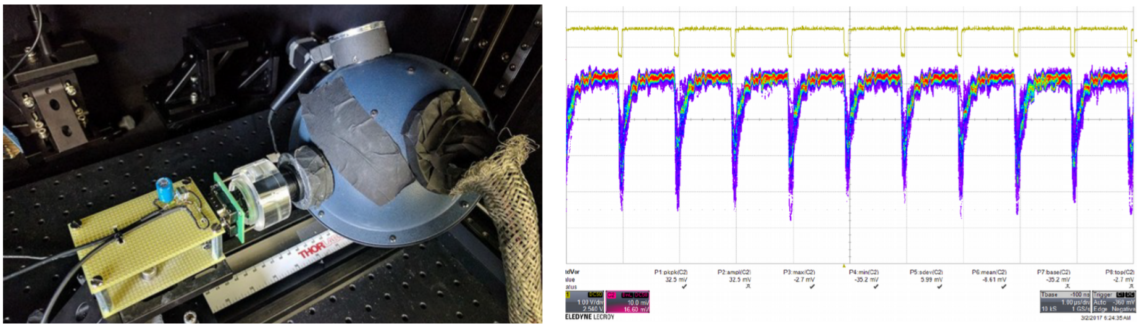

Figure 6.17: Left: Picture of the test setup to measure the cookie board, connected via optical glue to the cookie, included the 32 fiber which are cut off and the surface of the cookie was polished. The integrating sphere emit photons, produced in a LED array to the fiber which are transporting the photons to the SiPM surface. The integrating sphere and the LED array and its pulser is controlled via SPOCK, the analog SiPM signal is read out by an oscilloscope. Right: Screenshot of the oscilloscope, showing the SiPM response by emitting photons to the photosensitive area of the SiPM. The photon gates (~ 10-13 photons per pulse) is shown in yellow, the response of the SiPM is shown in persistence mode (heat map). The voltage scaling is 1 $\frac{V}{div}$ for the LED pulse and 10 $\frac{mV}{div}$ and the time scaling for both 1 $\frac{V}{div}$.

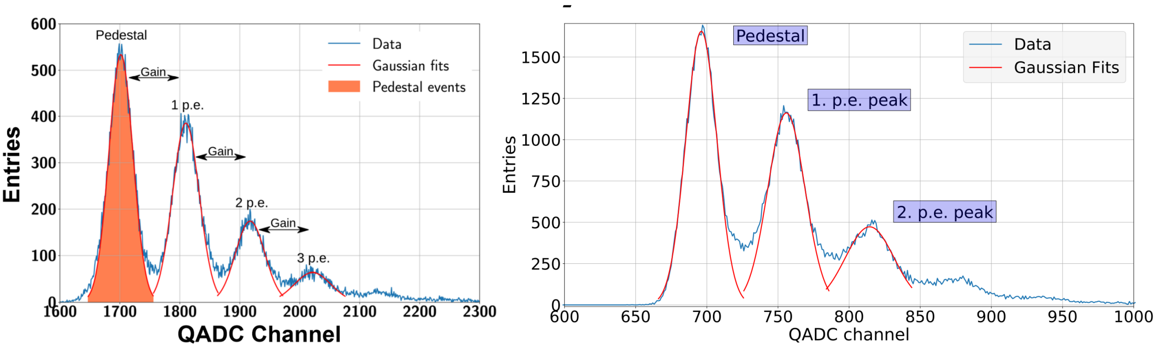

Figure 6.18: Left: SiPM single photoelectron charge spectrum measured by using the Hamamatsu SiPM evaluation board electronics [78] and SPOCK. This kind of (low charge range) spectra are called “finger spectra” since single photo electron “fingers” are visible. Right: Example of the SiPM finger spectrum resolution obtained within the within this thesis developed IceARM readout electronic for the IceScint scintillation detectors and with SPOCK. The dark count rate, the gain, the PDE, the after pulse rate and the crosstalk probability can be obtained from the finger spectrum.

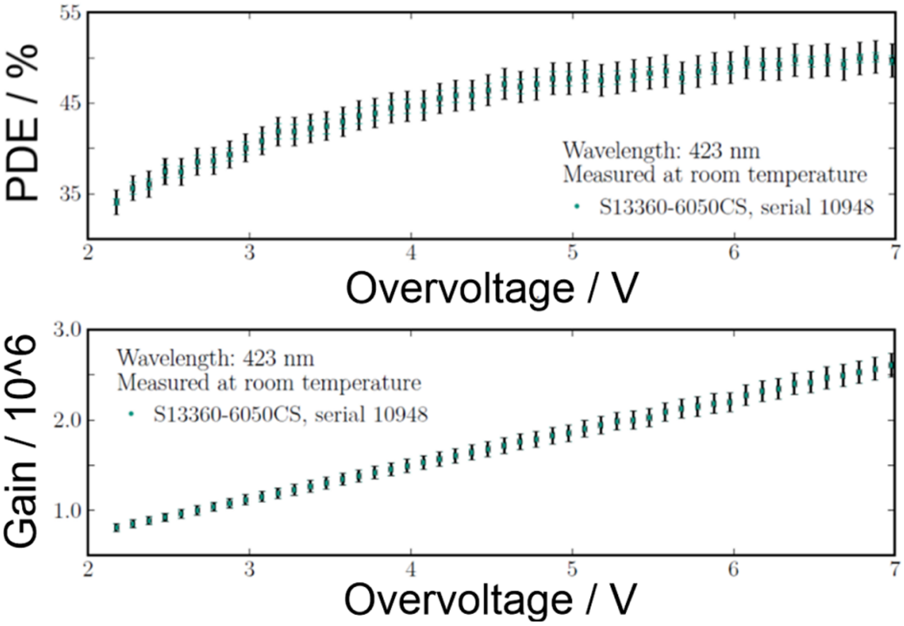

Figure 6.19: Calibration results for the installed SiPMs into an IceScint detector. It shows the PDE and the Gain of one specific SiPM versus the applied overvoltage [79]. The behavior is as expected as known from the working principle of SiPMs. With a higher overvoltage the gain of the SiPM increases, but the Dark Count rate, too. The calibration results were obtained out of the recorded finger spectra with SPOCK at a specific wavelength and at room temperature.

all the used SiPM [79]. A systematic derivation of how to obtain the these key metrics of the used SiPMs can be found in this thesis.

The increase of the dark count rate and the crosstalk probability is negligible for scintillators, because the MIP hits and its light yield with IceScint (Figure 6.36), are with $\sim\frac{40PE}{MIP}$ significantly higher than these noise effects. For the construction of a imaging camera out of SiPMs for air shower fluorescence light detection the crosstalk probability and the dark count rate contribute a great part to the signal-to-noise ratio [20], see also Chapter 2.

Since the amplification factor (gain) of SiPM is of great interest for the uniformity of as example the IceScint detector array and how to distinguish operation parameters for SiPMs, a short derivation of how the gain of SiPMs can be determined under laboratory conditions follows. The quality of the uniformity regarding the gain of the IceScint array prototype station in real measurement conditions at the South Pole is under investigation in Chapter 8. In addition, the gain is of interest for the Cold-SPOCK upgrade which was developed within this thesis to obtain finger spectra for low temperature SiPM characterizations described in the Subchapter 6.6.

The p-n junction of a SiPM can be seen as a capacitor with capacitance C:

$$G = \frac{Q}{e} = C \cdot \frac{V_{ov}}{e} \qquad (6.5.1)$$

Where Q is the charge deposit into the DAQ, e the elementary charge and V_{ov} the overvoltage with $V_{ov} = V_{bias} - V_{break}$. Where V_{bias} is the applied voltage on the SiPM and V_{break}

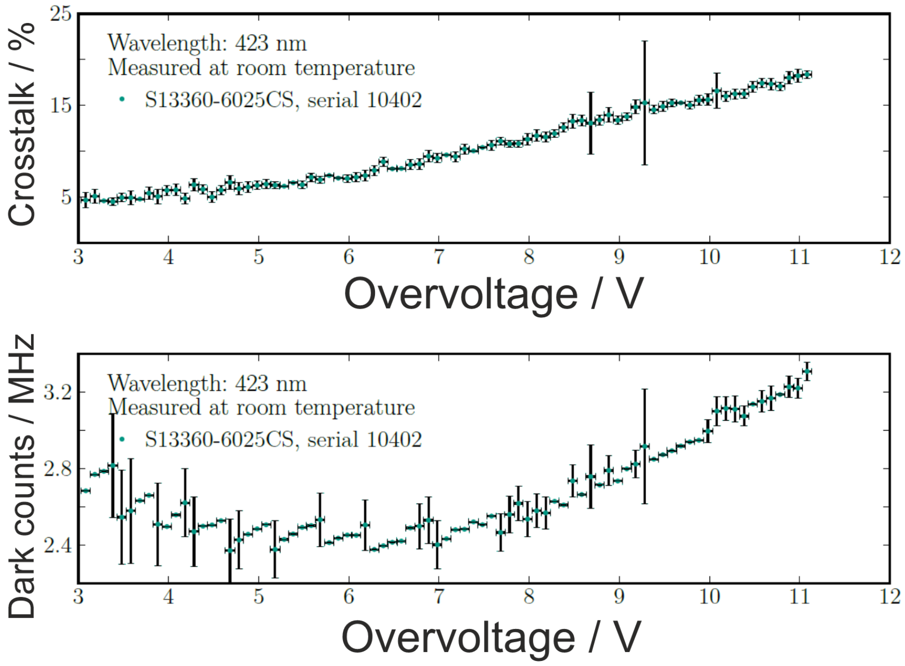

Figure 6.20: Calibration results for the installed SiPMs into an IceScint detector. It shows the Crosstalk probability and the dark count rate of one specific SiPM versus the applied overvoltage [79]. The behavior is as expected as known from the working principle of SiPMs. With a higher overvoltage the crosstalk probability and the dark count rate of the SiPM increases. The calibrations results were obtained out of the recorded finger spectra with SPOCK at a specific wavelength and at room temperature. The increase of the dark count rate and the crosstalk probability is negligible for scintillators, because the MIP hits and its light yield with IceScint are significantly higher than these noise effects.

the break down voltage of the SiPM.

It follows that the gain G is proportional to the overvoltage V_{ov}. To determine G at a given V_{ov}, a finger spectrum is recorded, as shown in Figure 6.18. The positions of the individual peaks are determined by fitting Gaussian curves with the following shape:

$$f\left(x\right) = \frac{A_{peak}}{\sqrt{2\pi\sigma^2}} \cdot \exp\left(-2 \cdot \left(\frac{x - x_{peak}}{2\sigma}\right)^2\right) \tag{6.5.2}$$

Where x is the QADC channel, $f\left(x\right)$ the QADC channel entries, x_{peak} the peak position in the charge spectrum, A_{peak} the events in the Gaussian fit and σ the standard deviation.

The distances of the individual peaks in the spectrum to their neighboring peaks correspond to the gain in units of the QADC channels. The conversion to the actual gain $G$is done with

$$G = \frac{G_{channel} \cdot k}{A \cdot e}. \tag{6.5.3}$$

With the amplification in units of the QADC channels $G_{channel}$, the transformation factor from channel to charge k and the amplification factor of the signal A. The statistical and systematic uncertainties on the value of the gain result from the uncertainties on the conversion of QADC channels to the actual gain and the uncertainties on the determination of the peak positions. This leads to the statistical uncertainty on the gain factor σ_G^2 :

$$\sigma_G^2 = \left(\frac{k}{A \cdot e} \cdot \sigma_{G_{channel}} \right)^2 + \left(\frac{G_{channel}}{A \cdot e} \cdot \sigma_k \right)^2 , \tag{6.5.4}$$

and the systematic uncertainty on the gain Δ_G

$$\Delta_G^2 = \left(\frac{k}{A \cdot e} \cdot \sigma_{G_{channel}} \right)^2 + \left(\frac{G_{channel}}{A \cdot e} \cdot \sigma_k \right)^2 + \left(\frac{G_{channel} \cdot k}{A^2 \cdot e} \cdot \sigma_A \right)^2 , \tag{6.5.5}$$

with the uncertainty of the transformation factor σ_k and the amplification σ_A. These uncertainties are, as example, used in Figure 6.19.

Figure 6.22 shows a table with the performed measurements of each SiPM which is in use for the scintillator read out of the IceScint detectors. For the normalization of the charge histograms during the measurement runs at the South Pole the PDE is important. The gain and the bias voltage is used for the gain stabilizing temperature control loop of the SiPMs to ensure an uniform detector array (Chapter 6.7).

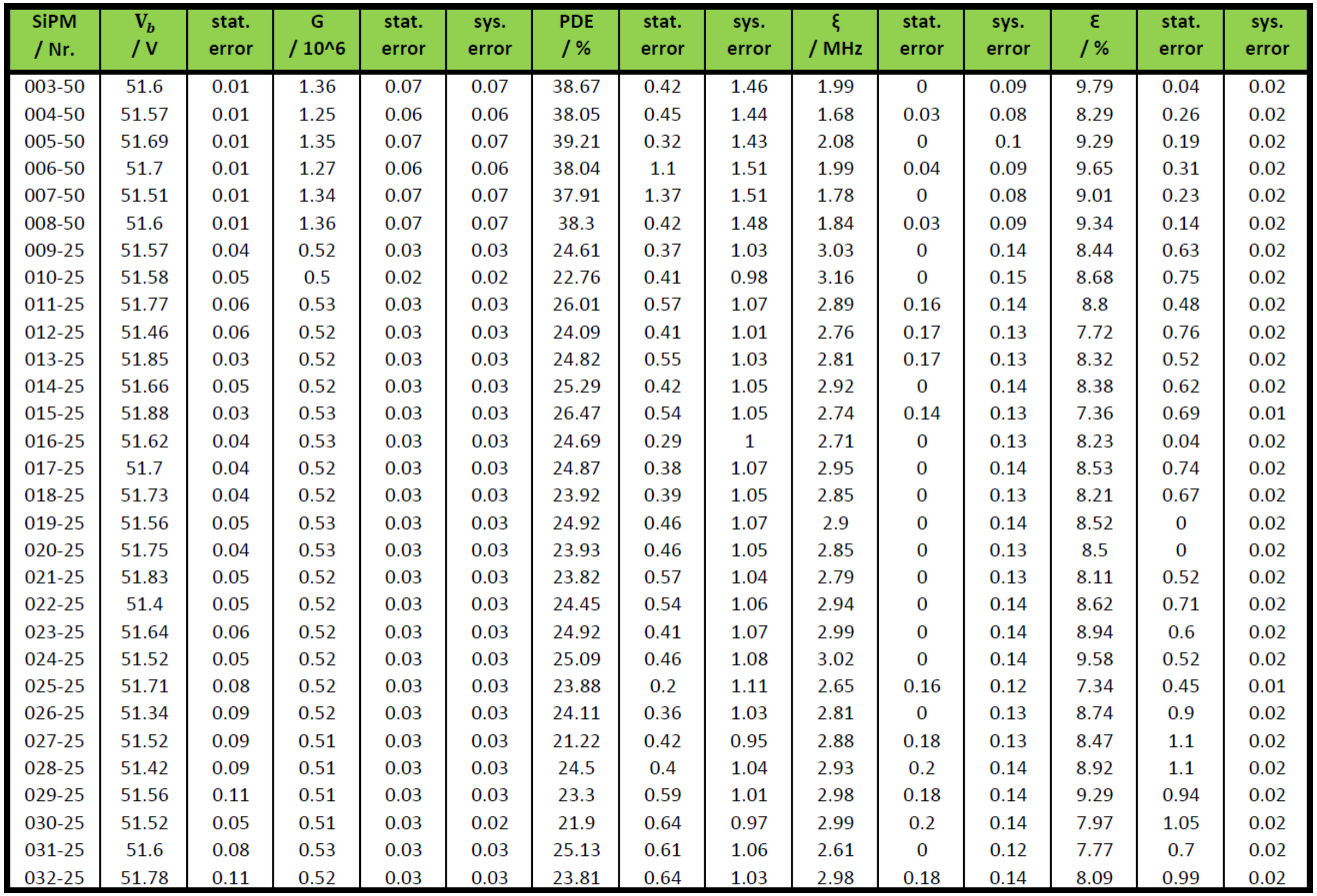

SiPM / Nr.	V_b / V	stat. error	G / 10^6	stat. error	sys. error	PDE / %	stat. error	sys. error	ξ / MHz	stat. error	sys. error	ε / %	stat. error	sys. error
003-50	51.6	0.01	1.36	0.07	0.07	38.67	0.42	1.46	1.99	0	0.09	9.79	0.04	0.02
004-50	51.57	0.01	1.25	0.06	0.06	38.05	0.45	1.44	1.68	0.03	0.08	8.29	0.26	0.02
005-50	51.69	0.01	1.35	0.07	0.07	39.21	0.32	1.43	2.08	0	0.1	9.29	0.19	0.02
006-50	51.7	0.01	1.27	0.06	0.06	38.04	1.1	1.51	1.99	0.04	0.09	9.65	0.31	0.02
007-50	51.51	0.01	1.34	0.07	0.07	37.91	1.37	1.51	1.78	0	0.08	9.01	0.23	0.02
008-50	51.6	0.01	1.36	0.07	0.07	38.3	0.42	1.48	1.84	0.03	0.09	9.34	0.14	0.02
009-25	51.57	0.04	0.52	0.03	0.03	24.61	0.37	1.03	3.03	0	0.14	8.44	0.63	0.02
010-25	51.58	0.05	0.5	0.02	0.02	22.76	0.41	0.98	3.16	0	0.15	8.68	0.75	0.02
011-25	51.77	0.06	0.53	0.03	0.03	26.01	0.57	1.07	2.89	0.16	0.14	8.8	0.48	0.02
012-25	51.46	0.06	0.52	0.03	0.03	24.09	0.41	1.01	2.76	0.17	0.13	7.72	0.76	0.02
013-25	51.85	0.03	0.52	0.03	0.03	24.82	0.55	1.03	2.81	0.17	0.13	8.32	0.52	0.02
014-25	51.66	0.05	0.52	0.03	0.03	25.29	0.42	1.05	2.92	0	0.14	8.38	0.62	0.02
015-25	51.88	0.03	0.53	0.03	0.03	26.47	0.54	1.05	2.74	0.14	0.13	7.36	0.69	0.01
016-25	51.62	0.04	0.53	0.03	0.03	24.69	0.29	1	2.71	0	0.13	8.23	0.04	0.02
017-25	51.7	0.04	0.52	0.03	0.03	24.87	0.38	1.07	2.95	0	0.14	8.53	0.74	0.02
018-25	51.73	0.04	0.52	0.03	0.03	23.92	0.39	1.05	2.85	0	0.13	8.21	0.67	0.02
019-25	51.56	0.05	0.53	0.03	0.03	24.92	0.46	1.07	2.9	0	0.14	8.52	0	0.02
020-25	51.75	0.04	0.53	0.03	0.03	23.93	0.46	1.05	2.85	0	0.13	8.5	0	0.02
021-25	51.83	0.05	0.52	0.03	0.03	23.82	0.57	1.04	2.79	0	0.13	8.11	0.52	0.02
022-25	51.4	0.05	0.52	0.03	0.03	24.45	0.54	1.06	2.94	0	0.14	8.62	0.71	0.02
023-25	51.64	0.06	0.52	0.03	0.03	24.92	0.41	1.07	2.99	0	0.14	8.94	0.6	0.02
024-25	51.52	0.05	0.52	0.03	0.03	25.09	0.46	1.08	3.02	0	0.14	9.58	0.52	0.02
025-25	51.71	0.08	0.52	0.03	0.03	23.88	0.2	1.11	2.65	0.16	0.12	7.34	0.45	0.01
026-25	51.34	0.09	0.52	0.03	0.03	24.11	0.36	1.03	2.81	0	0.13	8.74	0.9	0.02
027-25	51.52	0.09	0.51	0.03	0.03	21.22	0.42	0.95	2.88	0.18	0.13	8.47	1.1	0.02
028-25	51.42	0.09	0.51	0.03	0.03	24.5	0.4	1.04	2.93	0.2	0.14	8.92	1.1	0.02
029-25	51.56	0.11	0.51	0.03	0.03	23.3	0.59	1.01	2.98	0.18	0.14	9.29	0.94	0.02
030-25	51.52	0.05	0.51	0.03	0.02	21.9	0.64	0.97	2.99	0.2	0.14	7.97	1.05	0.02
031-25	51.6	0.08	0.53	0.03	0.03	25.13	0.61	1.06	2.61	0	0.12	7.77	0.7	0.02
032-25	51.78	0.11	0.52	0.03	0.03	23.81	0.64	1.03	2.98	0.18	0.14	8.09	0.99	0.02

Figure 6.21: SiPM characterization for the IceScint detectors Research and development phase and its final production. All SiPMs have been tested for functionality at low temperatures and the breakdown Voltage, the Gain, the PDE, the dark count rate, the cross-talk proability have been measured at room temperature with a 423nm light source.

Another example of a preparation test is the uniformity of the SiPM area. Figure 6.22 shows the setup for characterisation and functional tests of the Cookie board and the SiPM. Like with the IceARM electronics, each Cookie board was tested and each SiPM, soldered on it, tested and calibrated (Figure **??**). The uniformity regarding the gain and light yield of the IceScint detectors is influenced by a bunch of different components (Chapter 5). At the end of the optical part, i.e. the intersection between the fiber bundle and the SiPM, the uniformity of the photosensitive area of the SiPM regarding the photo detection efficiency (PDE) is important, since the light yield of the fiber, and therefore the MIP induced photon bunch from different parts of the scintillator bars of the detector, is distributed to a region of the photosensitive area (Figure 6.1). A SiPM which is used for IceScint was scanned via a collimator and the PDE was determined in different regions on the 6x6 mm^2 area with its ~56000 APDs. No significant differences were found between the regions (Figure 6.22, right) that would major affect the performance of the detector. At this point it is referred to [79] for further analysis and information.

6.6 SiPM calibration in a cold environment

To obtain the gain and the dark count spectrum of the SiPM as well as its changes during temperature cycles, first measurements were done by applying the bias voltage and connect the readout board to the SiPM, which was placed into the cooling chamber (Figure 6.23). Dark count spectra were recorded at days long measurement cycles to, as initial test, check if the chosen SiPM [52] is operating at low temperatures below $-70°$C since the data sheet only ensures a operation assurance at ambient temperatures of above 0°C. At a first glance, by analyzing the waveforms and the charge spectra of dark counts at low temperatures, no major changes in the operation of the SiPM was found. To ensure a stable photo detection efficiency and other key characteristics of SiPMs like the crosstalk probability, well defined light pulses have to be emitted to the photosensitive area of the SiPM and its flux counter-measured like with the SPOCK setup, as described above.

To enable these cold temperature measurements, an upgrade of the SPOCK setup was developed in the frame of this thesis. It includes several components in order to obtain key parameters for the operation of SiPM at low temperatures like down to -70°C. In this subchapter a short summary of Cold-SPOCK follows. In more detail, Cold-SPOCK is described in the bachelor thesis of Branko Mitic [80].

In order to ensure, for example, that the gain factor is correctly determined at low temperatures, only the collimator and the SiPM and its front-end electronic are allowed in the cold chamber (Figure 6.25). The reason for this is to avoid systematic and statistical uncertainties caused by temperature changes of as many components as possible, such as the narrowband LEDs. For this reason the integrating sphere and the photodiode are located outside the cold chamber and are in a dark box. The photon pulses are brought into the cold chamber via a light guide and onto the photosensitive surface of the SiPM.

Figure 6.26 shows one result of the Cold-SPOCK measurements. The gain of an identical SiPM was measured at different temperatures at two different measurement cycles. The pre-measurements, like the temperature dependency of the collimator or the change in the sensitivity of the photodiode can be found in this [80]. In addition, the changes in the dark count rate of the SiPMs at different temperatures are also detailed in [80]. For

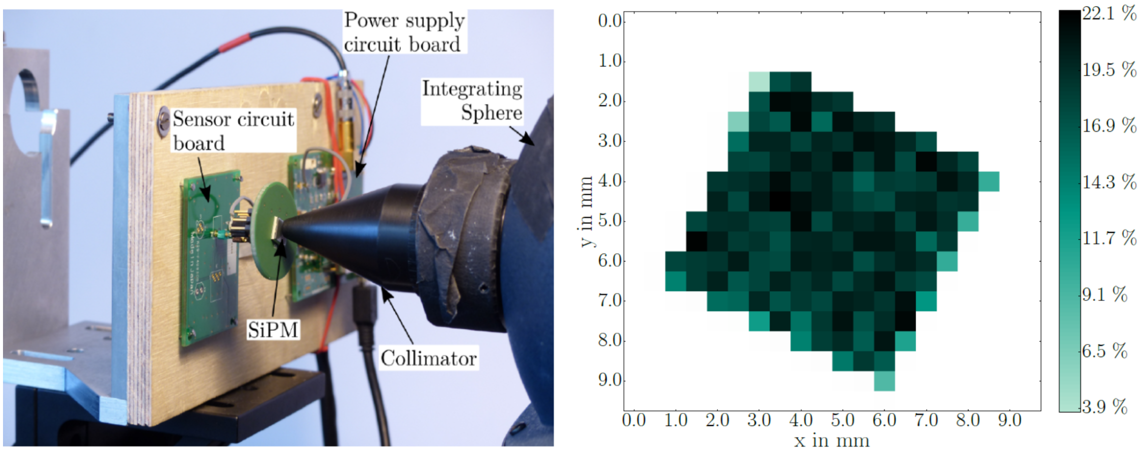

Figure 6.22: Right: Close-up of the measurement setup for characterizing cookie board and the SiPMs mounted on it. The reference light source consists of the integrating sphere, the collimator and a LED-array which is not shown in the photo but explained in Chapter 5. The light pulses from the LED become isotropically distributed by the integrating sphere; The collimator attenuates the intensity of the light exiting the integrating sphere down to a level of one photon per pulse hitting the SiPM surface. The photo was taken with a white cardboard inside of SPOCK in respect for a better contrast [79]. Right: Scanning the of different regions of the SiPM photosensitive area (6x6 mm^2) with its ~56000 APDs. In respect of the statistical uncertainty of the PDE measurement routine and the collimator positioning, no significant differences were found in the uniformity of the PDE of the SiPM regarding the illuminated APD region.

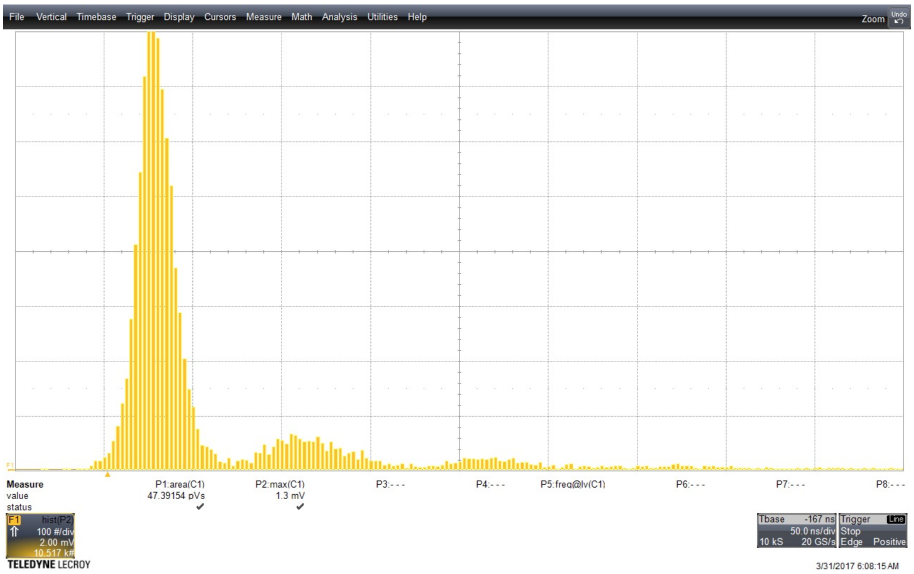

```
Measure   P1:area(C1)     P2:max(C1)   P3:---   P4:---   P5:freq@lv(C1)   P6:---   P7:---   P8:---
value     47.39154 pVs    1.3 mV
status    ✓               ✓
F1 hist(P2)
100 #/div
2.00 mV
10.517 k#
Tbase   -167 ns   Trigger   Line
50.0 ns/div       Stop
10 kS   20 GS/s   Edge   Positive
3/31/2017 6:08:15 AM
```

Figure 6.23: Dark count spectrum obtained with ARM and the full optical coupling at −70°C. The full device is working at low temperatures. The measurement was done with the IceARM readout, the optical coupling, the temperature chamber and an oscilloscope. The whole system (SiPM and IceARM) is operating at −70°C. Small p.e. fingers are visible since the temperature chamber was, at this point, not as light tight as SPOCK.

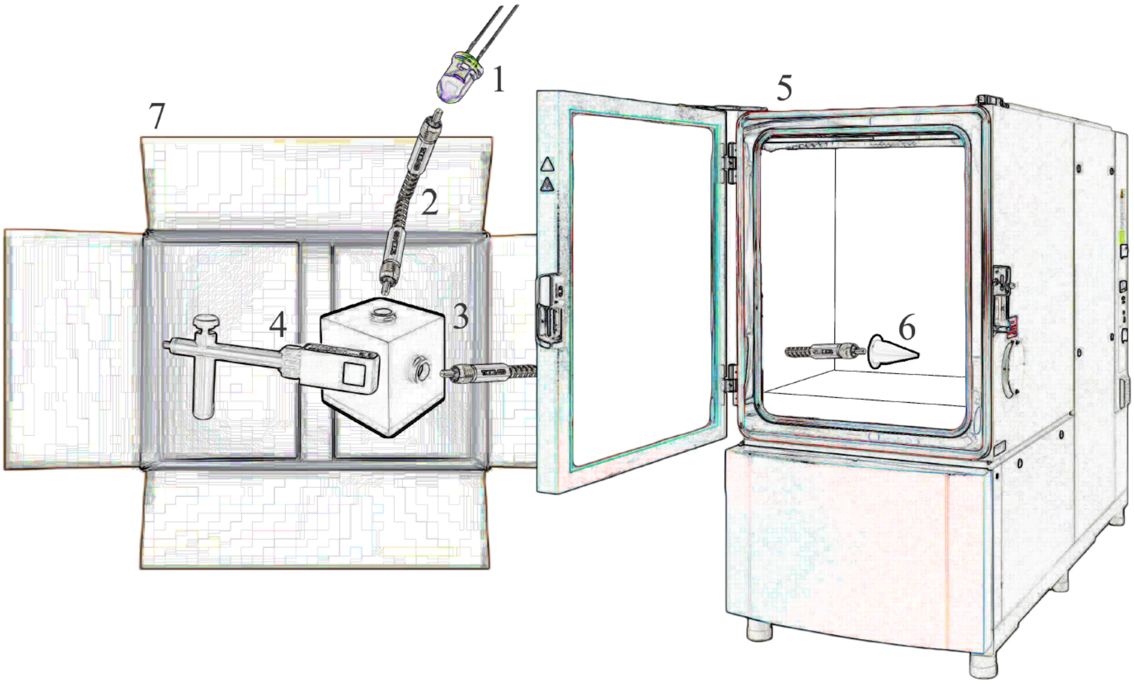

Figure 6.24: Sketch of Cold-SPOCK, edited from [80]. The developed components are numbered.
1. LED (different wavelengths with narrow-band emission distribution)
2. Optical fiber (Thorlabs M93L01 [81])
3. Integrating Sphere (Labsphere 4P-GPS-010-SL [82])
4. Photodiode with new fixture (Ophir Photonics PD-300 and PD300UV [83])
5. Temperature Chamber (Vötsch VT 7021 [84])
6. New developed collimator
7 Additional photon shielding

the gain measurements, since it was not sure not sure if, as example, the wafer or the outer surface layer of the SiPM survives both, a cooling cycle and a heating cycle, in both temperature directions were changed.

The linear fit function parameters for the whole measurement cycle of this example IceSinct SiPM characterization, so cooling down and heating up combined, are shown in Table 6.2.

The value for R^2 is close to 1, the normalized RMSE is sufficiently small at 1.2 % and the Chi-square test of goodness-of-fit shows that the variables are interdependent. Therefore the gain is highly temperature dependent and needs to be stabilized for a uniform IceScint detector array, which is described in the next subchapter.

Figure 6.27 shows the origin of one single measurement point of Figure 6.26. The gain was obtained by fitting the finger spectra peaks, which was recorded at a specific temperature, like described above when we discussed SPOCK. In addition, it shows the huge difference of operating SiPMs at room temperatures or at temperatures like found at the South Pole.

As example, the dark counts nearly vanish at low temperatures. This can be seen by the entries between the pedestal and 1 PE fingers which is showcasing the capabilities and advantages of the usage of SiPM at low temperatures. Since the light yield of the

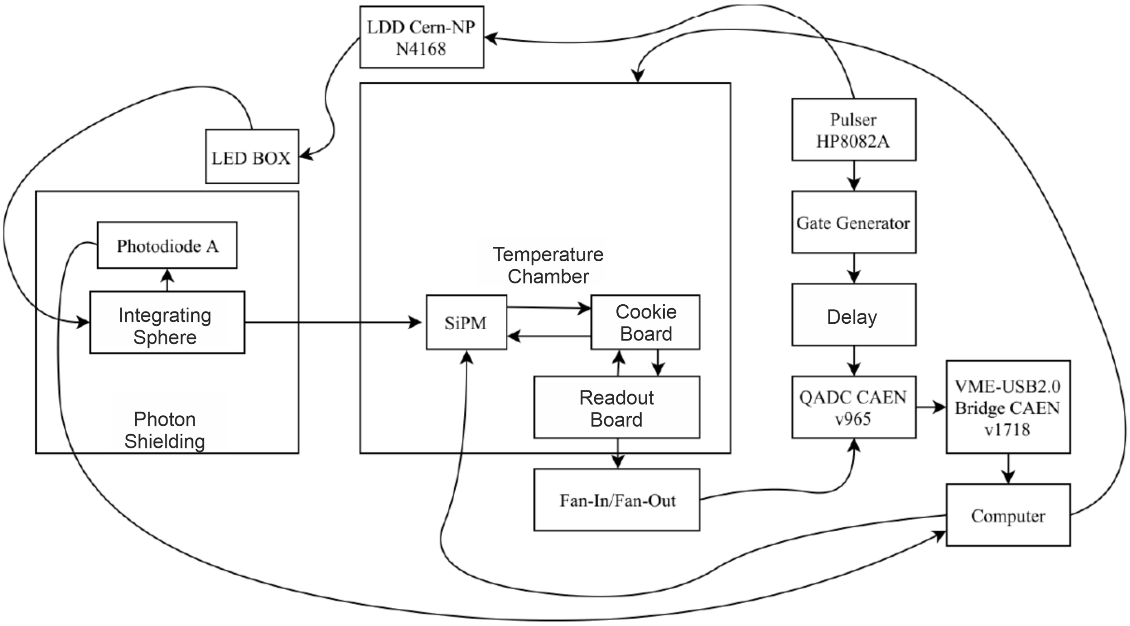

Figure 6.25: Block diagram of the Cold-SPOCK upgrade (edited from [80]). All components which are not drawn inside the temperature chamber (center) or the new photon shielding (left) are part of SPOCK. The addon consists of the new mechanical and electrical interface for the SiPM inside of the temperature chamber, a new photon shielding, a new integrating sphere and its ports.

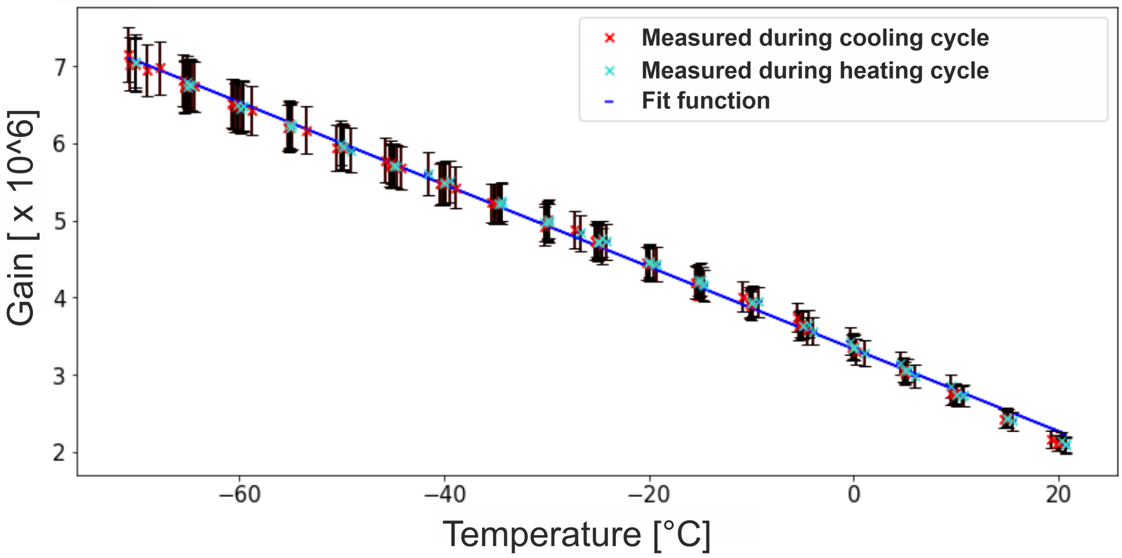

Figure 6.26: The gain of a IceScint SiPM versus the temperature during the cooling and heating process from 20°C to -70°C and back to 20°C, edited from [80]. The linear behaviour, when plotted logarithmically, is also clearly visible for the combined data sets. As shown, the gain is highly temperature dependent and needs to be stabilized for a uniform IceScint detector array.

Table 6.2: Fit function parameters for Figure 6.26.

Gradient	$-5.34{\cdot}10^4 \pm 1.87{\cdot}10^2$
Y-axis intercept	$3.33{\cdot}10^6 \pm 6.84{\cdot}10^3$
Standard derivation	$1.86 \cdot 10^2$
R^2	0.998
RMSE	$6.28 \cdot 10^4$
RMSE (normalized)	1.21^{-2}
χ^2	$\text{static} = 1.86 \cdot 10^5, \text{pvalue} = 0.0$

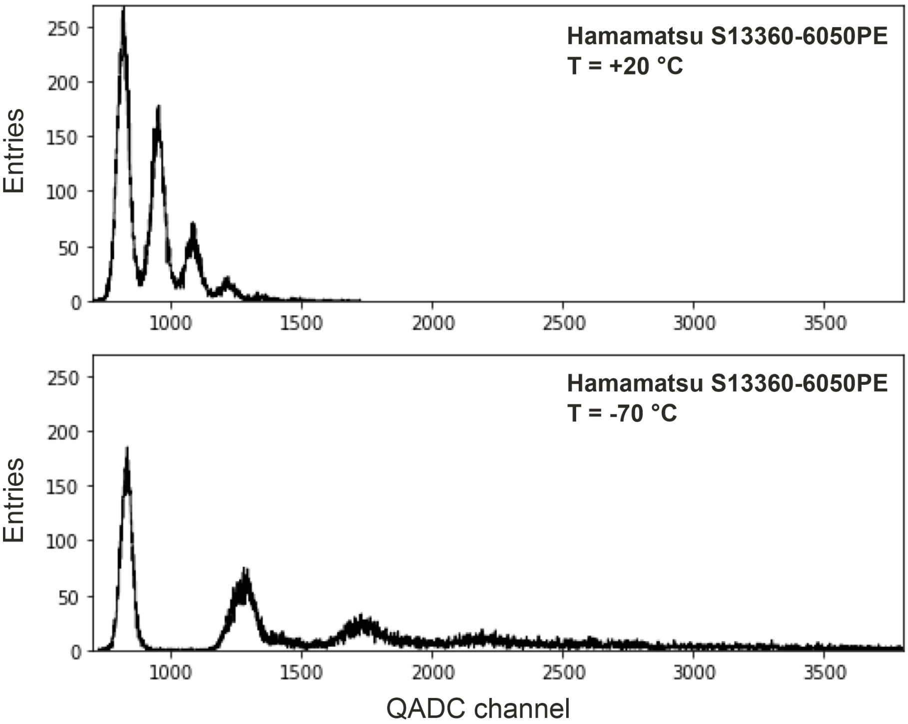

Figure 6.27: Top: Finger spectra of one IceScint SiPM at $20°C$, recorded with the Cold-SPOCK setup. Bottom: Same measurement with the same SiPM operation voltage, same setup but recorded at $-70°C$ (edited from [80]). It shows the increase of gain of the SiPM by decreasing temperature. For a uniform IceScint detector array, the gain have to be stabilized for each detector. In addition the dark count rate nearly vanish at temperatures like found at the South Pole.

IceScint detectors is high, the dark count rate is not as important as like with imaging telescopes.

The next subchapter explains the stabilization of the gain by using a temperature control loop which was developed within this thesis.

6.7 Temperature control loop for the SiPMs

Since SiPMs are semiconductor-based, their characteristics are highly temperature dependent. The temperature dependence of the breakdown voltage can be explained by the ionization rate $\beta\left(E,T\right)$ [7]. Due to Brownian motion at higher temperatures, charge carriers lose more energy through crystal lattice scattering. Therefore, the electric field strength must be increased to provide sufficient energy for ionization. The ionization rate (E, T) depends on three parameters, the ionization energy threshold ε_i, the energy of the optical phonons ε_τ and the mean free path length of a charge carrier $\lambda\left(T\right)$ within the crystal lattice.

The ionization rate can be expressed by two different models in relation to the strength of the electric field. For weak electric fields, the charge carriers would have to move within the crystal lattice without scattering to reach the ionization energy threshold ε_i. The ionization rate $\beta\left(E,T\right)$ can be described, with the electric field strength E, the temperature T and the elementary charge q as

$$\beta\left(E,T\right) = \frac{q\cdot E}{\varepsilon_\tau}\cdot\exp\left(\frac{-\varepsilon_i}{q\cdot\lambda\left(T\right)\cdot E}\right).$$

At strong electric field strength, i.e. the SiPMs operate in Geiger mode [7], the energy loss of the charge carriers due to scattering is smaller than the energy gained during acceleration by the electric field. The ionization rate can be approximated to

$$\beta\left(E,T\right)\approx\exp\left(\frac{-3\cdot\varepsilon_i\cdot\varepsilon_\tau}{\left(q\cdot\lambda\left(T\right)\cdot E\right)^2}\right).$$

A more detailed derivation can be found in my master thesis. Figure 6.28 shows the behaviour of the gain and breakdown voltage depending on temperature and illustrates the need to regulate the operating parameters of SiPMs in real time during scintillator measurements. If no control-loop would keep the, for example, gain stable, it would be unequal at different times and at different detectors at the South Pole and it would not be possible to deduce from the charge deposition the number of ionized particles interacting with the scintillator material. In addition, it is visible that the producer of the used SiPM for IceScint, Hamamatsu photonics, just checked the operating temperature and the performance of SiPMs only to $-20^\circ C$. To ensure the operation of the SiPMs at South Pole temperature conditions, the SPOCK upgrade was necessary and applied.

The invented control loop was realized based on controlling the bias voltage of the SiPMs during operation, with simultaneous temperature measurement directly at the SiPM inside the detectors. To achieve this, detailed pre-measurements in the lab were necessary, such as the gradient ΔU_{SiPM} of the temperature dependence of the breakdown

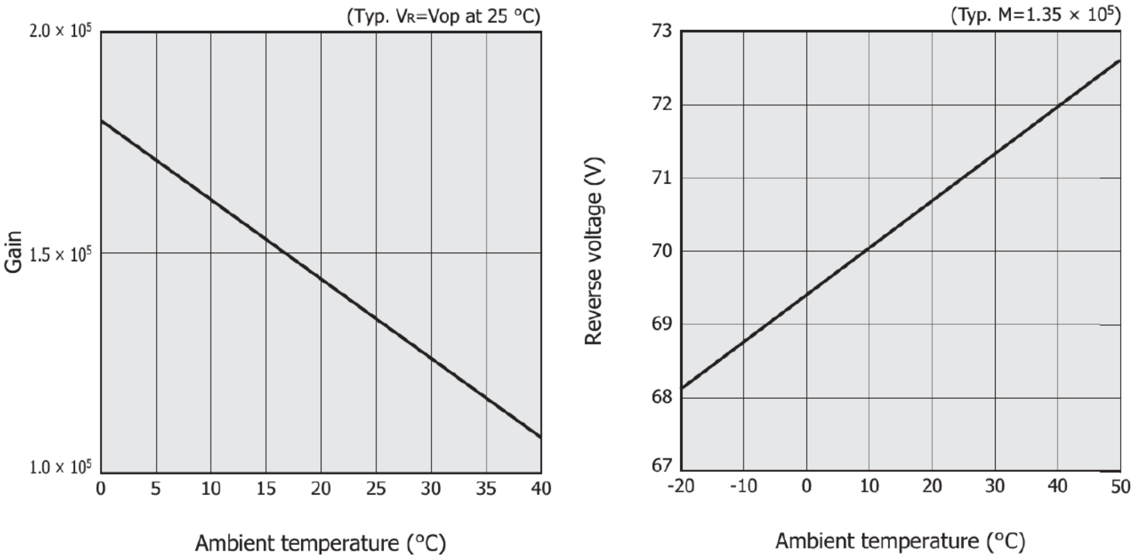

Figure 6.28: Left: Gain vs. ambient temperature of a typical SiPM used for IceScint at fixed reserve voltage. The idea of the temperature control loop is to keep the gain stable, therefore keeping the gradient $\frac{\text{Gain}}{°\text{C}}$ close to zero. Right: Reserve or breakdown voltage vs ambient temperature with fixed gain [85]. At this point the temperature control loop has its working principle. By adjusting the bias voltage the gain of the SiPM can be stabilized at changing ambient temperature.

voltage of the SiPM, the optimal operating voltage of the SiPM at room temperature $U_{SiPM\,(25°\text{C})}$, determined with SPOCK and the conversion of the values of the analog temperature sensor. These two parameters were measured for each produced IceARM and each installed SiPM into the detectors.

The conversion between the decimal values, i.e. the values given by IceTAXI, and the temperature next to the SiPMs can be calculated to [6]

$$\begin{aligned} T_{dec,fit} &= 0,08 \cdot T^2 - 209 \cdot T + 43562 && (6.7.6) \\ T_{dec} &\approx -209 \cdot \frac{dec}{°\text{C}} \cdot T + 43562 \cdot dec && (6.7.7) \\ \Rightarrow\ T &\approx \frac{43562 - T_{dec}}{209}. && (6.7.8) \end{aligned}$$

By distinguishing ΔU_{SiPM} and $U_{SiPM\,(25°\text{C})}$ in the lab, the only necessary input of the control loop during the air-shower measurements at the South Pole are

$$\begin{aligned} U_{SiPM} &= \text{Function of temperature } T \\ T &= \text{Function of decimal value.} \end{aligned}$$

---

[6] The quadratic term is dropped in respect of the larger systematic measurement uncertainties.

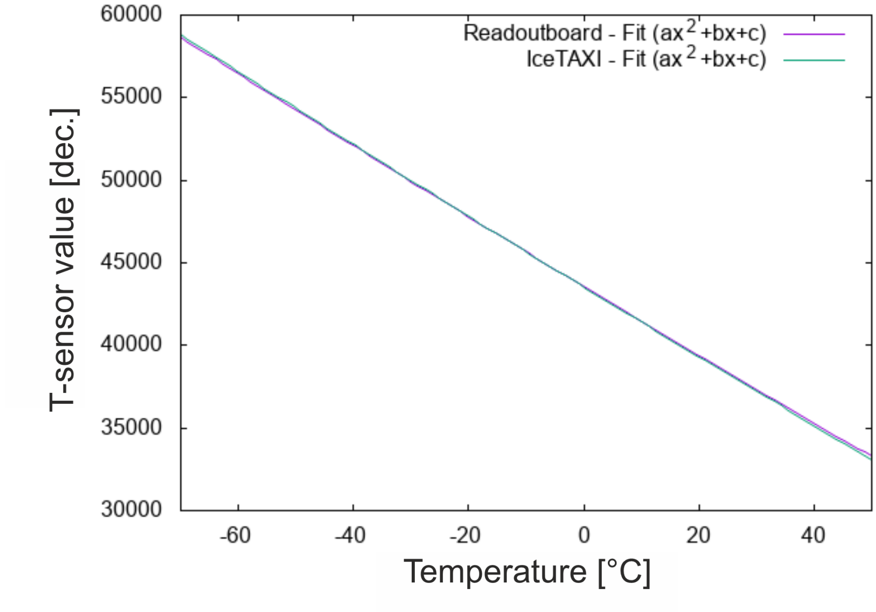

Figure 6.29: Shown is one calibration example of the temperature sensor behaviour of one of the 26 IceARM electronics for the IceScint detectors, measured in the IKP cooling chamber. To investigate possible influence of the IceTAXI DAQ and in order to cross-check the readout software on IceTAXI, the temperature was read out analogue and fitted with the readout board (lila) and with the full DAQ system (green) each. The influence of the data processing and conversation by IceTAXI is negligible in respect of the systematic uncertainty of the temperature sensor of $\Delta T = \pm 0.25°C$.

This leads to a general temperature-gain-control loop formula of:

$$U_{SiPM} = U_{SiPM\,(25°\mathrm{C})} V - \Delta U_{SiPM} \frac{mV}{°\mathrm{C}} \cdot \Delta T \tag{6.7.9}$$

$$U_{SiPM_{(T)}} = U_{SiPM\,(25°\mathrm{C})} V - \Delta U_{SiPM} \frac{mV}{°\mathrm{C}} \cdot (25°\mathrm{C} - T). \tag{6.7.10}$$

By using these two, in the lab, pre-measured values, the control loop formulas for the first IceScint station at the South Pole is given to:

$$U_{Panel\,002_{(T)}} = 56.89V - 0.022\,\frac{V}{°\text{C}} \cdot (25°\text{C} - \frac{43562 - T_{dec}}{209}) = IceTAXI_{Channel}\,3 \tag{6.7.11}$$

$$U_{Panel\,004_{(T)}} = 56.61V - 0.021\,\frac{V}{°\text{C}} \cdot (25°\text{C} - \frac{43562 - T_{dec}}{209}) = IceTAXI_{Channel}\,4 \tag{6.7.12}$$

$$U_{Panel\,005_{(T)}} = 56.45V - 0.019\,\frac{V}{°\text{C}} \cdot (25°\text{C} - \frac{43562 - T_{dec}}{209}) = IceTAXI_{Channel}\,2 \tag{6.7.13}$$

$$U_{Panel\,006_{(T)}} = 56.56V - 0.022\,\frac{V}{°\text{C}} \cdot (25°\text{C} - \frac{43562 - T_{dec}}{209}) = IceTAXI_{Channel}\,6 \tag{6.7.14}$$

$$U_{Panel\,007_{(T)}} = 56.76V - 0.024\,\frac{V}{°\text{C}} \cdot (25°\text{C} - \frac{43562 - T_{dec}}{209}) = IceTAXI_{Channel}\,5 \tag{6.7.15}$$

$$U_{Panel\,008_{(T)}} = 56.64V - 0.022\,\frac{V}{°\text{C}} \cdot (25°\text{C} - \frac{43562 - T_{dec}}{209}) = IceTAXI_{Channel}\,0 \tag{6.7.16}$$

$$U_{Panel\,009_{(T)}} = 56.84V - 0.020\,\frac{V}{°\text{C}} \cdot (25°\text{C} - \frac{43562 - T_{dec}}{209}) = IceTAXI_{Channel}\,1. \tag{6.7.17}$$

After all, the control-loop stabilize the gain of each at the South Pole deployed IceScint detector and enables a uniform IceScint detector station in which the integrated charge deposition per detector is only dependent on the incident particles and is not affected by the thermal fluctuations of the p.e. gain of the individual SiPM. The performance of this control-loop is discussed in Chapters 8 and 9.

6.8 Test Measurements with the KIT Muon Tracking Detector

In order to examine the developed and built IceScint scintillation detectors for functionality and to determine their efficiency, the muon tracking tower is available at the IKP. This setup allows semi-automated determination of general parameters, such as the $\frac{PE}{MIP}$ ratio, but also to determine the uniformity and efficiency with respect to the scintillator and the optical coupling in different areas of the detector by means of a $1x1\,\text{cm}^2$ spatial resolution of the incoming HE electrons and muons.

In this subchapter the operation of the muon tower is explained, the measurements performed and an analysis of the efficiency distribution of the individual IceScint detectors described.

6.8.1 Measurement principle of the muon tracking detector

At the KASCADE experiment at Karlsruhe, a muon detector with limited streamer tube (LST) chambers was in operation [86]. The muon detector was placed close the central detector and its purpose was to investigate the muonic component of air showers Figure (6.30). Next to the usage in classical hodoscope conditions (placement of detectors on top of each other, different trigger levels at each stage), the muon detector is able to track muons due to its good spatial resolution of LST chambers. The design and the size of the chambers allowed a spatial resolution of $1x1\,\text{cm}^2$.

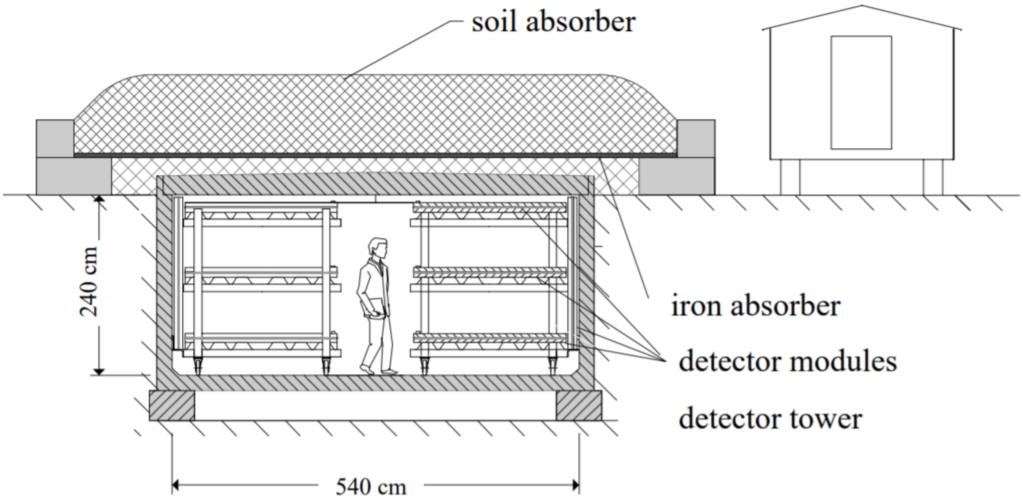

Figure 6.30: Cross-section of the KASCADE Muon tracking detector, the origin of the muon tower [86].

In recent past, for the calibration of surface detectors like the AugerPrime SSD (Chapter 2), a part of the KASCADE muon detector was refurbished, fitted to the purpose of obtaining key parameters of new surface detectors.

For the IceScint prototypes and the first three IceScint stations with 7 detectors each, the muon tracking detector was adjusted to read out IceARM and, later, use IceTAXI in between, in order to calibrate the IceScint detectors, too. An example of the placement of an IceScint detector can be seen in Figure 6.31.

6.8.2 Calibration procedure of the IceScint detectors

In order to define the amount of photo electrons (PE) per MIP, for check of production errors like broken optical fiber routing, uniformity of the sensitive area, electrotechnical issues and for general functionality per developed and produced detector, each detector was tested in several measurement procedures before shipping to the South Pole or the Physical Science Lab in Madison. For the following measurements, following colour code and units for the charge histograms and the muon tomography are used:

- Green: All pulses respectively charged particles which fulfilled the trigger condition of the muon tower
- Blue: MIP - Window selected pulses
- Red: MIP -Window selected pulses with charge corrected by $\cos(\theta)$ of the muon track
- Black: Only PE / pulses
- h: Pulse height or peak (usually given in V units)
- q: Charge of the pulse (usually in Me units)
- AoP: Area over Peak, $AoP = \frac{q}{h}$. Effective pulse length (usually given in ns units)

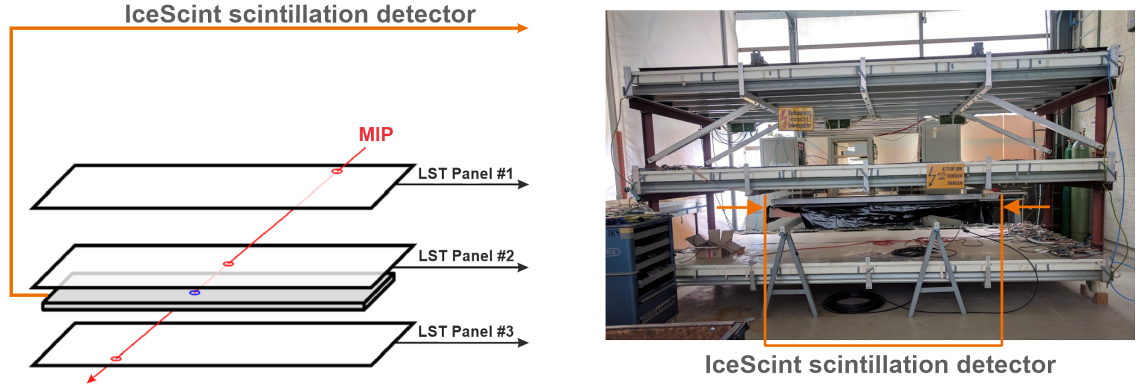

Figure 6.31: Left: Setup for the calibration and efficiency measurements with the muon tracking detector. Right: Photo of the setup. Every IceScint detector was place at the same position and height, between the bottom and middle LST panel (#2 and #3).

6.8.3 Muon tower tomography and charge histograms

Just before the final production step of one IceScint detector, the riveting of the aluminium housing in order to mechanically close the detector, a final test procedure was performed to each detector. For this purpose the muon tower was used. The Setup of the calibration measurements with the muon tower can be seen as schematic and as photo in Figure 6.31). In order to increase the analysis speed, every IceScint detector was placed at the same position in comparison with the three LST panels of the muon tower.

The results of the muon tower measurements are explained exemplary at one IceScint detector (#006), since the performance of all detectors is very similar (Figure 6.36). The measurement results for all the other IceScint detectors can be found in the Appendix. The main performance results like the charge histogram with the MIP peaks and the efficiency of the detectors are discussed in more detail in the following.

During the first series of test measurements a high-frequency (MHz) oscillating noise was registered by the Muon Tower DAQ. This resulted from a common-mode noise, induced by the different terminating resistors of IceARM respectively the GP-Board, which were chosen for the readout by IceTAXI, and the Muon Tower DAQ. Common-mode disturbances are caused by common-mode interference sources, the origin of which can be found in capacitive coupling, potential elevations of ground or grounding points or in potential differences of grounding points that are spatially separated. Common mode interference sources occur in an equivalent electrical circuit between a circuit and ground. A common mode noise filter (CMNF) removes the source of interference (Figure 6.32). Due to time pressure, a CMNF from an old Ethernet network card was used. This enabled the following analysis of the IceScint detectors with the Muon Tower.

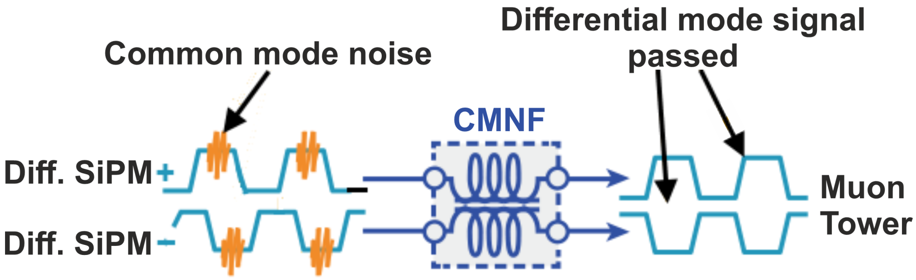

Figure 6.32: Sketch of the common mode noise cancellation between the differential analog SiPM signal and the muon tower.

Caption for Figure 6.33; Muon tower histograms:

- **(a)** Charge histogram recorded and integrated with the muon tower and integrated after the usage of the peak finding algorithm which seeks the recorded waveform traces of the IceScint detector during the coincidence gate of the muon tower for SiPM peaks.
- **(b)** Charge histogram of **(a)**, but of the logarithm of the charge. This graph provides a quick indication of the signal-to-noise ratio (MIP/VMIP peak vs. Noise/PE peak), i.e. the functionality of the detector.
- **(c)** Pulse height (peak) histogram. The average pulse height of the detector, after the SiPM amplification, the readout board amplification and the cable suppression can be seen.
- **(d)** Area-over-peak (AoP) histogram. Pulses are affectively 130 ns long. This scales with the full-system amplification and shows, among others, if the used 70 m cable shows a higher impedance is eventually damaged.
- **(e)** Histogram of number of pulses per trace. Increased tail means light leakage, i.e. a damaged photon shielding of the detector or increased electronic noise or common-mode interferences.
- **(f)** Pulse arrival times (x-axis) and $\lg\left(\frac{q}{\mathrm{Me}}\right)$ (y-axis) vs. the muon trigger (at $t = 0$). This basic plot contains a lot of information about the actual detector performance.

Caption for Figure 6.34; Muon tower tomography plots:

- **(g)** Mean vertical-equivalent charge $\langle q \rangle$ over the detector. The uniformity shows that the amount of generated and collected photons in the scintillator are uniform distributed over the whole detector area and that the optical coupling with the fiber to the SiPM is uniform, too.
- **(h)** The same figure as **(g)**, but in logarithmic scale. In this scale of the vertical-equivalent charge the single fiber of the detector are visible.
- **(i)** Mean Area-over-Peak (AoP) over the detector. It shows the mean of the recorded and integrated SiPM pulses. The detector shows an uniform distribution of the SiPM pulses. In addition, even the fiber bundle (x = 0.8-1.4 m and y = 2.7-3.1 m) are visible, therefore the fibers are detecting a significant amount of MIP induced

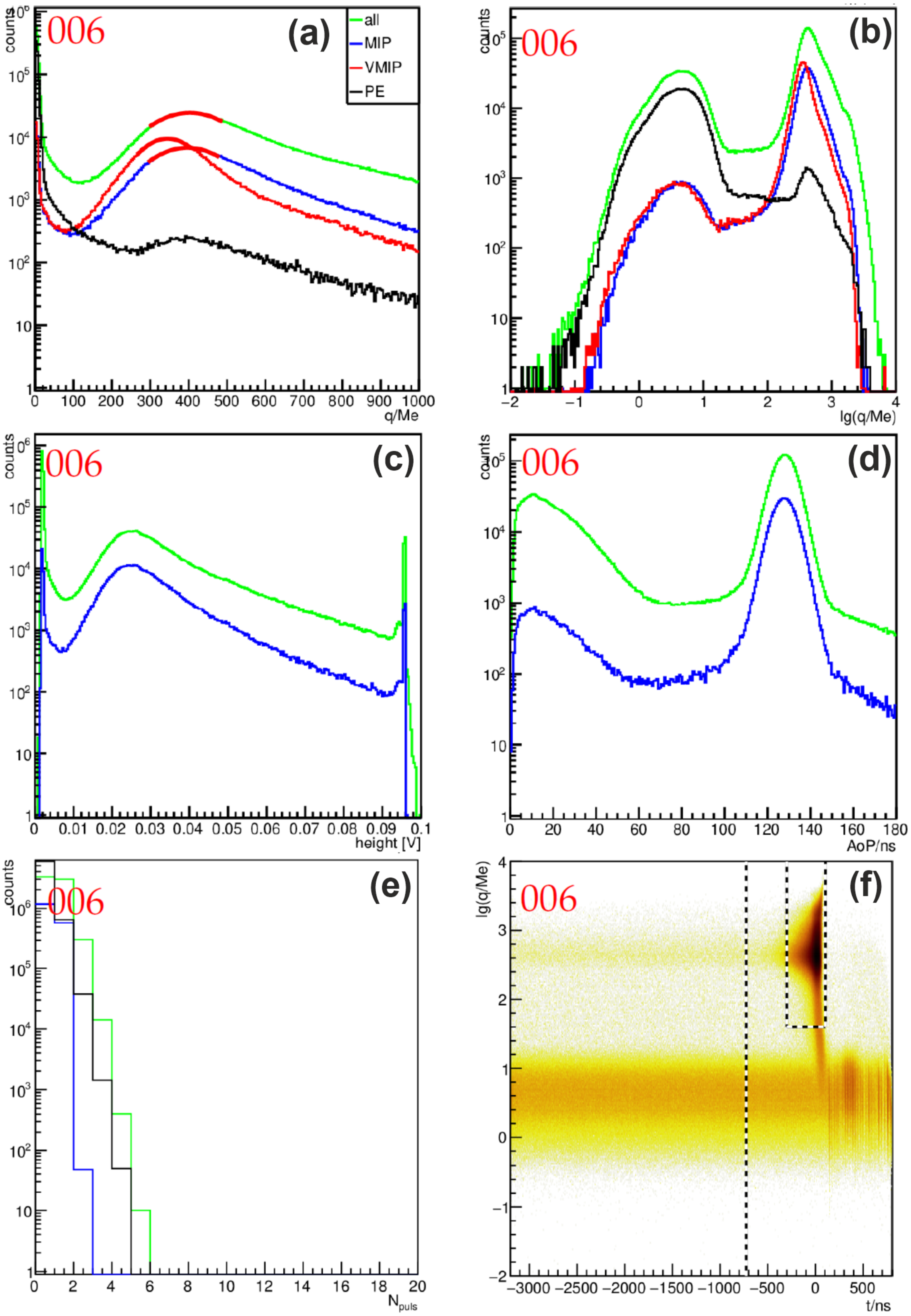

Figure 6.33: Muon tower histograms for (exemplary) the IceScint #006 detector. The figures (a) - (f) are explained in the text.

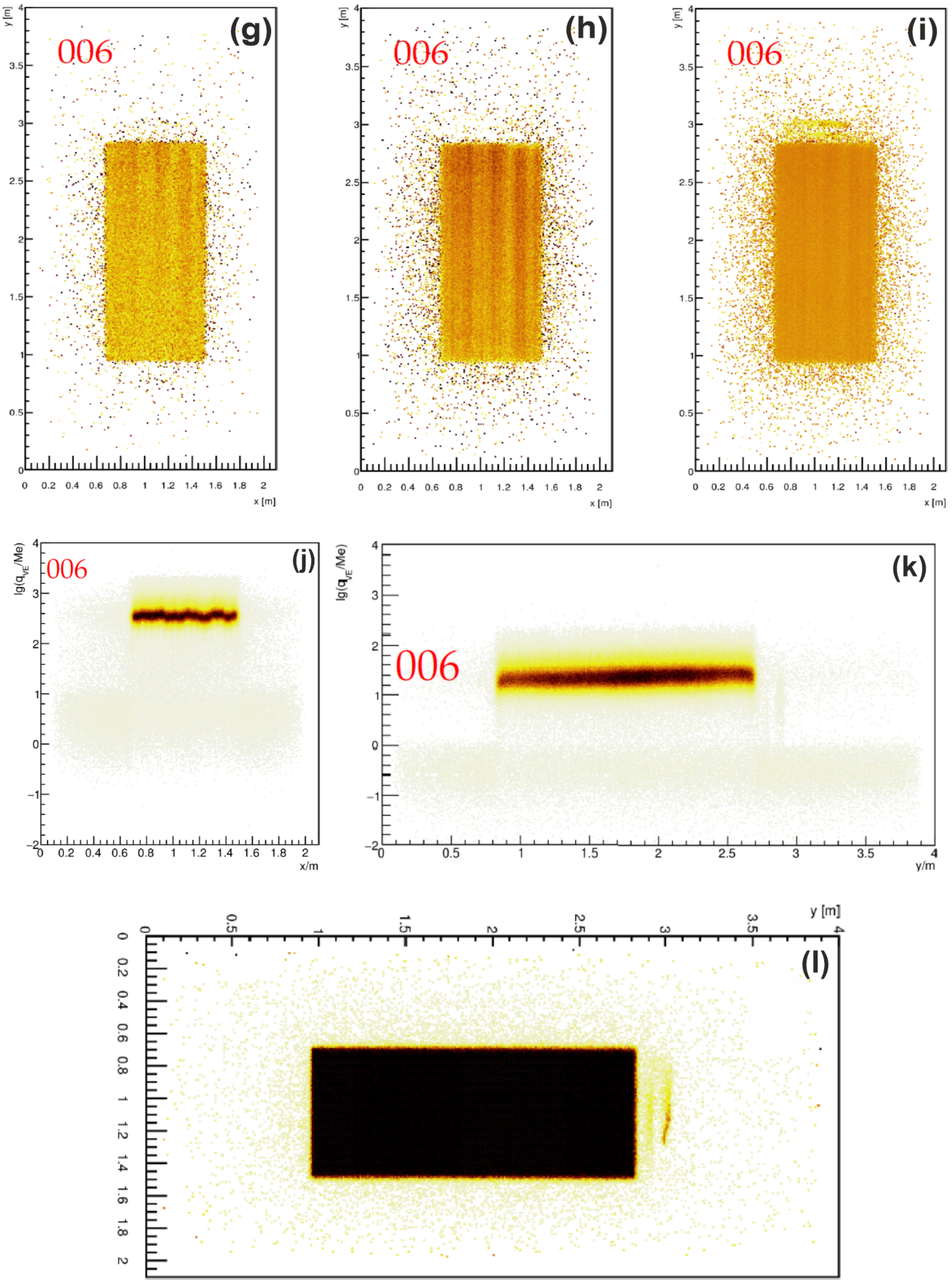

Figure 6.34: Muon tower tomography plots for (exemplary) the IceScint #006 detector. The figures (g) - (l) are explained in the text.

Maximum	45.55 $\frac{PE}{MIP}$
Minimum	35.56 $\frac{PE}{MIP}$
Mean	39.43 ± 0,57 $\frac{PE}{MIP}$
σ	2.47

Table 6.3: Distribution properties of the $\frac{PE}{MIP}$ histogram. In mean, the produced series of 23 detectors have in mean a yield of 39.43 $\frac{PE}{MIP}$ with, as far as possible to distinguish with this small series production, very less variation in the performance.

photons without scintillation bars. This effect is slightly different used for an outreach experiment (Chapter 10).

- **(j)** Projection of the mean log-charge along the x-axis. Shown is the charge distribution along the width of the detector, the length is in "z-axis". It shows the uniformity of detector and would reveal a cracked optical fiber or a bad optical coupling.
- **(k)** Projection of the mean log-charge along the y-axis. Shown is the charge distribution along the length of the detector, the width is in "z-axis". It also shows the uniformity of detector and would reveal a cracked optical fiber or a bad optical coupling, too.
- **(l)** IceScint detector hits divided by total muon tracks of the muon tower which equals to the efficiency of the detector. Black equals 100 percent. Like in (i), even the fiber bundle towards the SiPM coupling is visible.

6.8.4 Results charge deposits and histograms

In this subchapter, the most important measurements are explained and analysed in detail in order to be able to make reliable statements about the performance and efficiency of the IceScint 001-023 detectors. To obtain the performance and the functionality of each produced detector, a (by the muon tower) triggered charged histogram was recorded. Each detector is showing the typical behaviour of the charge deposit (Figure 6.35). At low charges (0-120 Me) the Single Photo Electron (SPE) "bumps" can be found, including the electronical noise, between 120-300 Me is the valley is placed and afterwards the MIP peak arises. It was checked if the MIP peak charge is at every detector at the same value in order to guarantee uniform detector and so an uniform detector array for deployment at the three different locations (Hybrid-Array at KIT , Physical Science Lab near UW-Madison, geographical South Pole).

For the 22 IceScint detectors (panels) with aluminium housing and with a 25 μm pitch SiPM, following properties can be obtained of the histogram with the $\frac{PE}{MIP}$ distribution (Figure 6.36). Whereby SD is the standard derivation, the square root of the variance σ, defined as

$$\sigma = \frac{1}{N} \sum_{i=0}^{N} (x - \bar{x})^2 . \tag{6.8.18}$$

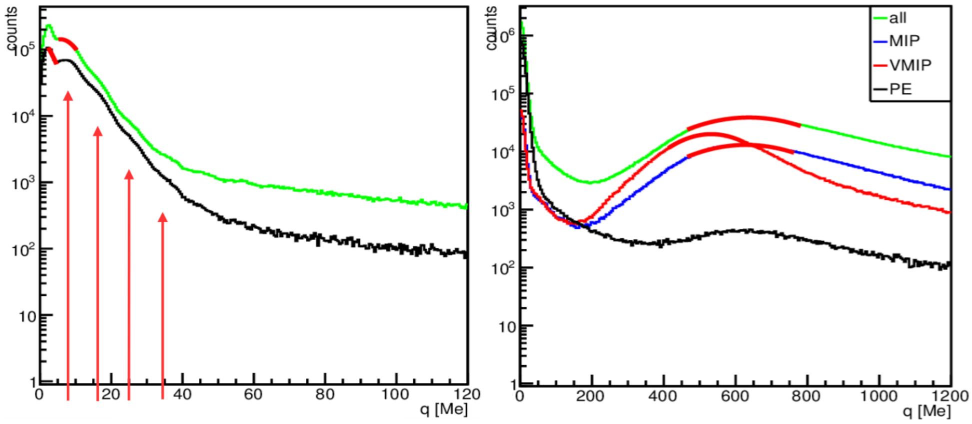

Figure 6.35: Left: Part of the recorded charge histogram, zoomed into the low charges (0-120 Me). The single SPE "bumps" at low charges were visible in the wooden prototype detector with 50 μm pitch SiPMs. Right: Charge histogram from the muon tower measurements for the wooden prototype detector with 25 μm pitch SiPM. Due to the higher PDE of these SiPMs, the $\frac{PE}{MIP}$ ratio is higher compared to the followed and deployed series with 25 μm pitch SiPMs

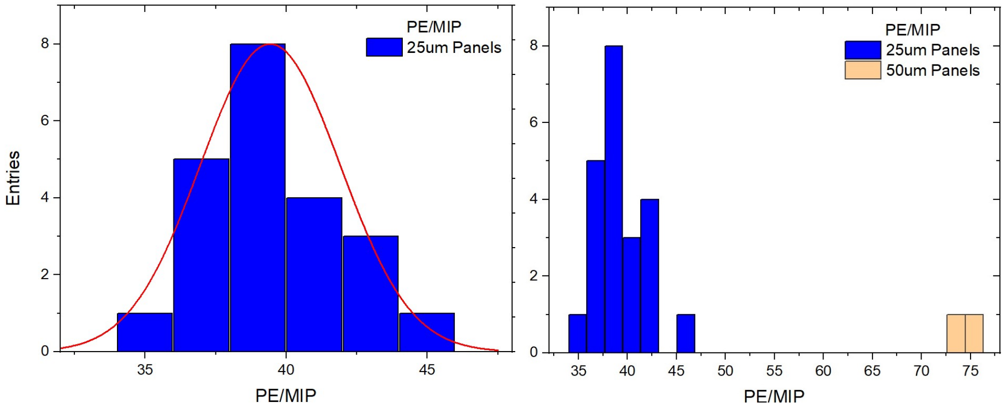

Figure 6.36: Left: Distribution of the Photo Electrons (PE) per minimum ionizing particle (MIP), as measured with the muon tower for all IceScint detectors with a 50 μm pitch SiPM, as deployed at PSL, KIT and at the South Pole. Right: In comparison the two benchmark respectively prototype detectors with a 50 μm pitch SiPM. Due to a higher photo detection efficiency which goes with a larger APD cell size (Chapter 5), the PE/MIP ratio is higher.

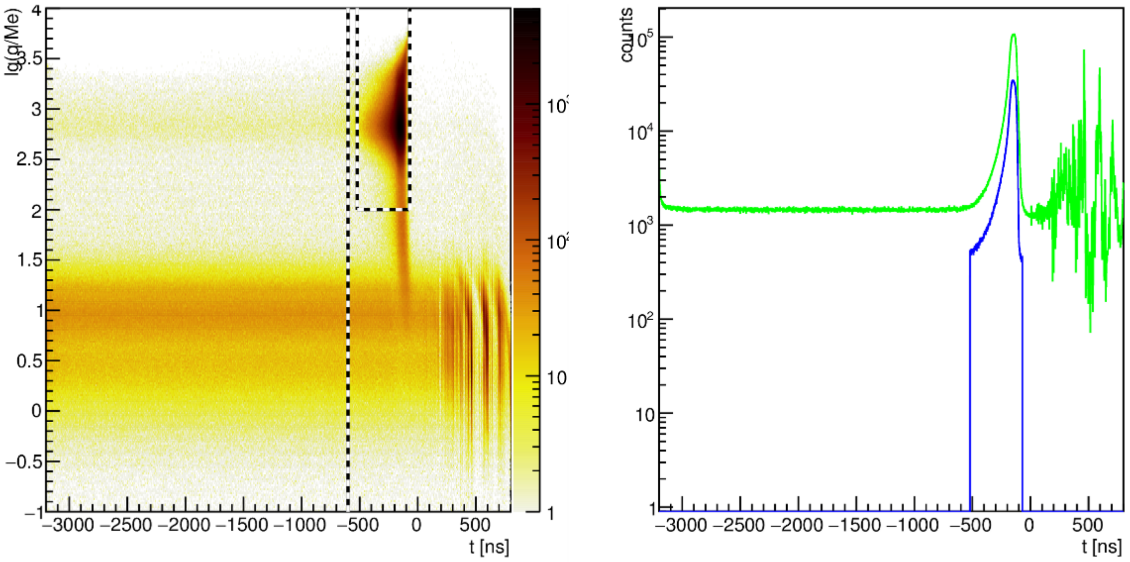

Figure 6.37: Left: Charge and time distribution of pulses detected with the prototype detector. The top region shows the high-charge band. The lower region the low-charge band therefore the SPE and the baseline and electronic rippling noise. The dashed rectangle shows the quality cut for the MIPs (blue line in the right hand side plot). The distance between the high and low charge band shows the high light yield and therefore the signal-to-noise ratio of a MIP compared to the base line. Right: Counts vs time of the pulses of the prototype detector. In green all signal counts are shown. The blue line shows the MIP counts.

6.8.5 Results muon tomography

For a brief overview of the detector performance, Figure 6.34, (f) and (d) are showing in two plots the signal-to-noise ratio and a possible light leakage, i.e. a damaged photon shielding of the detector or increased electronic noise or common-mode interference. Where (f) shows the detector performance, (d) shows major issues in the electronics or in the external cabling of the detector.

The charge spectrum for through-going muons is shown in Figure 6.35. At this first prototype detector, one MIP produces an average charge of 75 p.e. Correcting for the muon zenith angle that is known from the spatial resolution feature of the Muon Tower leads to an average charge for a vertical muon (VMIP, red curve) of 63 p.e.

In Figure 6.34 the efficiency of the detector is shown. Due to the optimal optical coupling, less electronic noise of ARM and the good SiPM response of the single APDs the efficiency of the detector is close to 100 percent. Every MIP, no matter of the energy deposit location, which is triggering the muon tower also appears at the prototype detector. Even the pulses generated by MIPs only crossing the optical fibers are visible.

The uniformity of the detector is highly uniform (Figure 6.34). In this plot the average pulse charge depending on the particle detection position in logarithmic scale is shown. Due to the optimal positioning of the fibers to the SiPMs the routing of the single fibers are visible. The pulse width, so the signal of the energy deposit of a MIP, is equal in every region of the detector.

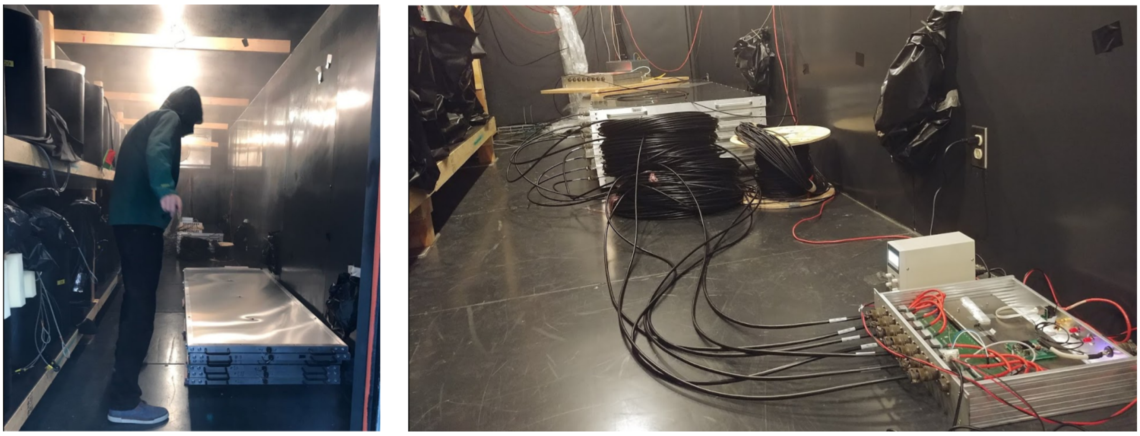

Figure 6.38: Left: Inside view of one of 3 cooling chambers of PSL. Two or even more IceScint stations can be tested and calibrated simultaneously. Right: One full IceScint station installed close together inside a cooling chamber. It contains 7 IceScint detectors, the IceTAXI DAQ, a power supply that provides the power that, in field, the field hub will deliver an 7 by 70 m of cable.

6.9 Full IceScint system test at PSL cooling chambers

In Summer 2017 a full system test was performed at the Physical Science Lab (PSL), Illinois, which cooperates with the UW-Madison and WIPAC. This full system test of an IceScint prototype array in was performed in the large cold chambers (Figure 6.38) which are used for the low temperature tests calibration of the IceCube Observatory components.

In Figure 6.38 the IceScint panels, the IceTAXI DAQ with its housing and the cables are visible inside the large cooling chamber. The difference to the, at this point, proposed measurements at the South Pole is that the IceScint detectors are operated in a hodoscope condition due to the lack of space in the cooling chamber for installing an array. Therefore the following presented measurements with a high coincide level are predominantly high energetic muons that propagate through all detectors and deposit energy in the scintillator bars.

For the full system test we shipped by cargo flights and by hand carry all components of the IceScint station to the PSL, including a set of 70 m cable.The commissioning of the IceScint Station was not dissimilar to the requirements to the South Pole deployment and consisted on the first hand of setting up IceTAXI: Establishing a TCP/IP connection with the PSL system, setting up access to IceTAXI external to the institute network and writing automated configuration and boot scripts.

For this purpose, threshold scans (Figure 6.39) and calibration charge histograms (Figure 6.38) had to be performed to find the correct operating parameters for the detectors and the trigger unit of IceTAXI. In addition, all IceScint detectors were individually checked for possible transport damage by comparing them with the calibration measurements at KIT. Due to the robust detector design, the choice of the right tube foil and the consideration that no parts of the detectors have a degree of freedom of movement, the comparison measurements were identical to the KIT measurements.

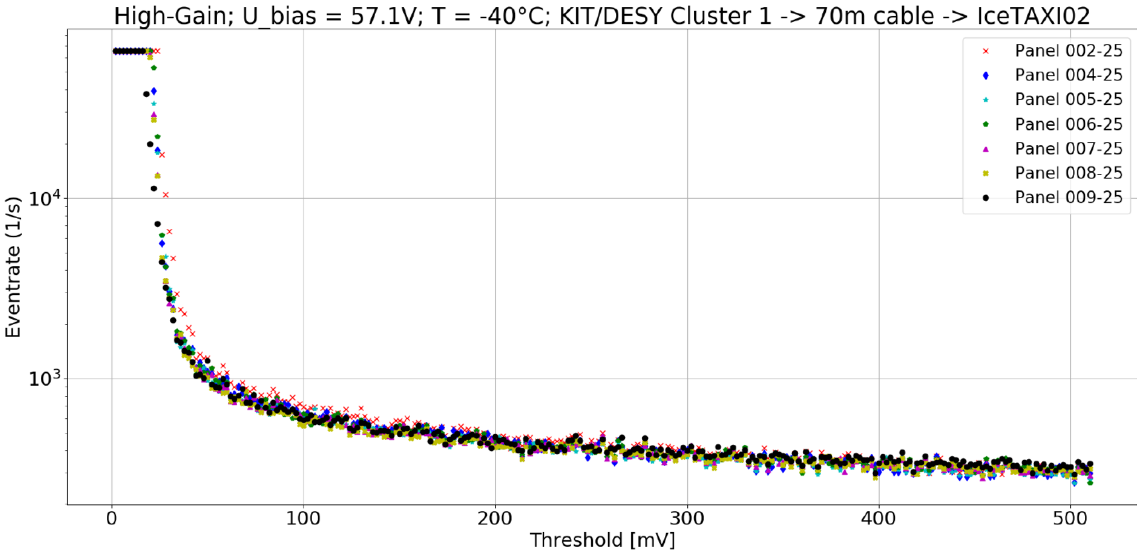

Figure 6.39: Example of one performed threshold scan with the IceScint station in hodoscope condition. Shown is the variation of the discriminator threshold in mV compared to the measured eventrate, seen by IceTAXI. For the altitude of the PSL and the present detector area a muon rate of 200 $\frac{1}{s}$ is estimated, which, in addition to noise components, fits to the detector response at a threshold level which is set high enough to trigger only on MIPs. This threshold scan was made at -40°C, the scintillators read out at high-gain mode and with the full IceScint detector chain, including 70 m of cable to IceTAXI, each.

Figure 6.39 shows the behavior of the detector eventrate, seen by IceTAXI at different signal-over-threshold voltage levels, called threshold scan. A bash script was written which starts to distinguish the eventrate by calculating the mean value of the eventrate within a 3 second interval and continues to the next possible discriminator threshold voltage value [7] and repeat the measurement till the whole threshold range is scanned. As expected, if the threshold is set low, both electronic and SiPM noise is also considered a signal and a high event rate is recorded by IceTAXI.

If the discriminator levels are increased, the event rate decreases significantly, changes into a gradient and then remains almost constant at high threshold voltage. This gradient can be explained in analogy to the charge histograms [8] of the detectors. At low threshold voltage the number of entries of low deposited charge is increased, i.e. the SPE peak is increased, the gradient towards the almost constant event rate corresponds to the "valley" in the charge histograms and the constant event rate at high threshold increases the number of measured MIPs, i.e. increases the signal-to-noise ratio.

Figure 6.40 shows a 7 times coincidence event in terms of response of the SiPM, so most likely one muon crossing all 7 detectors, depositing an amount of energy into the scintillator bars, each. The waveforms are showing the typical SiPM characteristics like a fast increasing flank and an exponential decreasing flank [7]. Due to the alignment of the detectors (stacked to each other) the time difference between the single SiPM pulses

---

[7] Range: 0-512 mV

[8] Detailed charge histogram analysis can be found in Chapter 9

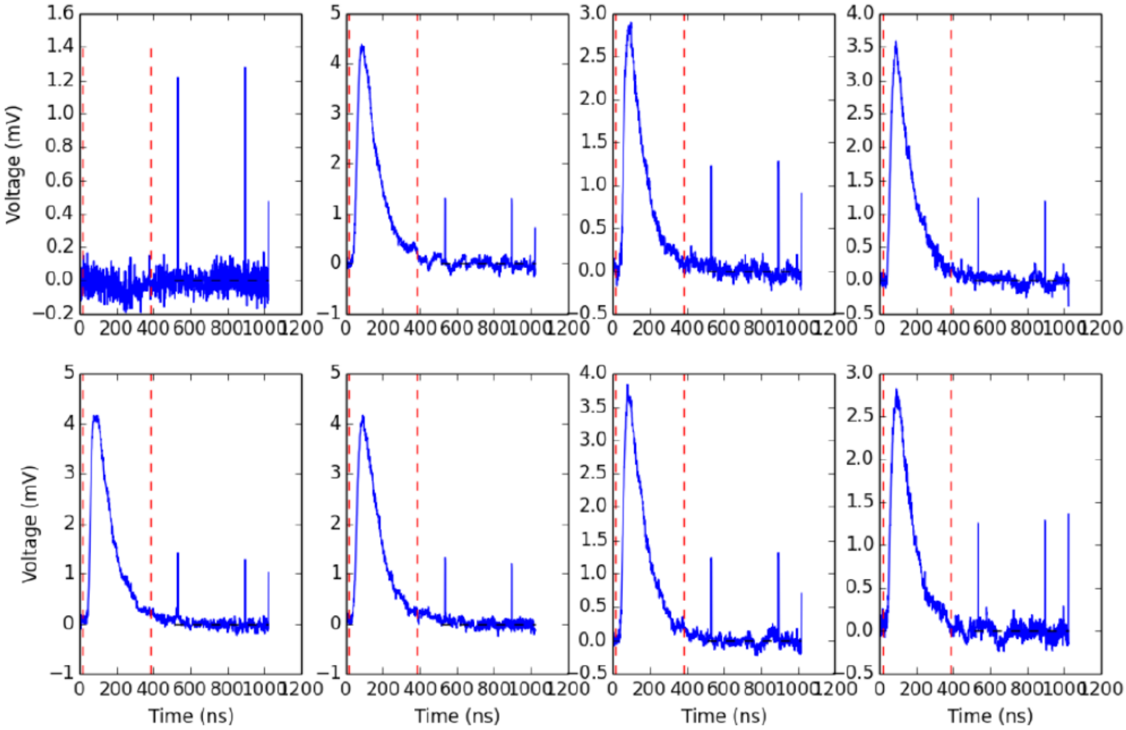

Figure 6.40: Example waveform plot of the individual IceTAXI channels during a 7 times coincidence event, measured at High Gain with a SiPM bias voltage of 56.1 V. The whole IceScint system, including IceTAXI and 7 by 70 m cable, is cooled down to -60°C. Each subplot shows the waveform, sampled by the DRS4 chip, at a signal-over-threshold event of one detector, from the set trigger time (~ at 70 ns) -70 ns before the trigger and 954 ns after it, so in total 1024 ns (Chapter 5).

is very short (ns region, indicating a muon propagation through all 7 detectors, therefore through a total geometrical dimension of at least (in terms of a total vertical muon) 7·50 mm detector and 7·10 mm scintillator bars. Channel 0 (first row, first column) shows the noise channel where no detector is connected. The noise channel is used in the measurements in Chapter 9 to estimate the baseline of the detectors.

By integrating the measured waveforms (a.e. Figure 6.40) at a signal-over-threshold event, a charge histogram, like explained in Chapter 5, can be obtained. If there is in one channel a amplitude seen which is over the set discriminator threshold, the waveform in this time interval (0 ns to 1024 ns) of all 8 IceTAXI channel is stored. By a following integration, in respect of the amplification, SiPM gain and elementary charge (Chapter 9), a charge spectra like Figure 6.41 can be created.

For the IceScint scintillators with a low to medium threshold set, the SPE peak at low charges, the valley and the MIP peak are expected to be visible. This typical spectra is visible in measurement runs. The mean charge deposit at the MIP peak position indicates the uniformity of the single detectors. The mean width of the MIP peak indicates the variation of the light yield, e.g. how much photon loss or reflection by the fiber routing of the scintillator bars till they are detected by the SiPM (including the uniformity of illuminating all of the APD cells of the SiPM by the optical coupling).

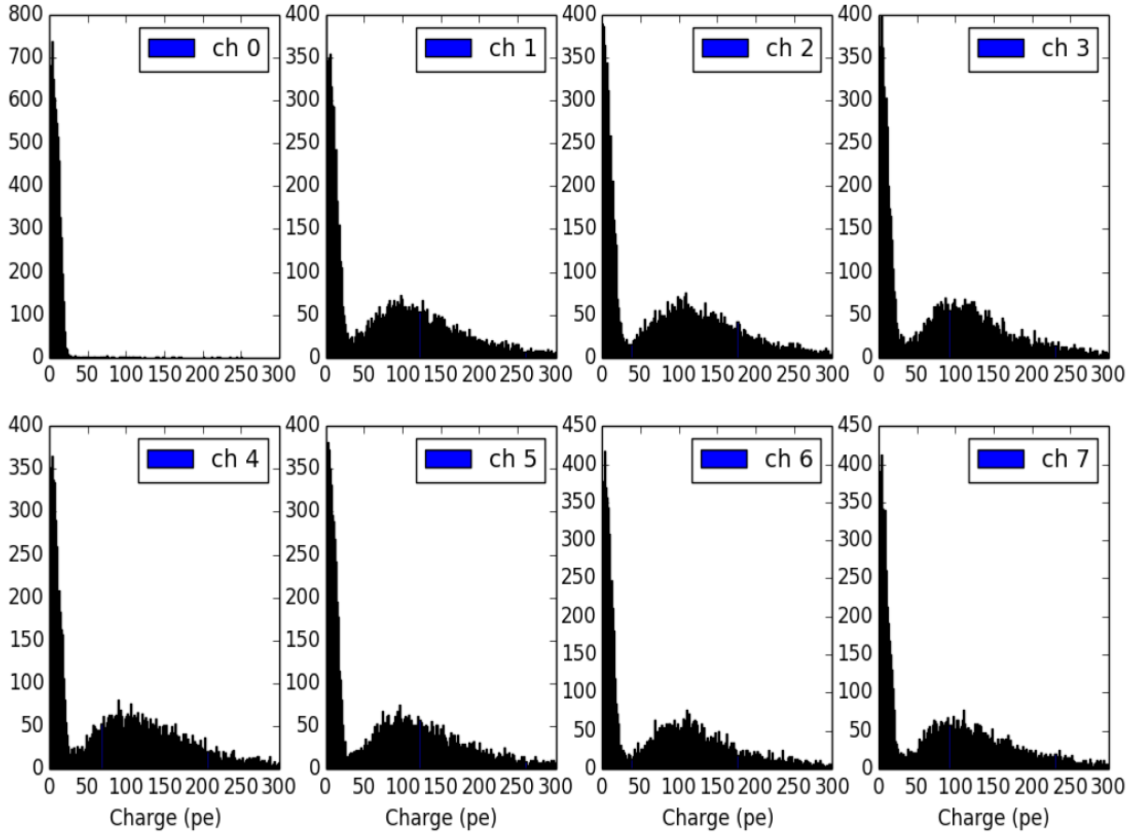

Figure 6.41: Example of charge spectra of the individual IceTAXI channels, out of integrated waveforms from (a. e.) Figure 6.40. The whole IceScint system, including IceTAXI and 7 by 70 m cable, is cooled down to $-60°$C. Each subplot shows the charge histogram, integrated from the signal-over-threshold waveform events. The measurement time was around 4 hours and IceTAXI and the IceScint detectors were set at proposed operation parameters, measured before at KIT. All channels and therefore all detectors are showing the SPE peak and the MIP peak at close the same charge deposit position, which indicates for a uniform processing of all IceTAXI channels and uniform detectors, which proves the muon tower measurements at KIT. The whole system was checked and was afterwards ready to ship from PSL directly to the South Pole. The channel 0 is the noise channel where no scintillator is connected.

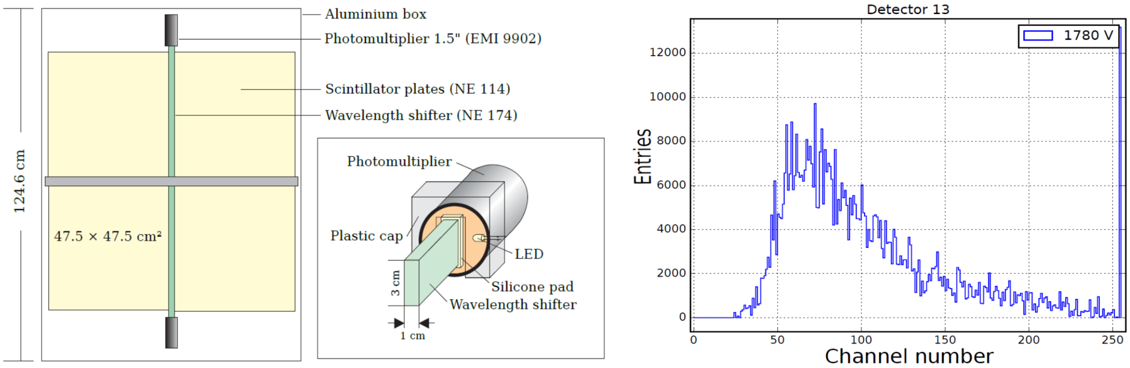

Figure 6.42: Left: Two scintillation detectors in one aluminum box which was formerly used a trigger unit for the KASCADE central detector [87]. Compared to IceScint detectors, the scintillation material consists out of one solid block of scintillator which is read out by one wavelength shifting block. Due to the different transmission and reflection of scintillation light because of the large variety of transmission length to the wavelength shifter (green colored), photons are getting absorbed again and do not reach the PMT. This results in a dependency of the charge deposit, seen by the DAQ after the PMT photon detection, from the location where the ionizing particle was hitting the detector. This results in a large width of the MIP peak (Right). It shows the charge spectrum of one detector in units of ADC channels for a cut above the SPE peak and the valley.

The narrow width of the histogram shows that even a single detector forms a uniform detecting area for ionizing particles, i.e. it is negligible at which spot of the 1.5 square meter sensitive area the particle generates a light signal. This uniformity distinguishes a detector system consisting of scintillator bars with optical routing from a scintillator block that is coupled only with one single wavelength shifting block (Figure 6.42) attached to the scintillator material, transferring the photons to a PMT or SiPM ([87], [88]).

After 2 weeks of testing and calibration, the IceScint system was fully tested and stable recording MIP events. The remote control of the IceScint station was already working via SSH control and therefore, it was shown that following items works successfully:

- the by the DRS4 sample waveforms of the SiPM show typical signal shapes, indicating for example, the optical coupling did not crack during transport,
- the threshold scans show a similar behaviour with expected event rates, indicating that the detectors are uniform and inside the detectors all scintillator bars and its fiber routing are fully operational, means they all form a 1.5 m² detector surface for ionizing particles, therefore no fiber is broken or the scintillator bars moved out of position,
- the charge histogram is typical for scintillators. The SPE peak, the “valley” and, most important, the MIP peak is clearly visible. The mean charge deposit in each detector is close to identical, showcasing uniform detectors with no broken or damaged components,
- the serial 486 interface for the slow mode control of the detectors (detector software communication),

- the Ethernet and WR connection to a remote control PC via EventSender and EventReceiver software (measurement data communication, WR communication),
- turning on/off the detectors, switching between high and low gain, adjusting the bias voltage of the SiPM (Detector configuration communication),
- activating / deactivating the DRS4 waveform sampling, the data stream packages transferred and the FPGA online integration for online generated charge histograms (FPGA control communication)

This is true for temperatures below $-60°$C, so at this point the whole IceScint prototype station was ready to be shipped to the South Pole.

7 Deployment at the South Pole

In the frame of the IceCube Collaboration an enhancement to IceTop was designed and proposed consisting of an homogeneously-spaced scintillator array (IceScint) with an areal coverage similar to IceTop. It was planned to deploy up to 37 scintillator stations over several years as shown in Chapter 4. Each IceScint station in the first design comprise of seven scintillation detectors. In 2020 the layout of the proposed deployment map and the layout of the individual station changed [41, 42].

This Chapter describes the deployment of the first IceScint prototype station, the positioning of the station, the scintillators and their different arrangements and the location of IceTAXI in respect to the ICL and the geographic South Pole. Furthermore, a selection of the results of the first commissioning measurements and the operational functional tests are discussed and the setup of the satellite uplink for slow control and data transfer is presented. In addition, some remarks useful for future deployments are noted. In Figure 7.1 the deployment sketch for the first IceScint station including the central surface Fieldhub (SFH) with the DAQ systems, can be seen. In that season, two different scintillator stations with different scintillators and DAQ were tested. The IceTAXI one, which is in focus of this thesis and "uDAQ" [89] which is mainly developed by colleagues at UW-Madison.

The concept and the components of the FieldHub and its cabling is simplified sketched

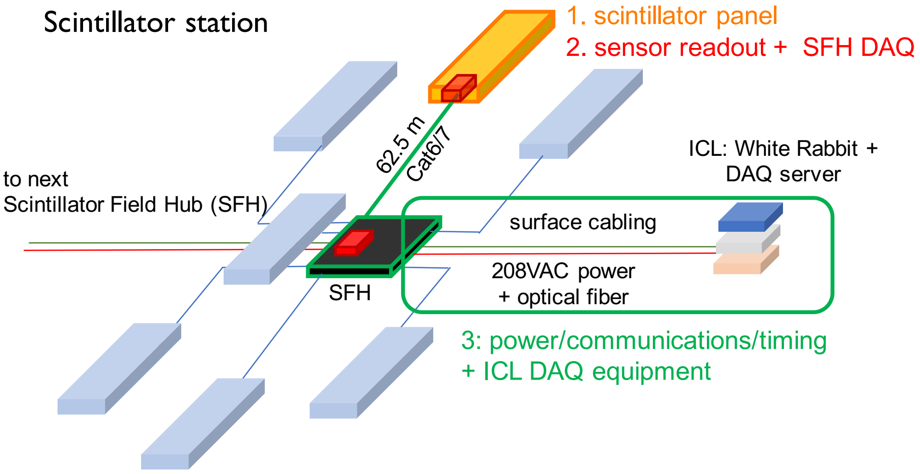

Figure 7.1: Deployment sketch of one of the 37 forseen scintillator stations as planned in 2017. Seven scintillation detectors are connected to a central surface field hub (SFH), which includes the IceTAXI DAQ, the power supply and timing and communication via a white rabbit (WR) node. The IceScintprototype station installed in early 2018 follows this deployment plan [89]. The WR node communicates with the central IceCube DAQ, the IceCube Lab (ICL).

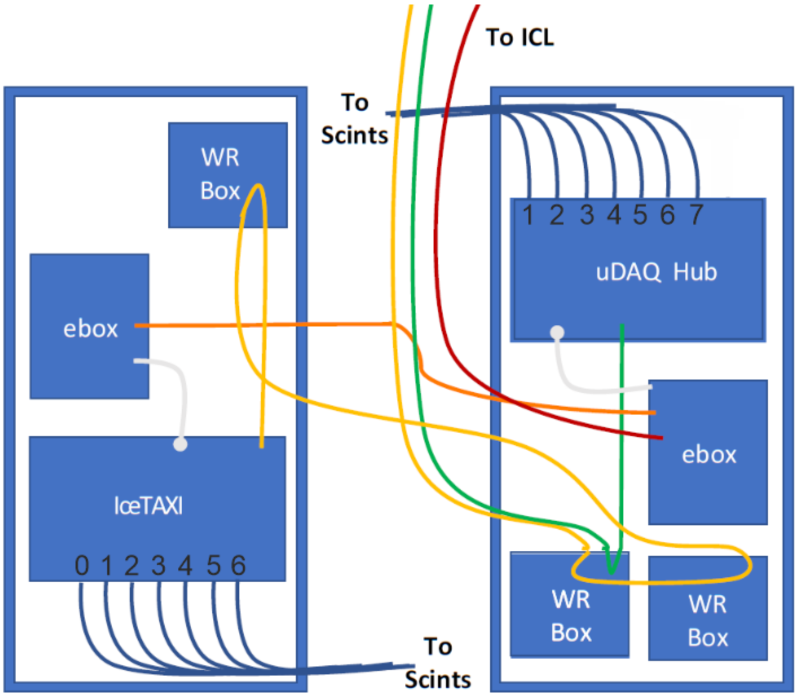

Figure 7.2: Simplified FieldHub Schematic, edited from [90]. It shows the two housings of the IceTAXI and uDAQ DAQ, the White Rabbit System and the "ebox" Power Supplies. In addition a simplified cabling of the Fieldhub is drawn. The blue cables are going to the IceScint detector positions, yellow connects the IceTAXI WR node with the FieldHub WR switch, the orange one loops the current from the uDAQ box to the IceTAXI voltage converter. Green connects the WR node of the uDAQ hub and red supplies the current from the ICL to the Field Hub.

in Figure 7.2.

At the FieldHub the uDAQ and the IceTAXI system are divided into two crates. The crates consist of standard PE plastic casings (one box with a lid each) from the hardware store, which were prepared during the two-week PSL stay in August 2017. In order to fix the components an approximately 1 cm thick plywood plate was fixed. IceTAXI, the voltage converter and the White Rabbit system were mounted on this plate. In the uDAQ box there is a WR switch, which transfers the WR signal to the two WR nodes. A picture of the deployed FieldHub can be seen in Figure 7.6.

7.1 Alignment and positioning of the first IceScint station

Figure 7.3 shows an edited photo of the first IceScint station which was made by the USAP[1] staff during a fly over is shown. Visible are the ICL, the IceCube specific cargo crates in front of it, the ~350 m path to Position A which includes the fieldhub with IceTAXI and the hexagonal shaped IceScint prototype station (A-G). The Amundsen-Scott South Pole Station is around 800 m distance to the ICL.

---

[1] United States Antarctic Program. In specific: Jeff Warneck, National Science Foundation

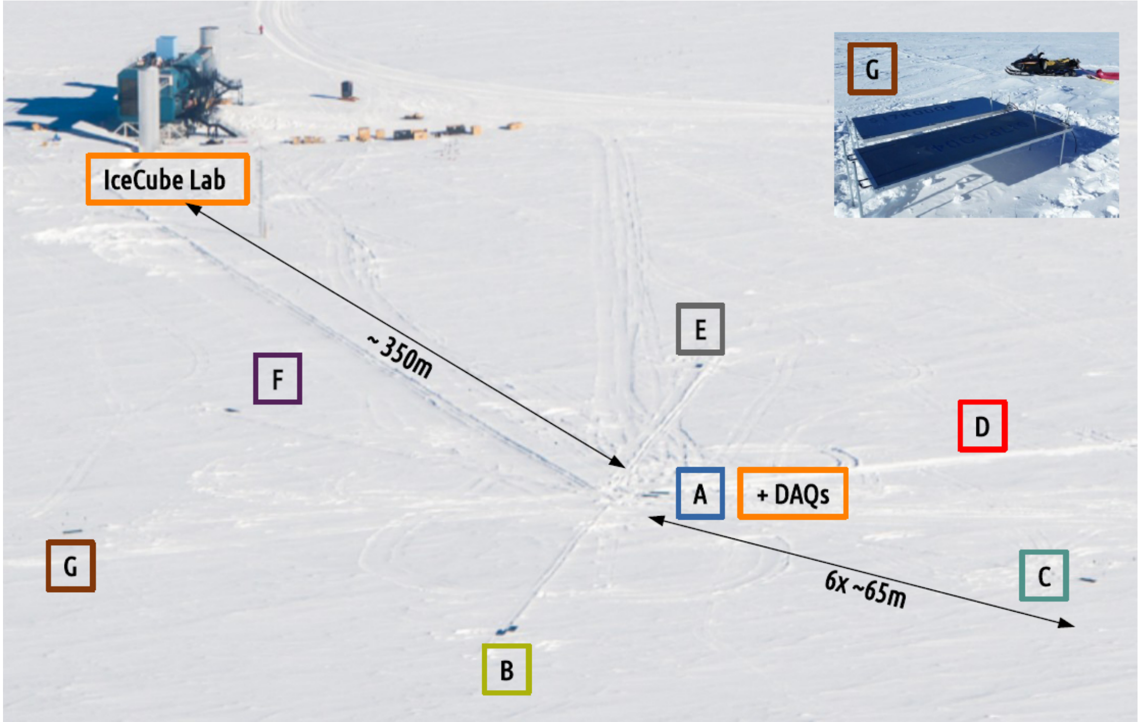

Figure 7.3: Edited Photo of a fly by over the IceScint prototype station, taken by the United States Antarctic Program (USAP) staff [91]. The distance to the ICL to the detector location “A” and the IceTAXI DAQ is around 350m. The hexagon alignment of the IceScint detectors is visible and, by close look, the new trenching for the cables. Top right corner shows a photo of one location of the IceScint detectors.

The cable and fiber trenching between the ICL and IceTAXI and between the IceScint detector positions are visible as small “bumps” in the snow. The 6 overlapping IceTop tanks at this aera (Figure 7.4) are buried under snow and are, like each other IceTop tank, not visible anymore.

The accumulating snow of the IceTop tanks is continuously increasing the energy threshold for the detection of cosmic ray induced air showers (Chapter 4). The attenuation effects of the snow add systematic uncertainties to air-shower measurements, particularly in the mass composition analysis [91]. In order to acquire first experimental data on the charge deposition and the event rates between the IceScint detectors and the IceTop tanks covered with snow, the deployment plan was developed with the hexagon, which is mainly limited by the cable length due to the star-like positioning of the DAQ in the middle of the hexagon, to achieve as much overlap as possible between IceScint detectors and IceTop tanks. The result of these efforts can be seen in Figure 7.4. With the hexagon spanned by 70 meters of cable length it was possible to cover three IceTop stations with 2 tanks each by the positioning of the IceScint detectors.

Since the positioning of each IceScint detector was determined at all 4 corners of the detector with a dual GPS receiver, the radial alignment of the detectors with respect to each other is also visible. It was found that after one year it makes a considerable difference in the height of the snowdrift whether the scintillators are placed in or against the wind direction at the South Pole. The impact and an option to align quickly future detectors, all longitudinal parallel to or against the wind direction was investigated and worked out by a group of three high school students in form of a cooperation of KCETA at KIT with the Thomas-Mann-Gymnasium in Stutensee. These results were applied to the new IceScint array layout, which is presented in Chapter 11 as an outlook and can be found in detail in the PhD thesis of A. Leszczynska [42].

7.1.1 GPS coordinates

Once the IceScint Station was fully cabled and installed, a USAP landscape surveyor was called-in to record the trenching and positioning of the detectors and the fieldhub DAQ. A mobile stereo GPS was used and the individual detectors with 4 measuring points each (at the corners of the detectors) were added to the system. The resulting map can be found below.

Figure 7.5 shows a general overview of the first IceScint station in respect of the series number of the detector, the connected port at IceTAXI and uDAQ the alignment of each detector. This illustration was largely used since it gives an "one glance" overview of the IceScint station during working with the measurement data in terms of commissioning and first analysis. The black numbers with a cross inside of the drawn circle is showing the number of the IceTop tank nearby or next to the Scintillators. The numbers with dots corresponds to the IceCube strings with DOMs. The central FieldHub, which contains among others the uDAQ readout and the IceTAXI DAQ, was placed in the middle of the hexagon at position A (Figure 7.6).

USER: TURNERRA FILENAME: EN-FILE02-PV\common\Collaboration\PMPSDesignerWorkspace\South_Pole_Working_Drawings\SSE_Station_Science_Experiments\Scintillator A-333-S\Civil\XXXXXXSPSSSEC-101-R1.DWG 22 MAR 2018 12:19

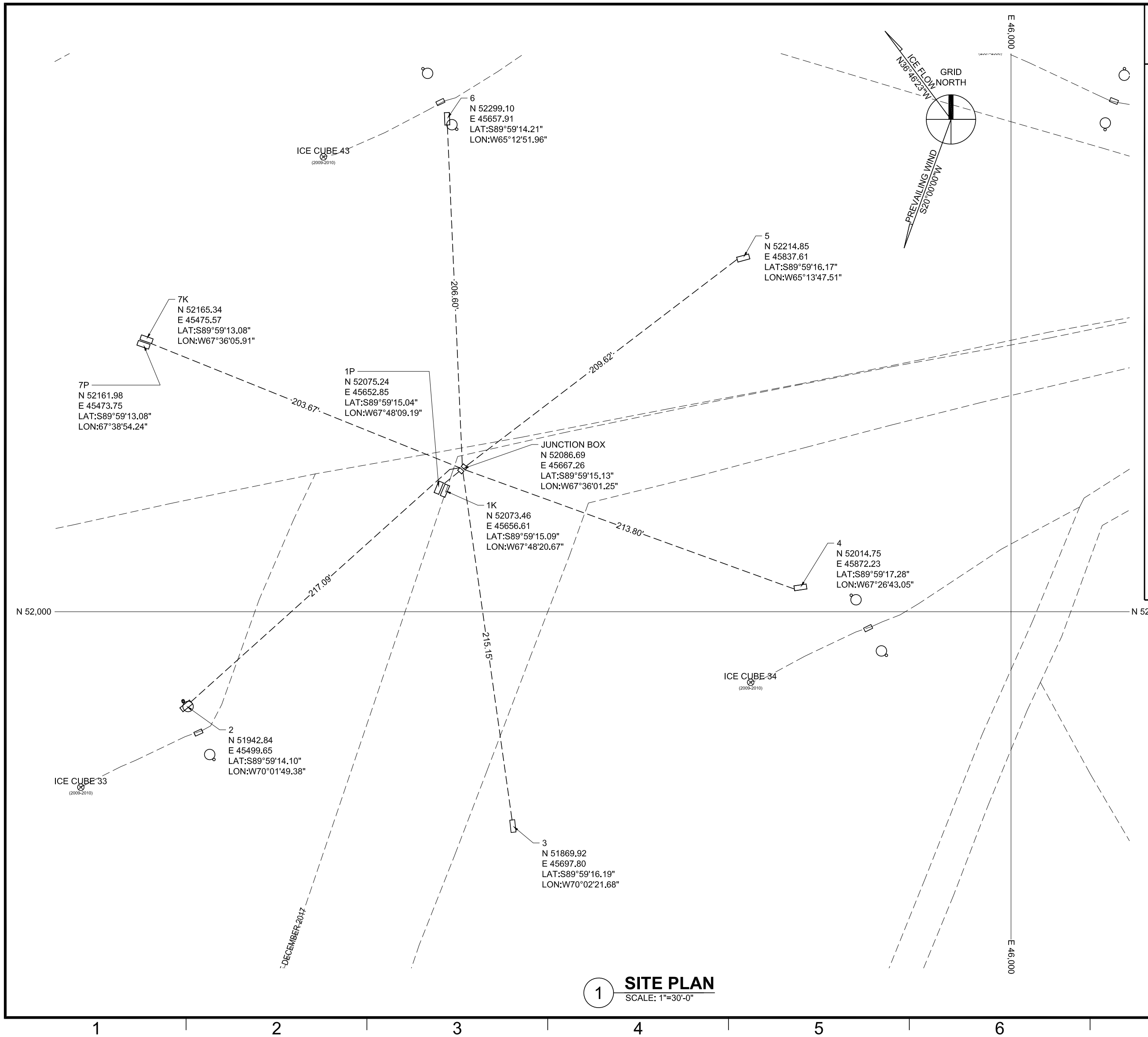

① SITE PLAN
SCALE: 1"=30'-0"

PRELIMINARY DRAWING
FOR REVIEW ONLY - NOT FOR CONSTRUCTION

SCINTILLATOR PANEL COORDINATES

PANEL	LATITUDE	LONGITUDE	NORTHING	EASTING
1K	S089° 59' 15.07"	W067° 51' 08.39"	52,070.60	45,653.76
1K	S089° 59' 15.07"	W067° 45' 28.14"	52,077.48	45,656.72
1K	S089° 59' 15.10"	W067° 45' 30.12"	52,076.32	45,659.46
1K	S089° 59' 15.10"	W067° 51' 10.60"	52,069.42	45,656.52
1P	S089° 59' 15.03"	W067° 50' 57.88"	52,072.36	45,650.04
1P	S089° 59' 15.03"	W067° 45' 17.90"	52,079.32	45,652.86
1P	S089° 59' 15.06"	W067° 45' 17.65"	52,078.18	45,655.65
1P	S089° 59' 15.06"	W067° 50' 57.86"	52,071.23	45,652.82
2	S089° 59' 14.13"	W069° 59' 57.28"	51,944.07	45,503.52
2	S089° 59' 14.10"	W070° 04' 43.58"	51,939.31	45,497.70
2	S089° 59' 14.07"	W070° 03' 35.39"	51,941.63	45,495.80
2	S089° 59' 14.11"	W069° 58' 49.18"	51,946.38	45,501.61
3	S089° 59' 16.19"	W069° 59' 19.44"	51,873.81	45,698.88
3	S089° 59' 16.22"	W070° 04' 32.56"	51,866.35	45,699.70
3	S089° 59' 16.19"	W070° 05' 34.18"	51,866.03	45,696.72
3	S089° 59' 16.16"	W070° 00' 21.21"	51,873.48	45,695.90
4	S089° 59' 17.24"	W067° 27' 17.72"	52,015.68	45,868.30
4	S089° 59' 17.30"	W067° 24' 13.03"	52,016.77	45,875.71
4	S089° 59' 17.32"	W067° 26' 15.71"	52,013.82	45,876.17
4	S089° 59' 17.25"	W067° 29' 20.29"	52,012.70	45,868.76
5	S089° 59' 16.13"	W065° 14' 57.69"	52,215.06	45,833.54
5	S089° 59' 16.19"	W065° 11' 13.67"	52,217.04	45,840.79
5	S089° 59' 16.21"	W065° 13' 00.66"	52,214.13	45,841.56
5	S089° 59' 16.15"	W065° 16' 44.64"	52,212.15	45,834.31
6	S089° 59' 14.21"	W065° 15' 52.49"	52,295.29	45,656.57
6	S089° 59' 14.18"	W065° 10' 55.40"	52,302.79	45,656.26
6	S089° 59' 14.20"	W065° 09' 54.44"	52,302.91	45,659.26
6	S089° 59' 14.24"	W065° 14' 51.65"	52,295.43	45,659.58
7K	S089° 59' 13.12"	W067° 37' 09.89"	52,162.70	45,478.63
7K	S089° 59' 13.05"	W067° 37' 28.73"	52,165.15	45,471.54
7K	S089° 59' 13.05"	W067° 35' 18.70"	52,167.99	45,472.52
7K	S089° 59' 13.12"	W067° 34' 59.65"	52,165.54	45,479.61
7P	S089° 59' 13.12"	W067° 39' 54.96"	52,159.34	45,476.81
7P	S089° 59' 13.05"	W067° 40' 14.45"	52,161.77	45,469.72
7P	S089° 59' 13.04"	W067° 38' 04.44"	52,164.61	45,470.69
7P	S089° 59' 13.12"	W067° 37' 44.74"	52,162.18	45,477.78
JB	S089° 59' 15.14"	W067° 38' 17.12"	52,083.65	45,666.71
JB	S089° 59' 15.11"	W067° 37' 26.35"	52,085.86	45,664.29
JB	S089° 59' 15.13"	W067° 33' 42.88"	52,089.72	45,667.83
JB	S089° 59' 15.16"	W067° 34' 33.52"	52,087.51	45,670.22

INCHES 1 2
CENTIMETERS 1 2 3 4 5 6

NATIONAL SCIENCE FOUNDATION
OFFICE OF POLAR PROGRAMS
WASHINGTON, D.C. NSF
CONTRACT OPP. 0000373

REVISION LOG

REV.	DATE	DESCRIPTION	DFTG.	APPD.
1	MM/DD/YY	AS-BUILT	RJT	XXX

SOUTH POLE STATION
BUILDING / SITE NAME
SCINTILLATOR A-333-S
CIVIL

ASC
ANTARCTIC SUPPORT CONTRACT
7400 South Tucson Way
Centennial, Colorado
80112-3938 USA
303-790-8606
800-688-8606

PROJECT NUMBER:
FILE NAME: XXXXXXSPSSSEC-101-R1
DESIGNED BY:XXX
DRAWN BY:RJT
DATE CREATED:MM/DD/YY
SHEET TITLE: SITE PLAN
SHEET NUMBER: C-101

Figure: Preliminary GPS deployment survey map of the first IceScint station, as deployed and used for Season 2018. GPS coordinates obtained and measured by the United States Antarctic Program (USAP)

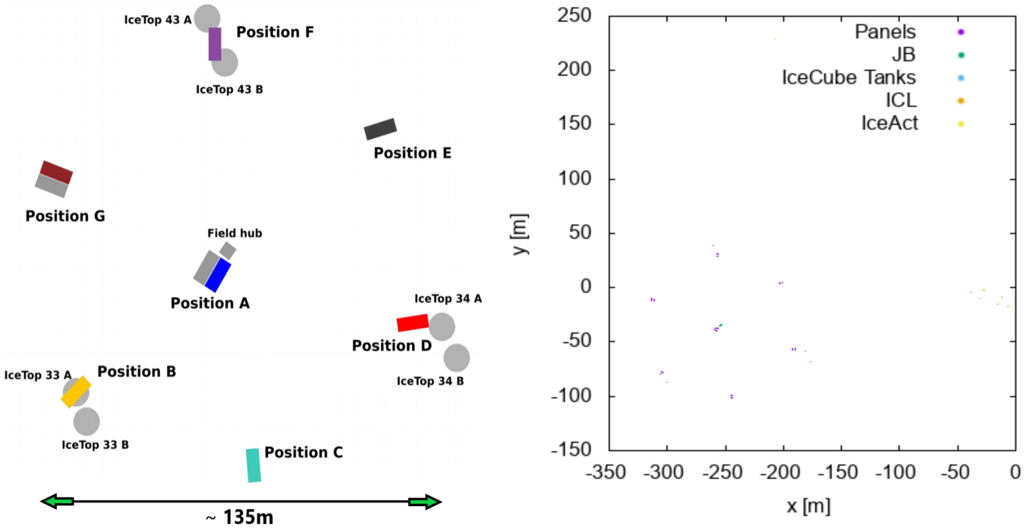

Figure 7.4: Left: GPS accurate positioning map of the first IceScint prototype station compared to the overlapping IceTop tanks. This map was made in order to showcase the rotational alignment of the IceScint detectors and its position in respect of the IceTop tanks. The distance between the Field Hub with IceTAXI (center) and the IceScint detector positions is shortened by a factor of~12. The single Positions (A- G) are in true scale in order to showcase the IceScint station. Left: The overall positioning map in true scale.

7.1.2 IceScint detector deployment

To check whether the IceScint detectors had survived the transport to the South Pole, an identical second IceTAXI(01) was brought to the pole in addition to the IceTAXI(02) to be installed in the field. Before the detectors were installed, a checklist was prepared for each detector, which covers the most important functional parameters in a brief time frame:

- Switching the operating voltage of the detectors on and off.
- Response to slow-mode read & write commands of the RS485 interface of IceARM.
- A feedback response to the setting of the discriminator threshold voltages and the SiPM operating voltage.
- A valuable monitoring data package of the Hamamatsu Power Supply on IceARM.
- Visible changes in the event rates registered by IceTAXI at different discriminator thresholds.
- Reasonable temperature sensor data of the cookie boards.

All detectors have withstood the transport without malfunction. The first detectors were driven into the field on the day of the last checks in the ICL. It was possible to install three

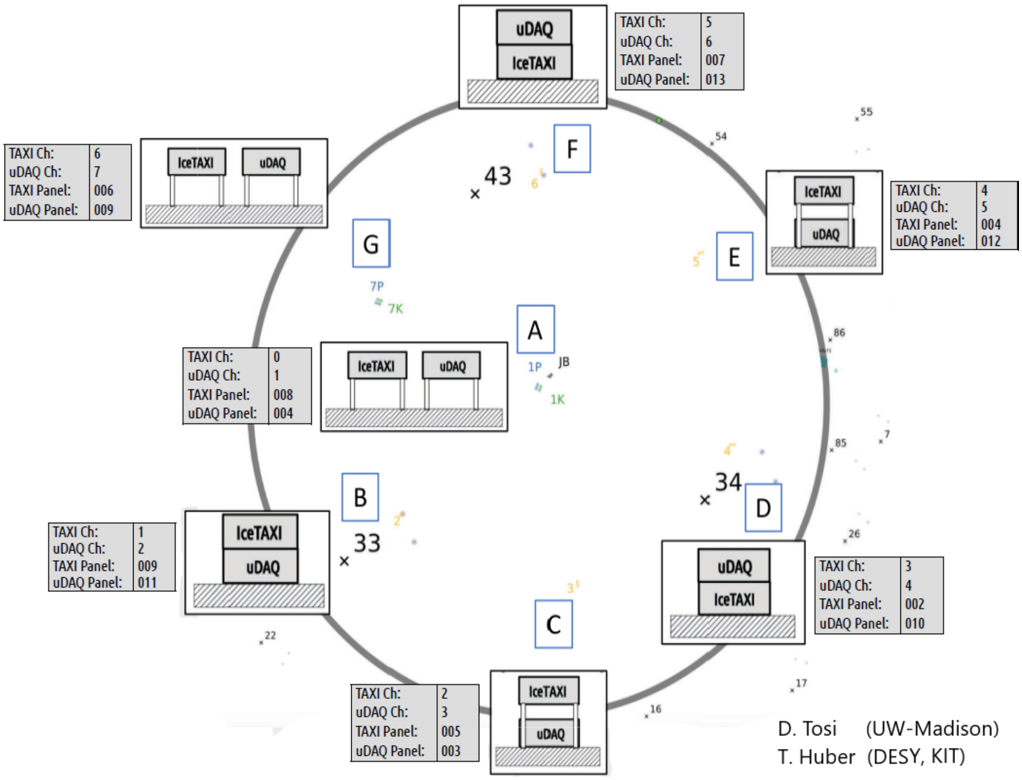

Figure 7.5: General overview of the first IceScint station with IceTAXI and uDAQ detector readout, in respect of the series number of the detector and the connected port at IceTAXI and uDAQ. In addition, the alignment of each detector is visible. Also the positioning at each location relate to the second station installed, uDAQ.

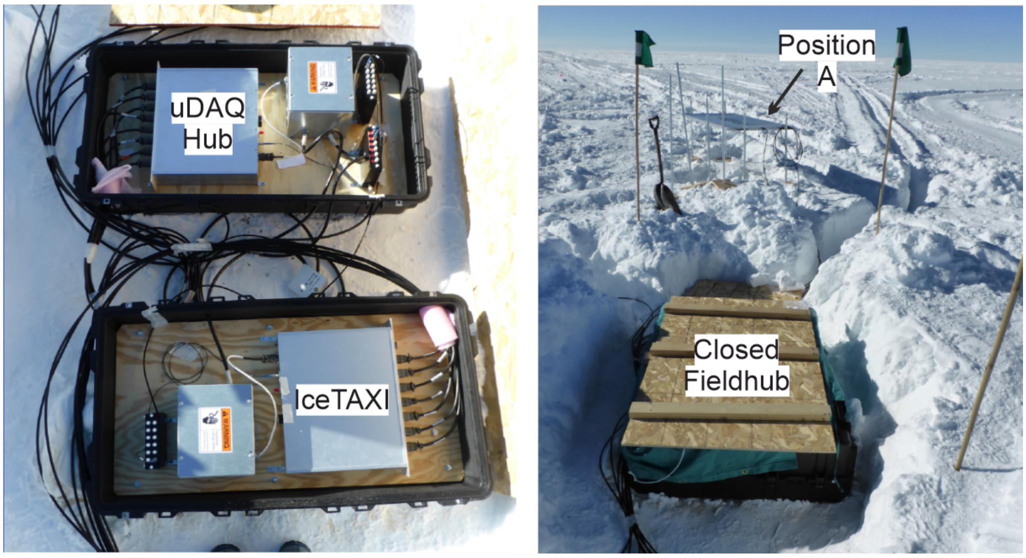

Figure 7.6: Left: The Fieldhub of the first IceScint station. The uDAQ hub and IceTAXI are placed in two separated black crates. Right: The closed fieldhub with additional protective plywood on the top.

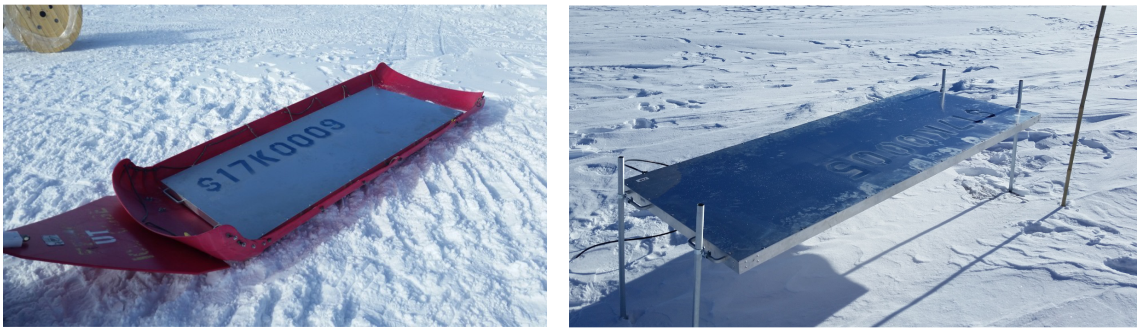

Figure 7.7: Left: The IceScint detectors were driven to their designated positions by a snowmobile with an attached sled. Due to the robust and vibration-resistant design of the detectors (Chapter 6), this method of transport was feasible and substantially speeded up the installation of the IceScint Station. Right: A fully-installed detector.

to four detectors in one day and connect them to IceTAXI. As this was the first IceScint station, every step was first thought about, executed and then evaluated. These steps are largely eliminated for subsequent stations and the deployment and connection of one IceScint station per day and per two technically qualified persons is quite realistic.

Figure 7.7 illustrates the deployment procedure. At each position of the bars, a cavity about half a meter deep was shovelled and the poles including a wooden board with a hole to give additional static stability were inserted. The IceScint detector was then placed on the transport handles in the hangers on the poles and the cavity was shovelled back up and the snow compacted. Since then not a single detector has fallen over or flown away.

Figure 7.9 shows the different alignments of each detector position. In order to compare the two different readout methods of the scintillators, via IceTAXI and via uDAQ, and to investigate the event rates and the charge deposits as a function of the snow coverage, different alignments have been chosen. Three different setups were deployed:

- The IceScint detectors placed on the surface, stacked to each other (Channel 1, 3 and 5).
- Next to each other on poles (Channel 0 and 6) and
- One detector on the surface and the other one hooked in poles (Channel 2 and 4).

The effect of the different alignments on the charge deposit and on the event rates at fixed discriminator threshold at all over the IceScint station is described in Chapters 8 and 9.

Figure 7.8: Left: Taken after the Fieldhub installation. From left to right: Matt Kauer (UW-Madison), Marko Kossatz (DESY), Thomas Huber (KIT/DESY). Right: Inside of the ICL.

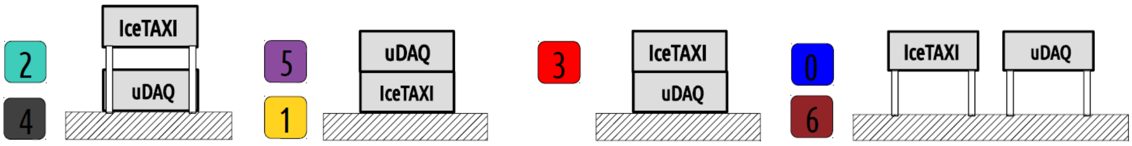

Figure 7.9: Illustration of the different alignments of the detectors. 4 different alignments have been chosen to compare the detector response between the IceTAXI and uDAQ systems. The coloured boxes indicate the IceTAXI channel and the for the IceScint detector specific chosen colour.

7.2 Satellite uplink and first data traffic analysis

After the IceScint detectors and IceTAXI were deployed in the field and the first local commissioning of the station was completed, it was necessary to compile the "EventReciever" system developed for IceTAXI on the computer in the ICL, which was designated for the readout and control of the stations. The data bus system combined with this software allows to switch on or off different data packages, e.g. whether the DRS4 sampled waveforms or the GPS time stamp should be transmitted in the stream. The coding of the bus system and the addresses of the individual data packets are documented and stored at dedicated institutes server. The companion piece, the "EventSender", was already installed on IceTAXI during the weeks of preparation at the PSL.

In order to transfer the data to the north, various cron jobs were set up which can be started and deactivated via SSH. The SSH tunnelling from the north to the IceTAXI system in the field was set up and documented.

To reach IceTAXI, the following SSH tunnelling is necessary:

– `username@msn-sps.icecube.wisc.edu` to
– `username@sps-access.icecube.usap.gov` to
– `pdaq@sdaq01` to
– `root@taxi02` .

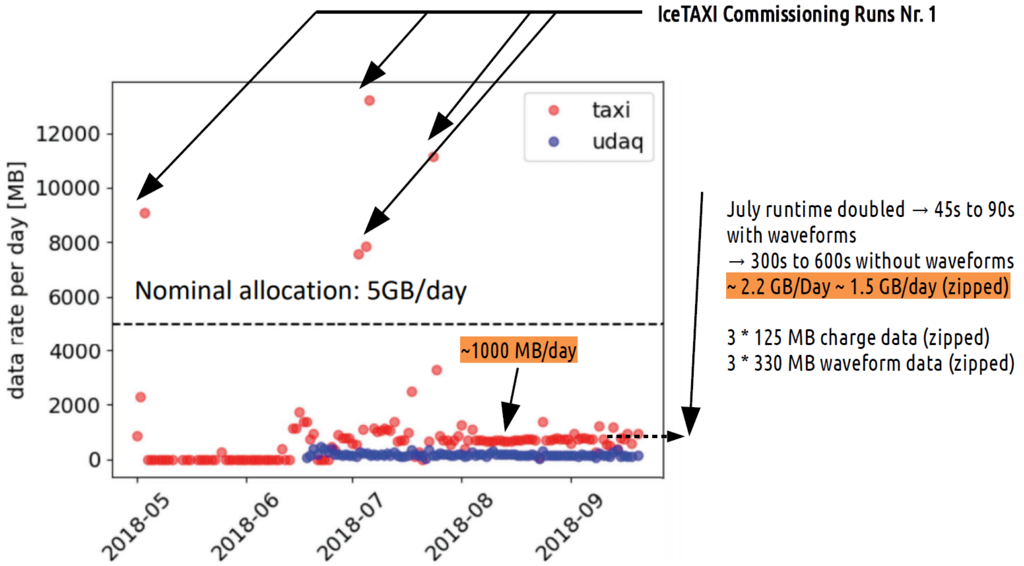

IceTAXI Commissioning Runs Nr. 1

~1000 MB/day

July runtime doubled → 45s to 90s
with waveforms
→ 300s to 600s without waveforms
~ 2.2 GB/Day ~ 1.5 GB/day (zipped)

3 * 125 MB charge data (zipped)
3 * 330 MB waveform data (zipped)

Figure 7.10: Data rate per day for the months May to September 2018 of the IceTAXI (red) and uDAQ (blue) system, edited from [92]. The nominal allocation was $5\frac{GB}{\text{day}}$. For the commissioning runs, more data at single runs were manually transferred. No one complained about that as for short periods it ins in the margins of the collaboration.

For an easier connection and to make it more accessible for more people working with the IceScint data, a simple bash script has been written and distributed to connect to IceTAXI at the South Pole.

Figure 7.10 shows the traffic of the IceTAXI and uDAQ system for the months May to September in the year 2018. Before deployment, a proposal was written to IceCube for a maximum data rate of $5\frac{GB}{\text{day}}$. In order to gradually familiarize and understand the data logistics of IceTAXI and the ICL and the satellite uplink (bottleneck), short daily measurement phases were set up first, with measurement times doubled in July. This is visible in the graph. In addition, the commissioning runs stand out, which were executed manually and were planned in advance, with which modified operating parameters of IceTAXI and the IceScint detectors the most findings and results can be expected.These runs are explained and analysed in detail in Chapters 8 and 9.

After deployment and after returning to KIT, an analysis was made for the data traffic. Figure 7.11 describes how a single data point of Figure 7.10 is created. The different packet types are listed, its address, single and total count and the size in units of Bytes. Next to the listing one high-coincidence air shower event measured by IceTAXI at the Pole is shown in order to showcase the larges packet type, the DRS4 sampling, with the addresses $0x4001$ to $0x43ff$. By enabling the DRS4 sampling, each single adress saves for a 1 ns intervall, which is correlated with the DRS4 single channel capacity of 1 nF (Chapter 5), the ADC counts at a specific time after a signal-over-threshold event. This

```
Size of Taxi data:
1 packet = 18 bytes
Typename  Typeno      Packet Count     Total Count Byte Size
Header    0x1000      1                1           18
Sampling  0x4000      1
          0x4001      1
          ...
          0x43ff      1                1024        18432
Baseline  0x5000      1
          0x5001      1                2           36
Charge    0x6000      1
          0x6001      1                2           36
Timing    0x7000      1                1           18

PixelRate 0x2000      1
          0x2001      1                2           36
WhiteRab  0x8000      1                1           18
GPS       0x9000      1                1           18
Misc      0xe000      1                1           18
```

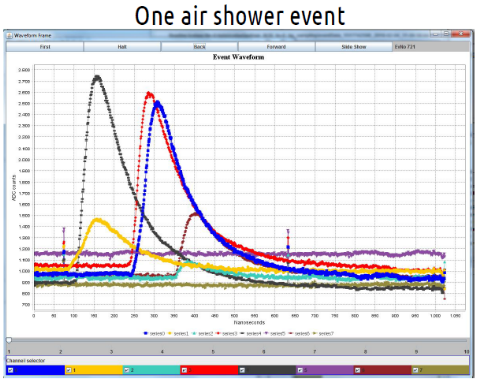

Figure 7.11: Left: Decoding of the datastream of IceTAXI in respect of the packet type and its size. Right: One high-coincidence air shower event measured by IceTAXI at the Pole. It showcases the largest packet type.

means the data transmission for the later analysis of the waveforms of a air-shower event increases by 18432 bytes. By an online waveform amplitude integration via the FPGA onboard of IceTAXI, only the charge and a timestamp is transmitted, which is basically the standard readout of scintillators, used a.e. at KASCADE-Grande or AugerPrime-SSDs.

The total event size with all packets[2] included sums up to:

$$(18 + 1843 + 36 + 36 + 18 + 36 + 18 + 18 + 18)\,\text{bytes} = 18630\,\text{bytes}.$$

The total event size for the same data stream, but the DRS4 waveform packages excluded:

$$(18 + 36 + 36 + 18 + 36 + 18 + 18 + 18)\,\text{bytes} = 198\,\text{bytes}.$$

The ratio of these two event sizes is already showcasing the large increase of data traffic by obtaining at a single signal-over-threshold-event the sampled waveforms. For a larger IceScint array with 31 stations as projected, regular waveform transmission is not feasible. Even with only one station with 7 detectors, the data volume increases rapidly. Therefore, an algorithm was written that filters out interesting events and automatically transmits the waveforms for these events. This algorithm is flexible and can be adapted as a boundary condition, e.g. only events with a detector signal that has reached a sufficiently high signal amplitude or only events with a 7-fold coincidence, i.e. most likely an air shower. Figure 7.12 shows the event rate vs. coincidence at a 12 hours long commissioning run. As higher the coincidence level, therefore more IceScint detectors are seeing a signal-over-threshold in the 1024 ns time frage, as most likely an air shower has been measured. The data volume per day would decrease rapidly by just transmitting the waveform at high coincidence levels.

---

[2] Important note: Including the DRS4 waveform sampling package

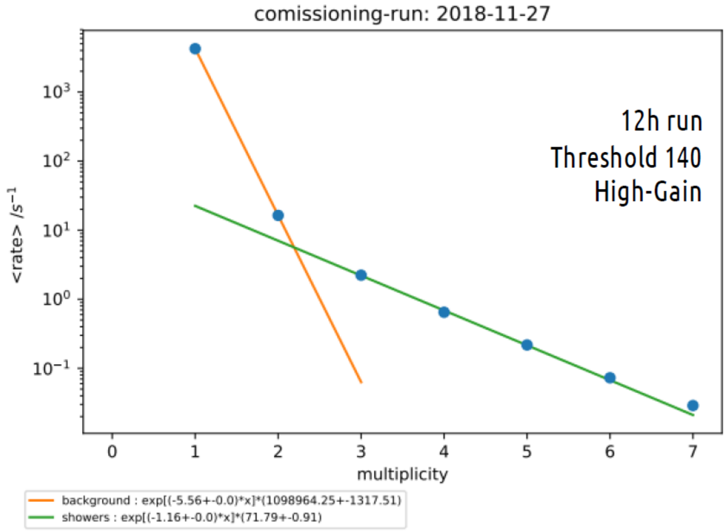

# Coin.	Rate 1/s
3	2.21166
4	0.693326
5	0.217348
6	0.0681356
7	0.0213596

Figure 7.12: Left: Event rate vs detector coincidence level or respectively multiplicity. A high multiplicity corresponds to more signal-over-threshold signals in a single IceScint detector in the 1024 ns time frame. By, as example, just transmitting the waveforms at a 7 times multiplicity, the data volume per (a.e.) day would decreasing rapidly.

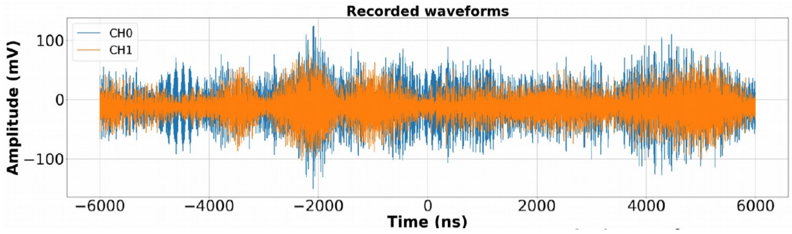

Figure 7.13: Showcasing a recorded waveform of the two polarisations of one SKA radio antenna with the DRS4 and IceTAXI [41].

Starting with the deployment season 2018 the surface extension was extended by antennas [47]. Since the Fourier transformation of the radio traces, which is usually necessary for radio data of air show experiments to deduce interesting events [41], it was decided to use the DRS4 chips and the connected waveform sampling for the radio traces and no longer for the IceScint detectors. Figure 7.13 is showcasing a radio trace, sampled by connecting several DRS4 channels[3] of IceTAXI.

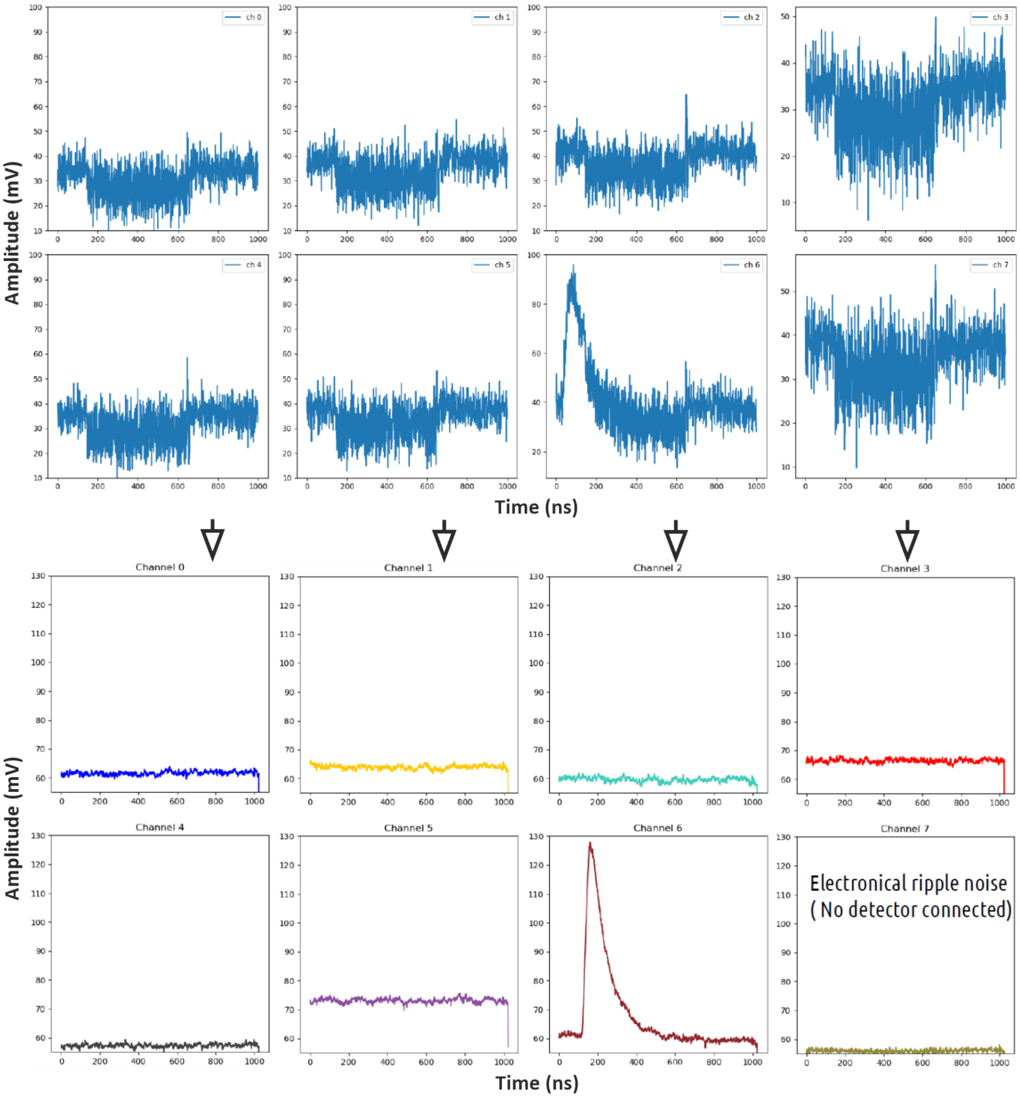

Figure 7.14: DRS4 calibration performed during the first functional test at the South Pole. The top shows the used, but uncalibrated DRS4 chip of IceTAXI and its sampled waveforms received from the SiPMs of the IceScint detectors at a signal-over-threshold MIP event (Channel #6) right after deployment of the station. After the DRS4 calibration process, the bottom shows the DRS4 sampled waveform of each IceScint detector (Channel #0 to #6) and the noise channel #7.

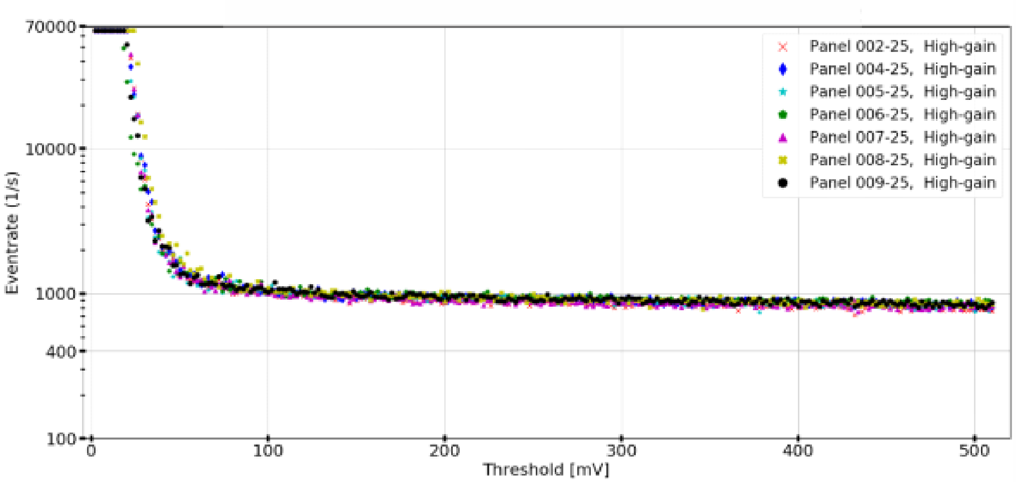

Figure 7.15: Eventrate vs. the set discriminator threshold, measured during the first commissioning runs at the South Pole. Plotted is each IceScint detector of the station. At a higher threshold voltage, only MIP events are registered as event. If the threshold is set too low (< 50 mV) electronic noise triggers IceTAXI, too.

7.3 First functional test runs during the South Pole stay

In order to check the functionality of the IceScint Station and thus the set operating parameters, it has been found that a threshold scan quickly reveals any problems or whether the station is measuring correctly. Increasing the discriminator threshold voltage onboard of IceTAXI will raise the required value of the SiPM amplitude, which will generate a signal-over-threshold trigger at IceTAXI and thus store an event (Chapter 5). If the threshold is set low, the event rate increases and if the threshold is high, the event rate decreases. In the former case (< 50 mV), electronic noise also triggers, and in the latter case, only SiPM amplitudes generated by a MIP in the detector will trigger. This can be seen in Figure 7.15. For this figure, a bash script has been written which automaticity increases the threshold, is recording the eventrate for 30 seconds for all detectors and which is saving the mean of measured event rates.

First, it can be seen that every detector behaves identical, which is showcasing the great uniformity of the IceScint detectors and its whole readout chain. At higher thresholds, the rate stabilizes at around 1000 Hz, which is in good agreement with the expected MIP flux at 3000 m altitude and in a scintillator volume of $1.5\,\mathrm{m}^2 \cdot 0.01\,\mathrm{m}$ (Chapter 2), In Figure 7.16 another threshold scan is shown. It shows one IceScint detector operated once

---

[3] In order to increase track length.

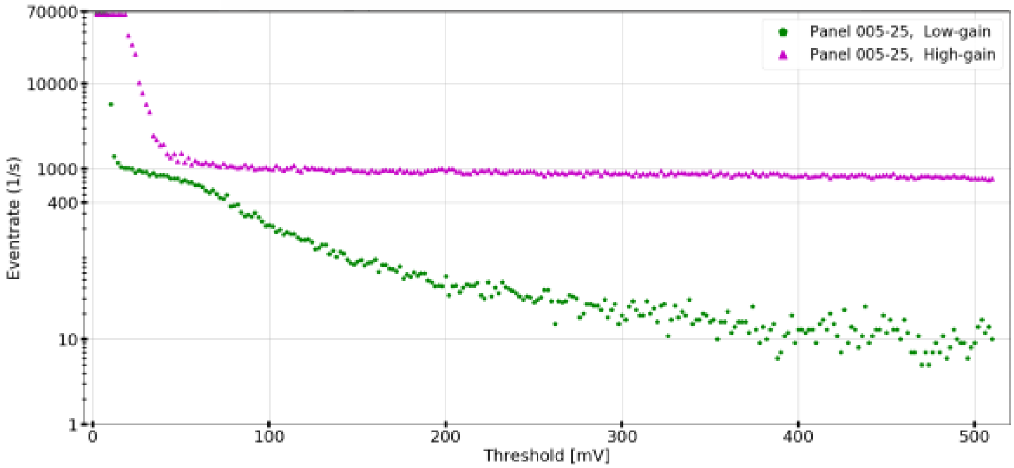

Figure 7.16: Eventrate vs. the set discriminator threshold, measured during the first commissioning runs at the South Pole. Plotted is one IceScint detector in the two Op-Amp modes High-Gain and Low-Gain.

in High-Gain and Low-Gain. At the low-Gain Channel, the SiPM signal is only amplified by a factor of 1,1. At higher threshold, the rate drops faster then by operating the IceScint detector in High-Gain, since not that much SiPM signal amplitudes are reaching the discriminator level. The larger scattering at higher threshold voltages is due to the few events where the SiPM amplitude is over the threshold.

One of the last steps of being sure that the first IceScint station was operating was to check if the detectors are seeing MIPs. Charge histograms were generated to verify this. The EventSender and the EventReciever software was used to send event packets with DRS4 sampling switched on to the sDAQ machine and then the waveforms are integrated with a Python script.

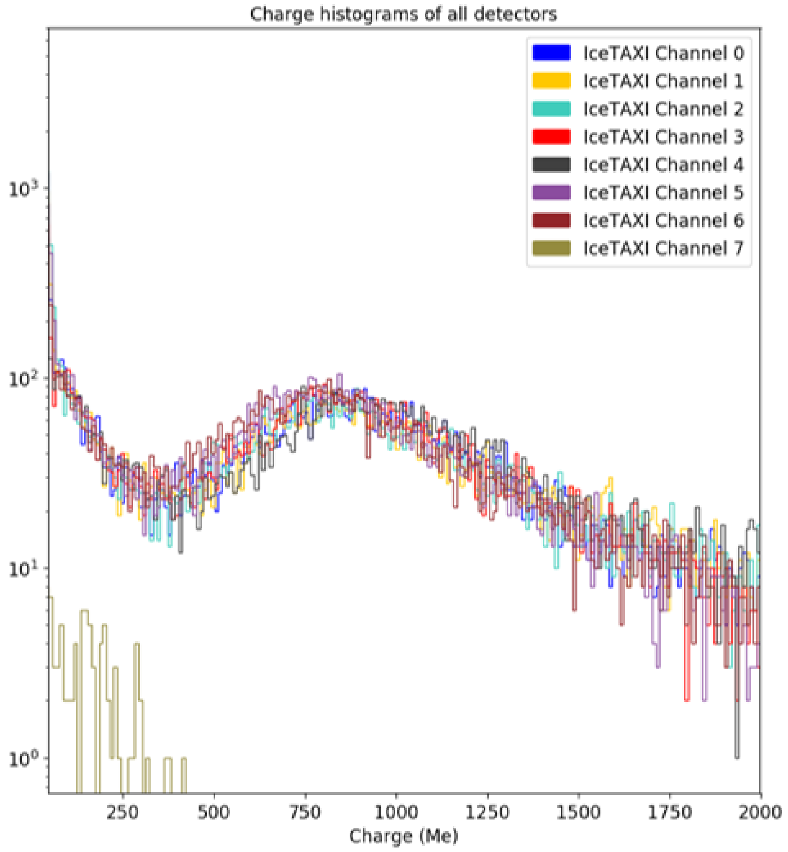

Figure 7.17: "Hello world" charge histogram of the first IceScint station at the South Pole. This was one of the first generated charge histogram out of the IceScint station at the South Pole during the first commissioning phase. The integration has been done "offline" via manually integrating the DRS4 sampled waveforms. The noise and the P.E. peaks can be found at low charges, followed by the "valleys" and afterwards at around 750 Me the MIP peaks arises. The nearly identical charge deposit in each detector is showcasing the uniformity of the IceScint detectors with its whole readout chain.

One of the first[4] charge histograms can be seen in Figure 7.17. The noise and the P.E. peaks can be found at low charges, followed by the "valleys" and afterwards at around 750 Me the MIP peaks arises. The nearly identical charge deposit in each detector is showcasing the great uniformity of the IceScint detectors with its whole readout chain in respect of the fiber efficiency, the identical bending radius and therefore the constant reflection coefficient of the fiber, the optical coupling with its constant distance to the SiPM surface, the uniformity of the SiPM photosensitive surface, the working temperature-control-loop to stabilize the gain, the pre-measured electronics i.e. the Op-Amps at the readout board, the less noise catching 70 m double-ended differential SiPM signal transmission from IceScint to IceTAXI and the general intactness of the detectors after the long and bumpy transport to the South Pole as well as the bumpy transport of the detectors via snowmobile and sleds to their positions in the hexagonal alignment.

---

[4] The "Hello World" charge histogram

8 Commissioning and on-site calibration of IceScint

This Chapter describes the calibration of the IceTAXI DAQ using measurement data from the station at the South Pole and the local IceScint station clone at KIT. The station is integrated in a hybrid array consisting of Mini-KASCADE and radio antennas. The procedure of daily runs and commissioning runs are discussed in detail as well as the results of the initial analysis. A function for fitting the charge histograms generated by the IceScint Station and the MIP peak contained therein was determined and compared with fit functions used for data of the IceTop Cherenkov tanks.

8.1 Hybrid array at KIT

The hybrid array is located at the Campus North of KIT, in and around a available barrack (Figure 8.1). Eight IceScint[1] panels and 12 detectors[2] of Mini-KASCADE (Chapter 2) are in use. In addition, for the radio enhancement of IceTop, SKA antennas are placed in order to integrate the antennas into the IceTAXI DAQ chain and to perform prototyping measurements [41]. For reading out the Mini-KASCADE detectors, the KASCADE electronics KAFE[3] [93] and a specific for Mini-KASCADE rewritten software is in use. Mini-KASCADE provides besides the trigger signal a calculation of the center-of-gravity of the shower core and the shower arrival direction in polar coordinates [87, 88]. The DAQ of the IceScint detectors is by IceTAXI which is an exact copy of the deployed first IceScint station at the South Pole, including the 70m long cable length between IceScint and IceTAXI.

This novel experimental setup allows detailed combined studies of IceScint, IceTAXI and the radio antennas, like the reconstruction accuracy and center-of-gravity location in respect of Mini-KASCADE as well known detectors and DAQ. Since the data connection to the Amundsen-Scott Station, and thus to the ICL, is very limited or even partially extremely limited depending on the satellite uplink availability in terms of bandwidth and time , the cloned IceScint station at the Hybrid Array can be used to perform bugfixing, test new firmware and obtain more valid and detailed information about the detector and IceTAXI response than would be possible with only one station at the South Pole. This was used inventively during the commissioning phase after the deployment.

---

[1] 7x with 25 μm and one with 50 μm pitch SiPM readout

[2] 2 detectors each in one aluminium housing

[3] KASCADE Array Front-End Electronic

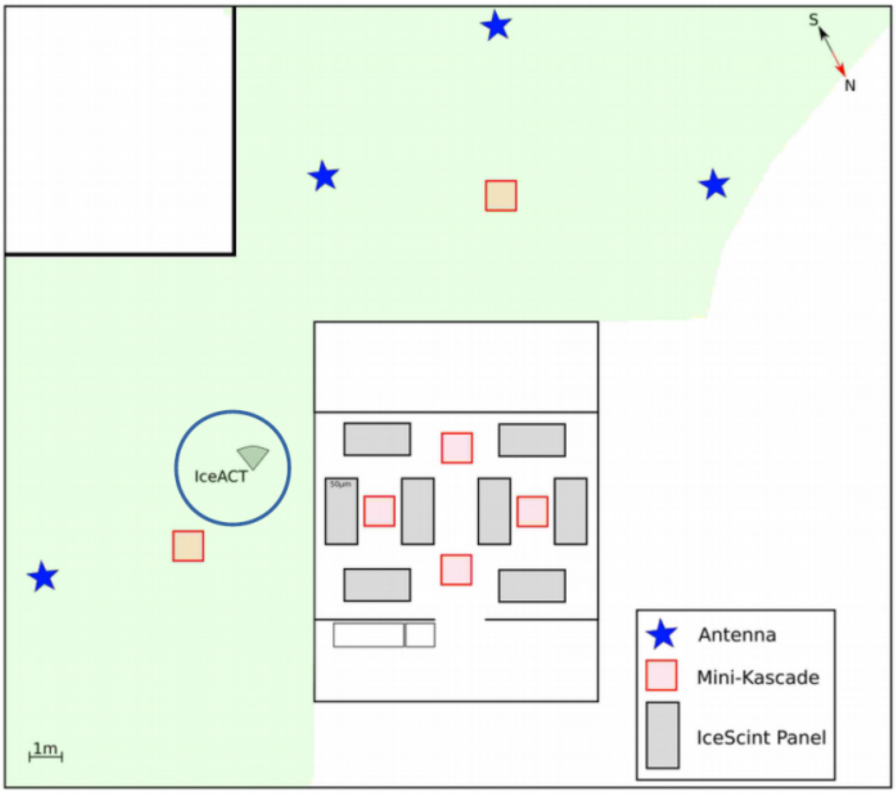

Figure 8.1: Left: Sketch of the hybrid array at KIT as in October 2018 [41]. The IceScint clone station (boxes filled in Grey) and a part of Mini-KASCADE (squared red boxes) are placed inside a barrack. The antennas (blue stars) are placed around the barrack (modified). For the IceCube deployment season 2018/19 three of them were shipped to the South Pole. For a short time also the IceACT telescope was installed in this environment for specific tests.

8.2 IceARM and IceTAXI calibration

In this subchapter, the calibration of the scintillator readout and the IceTAXI DAQ will be explained and shown. Since for future upgrade and enhancements, like with radio antennas, the TAXI DAQ system will further be used, the focus aims on the results of the behaviour of discriminator threshold, the trigger timing, the DRS4 and the ADC. In addition, the overall amplification of the IceARM plus IceTAXI system will be shown. Most of the calibration process and analysis was performed in terms of the supervision of the bachelor thesis of Eugen Raspopin. The measurements were done at the hybrid array at KIT and part of the the setup can be seen in Figure 8.3. On the 8 channels of IceTAXI 7 IceScint detectors and one pulse generator were connected. In order to calibrate each channel of IceTAXI, the pulse generator was permuted between each channel. The measurements and analysis shown above are exemplary for one channel.

Unless otherwise stated, the incoming signal shape used to calibrate the IceARM and IceTAXI is pictured in Figure 8.4. The amplitude, pulse width and frequency were, as long at is was possible for the specific measurement, chosen in a dynamic range of the

Figure 8.2: Left: Inside the barrack. Visible are eight IceScint detectors and four Mini-KASCADE detector housings with 2 detectors each. The DAQ, IceTAXI for IceScint and KAFE for Mini-KASCADE, is in another room of the barrack, visible behind the open door top left left of the picture. Right: Photo of one of the SKA antennas in front of the barrack with the mechanical structure as used in season 2018/19.

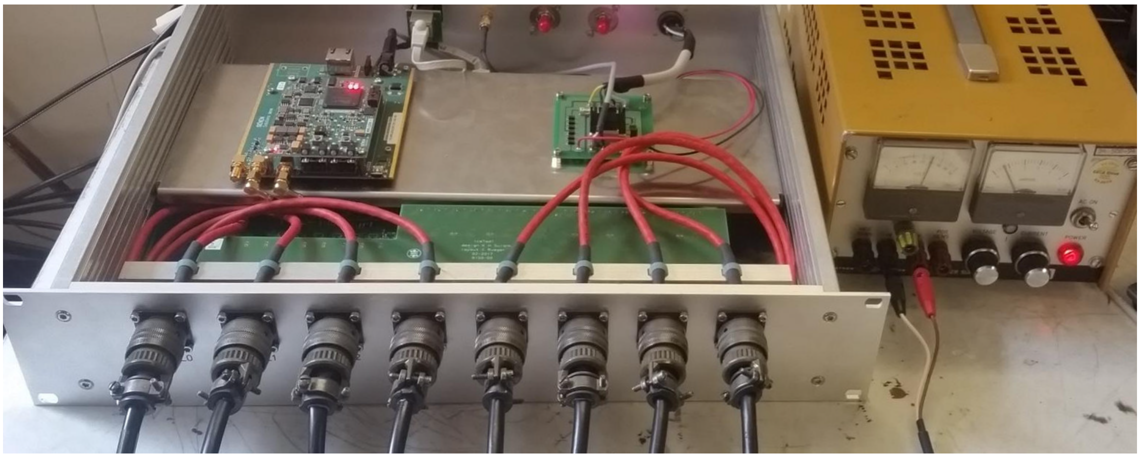

Figure 8.3: IceTAXI DAQ in its housing at the Hybrid array at KIT. 8 channels, connected with 7 scintillation detectors and one modified cable for a pulse generator input. The White Rabbit Node can be seen on the left side, a network which is used for timing, synchronization between different stations. The power supply is located on the right-hand side of IceTAXI. The main board of IceTAXI is below the aluminum holder and the IceTAD board. An external power supply for operating IceTAXI can be seen at the right.

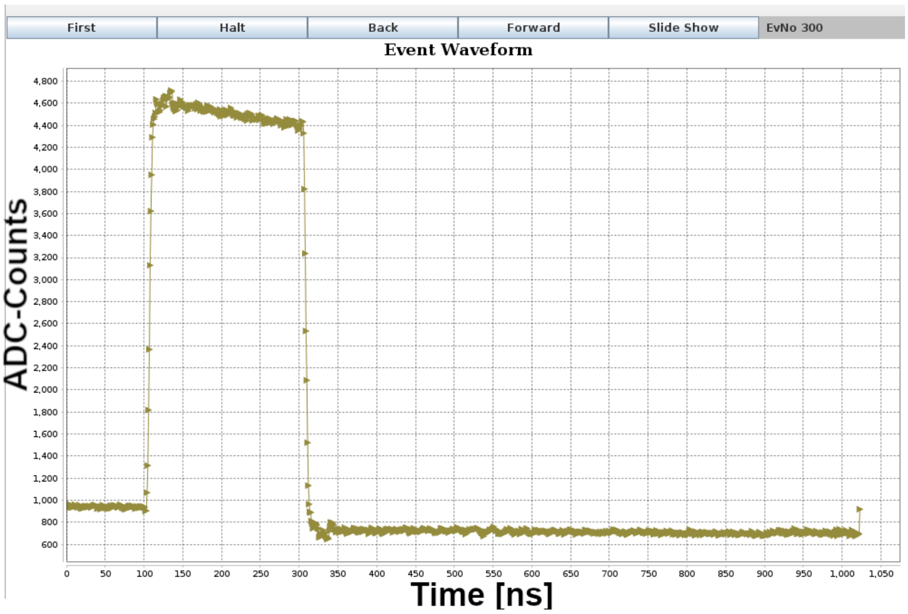

Figure 8.4: Signal form of the input pulse. In this example, the amplitude of the pulse generator signal is 200 mV and the pulse width 200 ns. Unless otherwise stated, this waveform shape was used to calibrate IceARM and IceTAXI. Visible on the signal shape is that the baseline and the square-wave pulse are lowered at the same time. The reason for this is an AC coupling, described in the text.

incoming SiPM signals. Also visible in Figure 8.4 is that the symmetrical square wave signal input is amplitude shifted between the increasing flank and the decreasing flank of the signal. This is due to the AC coupling of the used signal transmission method.

With an AC-coupled signal, the coupling capacitor stores the sum mean values of the signal . The figure shows the difference in bias voltage between a sine wave and a square wave or pulse signal, both being AC-coupled and having a ground related load resistance. At the input both signals vary by the same voltage. After the capacitor there is a difference: The signal varies by the amplitude while the pulse signal varies by a voltage that depends on the duty cycle. How strong it varies depends on the frequency of the signal and on the time constants of the capacitor capacitance C and the loop resistance R, which is in most cases the input resistance i.e. the whole amplifier.

Therefore, AC coupling requires a wider dynamic range for a square wave signal with variable duty cycle than for an equivalent sinusoidal signal. For this reason, all amplifiers are DC-coupled for pulse applications to maintain the dynamic range. SiPM signals from a scintillator behaves like a pulse signal and is therefore best DC-coupled. Nevertheless, signals must be AC-coupled as soon as two parts of a system have separate power supplies. A DC connection of two power supplies is dangerous and normally prohibited by regulations.

8.2.1 jTAXI analysis framework

jTAXI is a Java framework to visualize, analyze and debug the IceTAXI DAQ with recorded (sample) events offline or online by connection directly to the Linux system embedded in IceTAXI. It was developed and self-debugged together with A. Weindl [94]. Next to the easier access of the data from the IceTAXI DAQ, it was used to have a quick look into the South Pole data files and in addition, to give the original developer of the IceTAXI system in DESY Zeuthen a quick feedback on new firmware updates. For the commissioning runs it was used to cross check the set parameters of IceTAXI and IceARM in order to ensure valid IceScint data without wasting too much satellite link time and, in specific, bandwidth. It is up to now in steady development to visualize and analyze the radio antenna data, too.

The key features of jTAXI are:

- Executable in Windows and Linux, operatable via an graphical user-interface (GUI) or command line.
- Designed for commissioning and debugging the IceTAXI DAQ with over 80 classes, still in development.
- Configurable by a xml configuration file. Version control via apache subversion (SVN) control.
- Able to process offline and online data from IceTAXI, direct-connect realized via jermoq package to IceTAXI.
- Adjustable to different IceTAXI data streams, depending on the firmware and the connected detector system.

The graphical user interface of jTAXI can be seen in Figure 8.5. It provides several save options which can be seen as “export option” for students as an easier access to the IceTAXI data format. Next to the information about the current signal-over-threshold event, it gives several options to visualize one specific event or a selection of several events at one, like with the option to display the charge histogram.

jTAXI can be, among others, used to:

- Debug the IceTAXI data stream and display event and monitoring information.
- Display the waveform sampled by the DRS4 chip, showing event and arrival time distribution with the jfreechart package.
- Loop manually Trough (interesting) buffered events.
- Performing several analysis (among others determine the signal baseline, integrate waveform, create charge histograms, show arrival direction and statistics like the array trigger multiplicity for selected events).
- Calibrate the ADCs (Chapter 8.2.2), do an event selection on the charge (or ADC value).
- Save event selection in ASCII format
- Adjustable to do all above with different detector systems and different array alignments and positioning (coordinate files).

For future ugrades of the jTAXI framework the development is focussed on the visualisation and progressing abilities of radio traces, since the DRS4 onboard IceTAXI will

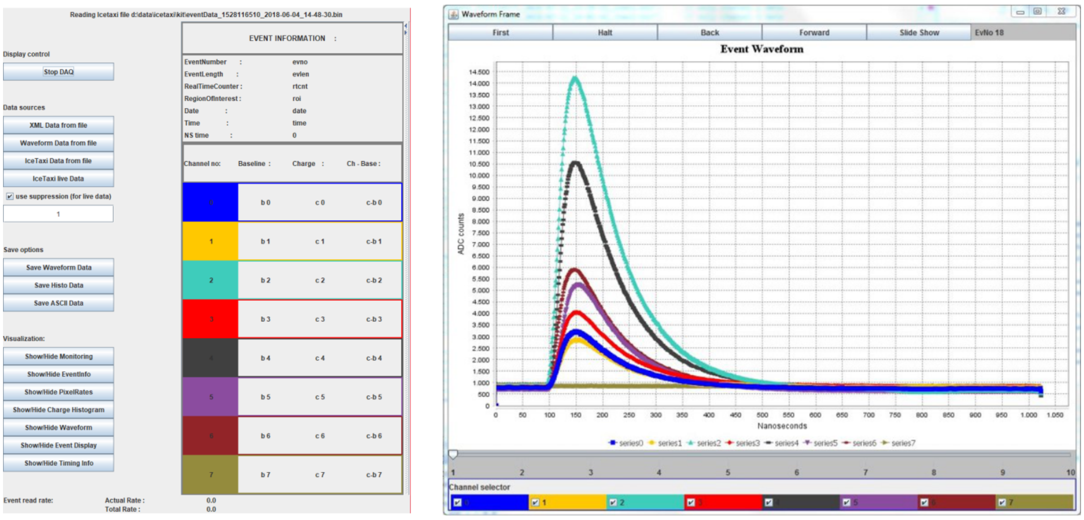

Reading Icetaxi file d:\data\icetaxi\kit\eventData_1528116510_2018-06-04_14-48-30.bin

EVENT INFORMATION :

EventNumber : evno
EventLength : evlen
RealTimeCounter : rtcnt
RegionOfInterest : roi
Date : date
Time : time
NS time : 0

☑ use suppression (for live data)

1

Channel no:	Baseline :	Charge :	Ch - Base :
0	b 0	c 0	c-b 0
1	b 1	c 1	c-b 1
2	b 2	c 2	c-b 2
3	b 3	c 3	c-b 3
4	b 4	c 4	c-b 4
5	b 5	c 5	c-b 5
6	b 6	c 6	c-b 6
7	b 7	c 7	c-b 7

Event read rate: Actual Rate : 0.0
Total Rate : 0.0

Figure 8.5: Left: Main control panel of the graphical user-interface of the jTAXI. The different options and displays can be shown by clicking on the the items in the menu on the left. The raw information about the actual event of the station is shown on the right. The top shows the event identification numbers, in color the 8 channels of IceTAXI, or, respectively, the 7 IceScint detectors. Right: A high coincidence event of an air-shower, measured with the IceScint station at the South Pole. The Y-axis shows the ADC counts, so the sampled voltage of each SiPM peak of the IceScint detectors and the X-axis the time in Nanoseconds. The air-shower plane axis of this event is most likely vertical to the South Pole surface, due to the small time difference between the increasing flanks of two detectors.

most likely used for the read out and sampling of the radio antennas of the stations. This includes the implementation of the DRS4 cascading mode, used for sampling the radio traces, radio calibration methods, a peak finding and fitting functionality and the ability to Fast-Fourier-Transform (FFT) radio traces. An institutes internal SVN repository is provided.

8.2.2 ADC and discriminator calibration via pulse generator

The underlying idea of the measurements was to feed a well-defined reference pulse (Figure 8.6), which in its amplitude, frequency and pulse width approximately corresponds to the pre-amplified SiPM signal, into the whole IceARM-IceTAXI DAQ chain in order to analyse the sampled and integrated signal.

This enables conclusions about the operational functionality of the individual IceTAXI channels, the limitations of the DRS4 sampling, the linearity and the saturation of the ADCs. In addition, the maximum possible event rate that IceTAXI can process can be examined. The accuracy and scaling of the discriminator circuits are also determined by measurements with a reference input signal.

In addition, the time stability of the trigger is examined. This measurement is crucial for the accuracy of reconstruction of the air shower and becomes increasingly important when the IceScint Station is correlated with IceTop, radio antennas or, as a large new surface array, with other IceScint Stations.

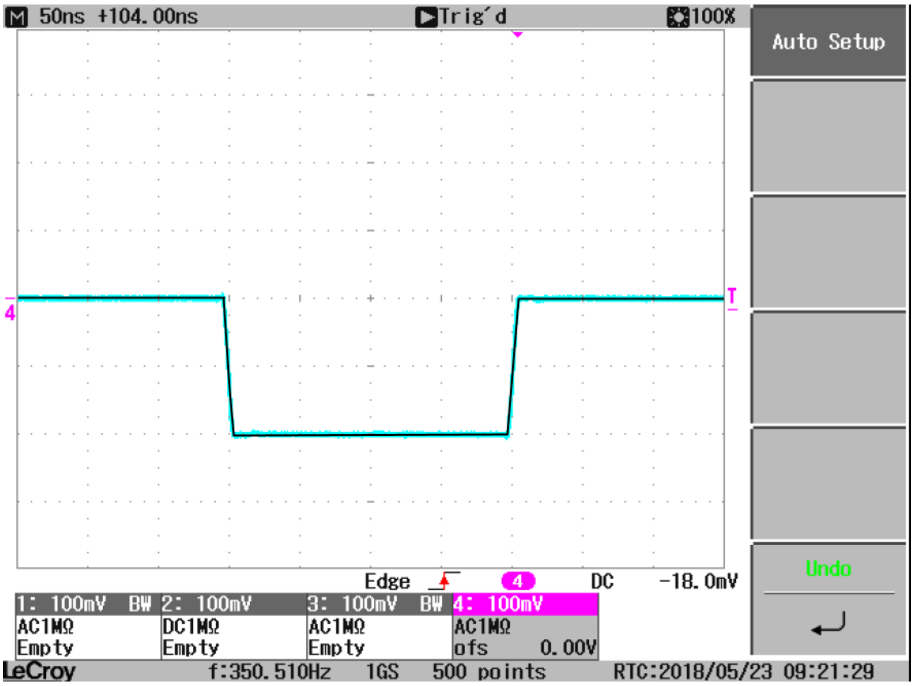

50ns +104.00ns
Trig´d
100%
Edge 4 DC −18.0mV
1: 100mV BW AC1MΩ Empty
2: 100mV DC1MΩ Empty
3: 100mV BW AC1MΩ Empty
4: 100mV AC1MΩ ofs 0.00V
f:350.510Hz 1GS 500 points
RTC:2018/05/23 09:21:29

Figure 8.6: Screenshot of an exemplary reference pulse used for the following measurements, generated with an Agilent 81101A pulser. Its amplitude, pulse width and frequency was chosen to be SiPM like. Its frequency as it is expected for the MIP rate at South Pole conditions measured by an IceScint detector.

The measurement setup for analysing the discriminator threshold and calibrating the station's ADC at KIT is shown as block diagram in Figure 8.7. The red framed segments in the diagram correspond to components placed on IceTAXI. A pulse generator[4] is used for the input signal.

For each IceTAXI channel a calibration was done to distinguish the behaviour of the incoming signal amplitude and its corresponding ADC-Counts (Figure 8.8). These investigations give a conclusion on the linearity of the ADCs, their real saturation values and thus the dynamic range, with regard to the maximum possible ADC values to be assigned before they go into saturation. The slopes in the linear transformation range of incoming amplitude and ADC values are used to adjust the scripts for the analysis of the charge generation per channel from a signal over threshold event.

In Figure 8.9 the maximum ADC value of 4 IceTAXI input channels is exemplary shown. The measurement (16702.34 ± 54.33) is in good agreement to the maximal values of the used 14 bit ADCs[5]. The detailed quality cut for the approximated stop of the linear region of the ADC can be found in [95].

Figure 8.10 shows the pixel rate as a function of the threshold. The pixel rate is in good approximation, down to single losses per second, equivalent to the (MIP-) event rate transmitted from the IceScint detectors to IceTAXI and passing the discriminator threshold set at the start of the measurement. The pixel rate behaves like expected. It

---

[4] Agilent 81101A 50 MHz

[5] $14^2 = 16384$

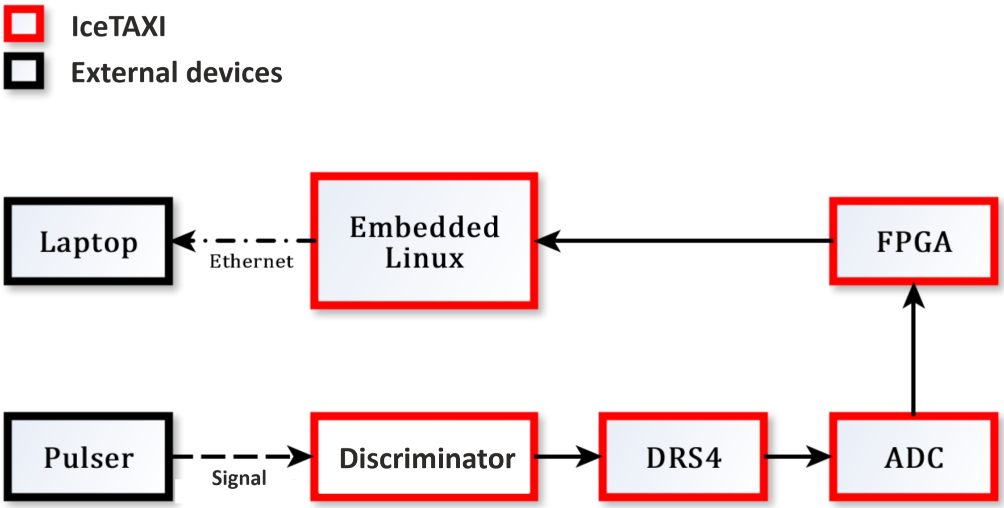

Figure 8.7: Block diagram for the analysis of the discriminator threshold and ADC calibration per channel. The analog signal is fed-in using the pulse generator. The signal is processed and digitized in the IceTAXI data acquisition system. The data can then be transmitted and evaluated via Ethernet. The exact processing of the signal with IceTAXI is described in Chapter 5.

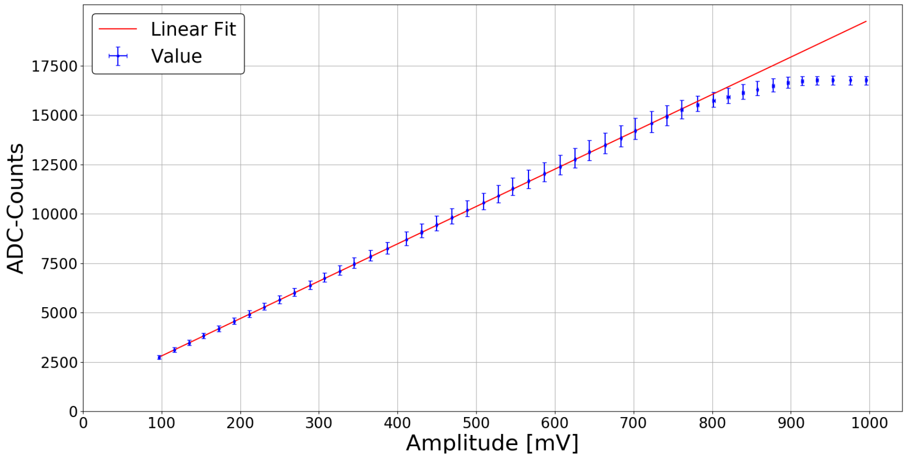

Figure 8.8: ADC values plotted versus the analog signal of the pulse generator for Channel 0. At 800 mV the saturation of the ADC starts. The IceTAXI option of the Op-Amps choice is set to high gain. The linearity is proven with a gradient of $(18.91 \pm 0.02)\,\frac{1}{\mathrm{mV}}$ and the intersection of the ordinate is 910.87 ± 6.57.

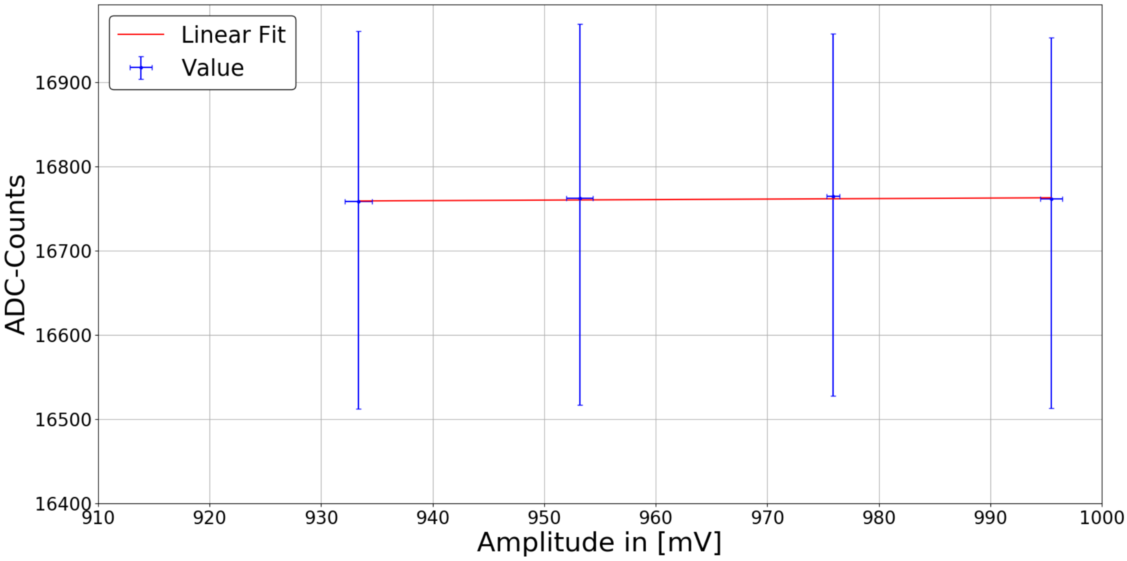

Figure 8.9: Consideration of the maximum ADC value at which saturation of the ADC occurs. The last four points of Figure 8.8 are used, fitted which a linear regression. The intersection of the ordinate is 16702.34 ± 54.33.

is noticeable that the pixel rate increases close to the threshold set by the discriminator voltage, the formation of a plateau. Close to the threshold voltage, the signal fluctuates due to electronic high-frequency interference signals[6], which is raised to a level close to the threshold voltage.

8.2.3 ADC and discriminator calibration via IceARM input

This measurement equals the setup described before, beside of that the IceARM electronic, which is usually inside of the IceScint detectors, was included into the readout chain (Figure 8.11) in order to cross-check if the IceARM signal and its GP-board signal modulation changes the behaviour of the characteristics. In addition, this setup equals the whole DAQ chain at the South Pole IceScint station, whereby Setction 8.2.2. is for detailed interest for the connection of radio antennas to the input signals of IceTAXI. For this purpose one IceARM was electronical adjusted so that, instead of a SiPM signal, a pulser can be connected to the Adapter board. The measurement procedure was the same like without IceARM and the detailed results can be found in [95].

Figure 8.12 shows how the incoming pulser signal (Figure 8.6) is modulated by the GP-board. The signal shape of the pulse is viewed with the jTAXI software. The amplitude of the pulse generator at high gain is 400 mV and the pulse width is 200 ns. The pulse generator is connected to input the High-Gain input of the GP-board of IceARM.

Figures 8.13, 8.14, 8.15 show, exemplary, for the different IceTAXI input channels the results of the calibration. The general behaviour follows the results of the measurement described in the last Subchapter 8.2.2.

As one main result of these calibration measurements, Figure 8.16 shows exemplary for

---

[6] Therefore: Noise.

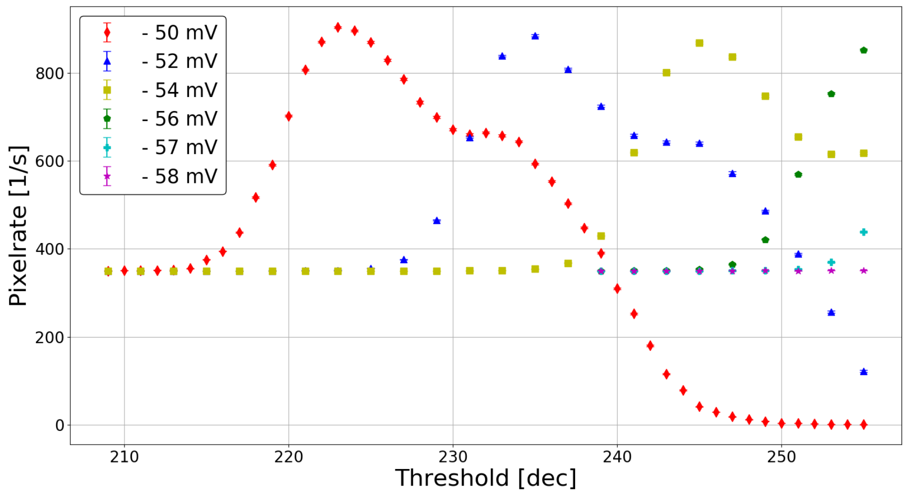

Figure 8.10: Pixel rate as a function of the threshold. The threshold is dimensionless and makes it clear that the size is given in decimal. The pixel rate rises and forms a plateau before reaching zero. The increase is caused by high-frequency interference signals, which are related to the amplitude of the superimposed square-wave pulse [95].

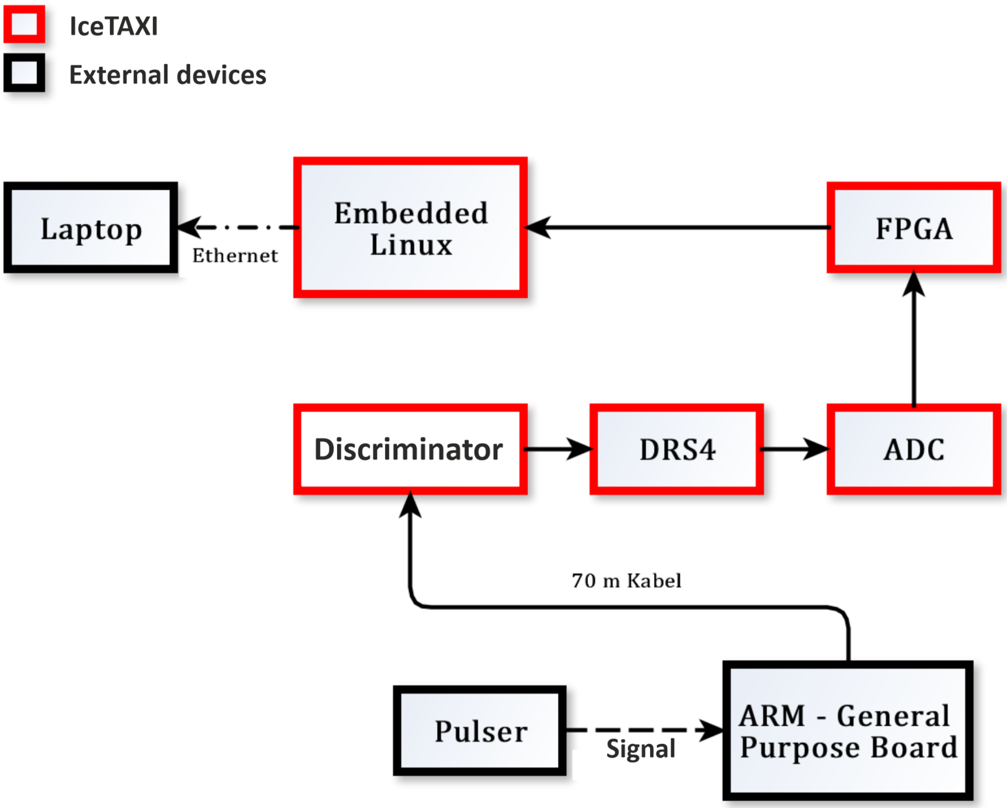

Figure 8.11: Block diagram for the calibration of the discriminator threshold and the ADC linearity behavior included the Analog Readout Module (ARM), used for IceScint.

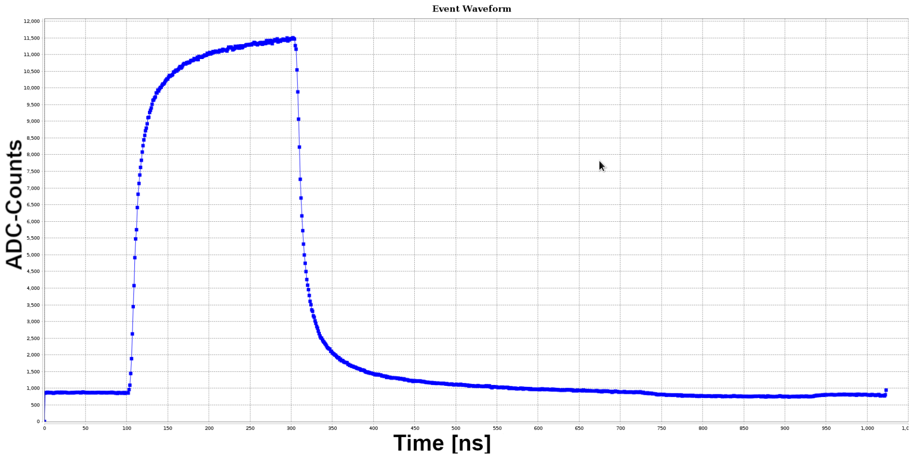

Figure 8.12: Signal shape of the input pulse, viewed with the jTAXI program. The amplitude of the pulse generator at high gain is 400 mV and the pulse width is 200 ns. The pulse generator is connected to input HG of the GP-Board.

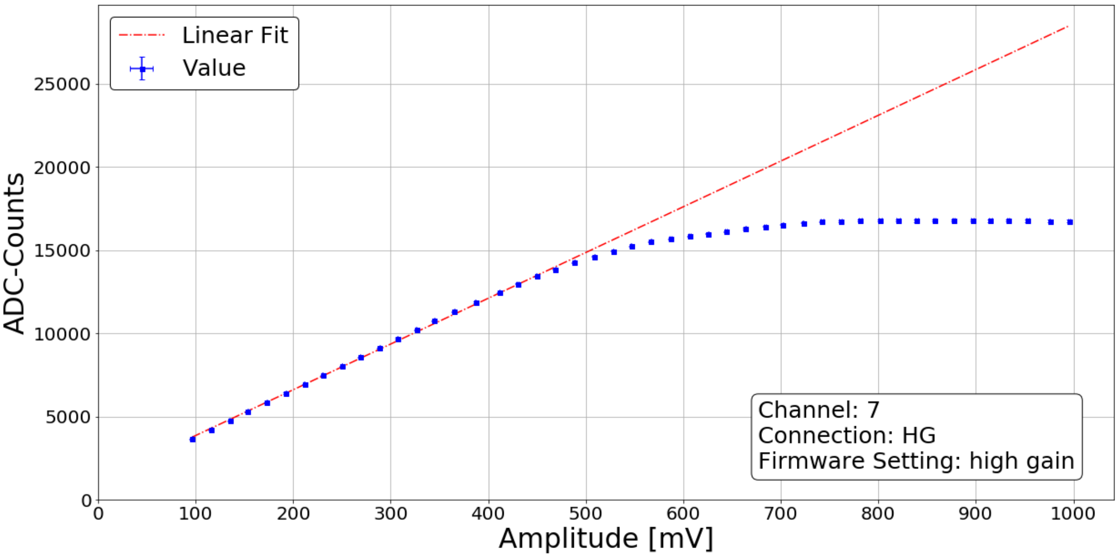

Figure 8.13: Linear trend and the saturation range of the ADC values for channel 7 of IceTAXI, plotted versus the analog signal of the pulse generator connected to the HG of the GPB. The option of the IceTAXI firmware is set to high gain. The selected range for linear regression is (100 - 500) mV. The gradient is (27.49 ± 0.19) $\frac{1}{\mathrm{mV}}$ and the intersection of the ordinates is 1102.48 ± 61.28 [95]

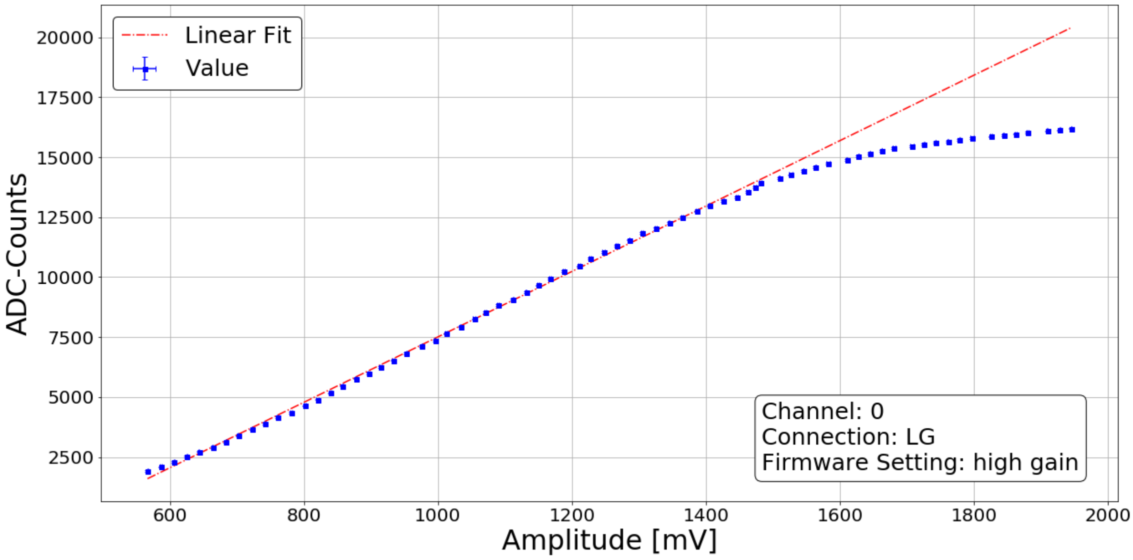

Figure 8.14: For this test the physical connection of the Low-Gain socket on the readout board was mixed with the firmware setting for High-Gain to exclude conflicts and issues in the firmware channel assignment. The fit parameters ((580 - 1500) mV, (13.64 ± 0.07) $\frac{1}{\mathrm{mV}}$, -6133.39 ± 69.81) did not change compared to the normal setup with Low-Gain socket to Low-Gain firmware [95].

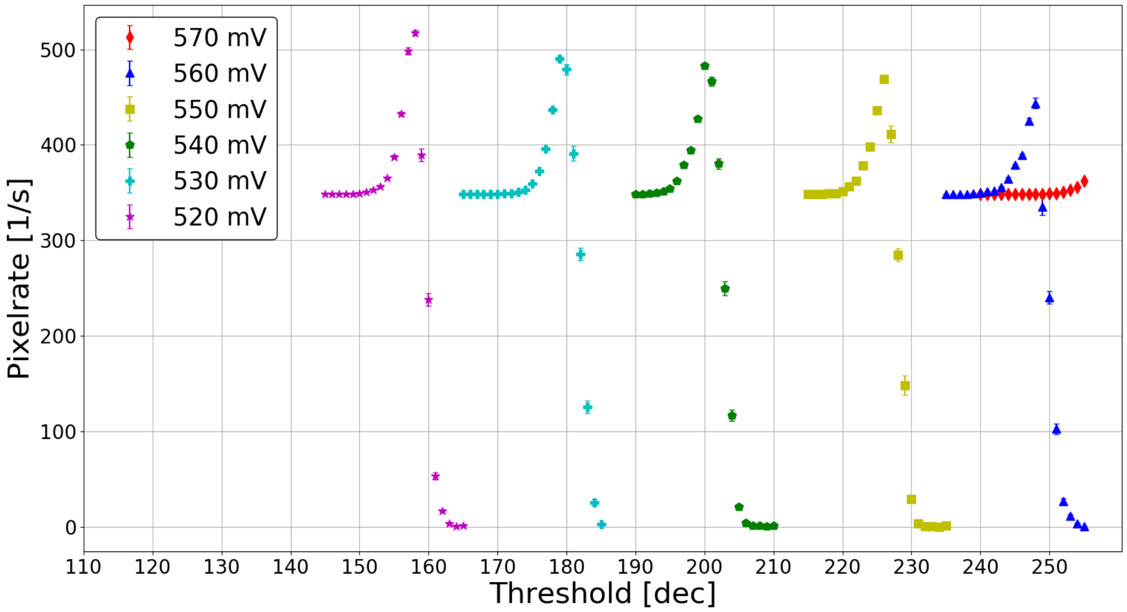

Figure 8.15: Pixel rate trend as a function of the threshold in the voltage range of (520 - 570) mV. The pulse generator was connected to the low gain and the firmware option of IceTAXI was set to high gain. Like seen in the measurement without ARM, the values of the maxima decrease with the height of the amplitude.

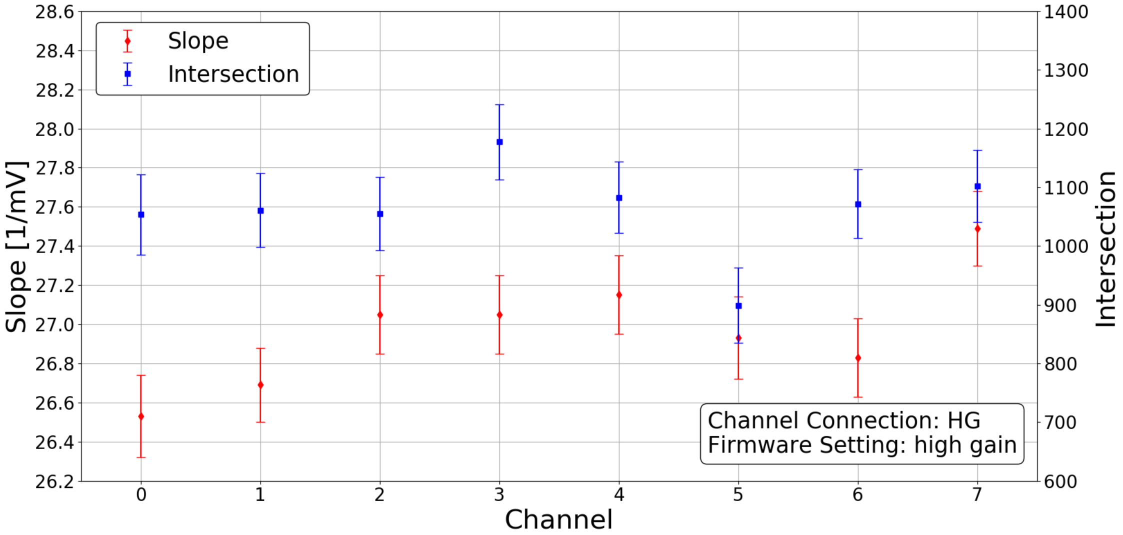

Figure 8.16: Comparison of slopes and intersections at the ordinate for all channels of IceTAXI. The pulse generator is connected to the HG of the GPB and the option of the IceTAXI firmware is set to high gain.

the High-Gain setup of the IceScint station at the Hybrid Array a comparison of the slops and intersections at the ordinate for all 8 input channels. These values are used in the analysis tools, described in Chapter 6 and for the analysis of the air shower reconstruction and IceScint detectors performance which are discussed in Chapter 9.

8.2.4 Readout time behaviour of IceTAXI

In this measurement, the behaviour of the readout time and thus the trigger time was investigated. Using jTAXI, it was observed at what point in time the pulse is completely mapped as a function of frequency. The difference to the previously presented calibration measurements is that the frequency of the reference pulse was varied.

The threshold of the discriminators is set to the fixed decimal value of 84. At this value, the frequency of the pulse generator matches the rate of the signals registered on the IceTAXI. The amplitude at the pulse generator is 200mV. The entire measurement series was performed on channel 7 of IceTAXI.

The data flow was written to a ".bin" file with the "eventReceiver" for 20 seconds at a fixed frequency. Afterwards, 10 events at each fixed frequency were examined. The time at which the ADC value begins to rise to the square pulse is noted. It was found an issue with the stability of the trigger time at, compared to the expected MIP-rate, high income signal rates. Figure 8.17 shows exemplary that the trigger time is not stable to a fixed value. Indeed, it varies over the whole 1024 ns region. This issue could be solved by a firmware bugfix.

After the firmware upgrade of IceTAXI the trigger time dependency of the signal rate was measured again (Figure 8.18). Over the whole range IceTAXI was able to set the signal start after it passes the signal-over-threshold trigger at one specific time. A detailed discussion and the analysis of systematic uncertainty can be found in [95].

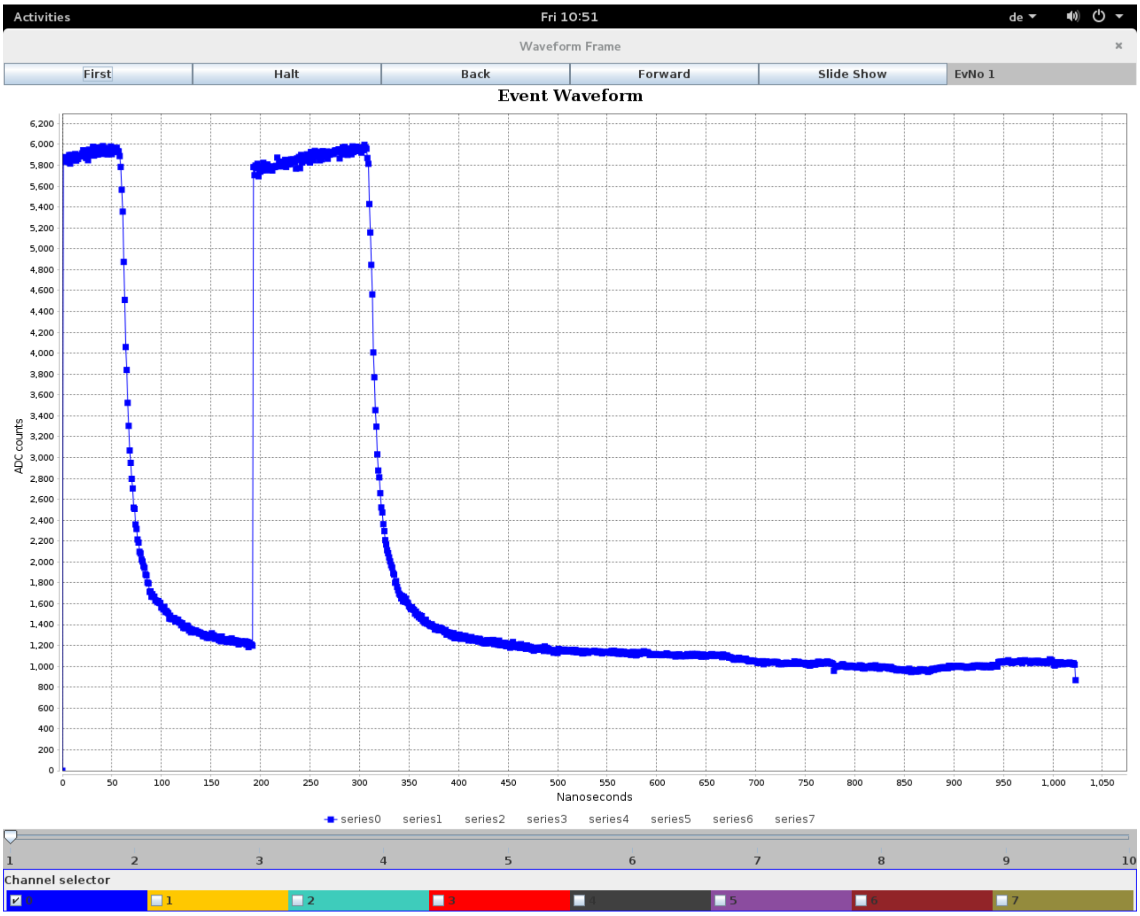

Figure 8.17: Signal shape at 57500 Hz, viewed with the program jTAXI. The trigger fluctuated at very high pixel rates over the whole range of 1024 ns. This could be solved by a firmware bugfix of IceTAXI.

In respect of this part of the calibration, it can be summarized that the behavior of the readout and trigger time is stable. The stability is important for the integration of signals, so that a fixed starting value can be set in order to identify signals of MIPs from charge histograms later. The previous issue with unstable trigger time at high frequencies were not really important for the performance of IceScint, since the expected MIP rate for the scintillator size and at 3000 m altitude is two orders of magnitude smaller.

8.2.5 Full system amplification

In order to be able to draw conclusions about the energy deposited (measured in charge) in IceScint by a MIP event, the overall gain of the electronics, i.e. of IceARM combined with IceTAXI, is of great interest. This was measured for all input channels of IceTAXI and in high-gain and low-gain mode. The measurement setup is the same as that used in the previous Subchapter. Figure 8.19 shows an example of the overall amplification of the full IceScint DAQ. Visible is the overall amplification depending on the pulse width for IceTAXI channel 7 in high gain mode. For the identical setup, but low gain mode, it

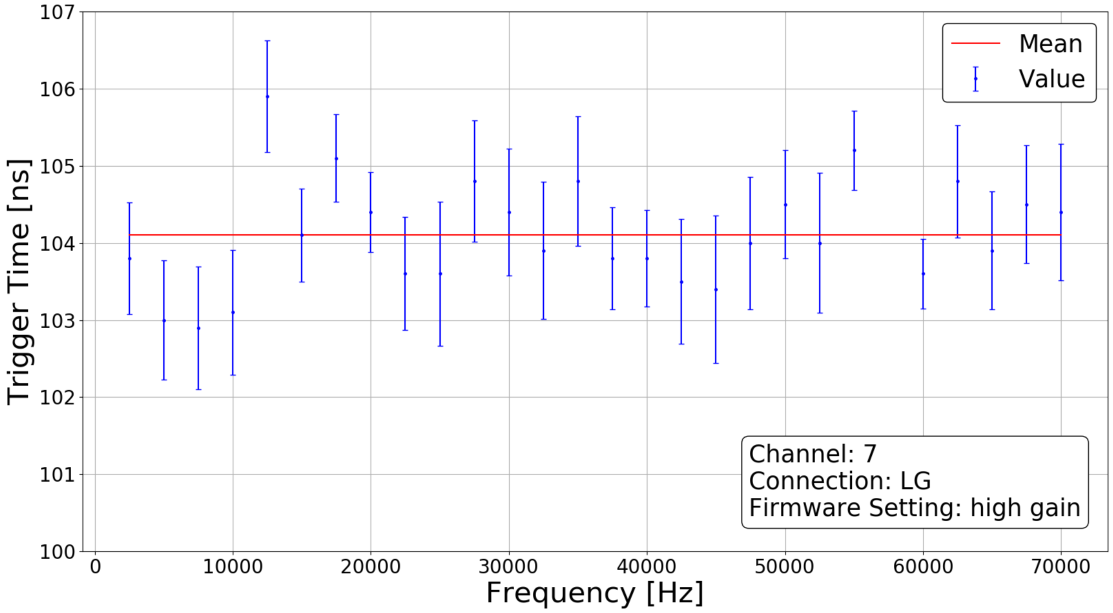

Figure 8.18: Readout time as a function of frequency. The average of the total readout time values for all frequencies is (104.10 ± 3.94) ns [95].

is shown in Figure 8.20. These measurements have been integrated into the calculation of the deposited charge for the charge histograms see Subchapter 8.3 and used the obtain the results of the South Pole IceScint Station described in Chapter 9.

The gain of the low-gain channel depends on the pulse width, due to the Op-Amps dynamic range, have been chosen for a stable amplification of the pulse width of SiPM signals. A smaller gain factor of about 8 was measured at high gain. According to the components used, a factor of 10 would have been expected. The gain loss is caused by the 70 m cable (i.e. cable supression). However, the attenuation does not cause any problems for the data acquisition of IceScint.

8.2.6 Dead time of the system

An important parameter for the performance of IceScint is the dead time between two signal-over-threshold events. Hence, the question how long IceTAXI is blind for short consecutive MIP events. The DRS4 requires a certain number of cycles to read a certain amount of data, which results in a dead time in which no new data can be read. This dead time can be estimated from signal-over threshold events, with a discriminator level set in the region of real MIP events measured with the IceScint station at the South Pole. Figure 8.21 shows a histogram of the time difference between two signal-over-threshold events, out of the commissioning runs.

The dead time was examined for each IceScint detector. On the one hand to exclude irregularities between individual detectors and its channels and on the other hand to increase the statistics. The dead time of IceScint, by summarizing each channel, results in a mean of $65.445 \pm 0.002 \mu s$. Figure 8.22 shows for a better visualization a “zoomed in” version of the last figure. The dead time is twice as much as expected for the DRS4 buffer

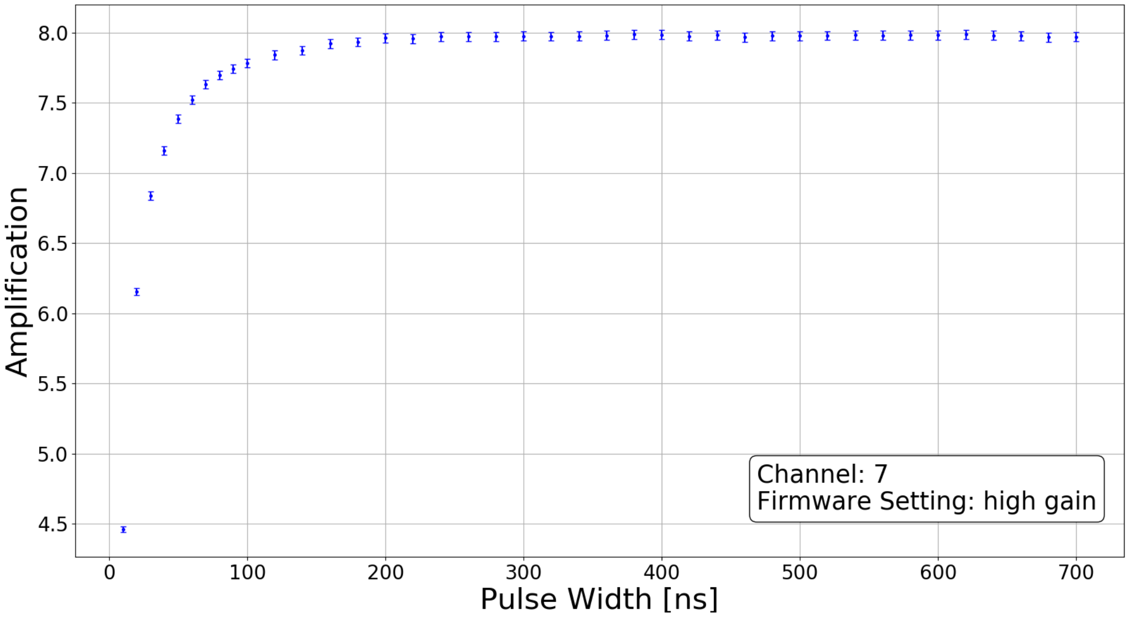

Figure 8.19: Gain at high gain as a function of the pulse width. After a rise up to 200 ns the gain remains constant at factor 8.

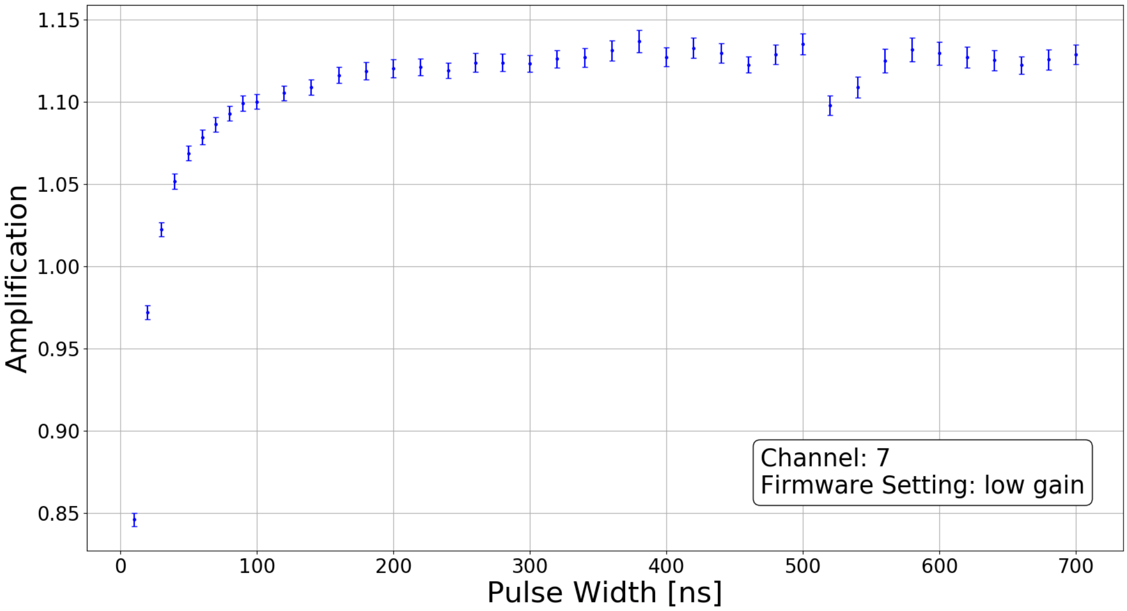

Figure 8.20: Identical to Figure 8.19, but for low-gain. Shown is the overall amplification as a function of the pulse width. After a rise up to 200 ns, the amplification factor remains approximately constant in the range 1.10 to 1.15. The gain at low gain depends on the pulse width. The Op-Amps dynamic range have been chosen for a stable amplification of the typical pulse width of SiPM signals.

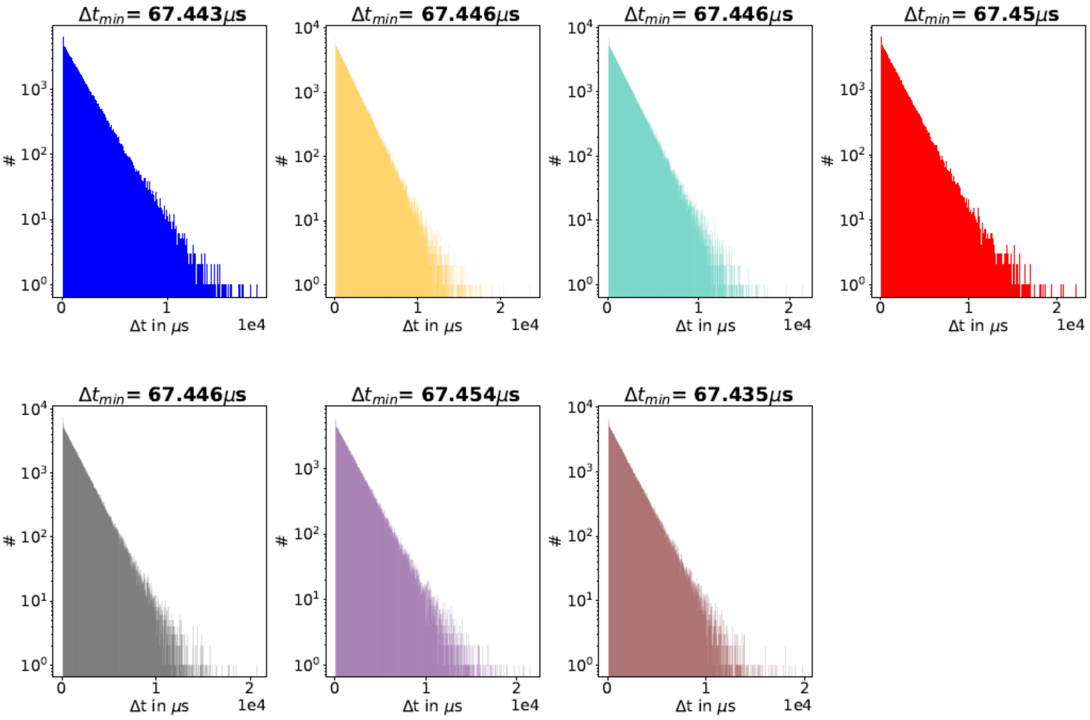

Figure 8.21: 4.13: Histograms of the time differences between two signal-over-threshold events, measured with the IceScint station at the South Pole. Δt_{min} corresponds to the smallest value in the histogram. [96].

cycle [65]. This was found to be due to signal redundancy considerations; each DRS4 buffer is read twice by the FPGA.

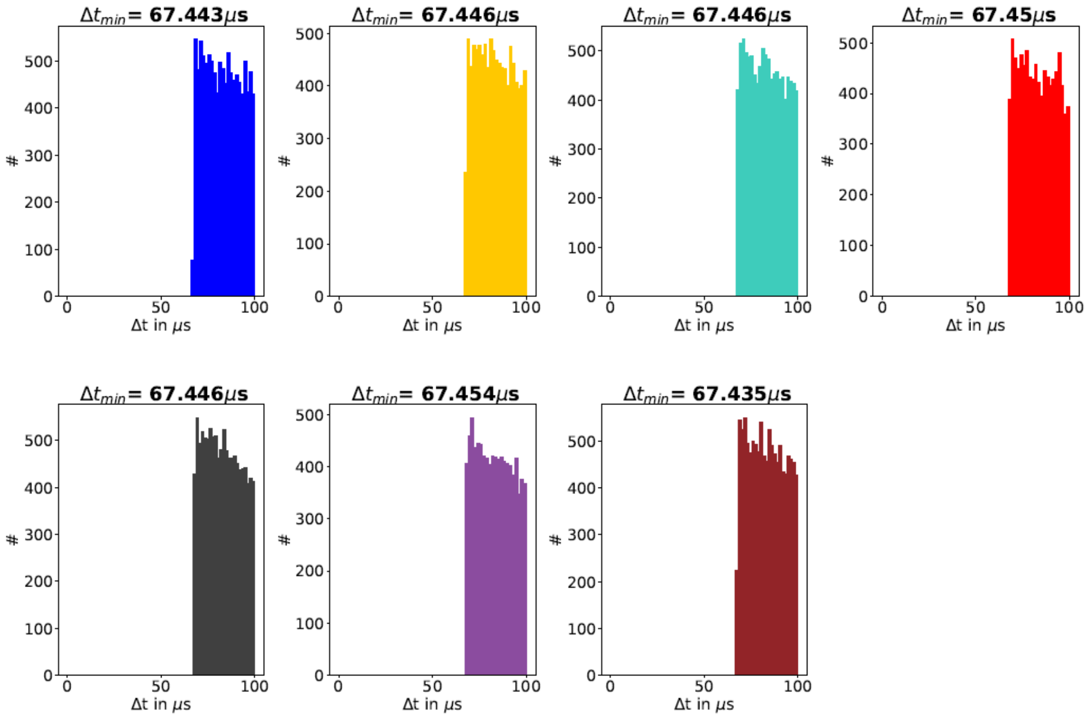

Figure 8.22: These histograms are showing for a better visualization, a "zoomed in" version into the bins between 0 and 100 μs of Figure 8.21 .

8.3 Commissioning of the first South Pole IceScint station

After the first tests of the functionality of the IceScint Station (Chapter 7) at the South Pole, a detailed analysis and adjustment of the operating parameters of the IceScint detectors and the IceTAXI DAQ was performed via SSH access. For this purpose, several commissioning measurement phases were carried out to study the behaviour of the IceScint detectors, in particular of the SiPMs at low temperatures and of IceTAXI, there in particular the FPGA programming.

In order to avoid, in the worst case, that the DRS4 Waveform sampling, for example, overloads the data connection to the ICL, every measurement was carefully considered and configured. Initially, before an automated daily data acquisition was set up, the data acquisition from IceTAXI and the transmission of the data in the entire chain IceScint detectors → IceTAXI → ICL → South Pole Station (sDAQ machine) → KIT was manually monitored.

The performed commissioning runs are described in Figure 8.23 and the daily measurement phases are listed and described in Table 8.1.

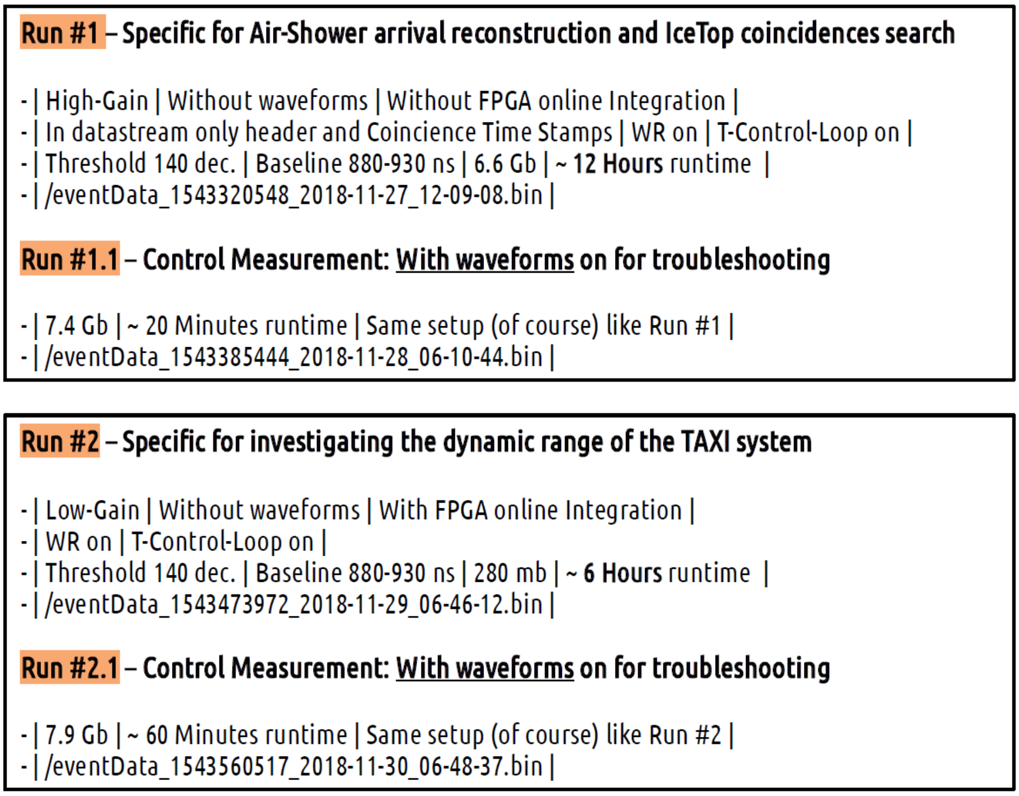

Run #1 – Specific for Air-Shower arrival reconstruction and IceTop coincidences search

- | High-Gain | Without waveforms | Without FPGA online Integration |
- | In datastream only header and Coincience Time Stamps | WR on | T-Control-Loop on |
- | Threshold 140 dec. | Baseline 880-930 ns | 6.6 Gb | ~ **12 Hours** runtime |
- | /eventData_1543320548_2018-11-27_12-09-08.bin |

Run #1.1 – Control Measurement: With waveforms on for troubleshooting

- | 7.4 Gb | ~ 20 Minutes runtime | Same setup (of course) like Run #1 |
- | /eventData_1543385444_2018-11-28_06-10-44.bin |

Run #2 – Specific for investigating the dynamic range of the TAXI system

- | Low-Gain | Without waveforms | With FPGA online Integration |
- | WR on | T-Control-Loop on |
- | Threshold 140 dec. | Baseline 880-930 ns | 280 mb | ~ **6 Hours** runtime |
- | /eventData_1543473972_2018-11-29_06-46-12.bin |

Run #2.1 – Control Measurement: With waveforms on for troubleshooting

- | 7.9 Gb | ~ 60 Minutes runtime | Same setup (of course) like Run #2 |
- | /eventData_1543560517_2018-11-30_06-48-37.bin |

Figure 8.23: The manually performed commissioning runs for the IceScint station. It exceeds the proposed daily traffic limit of $5\frac{GB}{\text{day}}$, but it was found that it is necessary to increase the runtime with actived DRS4 waveform sampling in order to increase the statistics for an air-shower coincidence rate estimation and for the SiPM waveform analysis.

Table 8.1: Setup of the daily IceScint measurement runs during Season 2018

From 14.06.2018	Application of the examined IceScint Data run parameters. Obtained by commissioning runs #1 First test: All 4 hours for 30 s, incl. DRS4 waveform (wf) sampling
From 19.06.2018	Start of "short runs": 3 times a day for 30 s, incl. DRS4 wf sampling (0:00 AM, 8:00 AM, 4:00 PM NZT-Zone).
↓	Start of "long runs": 3 times a day for 300 s online FPGA charge integration, no DRS4 wf sampling (4:00AM , 12:00 PM, 8:00 PM NZT-Zone)
To 01.10.2018	End of daily measurement runs, start of new deployment season at the South Pole, preparations for radio antenna integration

8.3.1 Temperature control loop analysis

For the operation of an array consisting of detectors like IceScint, which are spatially distributed but should measure identical observables, it is crucial that each individual detector operates with the same efficiency. This uniformity must be achieved in the best possible way. It should be as independent as possible from the detectors, which energy the ionizing particle emits into the scintillator material, and how the signal looks like. Hence, all detectors need to generate the same detector signal at a normalized energy output of an ionizing particle.

One disadvantage of SiPMs comes with the high temperature dependence of the gain (Chapter 5). To ensure a stable gain a temperature control loop was developed (Chapter 6), tested in the laboratory and applied in-field at the South Pole.

To check if the temperature control loop works, several commissioning runs have been recorded. Run 1, without control loop, consists of 47 measurements from 03.07 to 18.07 and run 2, with control loop, consists of 47 measurements from 23.07 to 07.08.2018 each at different day times, resulting in different temperatures during the runs (Figure 8.24).

The expectation is therefore that in the analysis of run 1 there will be a temperature dependent result and in the analysis of run 2 the temperature will not be a factor so that the gain is stable for all temperatures.

The first step of the analysis is the integration of the waveforms to get a charge spectrum. The gain can be determined by the position of the MIP peak in the charge spectrum (Chapter 6). Since only the position of the peak is to be determined, but not a fit for the entire spectrum, a simple fit is sufficient. A Gaussian fit is therefore performed. Figure 8.25 shows an example of such a fit of the MIP peak.

For each channel 47 Gaussian fits were done with ROOT version 5.34/30. Therefore,

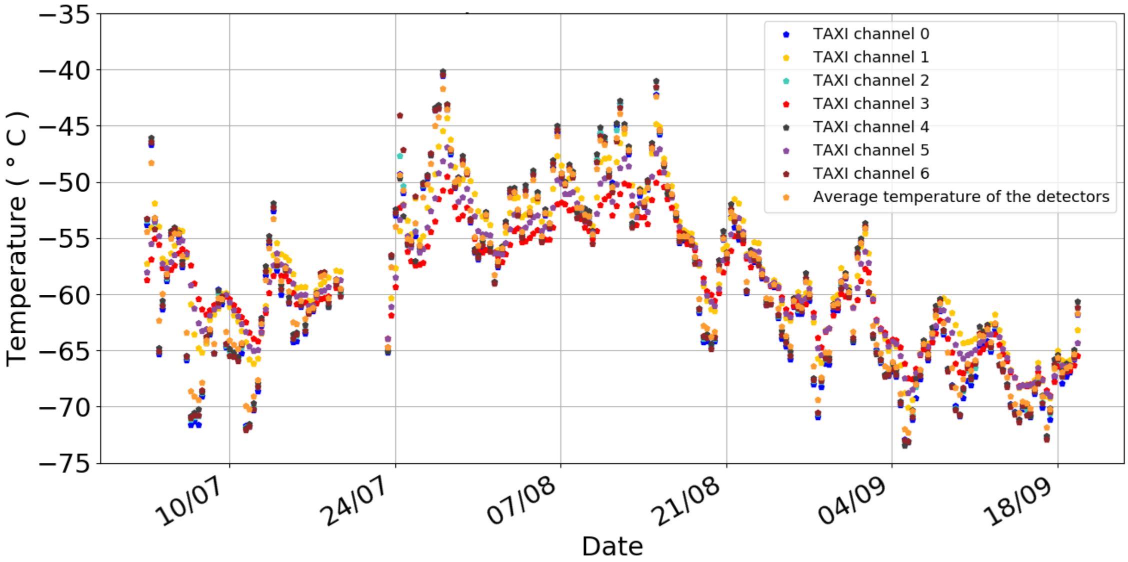

Figure 8.24: Temperature at the South Pole during arctic Winter, measured with the IceScint detectors. Noticeable is the huge temperature fluctuation of $\Delta_{max}T \approx 35°C$. At the gap around 22.07 IceTAXI was offline a few days.

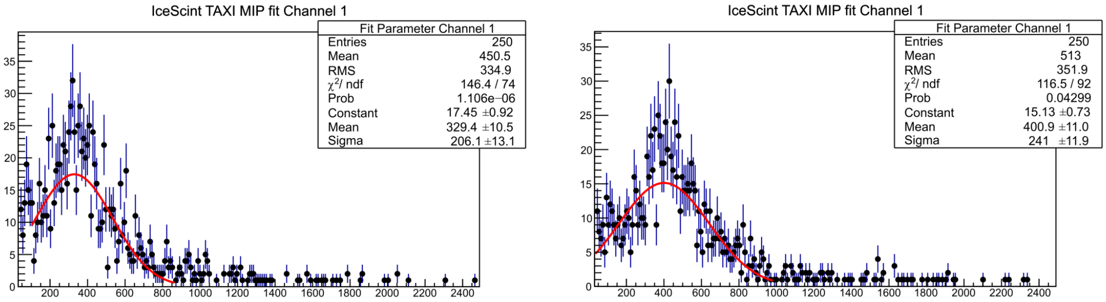

Figure 8.25: Exemplary MIP peaks of IceTAXI channel 1. The bin unit is in Me and is the charge deposit seen at IceTAXI. Left: Run 1 with control loop. Right: without control loop

two times 329 fits for run 1 and run 2 were made. The predefined fit function "gaus" is used. The range of the fit is carried out in such a way that more values are included on the high charge side of the peak, because the curve runs out long here and thus more measurement points are used, which increases the statistics.

To obtain more precise values, a longer measuring time to increase the statistics for the fit and more frequent measuring intervals would have been necessary. This was not possible at that time, because we would have exceeded the nominal bandwidth limit for the satellite uplink by transmitting the DRS4 waveforms.

Figure 8.26 shows the charge deposit at the MIP peak without (left) and with (right) enabled temperature control for two different detectors. The stabilisation of the gain with enabled control loop is visible. The charge deposit and therefore the gain is more stable over time and in addition, the mean charge is more identical between the IceScint detectors. The still visible slight variations could be due to a delay of the temperature change of the detectors.

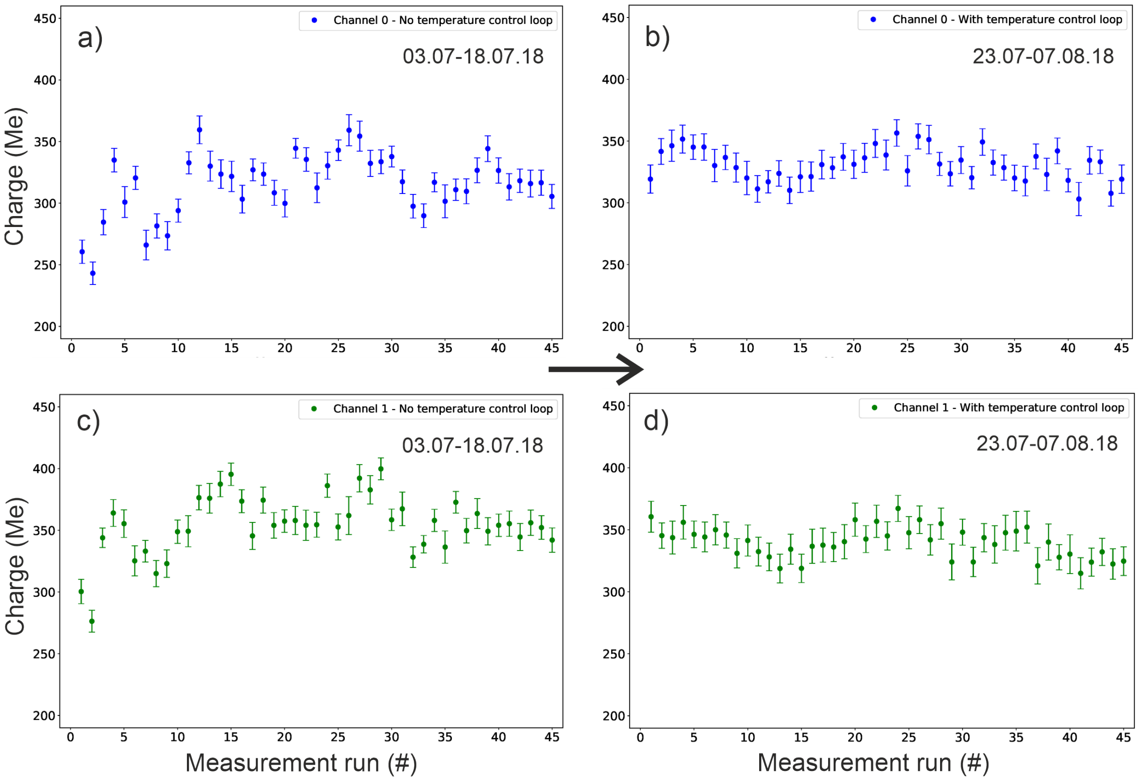

Figure 8.26: Charge deposit at the MIP peak in two detectors without (left) and with (right) enabled temperature control loop for two weeks of measurement time, each. At the top and at the bottom the same IceScint detectors are shown. The stabilization of the charge deposit and therefore of the gain with enabled temperature control loop is visible. The charge deposit is more stable over time and the mean charge (a) 315.2 ± 5.1 b) 330.7 ± 5.4 c) 354.2 ± 5.2 d) 339.6 ± 6.1) is more identical between two detectors.

8.3.2 Charge spectra analysis and calibration

For run 1 and run 2 the waveforms are integrated to obtain a charge spectrum. Exemplary, Figure 8.27[7] shows the charge histograms of run 2 in logarithmic scale for each detector. Notable is the uniform charge deposit of each IceScint detector in the same Me region. In the following, in order not to go beyond the scope of the thesis, only results of run 2 is shown.

To find fit functions for the IceScint charge histograms, different test fits were made. The aim was to find two different fit functions for IceScint: One for the analysis of the MIP peak and one for the whole charge histogram.

Fit function to determine the MIP peak in the charge spectrum

Two different fits are tested for the MIP peak region, namely a Gaussian and a Landau fit. Like for the temperature control loop validation, a Gaussian fit is tried first. Less measured values must be included on the high charge region of the curve, since the curve

---

[7] Settings: Baseline 880-930 ns, Gain factor 1.1 (LG), plotted range 0-7500 Me, number of bins 500

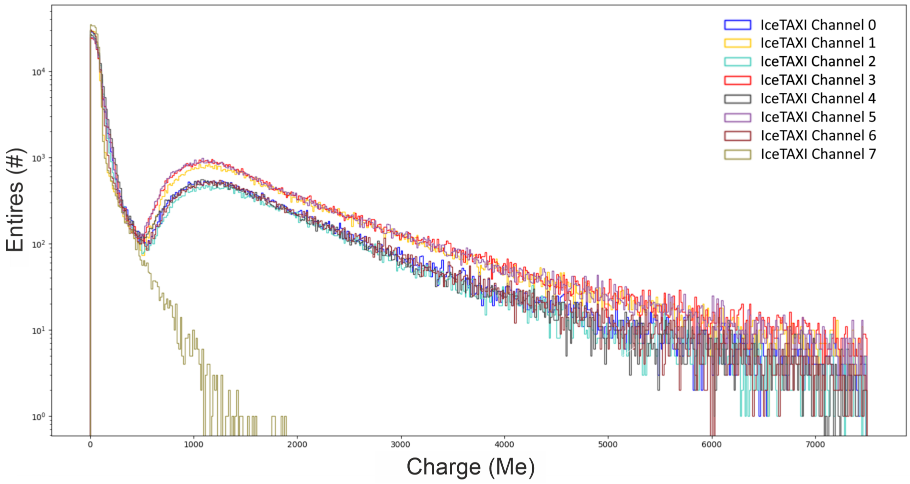

Figure 8.27: Charge histogram of run 2 in logarithmic scale. All 8 IceTAXI channels are plotted. The PE peak, the valley and the MIP peak are visible. Notable is the uniform charge deposit of each IceScint detector. At channel 7 (brown) no detector is connected. The two groups are due to absorber above the scintilaltor by snow or another detector and therefore different rate.

has a long slope to higher charges and is therefore not really following a Gaussian distribution. The range is optimized that as many values as possible are included. Figure 8.28 shows all applied Gaussian fits to run 2 charge histograms.

The curve has a long slope on the right and a steep rise on the left, which is more like a Landau function. Hence, a Landau fit is used to describe the peak and not the whole spectrum. For the fit the Landau function defined in root is used. The fit function describes the curve in the MIP peak area very well. Figure 8.29 shows all applied Landau fits to run 2 charge histograms. In Figure 8.30 the mean MIP peak values for the Gaussian and Landau fit are shown. The Landau function fits better as the Gaussian function since for the Gaussian function many higher charge values of the curve are excluded.

Fit function for the whole charge spectrum

A first approach on how to fit a whole charge spectrum,the IceTop data was examined. Two publications [18, 97] have been studied in which the fit functions for the charge spectrum of the IceTop tanks is discussed.

Muons are minimally ionizing particles (MIP), i.e. they lose a constant amount of energy per distance. The distribution of the charge deposit in the IceTop tanks is therefore dominated by muons traveling different distances, depending on the incident angle [18]. Figure 8.31 shows the distribution of the muon track lengths. The suggested fit for the charge spectrum of IceTop tanks is described as [18] :

$$f(x) = \underbrace{p_0 \left[\mathrm{L}(x; p_1, p_2) + \frac{1.85}{p_1} \cdot \frac{1}{\exp\left(\frac{x-p_1}{p_2}\right) + 1} \right]}_{f_\mu} + \underbrace{p_3 \cdot \exp(p_4 \cdot x)}_{f_{em}} . \tag{8.3.1}$$

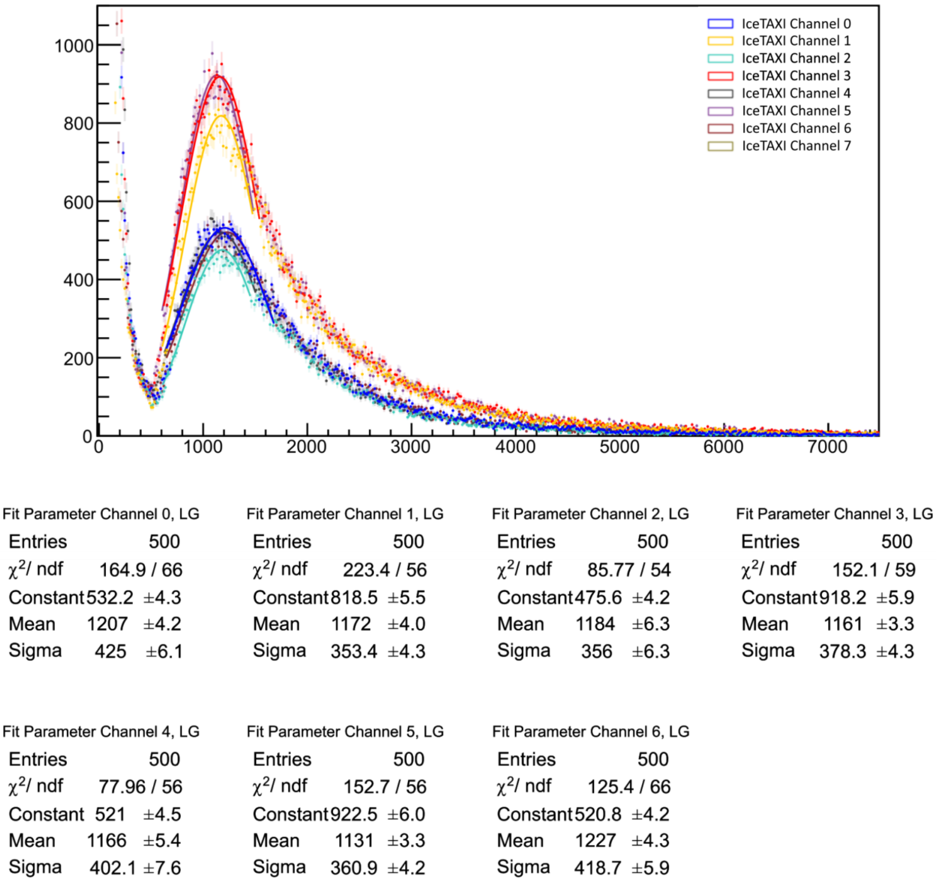

Fit Parameter Channel 0, LG

Entries	500
χ^2/ ndf	164.9 / 66
Constant	532.2 ±4.3
Mean	1207 ±4.2
Sigma	425 ±6.1

Fit Parameter Channel 1, LG

Entries	500
χ^2/ ndf	223.4 / 56
Constant	818.5 ±5.5
Mean	1172 ±4.0
Sigma	353.4 ±4.3

Fit Parameter Channel 2, LG

Entries	500
χ^2/ ndf	85.77 / 54
Constant	475.6 ±4.2
Mean	1184 ±6.3
Sigma	356 ±6.3

Fit Parameter Channel 3, LG

Entries	500
χ^2/ ndf	152.1 / 59
Constant	918.2 ±5.9
Mean	1161 ±3.3
Sigma	378.3 ±4.3

Fit Parameter Channel 4, LG

Entries	500
χ^2/ ndf	77.96 / 56
Constant	521 ±4.5
Mean	1166 ±5.4
Sigma	402.1 ±7.6

Fit Parameter Channel 5, LG

Entries	500
χ^2/ ndf	152.7 / 56
Constant	922.5 ±6.0
Mean	1131 ±3.3
Sigma	360.9 ±4.2

Fit Parameter Channel 6, LG

Entries	500
χ^2/ ndf	125.4 / 66
Constant	520.8 ±4.2
Mean	1227 ±4.3
Sigma	418.7 ±5.9

Figure 8.28: Charge spectra for all IceScint detectors with events recorded in run 2 with a Gaussian fit and its parameters for determine the MIP peak in the charge spectrum.

This formula includes a muon part f_μ consisting of vertical muons and edge clippers, and a part for the electromagnetic background f_{em}. In the muon part f_μ p_0 describes the number of muons which are not edge clipping. The number of edge clipping muons is $1.85 \cdot p_0$, the factor reveals the geometry of the IceTop tank. $\mathrm{L}(x; p_1, p_2)$ is the Landau distribution with the parameters p_1 and p_2, describing through-going muons. The second term is a Fermi-like function. This function describes the edge clipping muons. The part for the electromagnetic background f_{em} is a single exp() function [18]. Figure 8.31 shows a charge spectrum of one DOM in IceTop tank 61A. Equation (8.3.1) is used. The electromagnetic background is examined in more detail. A double exp() fit, a single exp() fit and a power law are applied. Figure 8.32 shows the three different background fits. It is concluded that a double exp() fit describes the electromagnetic background best [97]. In three different functions are suggested for the charge spectrum fit of the tanks. The first fit is a Landau distribution with a single exp() background:

$$\begin{aligned} p(x) = & p_0 \cdot \frac{1}{p_2\sqrt{2\pi}} \exp\left(-0.5\left(\frac{x-p_1}{p_2} + \exp\left(-\frac{x-p_1}{p_2}\right)\right)\right) \\ & + \exp(p_3 + p_4 \cdot x). \end{aligned} \tag{8.3.2}$$

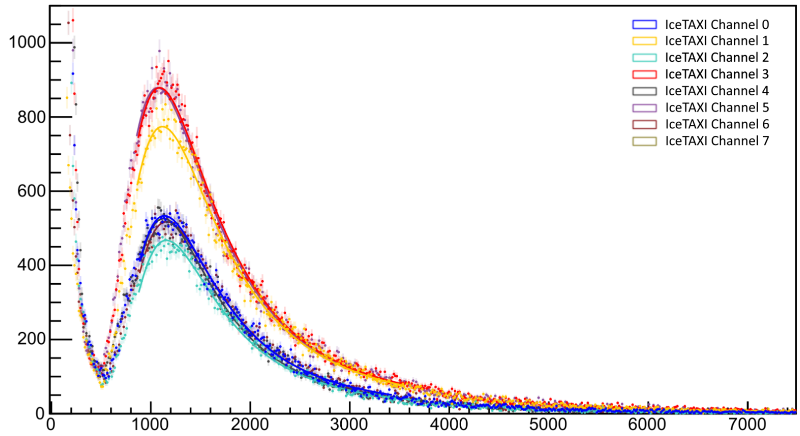

	Fit Parameter Channel 0, LG	Fit Parameter Channel 1, LG	Fit Parameter Channel 2, LG	Fit Parameter Channel 3, LG
Entries	500	500	500	500
Mean	436.2	609.8	388.1	664.8
Std Dev	861.1	1034	806.1	1056
χ^2 / ndf	202.7 / 168	232.9 / 178	224.7 / 186	247.2 / 176
p0	2954 ± 21.7	4286 ± 25.9	2589 ± 20.1	4866 ± 28.4
p1	1197 ± 5.5	1181 ± 5.2	1215 ± 5.2	1150 ± 5.4
p2	269.8 ± 2.5	291.2 ± 2.3	264.1 ± 2.4	282.2 ± 2.2

	Fit Parameter Channel 4, LG	Fit Parameter Channel 5, LG	Fit Parameter Channel 6, LG
Entries	500	500	500
Mean	419.9	647.4	428.7
Std Dev	825.4	1038	854.7
χ^2 / ndf	250.2 / 189	210.2 / 176	201 / 168
p0	2913 ± 21.8	4866 ± 28.4	2865 ± 21.3
p1	1186 ± 5.7	1132 ± 5.4	1218 ± 5.1
p2	257.6 ± 2.3	282 ± 2.2	271.9 ± 2.5

Figure 8.29: Same as above (Figure 8.28), but now fit with a Landau function. The landau function fits better since not that much higher charge values have to be excluded for the fit.

This fit version approximates the muon signal with most likely vertical muons. Edge clipping muons are not taken into account. To reduce parameters, the electromagnetic background is only described by a single exp() function [97].

The second fit is expressed as Landau distribution with a double exp() background:

$$\begin{aligned} p(x) = & p_0 \cdot \frac{1}{p_2\sqrt{2\pi}} \exp\left(-0.5\left(\frac{x-p_1}{p_2} + \exp\left(-\frac{x-p_1}{p_2}\right)\right)\right) \\ & + \exp(p_3 + p_4 \cdot x) + \exp(p_5 + p_6 \cdot x). \end{aligned} \tag{8.3.3}$$

As shown in Figure 8.32 the double exp() function describes the the electromagnetic background the most [97].

The third fit is a Landau distribution with a continuous step function and a double

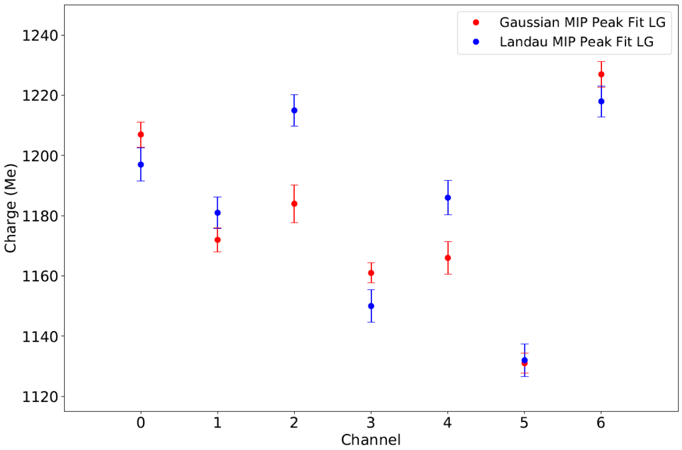

Figure 8.30: The mean of the MIP peak for Landau and Gaussian fit at run 2. Shown are all IceTAXI channels where a IceScint detector is connected. The Landau function fits better than the Gaussian function since, described in the text, many higher charge values of the curve have to be excluded for it to obtain a suitable fit. Although this is due to the quality cut of the Gaussian fit not visible here, it shows the uniformity of the IceScint Station again. The mean value of the MIP peak between the individual detectors varies only by ~3%.

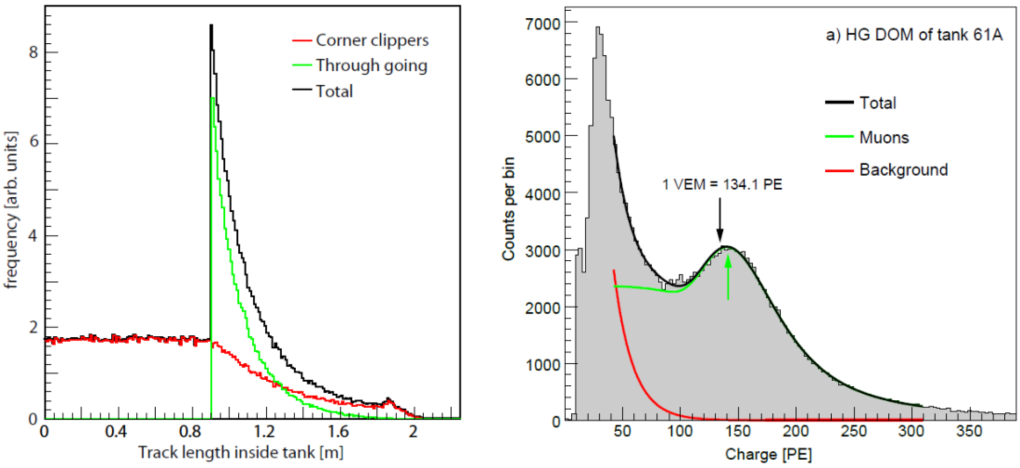

Figure 8.31: Left: Distribution of muon track lengths in an IceTop tank for a $\cos^{2.3}\Theta$ zenith angle distribution. In green the through-going muons are shown. The sharp peak at 90 cm is caused by vertical muon tracks. In red the clipper muons are shown [18]. Right: Charge spectrum of a DOM in IceTop tank 61A. The black curve equals the in equation 8.3.1 described fit with the muon part f_μ in green and the electromagnetic background f_{em} in red [18].

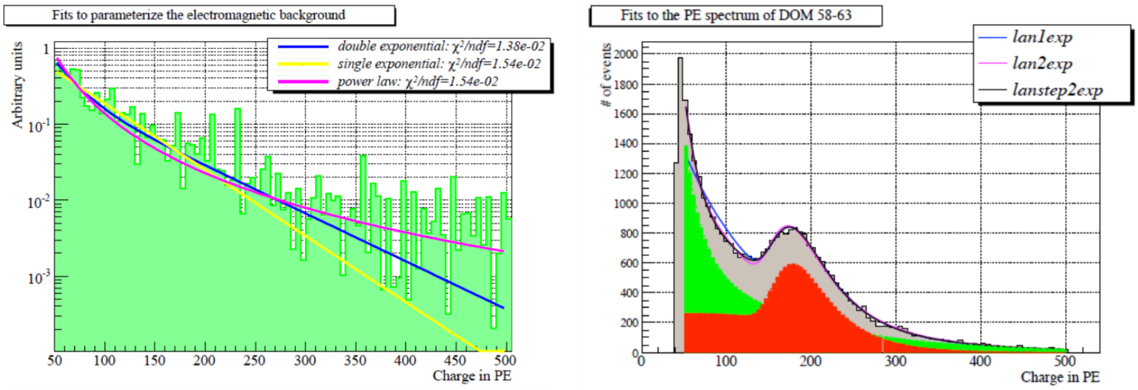

Figure 8.32: Left: Fit functions to the simulated electromagnetic background signal of IceTop tanks. A double exp() fit (blue), a single exp() fit (yellow) and a power law (pink) are applied. The best matching fit is the double exp() fit [97]. Right: Fit functions to the whole charge spectrum of an IceTop tank[97]. The shown fit functions are applied to IceScint data.

exp() background:

$$\begin{aligned} p(x) = & p_0 \cdot \frac{1}{p_2\sqrt{2\pi}} \exp\left(-0.5\left(\frac{x-p_1}{p_2} + \exp\left(-\frac{x-p_1}{p_2}\right)\right)\right) \\ & + p_8 \cdot 0.5 \cdot (1 - \tanh(p_7 \cdot (x - p_9))) \qquad (8.3.4) \\ & + \exp(p_3 + p_4 \cdot x) + \exp(p_5 + p_6 \cdot x). \qquad (8.3.5) \end{aligned}$$

The step function describes the edge clipping muons[97]. Figure 8.31 shows a charge spectrum of an IceTop tank. These functions, described in equations (8.3.2, 8.3.3 and 8.3.5) are investigated.

A possible fit for the whole charge spectrum of the scintillator signals contains of a Landau function describing the muons, a step function describing the laterally muons and one or better two exponential functions describing the electromagnetic background. As step function the Fermi function is used [97]. It is shown, that the most suitable fit function for the electromagnetic background is a double exponential fit, so this one is chosen [97]. Figure 8.33 shows results for this fit function applied to run 2 data.

The IceTop tanks have a larger detector volume compared to the IceScint detectors. Almost all muons go through the whole height of the Icescint detectors since the used scintillator bars are just 1 cm thick. Only a few muons cut the volume of the scintillator bars. Due to that, the step function is for IceScint not appropriate. A fit only containing the Landau function and the two exp() functions is applied. All applied fits of run 2 for this fit function are shown in Figure 8.34.

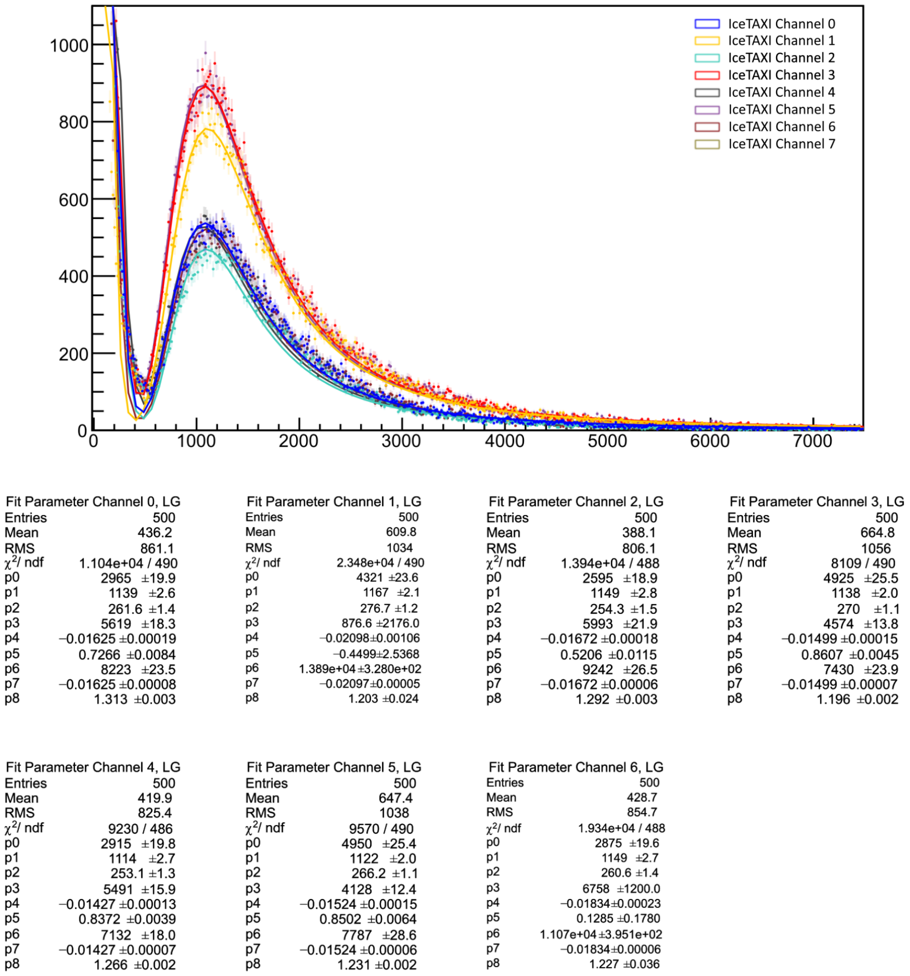

Fit Parameter Channel 0, LG	
Entries	500
Mean	436.2
RMS	861.1
χ^2/ ndf	1.104e+04 / 490
p0	2965 ±19.9
p1	1139 ±2.6
p2	261.6 ±1.4
p3	5619 ±18.3
p4	−0.01625 ±0.00019
p5	0.7266 ±0.0084
p6	8223 ±23.5
p7	−0.01625 ±0.00008
p8	1.313 ±0.003

Fit Parameter Channel 1, LG	
Entries	500
Mean	609.8
RMS	1034
χ^2/ ndf	2.348e+04 / 490
p0	4321 ±23.6
p1	1167 ±2.1
p2	276.7 ±1.2
p3	876.6 ±2176.0
p4	−0.02098±0.00106
p5	−0.4499±2.5368
p6	1.389e+04 ±3.280e+02
p7	−0.02097±0.00005
p8	1.203 ±0.024

Fit Parameter Channel 2, LG	
Entries	500
Mean	388.1
RMS	806.1
χ^2/ ndf	1.394e+04 / 488
p0	2595 ±18.9
p1	1149 ±2.8
p2	254.3 ±1.5
p3	5993 ±21.9
p4	−0.01672 ±0.00018
p5	0.5206 ±0.0115
p6	9242 ±26.5
p7	−0.01672 ±0.00006
p8	1.292 ±0.003

Fit Parameter Channel 3, LG	
Entries	500
Mean	664.8
RMS	1056
χ^2/ ndf	8109 / 490
p0	4925 ±25.5
p1	1138 ±2.0
p2	270 ±1.1
p3	4574 ±13.8
p4	−0.01499 ±0.00015
p5	0.8607 ±0.0045
p6	7430 ±23.9
p7	−0.01499 ±0.00007
p8	1.196 ±0.002

Fit Parameter Channel 4, LG	
Entries	500
Mean	419.9
RMS	825.4
χ^2/ ndf	9230 / 486
p0	2915 ±19.8
p1	1114 ±2.7
p2	253.1 ±1.3
p3	5491 ±15.9
p4	−0.01427 ±0.00013
p5	0.8372 ±0.0039
p6	7132 ±18.0
p7	−0.01427 ±0.00007
p8	1.266 ±0.002

Fit Parameter Channel 5, LG	
Entries	500
Mean	647.4
RMS	1038
χ^2/ ndf	9570 / 490
p0	4950 ±25.4
p1	1122 ±2.0
p2	266.2 ±1.1
p3	4128 ±12.4
p4	−0.01524 ±0.00015
p5	0.8502 ±0.0064
p6	7787 ±28.6
p7	−0.01524 ±0.00006
p8	1.231 ±0.002

Fit Parameter Channel 6, LG	
Entries	500
Mean	428.7
RMS	854.7
χ^2/ ndf	1.934e+04 / 488
p0	2875 ±19.6
p1	1149 ±2.7
p2	260.6 ±1.4
p3	6758 ±1200.0
p4	−0.01834±0.00023
p5	0.1285 ±0.1780
p6	1.107e+04 ±3.951e+02
p7	−0.01834±0.00006
p8	1.227 ±0.036

Figure 8.33: Charge spectra of IceScint recorded in run 2 and a with Landau()+Fermi()+exp()+exp() fit applied

In terms of these studies, the most suitable fit function for IceScint detectors are:

- A Landau function for analyzing the MIP peak and
- for the whole charge spectrum a Landau+exp()+exp() function.

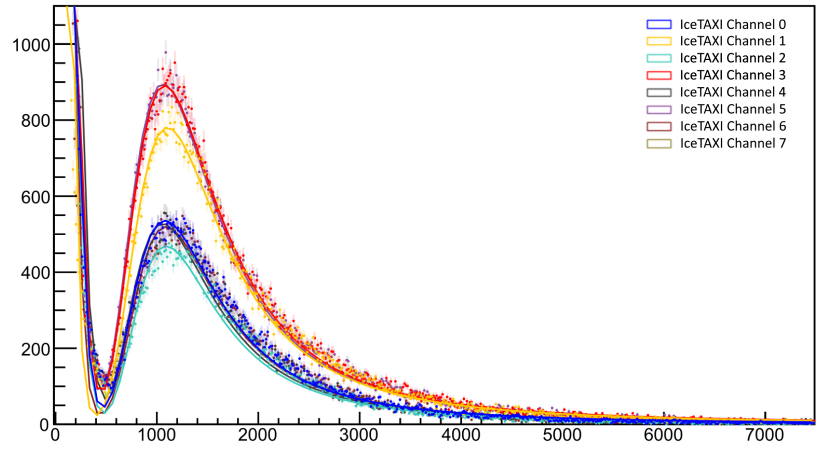

Fit Parameter Channel 0, LG	
Entries	500
Mean	436.2
RMS	861.1
χ^2/ ndf	1.107e+04 / 492
p0	2967 ±20.0
p1	1137 ±2.7
p2	262 ±1.4
p3	2.07e+04 ±6.91e+01
p4	−0.01624±0.00012
p5	2.146e+04 ±7.070e+01
p6	−0.01624±0.00012

Fit Parameter Channel 1, LG	
Entries	500
Mean	609.8
RMS	1034
χ^2/ ndf	2.353e+04 / 492
p0	4322 ±24.0
p1	1165 ±2.2
p2	277.3 ±1.2
p3	2.366e+04 ±8.193e+01
p4	−0.02096±0.00012
p5	2.314e+04 ±7.873e+01
p6	−0.02096±0.00013

Fit Parameter Channel 2, LG	
Entries	500
Mean	388.1
RMS	806.1
χ^2/ ndf	1.397e+04 / 490
p0	2596 ±18.9
p1	1147 ±2.8
p2	254.7 ±1.5
p3	2.173e+04 ±7.067e+01
p4	−0.01671±0.00010
p5	2.199e+04 ±7.018e+01
p6	−0.01671±0.00010

Fit Parameter Channel 3, LG	
Entries	500
Mean	664.8
RMS	1056
χ^2/ ndf	8107 / 492
p0	4934 ±25.6
p1	1137 ±2.0
p2	270.2 ±1.1
p3	1.733e+04 ±6.082e+01
p4	−0.01497±0.00011
p5	1.805e+04 ±6.178e+01
p6	−0.01497±0.00010

Fit Parameter Channel 4, LG	
Entries	500
Mean	419.9
RMS	825.4
χ^2/ ndf	9236 / 488
p0	2920 ±19.8
p1	1112 ±2.7
p2	253.2 ±1.3
p3	1.852e+04 ±6.080e+01
p4	−0.01426±0.00009
p5	1.943e+04 ±6.244e+01
p6	−0.01426±0.00009

Fit Parameter Channel 5, LG	
Entries	500
Mean	647.4
RMS	1038
χ^2/ ndf	9561 / 492
p0	4959 ±25.7
p1	1120 ±2.0
p2	266.3 ±1.1
p3	1.783e+04 ±6.120e+01
p4	−0.01522±0.00010
p5	1.848e+04 ±6.200e+01
p6	−0.01522±0.00009

Fit Parameter Channel 6, LG	
Entries	500
Mean	428.7
RMS	854.7
χ^2/ ndf	1.938e+04 / 490
p0	2875 ±19.7
p1	1147 ±2.7
p2	261.1 ±1.4
p3	2.282e+04 ±1.404e+03
p4	−0.01833±0.00011
p5	2.261e+04 ±1.404e+03
p6	−0.01833±0.00011

Figure 8.34: Charge spectra of IceScint recorded in run 2 and a with Landau()+exp()+exp() fit applied.

In this Chapter a part of the commission phase was described as well as the calibration of IceTAXI and the results of the initial analysis. For IceScint, suitable fit functions for charge histograms with a MIP peak could be found by a study of fit functions applied to the data of the well analysed IceTop Cherenkov tanks. Since the detector volume and the signal generation is different, the fit function of the whole charge spectra for IceScint could be simplified. These commissioning runs and its analysis were essential to show the presented capabilities of the IceScint Station and its air shower reconstruction results, presented in Chapter 9.

9 Results of the first South Pole IceScint station

In this Chapter first analysis of the data taken with the deployed IceScint station and the resulting capabilities of the station is shown. The air-shower and local single or twofold coincidence events were recorded between March and October 2018, with daily short and for long runs and in addition with the dedicated commissioning runs (Chapters 7 and 8).

The first part shows the detector focused performance with air-shower data. These analysis were made in close cooperation with [96], published as Bachelor thesis.

In addition, the effect of the temperature and the atmospheric pressure on the event rate as well as the light tightness of the detector housing and dead time of the measured charge deposit of the individual detectors were investigated. This is followed by the analysis of the air-shower physics capabilities of the IceScint station and in coincidence of the high multiplicity events with the IceTop array. In the last part of this Chapter a determination of the reconstruction accuracy with a quality cut of IceScint events in respect of in coincidence measured air showers with IceTop is shown. These analyse can be found in great detail in [96] and [42],. In addition, a summary of the most important results can be looked up in [91].

9.1 Event rates

The event rate in Figure 9.1 equals approximately (Chapter 8) the signal-over-threshold rate of one detector. Therefore, since the discriminator threshold was chosen above the valley in the charge histogram via threshold scans with pre-commissioning runs, it shows the MIP rate per IceScint detector. It includes the statistical Poisson error $\frac{\sqrt{N_{events}}}{t_{run}}$ and are exemplary taken from the runs of 21.08.2018. This was a typical daily measurement run with 6 runs in total, divided into 3 short runs and 3 long runs, recorded at different time of the day. The three runs at each day, long and short run, were recorded at different time at the day (Chapter 8).

Comparing these three measurements per day, no major difference in the rate can be found. The hit rate of the detectors seems to be independent of the time of day at the South Pole. As expected, the rate decreases with increasing multiplicity. These values can be used as approximation how much DRS4 sampled waveforms have to be transferred via the satellite uplink. Like discussed in Chapter 8, the size of the data packages increase significantly by enabling the DRS4 waveform data package.

The daily means of the event rate in Figure 9.2 were calculated according to

$$s_x = \sqrt{\frac{\sum_{i=1}^{n}(x_i - \bar{x})^2}{(n-1)\cdot n}} \tag{9.1.1}$$

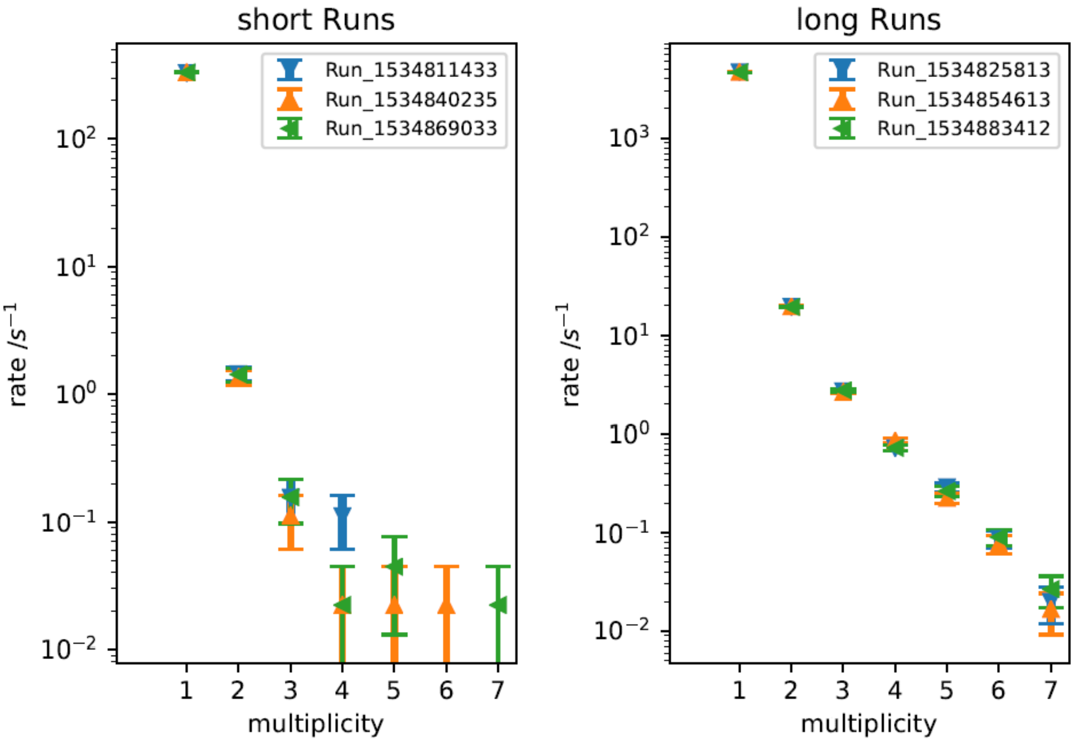

Figure 9.1: Event rate as a function of hit multiplicity. As expected, the rate decreases with increasing multiplicity [96]. In addition, it is visible that the statistics is lower and therefore the error is larger at the short runs (left) compared to the long runs (right).

where x_i is the rate of each run and $\bar{x}$ is the mean value per day. For these these figures, the daily runs of September 2018 have been used. The runs have been separated, like in Figure 9.1, between the daily short runs (left) and the long runs (right).

The behavior of the multiplicity of the IceScint array vs. the rate follows the expectation as seen for a daily run analysis. Due to the short measurement time of the short runs the errors bars are larger.

In conclusion, Figure 9.1 and Figure 9.2 shows that the multiplicity rate of the IceScint station changes neither on the day nor in the month. This is showcasing that, assuming an approximately constant MIP rate at the South Pole, this IceScint station is in stable operation and there are no large fluctuations due to, as example, temperature-related changes in either the IceTAXI DAQ or the IceScint detectors components. This allows reliable operation and gives good prospects for the future IceScint stations at the South Pole.

For completeness, Figure 9.3 shows the fit functions and their parameters. The details of the fits can be found in [96]. These functions can be used to estimate, in conjunction with the packet size prediction from Chapter 8, how many DRS4 sampled waveforms per day would have to be transmitted via satellite uplink if suspected and thus interesting high multiplicities of the IceScint station are to be transmitted for a detailed analysis, i.e. air shower events in conjunction with its SiPM peaks.

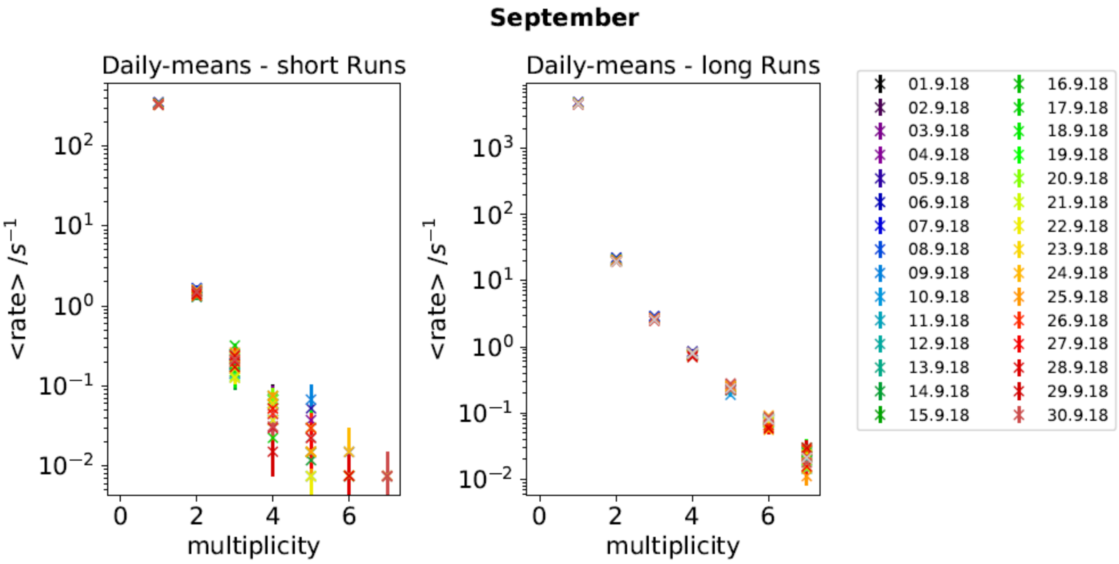

Figure 9.2: Daily means of the rates as function of the multiplicity for long and short runs plotted separately. The shown uncertainty is calculated by the standard error of the mean. The measurement run were performed the whole September on a daily basis [96]

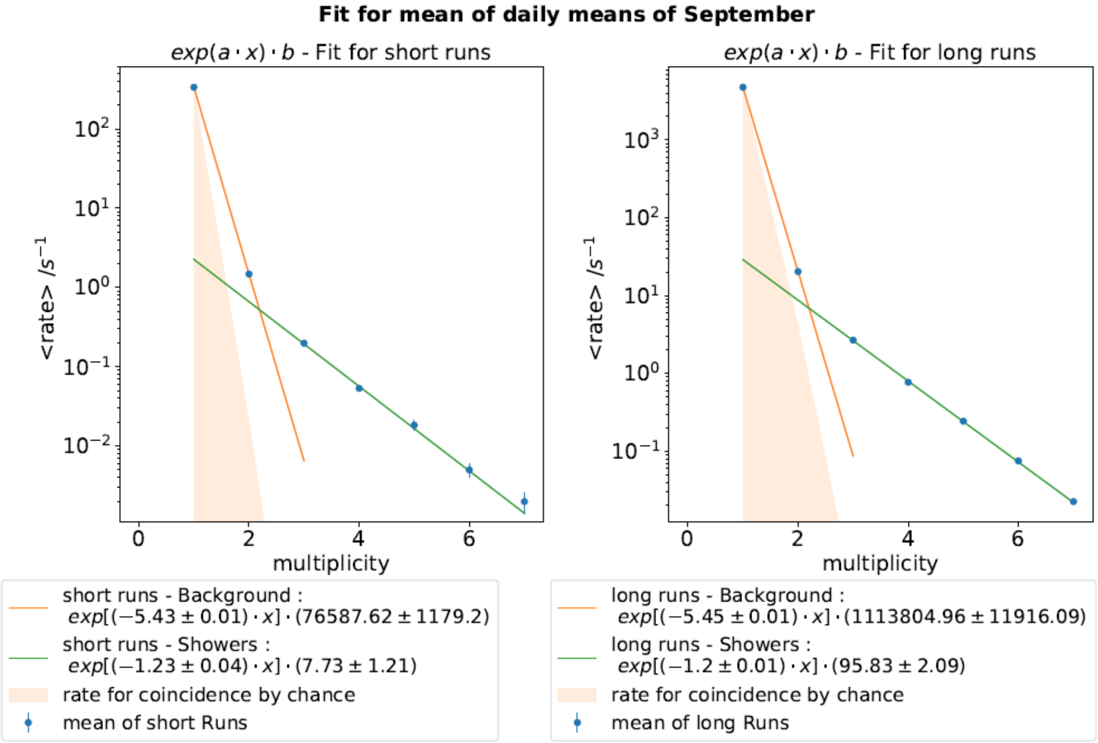

Figure 9.3: Fit functions, for background (orange) and most likely air-shower events (green) vs. the mean rate of the daily averages as a function of multiplicity [96].

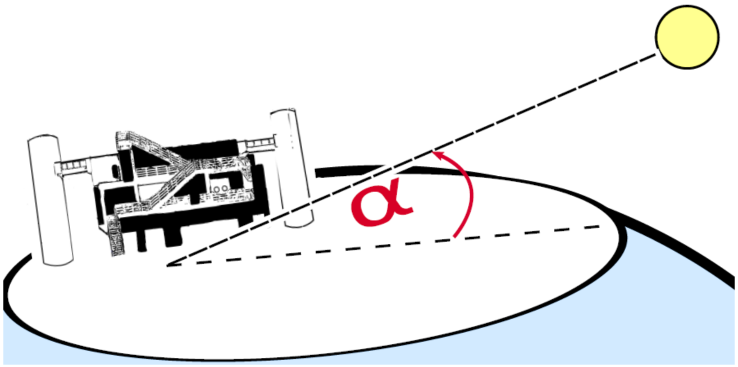

Figure 9.4: The sun altitude α in relation to the South Pole surface [96].

- versus solar altitude

Due to the special geographical latitude of the South Pole, it is possible to investigate how the IceScint station and its detectors behave during polar winters and summers. The sun, for example, moves very close to the horizon in polar summer, oscillating slightly throughout the day. The angle used and for illustration purposes are shown in Figure 9.4.

This means that the IceScint detectors, some of which are 1 meter elevated (Chapter 7), are laterally illuminated at different times of day. As the aluminium housing of the IceScint detectors is not completely closed by riveting the top and bottom plates, the black tube foil is illuminated. Experiments have been carried out (Chapter 6) with the foil used to determine whether it becomes brittle at low temperatures, but long-term testing was not possible.

This examination offers a natural possibility to find out if the foil has cracked and photons have fallen on the optical fiber or on the SiPM, thus increasing the event rate.

In Figure 9.5 the even rate in relation of the sun altitude α for different days and for the all IceScint detectors (IceTAXI channel 0-6) of the station is shown. A negative angle means the sun is below the South Pole surface. The sun altitude values taken from the data set of the “Time and Date AS” corporation [1].

The difference in the event rate between the individual IceScint detectors has its origin in the different installation (Chapter 7) of the detectors, i.e. if absorbing material like another detector or snow is present or not. In addition, the groupings in the plot show which detectors were installed in the same way, which is also reflected in the charge histograms (Chapter 8). The fluctuation of the event rate of the individual IceScint detectors over the days has its reason in the pressure dependence of the event rate. This in detail and a plot corrected, which is smoothing the event rates over time, in comparison to Figure 9.5 can be found in [96].

Already by when considering Figure 9.5, it is noticeable that there is no correlation between the sun latitude and the event rate. This demonstrates that the detectors are still sealed light-tight and that the used tube film has not become brittle and cracked.

---

[1] https://www.timeanddate.com/sun/antarctica/south-pole

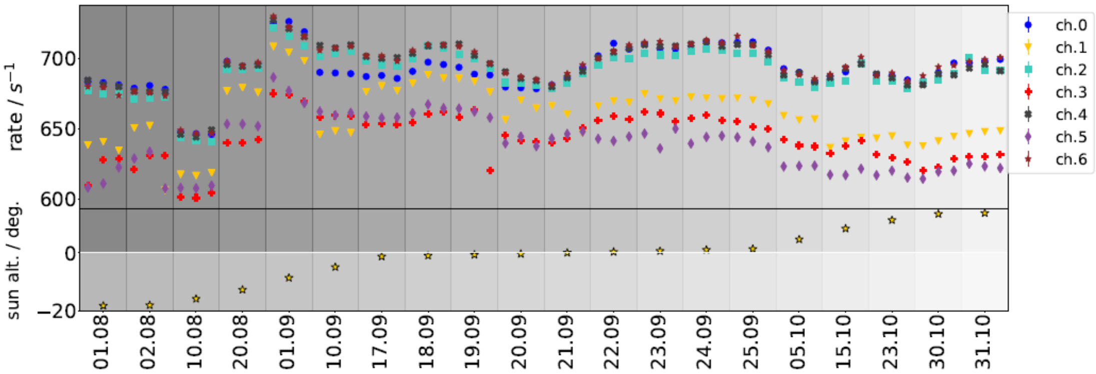

Figure 9.5: Event rate for each channel for long runs of some example days. In the lower part of the diagram the sun altitude of these days is plotted. A negative sun altitude means that the sun is below the horizon [96].

9.2 Air-Shower core determination with the IceScint station

For the analysis of the air-shower core determination with the IceScint station, the recorded event data from the IceScint station were taken between 01.08.18 to 31.10.18. The center of gravity (COG) of the air shower is calculated as an approximation with the weighted square root of their charge with the mean value of the IceScint detectors position in the event by

$$x_{\vec{COG}} = \frac{\sum_{om\epsilon pulses} \vec{x}[om] \cdot \sqrt{Q[om]}}{\sum_{om\epsilon pulses} \sqrt{Q[om]}} \tag{9.2.2}$$

where $Q[om]$ is the baseline correction charge and $\sum_{om\epsilon pulses}$ the pulses in ADC counts [96, 42].

For the shower core position (Figure 9.6) the short runs (Chapter 8) were used, since there is the DRS4 sampled waveform available. The overall reconstruction was successful for 78608 events.

However the COG positions are located inside of the area of where the IceScint detectors are placed. As the COG is the weighted average of the detector positions, no shower core can be reconstructed outside of this area. For the short runs 1626 events could be reconstructed.

In Figure 9.6 the events are displayed. The blue markers indicate the position of the 7 IceScint detectors and the reconstructed events are plotted as 2D-histogram.

No hot spot and no drift in one stations corner is visible and it can be assumed that the reconstruction with the event data is uniform. In case an IceScint detector would contribute a much higher signal rate, e.g. the overall gain would be different compared to other detectors, therefore more SiPM waveforms would initiate the signal-over-threshold trigger, a weighting would be visible.

This is another indication that the installed IceScint station behaves uniformly.

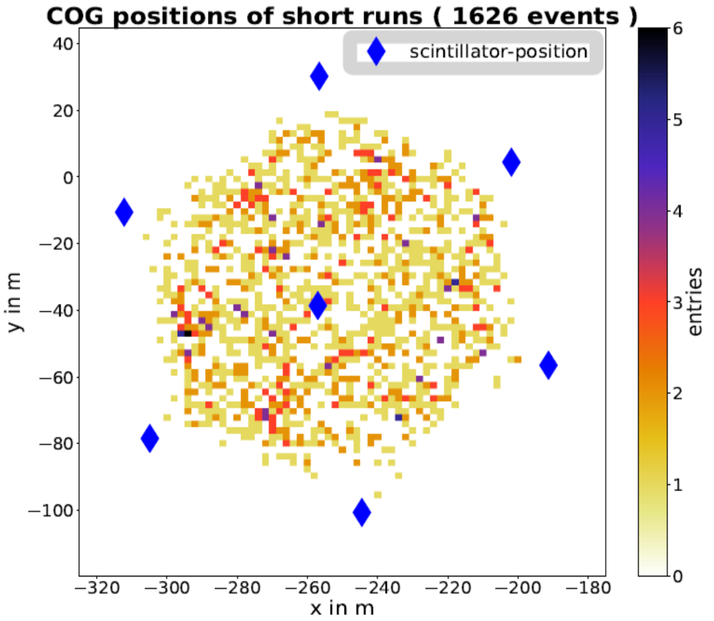

Figure 9.6: Positioning of the shower cores, plotted as 2D-histogram distribution in the instrumented area. The blue markers indicate the position of the IceScint detectors [96].

Shower core footprint IceScint vs. reconstructed IceTop shower core

For the IceTop shower size, shower direction and core the Laputop reconstruction software of the IceCube Collaboration is used. It is a maximum-likelihood reconstruction algorithm for IceTop air shower events and takes the first guesses of the shower core and plane as seed and makes a fit to the lateral distribution of charges in an event [98]. This software was used for all following comparisons between the IceScint station and the IceTop array, including the azimuth and zenith angular differences.

For the IceScint station, the same plane-front-fit like before is used and taken as seed for a fit to the lateral distribution of the shower parameters. Like before, only the short runs of the IceScint station and where the waveforms are available, were used. It was possible to find 8413 events where the reconstruction with Laputop was successful [96].

The slightly "donut"-shape in core positions is caused by the geometry of the small scintillator station inside the IceTop array. The distribution of the reconstructed shower core locations is like expected and fits to the results of the CoG reconstruction of only locally the IceScint station which were shown before.

9.3 Reconstructed IceScint versus IceTop arrival direction

The zenith and azimuth angle are in the following used as parameter for the air shower arrival direction (Figure 9.8). The incidence direction was reconstructed by the same plan-front-fit for the station and the IceTop reconstruction is made with Laputop.

9212 events were successful reconstructed with IceScint data. In total 20527 coincident events were found, the loss of events is caused by difficulties in determining the base-

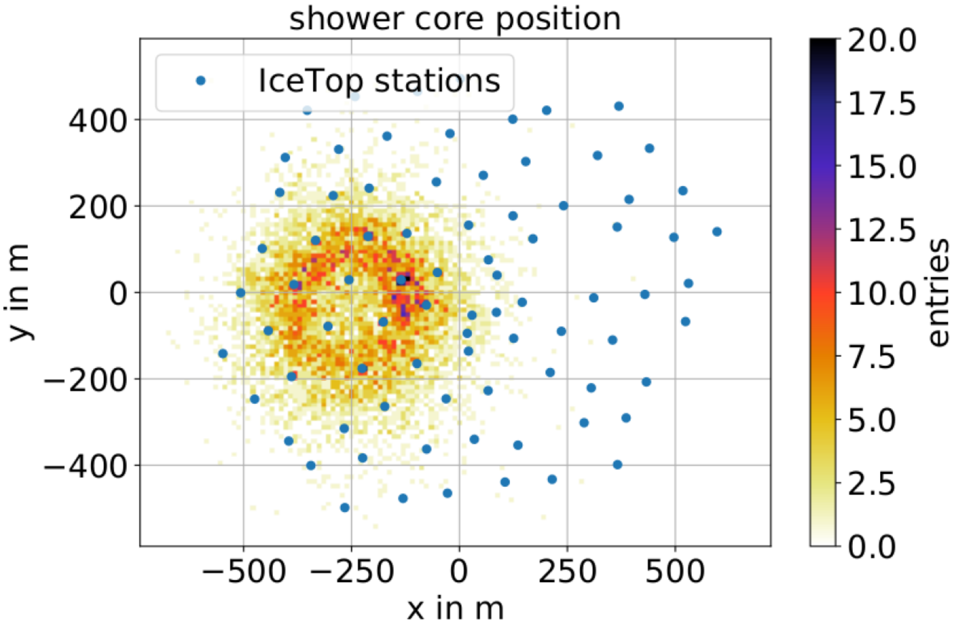

Figure 9.7: Shower core position for the IceTop reconstruction of events in coincidence with the IceScint data set. The blue dots are marking the position of the IceTop stations. Each of the station consists of 2 IceTop tanks. [96].

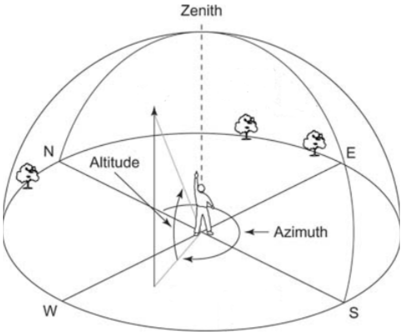

Figure 9.8: Illustration of the zenith and azimuth angle definition. Edited from [99]

line. Some events have a correct trigger timing but the charge of the pulse is negative. If the baseline estimates was badly estimated, these events have been rejected in the reconstruction [96]

The distribution of the zenith and azimuth is typical for an air shower array. Due to the small station size and the small amount detectors, no major findings can be expected apart from showcasing that the angular distribution is as it should be and that the IceScint station is therefore working properly.

Histogram of differences between IceScint and IceTop reconstructions

The accuracy of the scintillator air-shower reconstruction is estimated by comparing the reconstructed shower plane values with the ones obtained from IceTop data. In Fig-

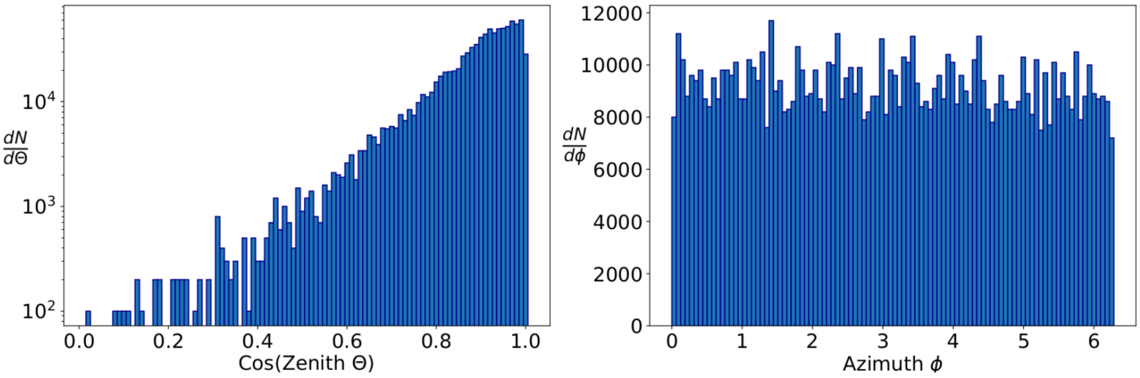

Figure 9.9: Distributions of the reconstructed zenith and azimuth angles of events detected by the IceScint station which are coincident with IceTop events. [91].

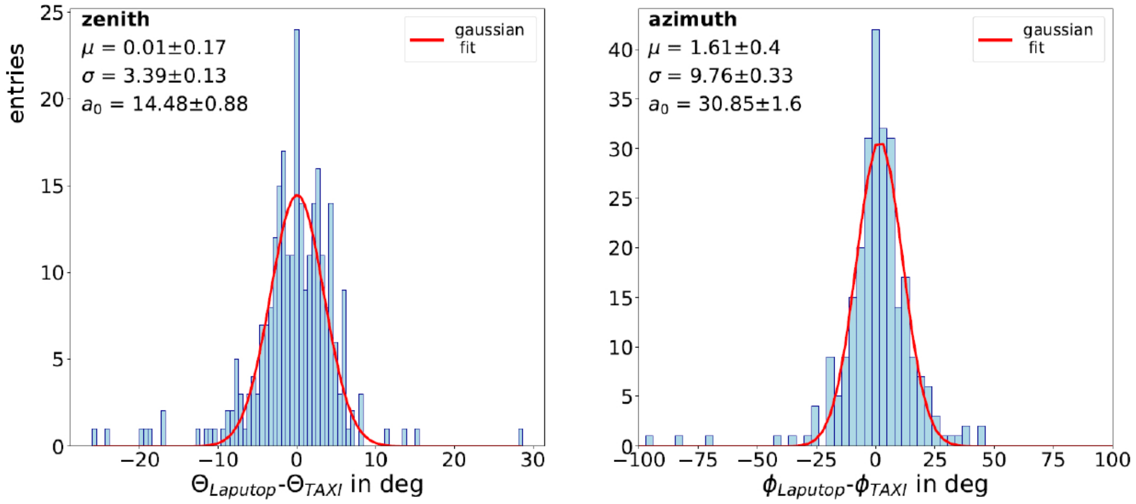

Figure 9.10: Histograms of the differences between the IceScint station event reconstruction zenith (left) and azimuth (right) angles and the IceTop Laputop reconstructions. Only IceTop events within the scintillator area are considered. The Gaussian fits are in red with fit results shown in the top-left [91].

ure 9.10 the differences in the zenith and azimuth angle of the plane front between the Icescint station and the IceTop Laputop reconstruction are shown. A quality cut for events with by Laputop reconstructed shower core inside the IceScint station from events with successful IceScint and IceTop reconstruction has been performed and led to 272 coincident air-shower events [96].

The via Laputop reconstructed angles of the IceTop events can be found in [96]. A good correspondence between the results of the reconstructions is obtained, therefore the quality of the timing information is rather good and sufficient for air shower detection.

The given resolution of ~3.4 and ~9.8 degree for zenith and azimuth are a folding of the resolutions by IceTop and IceScint. This is very good and promising as IceTop has a rather bad resolution of ~2-3 degree for these low-energy showers.

In conclusion, the direction of incident air showers are reconstructed accurately, taking into account the small number of the detectors and the size of the station. It shows no hints that one IceScint detector is not uniform or that an IceTAXI DAQ channel is processing the scintillator data differently. The reconstruction accuracy is well in agreement with the values obtained from simulations of the IceScint station [42] and with IceTop air shower events.

It is a proof of concept of the feasibility of the detector design and its IceTAXI DAQ of the deployed IceScint station and showcases it fulfills the requirements of a surface enhancement of the IceTop array with IceScint stations.

10 IceARM for teaching and outreach

Since the basic IceARM electronics is, without the signal modulation by the GP-board to a double ended differential, necessary for the South Pole IceScint station, a generic analog readout of the SiPM, it can be used as multi-purpose readout for several experiments which transforms light into an electronic signal by a SiPM. IceARM can handle a variety of different types of SiPMs. This is possible since the power supply at the readout board is fully programmable and as much variable as the following next part in the readout chain, the digitization and DAQ of the specific experiment. In this Chapter three applications of IceARM outside of IceScint are briefly presented. Additional applications, like a small SiPM based muon tower or a underground background detector for possible dark matter underground experiments are under discussion.

10.1 Low-Level-Light sensor demonstrator for SENSE

The SENSE project was a Horizon 2020[1] Coordination and Support Action aimed to coordinate research and development efforts in academia and industry in low light-level sensoring. In addition, SENSE aimed to transfer knowledge by initiating information and training events and material, for sharing the status of existing LLL sensors and providing information by outreach experiments and activities [100]. During my PhD thesis I used the previously and within the thesis learned expertise to contribute in the organization team and expert group of the SENSE project [2]. Next to small lectures about detectors and sensors in astroparticle physics, several demonstrators were developed and shown at different workshops and conferences (Figure 10.1). Most of the detector readout demonstrators were based on the developed IceScint detectors readout, IceARM.

As example, at the Baksan school for the lecture “Application of Photosensors for astroparticle physics experiments” IceARM was used as demonstrator for SiPM readout used and for the DPG spring meeting in Münster the readout board and the cookie board of IceARM with a SiPM soldered on it were used to showcasing dark box measurements like the gain and the breakdown voltage of one specific SiPM, including analysis software.

10.2 Mini-IceScint as student practice experiment

Based on the IceCube scintillation detectors, small scintillation detectors are built for the advanced physics lab course at KIT (“P3 Praktikum”) in the frame of the master thesis of Anja Schmidt [101]. The baseline design of the IceScint detectors is adopted with ad-

---

[1] Grant agreement no. 713171.

[2] https://www.sense-pro.org/about/organisation

Figure 10.1: Left: SENSE Project Logo. Right: SENSE at DPG Münster with readout demonstrator for several SiPMs.

justments in the detector dimensions and the in IceARM readout electronics and in the installed type of SiPM.

The dimensions, i.e. the MIP-sensitive area, is given by from the conditions in the practical course, especially from the already existing magnetic coil, into which one of the detectors will be placed in the experimental setup to determine the Landè Factor in terms of a lab course for students. As for the IceCube IceScint detector, aluminum U-profiles and aluminum sheets are used. Due to the height restriction in the magnetic coil, the detector is constructed from U-profiles of different heights. The part where the scintillators are located is lower, the part where the optical coupling and electronics are located is higher. The two parts are linked with connectors. The detectors for the physics lab course get an additional double bottom for more stability. It should be possible to open the detector at any time. Therefore sleeve nuts with matching screws are chosen instead of screws and nuts or rivets. Nuts are also not used for fastening the angles and connectors, instead the threads are cut directly into the components. Instead of one military connector, a couple of connectors are used so that the functioning can be demonstrated more clearly in the physics lab course.

The number and length of the scintillator bars is determined by the size of the magnetic coil. 10 bars with a length of about 93.5 cm are used, which is half the length of the IceCube scintillator bars (Figure 10.2). Therefore five scintillators are grouped together in the back routing instead of four. The front routing is also changed. A short straight piece is inserted. This further separates the electronics from the magnet and the wavelength-shifting fibers are long enough outside the scintillator to absorb the not desired wavelengths. Since reducing the number of scintillator bars also reduces the number of fibers, Michael Riegel designed a new 3d printed fiber-fit-in for the cookie.

Summarized, the changes in the front-end readout electronics, and the SiPM for Mini-IceScint are:

- The baseline design of the readout electronic is kept. Therefore an analog signal output of the scintillators is readout with IceARM.

Figure 10.2: Top: CAD of the housing of Mini-IceScint and the interior design. The baseline design of the IceScint detector was adopted and adjusted to the smaller dimensions in terms of MIP-sensitive area, therefore shorter and scintillator bars are used. The holder of IceARM was redesigned to fit into the experimental setup of the student practice "P3" experiment [101].

- The cookie board is used with no changes compared to IceScint.
- Since the cable length is short compared to the 70 m cable of IceScint to TAXI, and in addition the TAXI DAQ is not used, there is no need for a differential analog signal generation and, therefore, the General Purpose (GP) board is not used for Mini-IceScint,
- The Python control script of the Hamamatsu power supply onboard the readout board for adjusting the SiPM parameters is adjusted for easier use for students,
- Like discussed in Chapter 5 and 6, there is the option to use SiPMs with a larger or smaller amount of APD cells at the photosensitive area. For IceScint, the aim is to increase the dynamic range of the full system by choosing the smaller pitch (25 μm) which generates less charge and therefore needs lees ADC-counts to resolve the charge deposit. For Mini-IceScint it turns out that is more important for the DAQ to have a larger, more PMT-like, signal amplitude and shape. Therefore the version with the higher pitch (50 μm) is used. The series of SiPM is, beside of the pitch size, the same as described in Chapters 5 and 6.
- It is planned to digitize the analog signal of Mini-IceScint with a PicoScope. The software to analyse the digitized data will be written in the frame of a master thesis at KIT-ETP [102].

A "first light" was observed with the first full assembled detector (Figure 10.3). Shown is a screenshot of an oscilloscope, connected to the IceARM setup inside of Mini-IceScint. The waveforms of the three different (1x, 5x, 10x) amplifications (blue, pink, yellow)

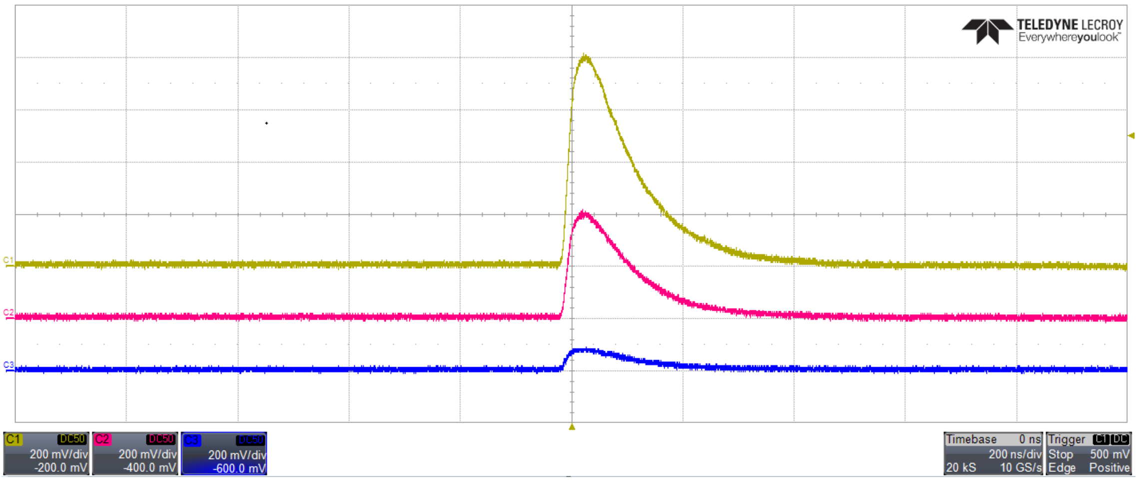

Figure 10.3: Screenshot of the LeCroy Waverunner 620z oscilloscope, connected to all 3 (different gain) connectors of the first assembled detector of IceScint. Visible is the waveform of the "first light" by a MIP event.

are triggered at high charge events, therefore MIP-events. The thermal noise, like dark counts, of the SiPM are visible as rippling noise at the baseline, which indicates the high signal-to-noise ratio of the detector.

The electronics were tested separately before being installed in the single Mini-IceScint detectors. This includes the check of the amplification factors of the readout-Board and the dependence of the amplification factor on the pulse length (Figure 10.4, left). It shows that, as it is fulfilled for IceScint (Chapter 8), the stable amplification of the SiPM signal in the pulse length interval which is expected for MIP induced photon bunches. The tests also include the determination of the SiPM breakdown voltage at 25°C (Figure 10.4, right), which were made for each used SiPM and is necessary for the temperature-control-loop formula (see Chapter 6).

The temperature dependence of the SiPM breakdown voltage was measured with the cooling chamber, analog to the procedure described in Chapter 6. The temperature sensor is also calibrated analog to [57]. With the results of these measurements, the temperature control loop is set up, which adjusts the bias voltage of the SiPM with temperature to stabilize the gain of the SiPM (Figure 10.5, right).

At this point of the PhD thesis, on basis of the developments for IceScint the detector for this special application could be designed, constructed and is now being tested and integrated in the lab course.

10.3 SiPM Muon Coffee Cans with IceARM readout

The "Kamiokanne" was originally developed in Mainz[3] to explain and demonstrate the Cherenkov Effect especially in schools and lab courses. Water-filled Cherenkov detectors are an omnipresent experiment technique in (astro) particle physics research. The effect is used, among others, in experiments like Super-Kamiokande in Japan to detect neutri-

---

[3] http://kamiokanne.uni-goettingen.de/geschichte.htm

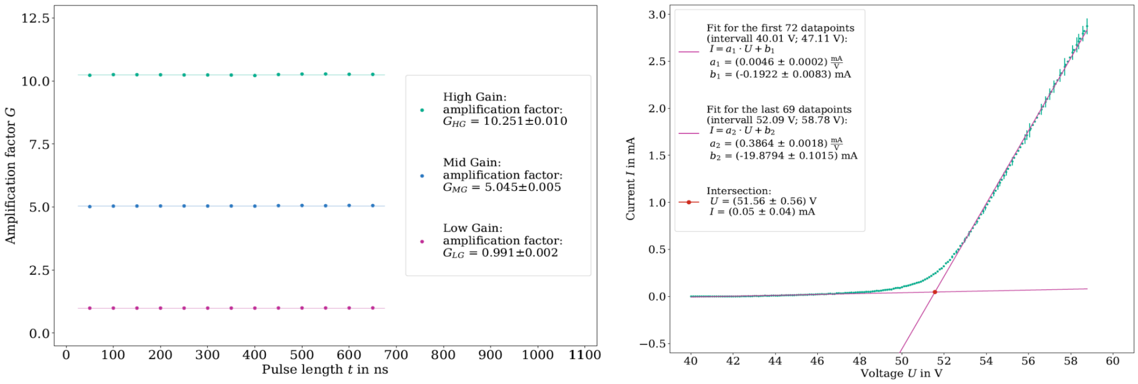

Figure 10.4: Left: Amplification factor G of the three Op-Amp paths onboard one of the readout boards. A stable amplification factor for typical MIP induced SiPM signals is expected. Right: Example I-V curve to obtain the breakdown voltage of one of the four used SiPMs at 25°C for Mini-IceScint. This specific breakdown voltage is necessary to distinguish for the usage of the temperature control loop [101].

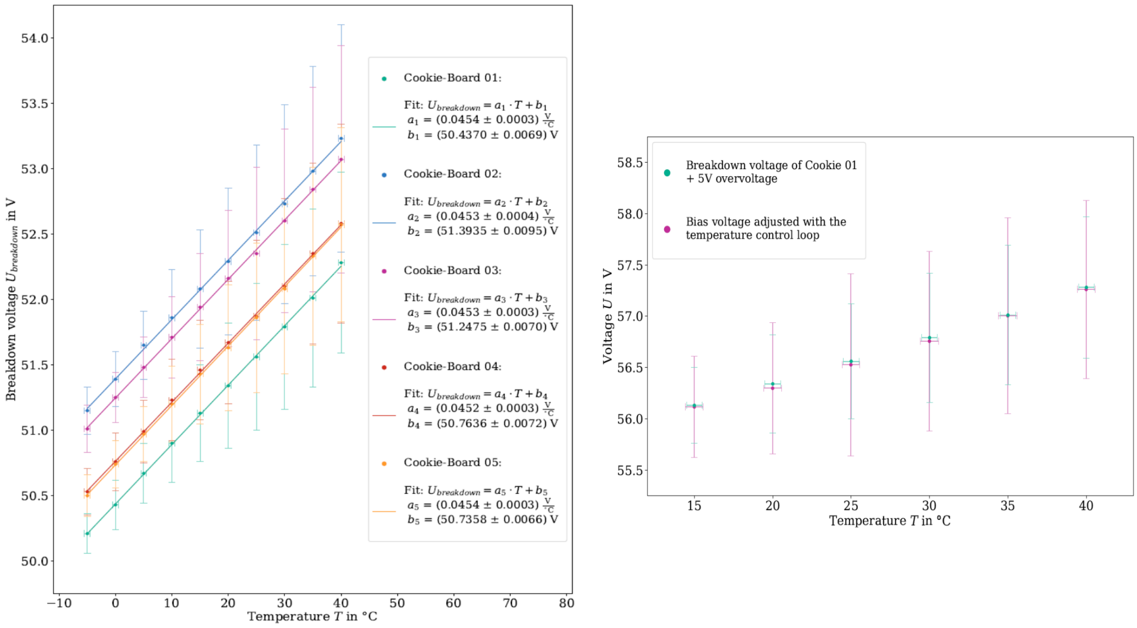

Figure 10.5: Left: Dependency of the breakdown voltage of all 5 SiPMs on the temperature. Each data point is obtained from one I-V curve (Figure 10.4, right). The slope of the linear fits follow the previous measurements for the IceScint detectors. Right: The operational voltage vs the temperature for different set voltages (blue). The adjustments by the temperature control loop are visible in pink [101].

nos and other astroparticle [103]. In addition, detectors of the Pierre-Auger-Observatory and IceCube are based on this effect. The condition for Cherenkov radiation is that a uniformly moving electric charge in the medium has a velocity greater than the speed of light in the medium. The speed of light in the medium is related to the speed of light in a vacuum via the refractive index $c_m = \frac{c}{n}$. In contrast to luminescence, the electromagnetic radiation emitted by the Cherenkov effect is a directional quantity, so that the radiation is emitted at a certain angle to the direction of propagation [104]. This angle is given by the relationship

$$\cos(\Theta) = \frac{c}{v \cdot n}. \tag{10.3.1}$$

The particle travels the distance $v \cdot \Delta t$ in the medium, while the wavefront, which travels at the velocity v, travels the distance $c_m \cdot \Delta t$. From trigonometric considerations, the angle is related to the distance traveled: $c_m \cdot \Delta t = \cos(\Theta) \cdot v \cdot \Delta t$. This leads to:

$$\cos(\Theta) = \frac{c_m \cdot \Delta t}{v \cdot \Delta t} = \frac{c}{n \cdot v}. \tag{10.3.2}$$

Traditionally, the Cherenkov light produced is detected in detector volumes via a photomultiplier tube whose cathode is mechanically connected to the water in the detector volume. This detector volume can be, as example, a coffee can filled with water. This means that for the (movable intended) experimental setup an operating voltage of more than 1000 V has to be generated to reach the breakdown voltage of the PMT. In addition, since a large part of the PMT consists of a vacuum tube, the handling and transport of the experiment is susceptible to shocks and breaks.

SiPMs have a lower operating voltage (~50 V) and the advantage over PMTs of not being permanently damaged or destroyed even in light exposure (Chapter 5). A disadvantage of SiPMs is the small photosensitive area of currently maximum 6x6 mm^2. This makes the sensor area about one order of magnitude smaller than the cathode of a conventional PMT. For example, the Kamiokanne, one of the first outreach detectors, has a PMT with a diameter of 50.8 mm and thus a detection area of 206 mm^2. This requires a redesigned optical coupling to the detector material, similar to the coupling of the scintillator bars of IceScint, which in this case is water.

In contrast to scintillators, the water, and thus the detector material, can be removed from the coffee can easily. In this way it can be made clear to pupils and students that light is produced in water due to the Cherenkov effect and it can be discussed how this effect is produced (Figure 10.6). Furthermore, by simple modifications (Figure 10.10) and enhancements of the setup, the rate, the penetrating ability, the direction of incidence, the velocity and the lifetime of muons can be determined [105].

To investigate the amount of light yield to obtain by the generated Cherenkov light, different modifications of the IceScint optical readout were developed. Figure 10.7 shows all used cookie boards for the first demonstrator at KIT for a cherenkov coffee can, with different optical fiber setups. On the left side two unglued Cookie Boards are shown. The other 3 boards are glued to the cookie with optical cement. All three mounts are equipped with light conducting fibers whose ends are directly directed to the SiPM. In the first cookie, the fibers are cut and polished so they are in line with the lower edge of

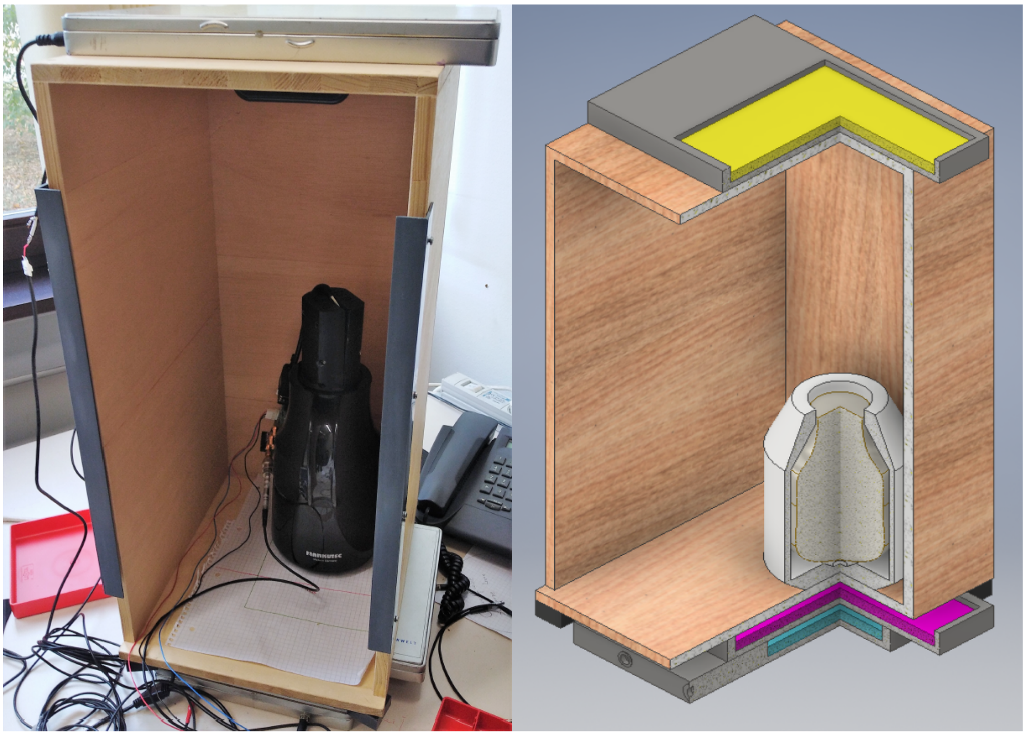

Figure 10.6: Shown is one setup (left) for the proof of concept of reading out Cherenkov coffee cans and its CAD (right). This setup was used for coincidence measurements with scintillators which are placed on top and on bottom of the coffee can [106].

the cookie. Fibers are glued to the right of the cookie, which are attached in a straight line, this shape is called "spaghetti". On the right side the cookie is glued with fibers which are arranged in the shape of an egg whisk, i.e. both cable ends are glued to the SiPM surface.

For the very first demonstrator of the readout of coffee cans with the IceScint front-end electronics and with SiPMs, the IceARM was used in nearly original state (Figure 10.8). By first measurements with an oscilloscope it was possible to trigger high-charge deposit events, which means above the noise level of the electronic and SiPM and therefore Cherenkov light. The trigger level threshold voltage was set to a value around hundred times above the SiPM thermal noise and still the coffee can setup produced a high charge event rate of ~4 Hz, inside of the lab building. This leads to further investigation of the setup and to improvements in the mechanical coupling and different test setups to distinguish the optical fiber alignment with the highest light yield.

The incident muons comply with the requirements of a Poisson process and thus the distances between the individual coincidences should be negatively exponentially distributed, analogous to the time interval between two high charge events measured and seen with the IceScint detectors (Chapter 9). The distribution of the time intervals between the three and four-fold coincidences was checked for several measurement and experimental setups. The exponential distribution was found in all measurements without significant scattering (Figure 10.9). It can be seen that an exponential fit describes the distribution of the time intervals well. From this it can be concluded that there is no interference from regular interference pulses, e.g. from a defective photon shielding.

Figure 10.7: Left: Picture of the different readouts of the SiPM and the different optical fiber setups to investigate the light yield produced by Cherenkov light. Right: Developed holder for the glued cookie with the SiPM and the optical fiber. In addition it serves as photon shielding and easy system to attach and detach different optical fiber setups by an integrated thread which fits to the thread of the used coffee cans.

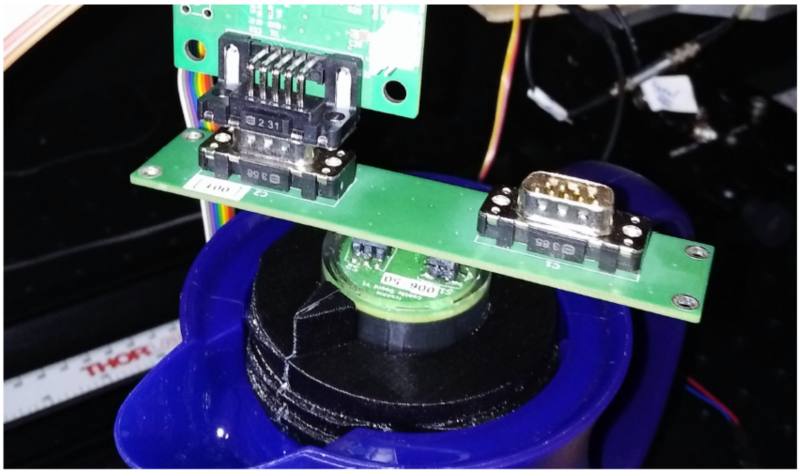

Figure 10.8: The first proof of principle electronic front-end setup for reading out the SiPM coffee cans. The original IceARM and its connectors were used without modification. Visible are the coffee can, the 3D-printed cookie holder, the adapter board and the readout board of IceARM. The GP-board is missing since it is not necessary to generate a analog differential SiPM signal [106].

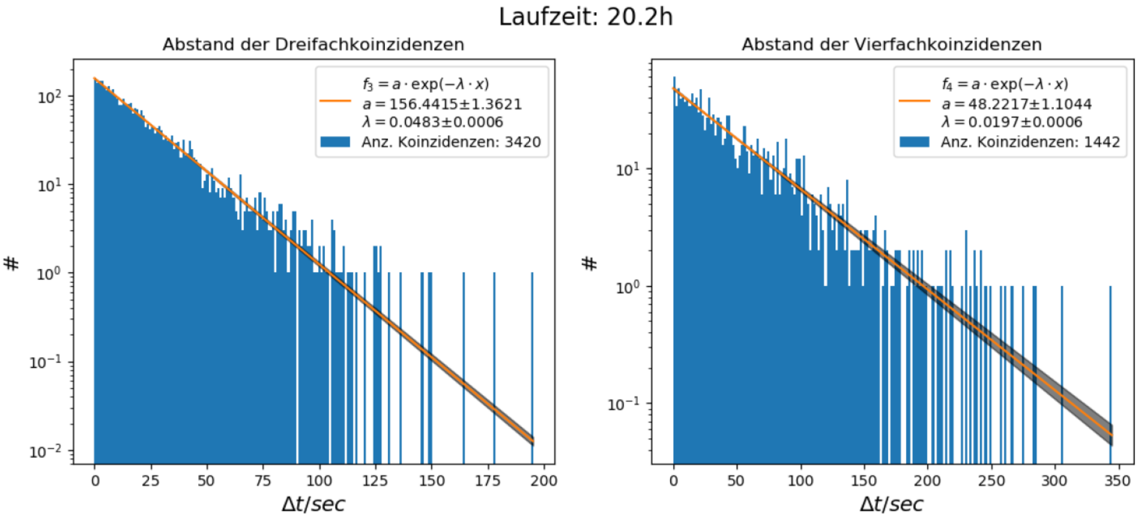

Figure 10.9: Distribution of the time intervals between threefold (left) and fourfold (right) coincidences. In this example, the black can with the spaghetti setup was measured for just over 20 hours. The height of the bins is plotted logarithmically [106].

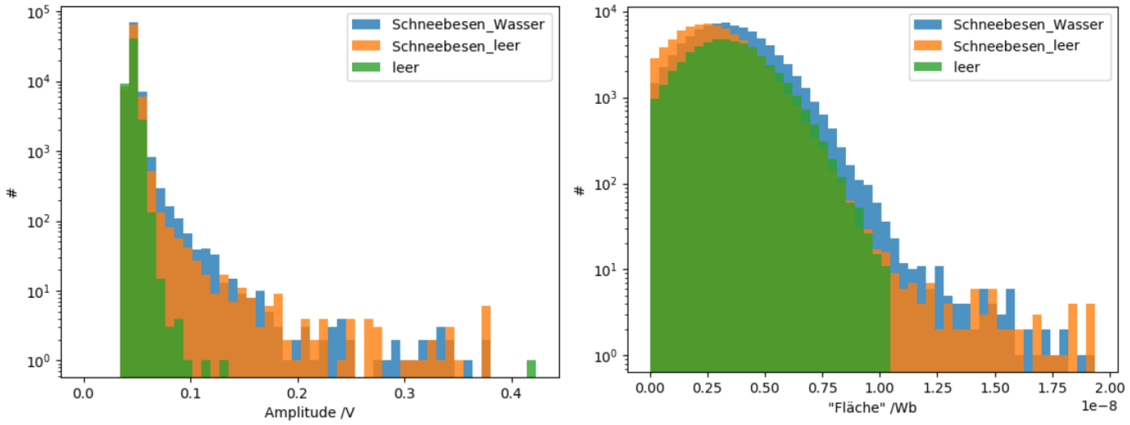

Figure 10.10: Comparison of amplitudes (left) and integrated charges (right) with three different configurations of SiPM Muon cans: With fiber and water (blue), only with fiber without water (orange) and without fiber and without water (green). The Cherenkov effect, induced by incident muons, is clearly visible.

In order to demonstrate to pupils and students the functionality of the SiPM coffee cans, i.e. that muons are actually measured via the Cherenkov effect, different amplitude and charge integrated histograms were compared (Figure 10.10). The difference between a SiPM muon can with optical fibers and water, only optical fibers without water and a can without fiber and without water is clearly visible and shows the functionality of the system of optical fibers, the Cookie and IceARM, adapted from IceScint.

With the Staatsexamen thesis of D. Schwer [106], in connection with an IceARM version from this thesis, which was still identical at that time to the one used for IceScint, it could be shown that muon coffee cans can also be read by a SiPM and that the cherenkov light can be distinguished from the noise of the SiPM and the electronics. The wavelength shifting fibers are collecting enough Cherenkov effect induced photons in an one liter detector volume enough Cherenkov effect induced photons that a SiPM can produce a signal resolvable for a Picoscope. Since the cookie board of IceARM was not developed to be exposed to moisture, further tests and prototypes are necessary to prevent short circuits.

11 Summary and outlook

The surface component of the IceCube Observatory, IceTop, will be enhanced by new detector components the coming years. IceTop examines the cosmic-ray sky by investigating the muonic and electromagnetic component of air showers. However, the accuracy of IceTop is limited and therefore more detailed measurements are needed to understand the astrophysics of high-energy cosmic-ray. As basic element of the necessary improvements to reach this goal, an enhancement of IceTop is proposed which consists of homogeneously-spaced scintillator stations, IceScint, with an areal coverage similar to IceTop.

Over the next few years, it is planned to deploy up to 37 stations including scintillation detectors (IceScint) and radio antennas. Each IceScint station comprises of seven scintillation detectors and three radio antennas communicating with a central DAQ.

For each IceScint detector 16 plastic scintillator bars are used in combination with wavelength shifting optical fibers to collect and guide the light produced by a minimum ionizing particle which is crossing the scintillator volume. The 32 optical fiber ends are read out by a silicon photomultiplier (SiPM). This new kind of low light-yield photo sensors have several advantages compared to classical photomultipliers like a more robust design, is more cost effective and has an operation voltage below the high-voltage region. In addition, the performance of SiPM increases at low temperatures.

A coupling is fixing the 32 optical fiber ends via optical cement along with the photosensitive area of the SiPM, which is soldered on a printed circuit board. This PCB is a part of IceARM, a new developed analog SiPM readout system which in addition consists of an adapter, a readout and a general purpose board. The SiPM signal is read out and amplified already inside the detector and the analog signal is transferred double-ended differential to IceTAXI.

The IceTAXI DAQ consists of an FPGA and a micro controller unit embedded Linux system. The used Spartan 6 FPGA timestamps the incoming scintillator signals with a nanosecond precision. After each of the eight income channels of IceTAXI is discriminated, the waveforms can either be sampled with a one nanosecond resolution by a switched capacitor array named DRS4 or charge-integrated online by the FPGA.

The characterization measurements for each individual IceARM and SiPM have been made and afterwards 24 detector units were built. A test procedure was developed and performed to each detector. A full system test of the set-up IceScint station was successfully made in cooling chambers in the Physical Science Lab in Stoughton, Illinois.

After the shipment of the station and the travel to the South Pole, the station was deployed and in a first commissioning phase installed and linked into the satellite uplink to receive data at the Northern Hemisphere. Afterwards, IceTAXI was calibrated using measurement data from the station at the South Pole and a cloned station set-up at KIT.

For the South Pole station a daily run procedure was set up and several commissioning runs performed. A SiPM temperature control loop to stabilize the gain of one IceScint detector was developed and analyzed for functionality. The charge histograms have been calibrated and fit functions developed. The performance status of the detectors at the South Pole was tested after several months of the deployment and the data of the IceScint station regarding air-shower reconstruction capabilities are analyzed.

The light yield of the IceScint detectors in terms of $\frac{PE}{MIP}$ is much higher then the set requirements. The relatively large dark current of SiPMs is even when operating the detectors at room temperature negligible. After the construction of the detectors each one was tested and characterized with the KIT muon tower. The detectors are highly uniform and operated as uniform station at the South Pole. It turned out that the development of the whole detector system is well thought out. Not a single detector was damaged by the hard transport to and at the South Pole. The climatic conditions did not affect the interaction of the individual components. The electronics did not show a single system failure during the whole measurement season.

The aim of this thesis was to develop and study this prototype IceScint scintillation detector station foreseen for the IceCube IceTop Enhancement. The focus of this thesis was to develop the scintillation detectors with its mechanical and electronic components. The interface of the detectors with the IceTAXI DAQ was clarified and characterized. It included the commissioning phase of the station and the characterization of IceTAXI after the deployment at the South Pole. Afterwards, the investigation of the gained measurement data from the South Pole and the analysis of air-shower reconstructions have shown the detector capabilities and proven to have a fully operating IceScint station.

The flexibility due to the modular design of IceARM has benefited several other experiments with needs of analog SiPM readout electronics, at the point of this thesis mostly located in student teaching and outreach experiments.

The thesis provide a proof of design and concept not only for the scintillation detector design with SiPMs but also for the IceTAXI data acquisition structure and the usage of the White Rabbit timing system. It brings a significant contribution to the enhancement of the current IceTop and paves the way for a new large-scale instrumentation of the South Pole surface for new discoveries and insights in astroparticle physics.

Acknowledgment

First of all I thank Prof. Dr. Marc Weber, head of the IPE, that he has given me the possibility to work in this interesting and diverse field of research. His advice helped me to find the right paths to realize IceScint and his institute helped a lot in terms of technical guidance and production of the electronics.

Prof. Dr. Günter Quast of the ETP was not only an important advisor during all the years in the readout of detectors, but also gave me insights into the science community and how best to perform.

It is difficult to overstate my gratitude to Dr. Andreas Haungs. With his enthusiasm and his inspiration he helped to make this thesis successful. His ability to select and to approach research problems, his high scientific standards and his hard work set an example. Thanks to him I was able to gain an immense amount of experience in presenting my ideas, my work and finally the results at many conferences and meetings. Thanks to him I was able to gain my first touches in teaching, from being head of a tutorium to be allowed giving my first lectures. He provided encouragement and sound advice. I would have been lost without him in many ways.

Thanks to Prof. Dr. Christian Stegmann and Prof. Dr. Marek Kowalski from DESY in Zeuthen I was able to do my doctorate at two Helmholtz research centers. It was only thanks to the trust placed in me to be able to further strengthen the partnership between DESY and KIT that I was capable to develop IceScint in such a short time. Special thanks go to the DESY secretaries in Zeuthen. Everything organizational went smoothly and I always felt very comfortable.

Due to the great interest, given advice and support of in the IceCube surface enhancement by the head of the IKP, Prof. Dr. Ralph Engel, many processes could be accelerated and in many aspects it was only possible to make progress so quickly thanks to his support.

I would also like to thank Dr. Timo Karg for the detailed answers to all my questions, the many explanations and for his extensive professional support for this thesis and IceScint. In particular, the introduction to IceCube and the TAXI DAQ during the Zeuthen stays and the pleasant and efficient help at the PSL in Stoughton was important for the successful full-system test of IceScint.

I would like to thank Dr. Harald Schieler for the discussions and the helpful support in the conception and planning of the production, Bernd Hoffmann not least for his help in the production of the IceScint detectors, his advice in the development of IceARM and the cabling of IceScint. Special thanks goes to Andreas Weindl, who not only gave me jTAXI, a visualization tool for the detector signals, helped me with the setup of the daily data recording of the IceScint station but, apart from that, was always there for me at professional and personal discussions.

I need to express my thanks to Mr. Weber and his team in the mechanical workshop of the IKP for the flawless and fast production of the required mechanical components of IceScint and for the loan of all the tools for the South Pole deployment. Special thanks go to the staff of the IPE for professional help and especially to Mr. Bacher for his great dedication in the component placement of all IceARM PCBs.

A lot of people of the Auger group helped me in many ways for IceScint. In particular thanks because of the great motivation of Michael Riegel it was possible to develop the optical coupling for IceScint in such a short time and without his assistance many steps up to the finished detectors would have been much slower. Thank you for the great help, not only at business but also on a friendly private basis. Thanks to Dr. Darko Veberic for the time spent with the muon tower measurements!

It would not have been possible to create IceTAXI in this short time without the great technical knowledge and dedication of DESY Zeuthen staff members. In specific, thanks for this to Karl-Heinz Sulanke and Marko Kossatz.

My further thanks goes to the staff of the IKP/EKP for their support and the friendly working atmosphere. I am grateful to the secretaries for helping the institute to run smoothly and for assisting me in many different ways. Sabine Bucher deserves a special mention. She had to deal with a lot of travel requests and with my silly jokes. Probably I would still be stuck in New Zealand without Sabine. Thanks to my office colleagues of the CRT group who always stood by me with advice and action. Thanks to Aswathi and Agnieszka for the nice discussions and the mutual support. Special thanks go to Max, who was always willing to help. William for the awesome help at and around the IKP and the fun evenings in and around Karlsruhe. Thanks to Frank Schröder of University of Delaware and KIT that we got the lecture module over the stage so successfully and that I was allowed to learn a lot of didactic skills.

Without all the students who decided to come and do their thesis at my place, IceScint would simply not have been possible. I cannot point out a single person, all your work and help was outstanding. Thanks to Anja Schmidt, Marie Oehler, Jainam Khara, Eugen Raspopin, David Schwer, Branko Mitic, Fiona Ellwanger and Amrit Nayak. Not to be forgotten are the high school students of the Thomas-Mann Gymnasium in Stutensee who made a real contribution to IceScint during their internship.

Thanks not least to the trust of WIPAC in Madison, I was allowed to prove myself at the South Pole. Thanks for that. For the great collaboration I thank Prof. Kael Hanson, Delia Tosi, Tim Bendfelt, Prof. Mike DuVernois, John Kelley, Perry Sandstrom, Chris Wendt and, last but not least, Matt Kauer. Thank you Matt for the great adventure. Who knows what the future will bring next :-)

Thanks to Dr. Med. Schmidt-Wenning and his entire practice team for all the examinations and the pleasant vaccinations and blood takings. His daughter Laura in particular, who also took time out of the normal practice hours. I would like to thank the MVZ Laboratory Passau for their engagement in translating the blood results for the " salary" of a postcard from the South Pole. The gynecologist Dr. med. Antje Kesel for the missing fast breast exam and dentist practice, DENTID Karlsruhe for the removal and replacement of the not suitable fillings. UTMB Texas and their nurses for answering questions about ambiguities in the requirements for the confirmation of the physical qualification (PQ).

At the end I would like to thank my family, thus Xaver Bauer, my brother Patrick and especially my mother Brigitte, who has not only supported me financially, but has been there for me at all times and in every way, despite the long distance from Bavaria. She raised me up, supported me and taught me to be a good person. To her I dedicate this thesis.

Bibliography

[1] Jörg R. Hörandel. "Early cosmic-ray work published in German". In: *AIP Conference Proceedings 1516* (2013), pp. 52–60. DOI: `10.1063/1.4792540`.

[2] Thomas Huber. "Development and test of a reference light source for the calibration of the EUSO photodetectors". Bachelor Thesis. Karlsruhe Institute for Technology - KIT, 2013.

[3] V. F. Hess. "Über Beobachtungen der durchdringenden Strahlung bei sieben Freiballonfahrten". In: *Phys. Z. 13(1912)1084* ().

[4] Karl-Heinz Kampert and Alan A. Watson. "Extensive air showers and ultra high-energy cosmic rays: a historical review". In: *The European Physical Journal H* 37 (2012), pp. 359–412. DOI: `10.1140/epjh/e2012-30013-x`.

[5] K.-H. Kampert and the Pierre-Auger-Collaboration. "Highlights from the Pierre Auger Observatory". In: *Talk* (2012). arXiv:1207.4823. eprint: `arXiv:1207.4823`.

[6] M.G. Aartsen and ohters. "The IceCube Neutrino Observatory: instrumentation and online systems". In: *Journal of Instrumentation* 12.03 (2017), P03012–P03012. DOI: `10.1088/1748-0221/12/03/p03012`.

[7] Thomas Huber. "Silicon Photomultiplier (SiPMs) for the space-based fluorescence telescope EUSO". Master Thesis. Karlsruhe Institute for Technology - KIT, 2015.

[8] H.V. Klapdor-Kleingrothaus. *Teilchenastrophysik*. 1. Ed. Berlin [u.a.]: Teubner, 1997.

[9] H. Kolanoski. "Vorlesungsscript: Einführung in die Astroteilchenphysik". In: *Institut für Physik, Humboldt-Universität Berlin* (2009).

[10] J. Blümer, R. Engel, and J. Hörandel. "Cosmic Rays from the Knee to the Highest Energies". In: *Progress in Particle and Nuclear Physics* 63 (2009), pp. 293–338.

[11] L. A. Anchordoqui, V. Barger, H. Goldberg, J. G. Learned, et al. "End of the cosmic neutrino energy spectrum". In: *Phys. Lett. B* 739 (2014), p. 99. DOI: `10.1016/j.physletb.2014.10.037`. arXiv: `1404.0622 [hep-ph]`.

[12] M.G. Aartsen et al. "The IceCube realtime alert system". In: *Astroparticle Physics* 92 (2017), pp. 30–41. DOI: `10.1016/j.astropartphys.2017.05.002`.

[13] Mark Aartsen et al. "Multimessenger observations of a flaring blazar coincident with high-energy neutrino IceCube-170922A". In: *Science* 361.6398 (2018). DOI: `10.1126/science.aat1378`.

[14] J. Matthews. "A Heitler model of extensive air showers". In: *Astrop. Physics 22 (2005) 387* (2005).

[15] Jim Schoorlemmer Harmand Hinton and Rubén López-Coto. “Characteristics of extensive air showers around the energy threshold for ground-particle-based gamma-ray observatories”. In: *The European Physical Journal C* 79.5 (May 2019). DOI: `10.1140/epjc/s10052-019-6942-x`.

[16] Carmen Gámez, Miguel Gutiérrez, Juan S. Martínez, and Manuel Masip. *High energy muons in extensive air showers*. 2019. eprint: `arXiv:1904.12547`.

[17] F. Schroeder et al. “Overview on the Tunka-Rex antenna array for cosmic-ray air showers”. In: *PoS* ICRC2017 (2017), p. 401.

[18] R. Abbasi et al. “IceTop: The surface component of IceCube”. In: *Nucl. Instrum. Meth. A* 700 (2013), pp. 188–220. DOI: `10.1016/j.nima.2012.10.067`.

[19] *The Pierre-Auger-Collaboration Collaboration Homepage - Press Photos*. `http://web.archive.org/web/20080207010024/http://www.808multimedia.com/winnt/kernel.htm`. Accessed: 2019-08-8.

[20] William Painter, Andreas Haungs, Thomas Huber, and Michael Karus. “Silicon Photomultipliers for Orbital Ultra High Energy Cosmic Ray Observation”. In: *Proceedings of the 36th International Cosmic Ray Conference* (2019).

[21] Max Renschler, Aswathi Balagopal, Andreas Haungs, Thomas Huber, et al. “Detector developments for a hybrid particle and radio array for cosmic-ray air-shower detection”. In: *Journal of Physics: Conference Series* 1181 (Feb. 2019), p. 012075. DOI: `10.1088/1742-6596/1181/1/012075`.

[22] Andreas Haungs. “A Scintillator and Radio Enhancement of the IceCube Surface Detector Array”. In: *EPJ Web Conf.* 210 (2019), p. 06009. DOI: `10.1051/epjconf/201921006009`. arXiv: `1903.04117 [astro-ph.IM]`.

[23] D. Groom et al. “Muon Stopping Power and Range”. In: *Atomic Data and Nuclear Data Tables* 76 (2001).

[24] N. Sakaki et al. “Energy estimation of AGASA events”. In: *Proceedings of the 27th International Cosmic Ray Conference* (2001).

[25] Peter Grieder. *Extensive Air Showers*. 1. ed. Berlin: Springer, 2010.

[26] D. Beznosko, A. Bross, A. Dyshkant, and P. -. V. Rykalin. “FNAL-NICADD extruded scintillator”. In: *IEEE Symposium Conference Record Nuclear Science 2004.* Vol. 2. 2004, 790–793 Vol. 2.

[27] *Private Correspondence with Dr. Matt Kauer, UW-Madison*. 2018.

[28] P. Destruel, M. Taufer, C. D’Ambrosio, C. Da Via, J.P. Fabre, J. Kirkby, and H. Leutz. “A new plastic scintillator with large stokes shift”. In: *Nuclear Instruments and Methods in Physics Research Section A: Accelerators, Spectrometers, Detectors and Associated Equipment* 276.1 (1989), pp. 69–77. ISSN: 0168-9002. DOI: `10.1016/0168-9002(89)90617-7`.

[29] Mathieu Bennet. “Multi-Parameter quantitative mapping of Microfluidic Devices”. PhD thesis. University of Edinburgh, Jan. 2011.

[30] Roberto P. M. Carvalhaes, Daniel A. B. Bonifácio, and Maurício Moralles. “Position Sensitive Detectors Mounted with Scintillators and Silicon Photomultipliers”. In: *AIP Conference Proceedings* 1351.1 (2011), pp. 202–206. DOI: `10.1063/1.3608957`.

[31] Logan James Wille. “The Search for High Energy Tau Neutrinos using the IceCube Neutrino Observatory”. PhD Thesis to be published. PhD thesis. University of Madison - Wisconsin, 2019.

[32] *The IceCube Collboration Collaboration Homepage - Press Photos*. `http://web.archive.org/web/20080207010024/http://www.808multimedia.com/winnt/kernel.htm`. Accessed: 2019-08-12.

[33] *The IceCube Collboration IceCube Reconstruction Introduction 2015*. `https://icecube.wisc.edu/~kjero/Bootcamp/2015/Notebooks/Reconstruction_Introduction.html`. Accessed: 2019-08-12.

[34] M. G. Aartsen et al. “Measurement of Atmospheric Tau Neutrino Appearance with IceCube DeepCore”. In: *Phys. Rev.* D99.3 (2019), p. 032007. DOI: `10.1103/PhysRevD.99.032007`. arXiv: `1901.05366 [hep-ex]`.

[35] M Tanabashi et al. “Review of Particle Physics: Particle Data Group”. In: *Physical Review D* 98 (Aug. 2018).

[36] *Landschaft der Forschungsinfrastrukturen - IceCube*. DESY - Deutsches Elektronen-Synchrotron, 2017.

[37] Aya Ishihara. “The IceCube Upgrade - Design and Science Goals”. In: *Proceedings of the 36th International Cosmic Ray Conference* (2019).

[38] M. C. Sanchez. *Muon Neutrino Disappearance and Tau Neutrino Appearance*. 2011. eprint: `arXiv:1112.0618`.

[39] Aartsen et al. “IceCube-Gen2: A Vision for the Future of Neutrino Astronomy in Antarctica”. In: *arXiv:1412.5106* (Dec. 2014).

[40] Jakob van Santen. “IceCube-Gen2: the next-generation neutrino observatory for the South Pole”. In: *PoS* ICRC2017 (2018), p. 991. DOI: `10.22323/1.301.0991`.

[41] Max Renschler. “A Prototype Radio Detector for the IceCube Surface Enhancement”. DOI:10.5445/IR/1000104529. PhD thesis. Karlsruhe Institute of Technology, 2020.

[42] Agnieszka Leszczynska. “Potential of the IceTop Enhancement with a Scintillation Detector Array”. to be published. PhD thesis. Karlsruhe Institute of Technology, 2020.

[43] D. H. Schaubert, A. O. Boryssenko, A. van Ardenne, J. G. Bij de Vaate, and C. Craeye. “The square kilometer array (SKA) antenna”. In: *IEEE International Symposium on Phased Array Systems and Technology, 2003.* 2003, pp. 351–358.

[44] A. Balagopal V., A. Haungs, T. Huege, and F. G. Schroeder. “Search for PeVatrons at the Galactic Center using a radio air-shower array at the South Pole”. In: *Eur. Phys. J.* C78.2 (2018), p. 111. arXiv: `1712.09042 [astro-ph.IM]`.

[45] P. Eger, G. Rowell, A. Kawamura, Y. Fukui, L. Rolland, and C. Stegmann. *A multi-wavelength study of the unidentified TeV gamma-ray source HESS J1626-490*. 2010. arXiv: `1009.1724 [astro-ph.HE]`.

[46] R. D. Parsons, M. Holler, J. King, V. Lefranc, et al. *Sgr A* Observations with H.E.S.S. II*. 2015. arXiv: `1509.03425 [astro-ph.HE]`.

[47] Frank Schröder. “Science Case of a Scintillator and Radio Surface Array at IceCube”. In: *PoS* ICRC2019 (2019), p. 418.

[48] T. Bretz, T. Hebbeker, J. Kemp, L. Middendorf, et al. “A compact and light-weight refractive telescope for the observation of extensive air showers”. In: *JINST* 13.07 (2018), P07024. DOI: `10.1088/1748-0221/13/07/P07024`. arXiv: `1804.01781 [astro-ph.IM]`.

[49] Andreas Haungs. “A Scintillator and Radio Enhancement of the IceCube Surface Detector Array”. In: *EPJ Web Conf.* 210 (2019), p. 06009. DOI: `10.1051/epjconf/201921006009`. arXiv: `1903.04117 [astro-ph.IM]`.

[50] The IceCube Collborattion. “The Effect of Snow Accumulation on Signals in IceTop”. In: *32st ICRC (2013)* (2012).

[51] Kuraray Co Ltd. *Plasting scintillating fiber datasheet*. 2017.

[52] HAMAMATSU Photonics Co. Ltd. *TSV-MPPC S13360-6050PE SiPM datasheet*. 2017.

[53] T. Karg, A. Haungs, M. Kleifges, et al. “Introducing TAXI: a Transportable Array for eXtremely large area Instrumentation studies”. In: *International Workshop on Acoustic and Radio EeV Neutrino detection Activities*. arXiv:1410.4685 [astro-ph.IM]. Annapolis, MD, USA, June 2014.

[54] *SPARTAN-6 family overview, datasheet*. XILINX Co Ltd., 2011.

[55] Alexander Streich. “Scintillator Surface Detector for the Upgrade of the Pierre Auger Observatory”. Master Thesis. Karlsruhe Institute for Technology - KIT, 2016.

[56] Pierre Auger Collaboration. *The Pierre Auger Observatory upgrade “AugerPrime”: Preliminary Design Report*. Tech. rep. arXiv:1604.03637 [astro-ph.IM]. -, 2016.

[57] Anja Schmidt. “Temperature characteristics of the IceCube-Gen2 surface detector”. Bachelor Thesis. Karlsruhe Institute for Technology - KIT, 2017.

[58] Michael Karus, Francesca Bisconti, Thomas Huber, and Andreas Haungs. “Ground Calibration of MAPMT and SiPM for JEM-EUSO”. In: *Proceedings of the 34th International Cosmic Ray Conference* 612 (2015).

[59] Amphenol Industrial Co. Ltd. *PT-Series Miniature Cylindrical Connectors datasheet*. 2017.

[60] M. Lipinski, T. Wlostowski, J. Serrano, and P. Alvarez. “White rabbit: a PTP application for robust sub-nanosecond synchronization”. In: - (2011), pp. 25–30. DOI: `10.1109/ISPCS.2011.6070148`.

[61] *Guidance Document to the IHS for importing Containers*. Ministry for Biosecurity New Zealand Branch, 2019.

[62] *Private Correspondence with Michael Riegel, KIT-IKP*. 2017-2019.

[63] *EJ-500 optical cement, datasheet*. Eljen Technology Co. Ltd., 2016.

[64] HAMAMATSU Photonics Co. Ltd. *C11204-2 Power supply for MPPCs, datasheet*. 2016.

[65] PSI DRS4 Homepage. *https://www.psi.ch/drs/evaluation-board*. Web Source. Feb. 2016.

[66] *Private Correspondence with Karl-Heinz Sulanke, DESY Zeuthen*. 2017-2019.

[67] Analog devices. *Data sheet LTM9007-14 low octoal ADC*. 2016.

[68] TasKit GmbH Homepage. *User manual Stamp9G45*. Feb. 2018.

[69] *Private Correspondence with Dr. Timo Karg, DESY Zeuthen*. 2017-2020.

[70] ECS Inc. *HC-49US Oscillator datasheet*. 2013.

[71] Alessandro Rubini et al. "White Rabitt user manual V. 5.0.1". In: - (2017).

[72] *ADA4932-1/ADA4932-2 Rev. E, datasheet*. Analog devices Co. Ltd., 2009.

[73] Analog Devices Co. Ltd. *Single-Supply LVDS Comparators ADCMP604 datasheet*. 2015.

[74] *FTSH Series Micro Terminal Strip Catalogue Page, datasheet*. SAMTEC Co. Ltd., 2012.

[75] Weiss Technik GmBH. *User manual Voetsch Temperaturpruefschrank VT 7021*. 2017.

[76] Michael Karus. "Development of a Calibration Stand for Photosensors for Extremely High-Energy Cosmic Ray Research". PhD Thesis. Karlsruhe Institute for Technology - KIT, 2016.

[77] Lapsphere Co. Ltd. *A Guide to integrating sphere - Theory and applications*. 2011.

[78] Max Renschler. "Characterisation of 64 channel SiPM arrays for the Silicon Elementary Cell Add-on". Master Thesis. Karlsruhe Institute for Technology - KIT, 2017.

[79] Marie Oehler. "Characterization of SiPMs for the Surface Array Enhancement of IceCube". Master Thesis. Karlsruhe Institute for Technology - KIT, 2018.

[80] Branko Mitic. "Cold-SPOCK; A Low Temperature Calibration Setup for Detector Research and Development within IceCube". Bachelor Thesis. Karlsruhe Institute for Technology - KIT, 2018.

[81] Thorlabs Co. Ltd. *M93L01 - Stainless Steel SMA-SMA Fiber Patch Cable datasheet*. 2018.

[82] Labsphere Inc. *General Purpose Integrating Spheres datasheet*. 2015.

[83] Ophir Optronics Solutions Ltd. *Photodiode Power Sensors product cataloge*. 2019.

[84] -. *Temperaturpruefstand HT4002 User Manual*. Heraeus Industrietechnik, 1995.

[85] -. *Handbook Si-APD, MPPC, 3rd Edition*. Hamamatsu Photonics, 2014.

[86] I. Atanasov et al. "Large Muon tracking detector in the air shower experiment KASCADE". In: *Forschungszentrum Karlsruhe,* FZKA6474 (2000), p. 06009.

[87] Jan-Ole Gosewisch. "Scintillation detector development Mini-KASCADE". Bachelor Thesis. Karlsruhe Institute for Technology - KIT, 2017.

[88] Alexander Schneider. "Air-Shower reconstruction software development Mini-KASCADE". Bachelor Thesis. Karlsruhe Institute for Technology - KIT, 2017.

[89] Thomas Huber et al. "The IceTop Scintillator Upgrade". In: *Proceedings of the 35th International Cosmic Ray Conference* (2017), p. 401. DOI: `10.22323/1.301.0401`.

[90] *Private Correspondence with Dr. John Kelley, UW-Madison*. 2018.

[91] Thomas Huber et al. "The Scintillator Upgrade of IceTop: Performance of the Prototype Array". In: *Proceedings of the 36th International Cosmic Ray Conference* ICRC2019 (2019), p. 309.

[92] *Private Correspondence with Dr. Delia Tosi, UW-Madison*. 2018.

[93] *Private Correspondence with Harald Schieler, KIT-IKP*. 2016-2020.

[94] *Private Correspondence with Andreas Weindl, KIT-IKP*. 2017-2020.

[95] Eugen Raspopin. "Bachelor Thesis: Calibration of the ADCs and discriminator threshold of the IceTAXI data aquisition system". Bachelor Thesis. Karlsruher Institute of Technology - IKP, 2018.

[96] Fiona Ellwanger. "Capabilities of the KIT/DESY IceScint scintillator station at the South Pole". Bachelor Thesis. Karlsruhe Institute for Technology - KIT, 2019.

[97] M. Beimforde. "Calibration of air shower signals in the IceTop detector using cosmic ray muons". In: *Diploma Thesis HU Berlin* (2007).

[98] *IceCube Laputop reconstruciton software - user manual*. `http://software.icecube.wisc.edu/documentation/projects/toprec/laputop.html`. Accessed: 2020-06-02.

[99] *Naked-Eye Astronomy - Homepage*. `https://www.cliffsnotes.com/study-guides/astronomy/observing-the-sky/naked-eye-astronomy`. Accessed: 2020-05-18.

[100] Thomas Huber. "The SENSE Project: Developments, Characteristics and Application of Low Light-Level Photosensors". In: *Proceedings of the 36th International Cosmic Ray Conference* ICRC2019 (2019), p. 146.

[101] Anja Schmidt. "Working-Title: Mini-IceScint for physics students lab courses (P3)". Master Thesis. Karlsruhe Institute for Technology - KIT, 2020.

[102] Christoph Mayer. "Working-Title: Software development for Mini-IceScint for physics students lab course (P3)". Master Thesis. Karlsruhe Institute for Technology - KIT, 2021.

[103] Christopher W. Walter and for the Super-Kamiokande collaboration. "The Super-Kamiokande Experiment". In: *Neutrino Oscillations*, pp. 19–43. DOI: `10.1142/9789812771971_0002`.

[104] Theo Mayer-Kuckuk. "Atomphysik - Eine Einführung". In: *Teubner Studienbücher Physik* (1997).

[105] T. Karg, A. Schulz, C. Schwerdt, and U. Behrens. *Teilchenphysik - Unterrichtsmaterial ab der 10. Klasse - Kosmische Strahlung*. Joachim Herz Stiftung und Netzwerk Teilchenwelt, 2016.

[106] David Schwer. "Analyse von Wasser-Cherenkov-Detektoren für physikalische Praktika mit SiPMs". Staatsexamen Arbeit. Karlsruhe Institute for Technology - KIT, 2018.

Appendix

This appendix shows only a selection of the many CADs, technical drawings, board designs, circuit diagrams, test routine instructions and commissioning protocols generated in the course of this thesis.

All material is located on a dedicated server of the IKP.

Table of Content

Example of one test protocol : Foregoing temperature sensor test for each IceScint detector

	getestet mit Readout-Board 003, 20.07.2017, 11:30 Uhr	getestet mit Readout-Board 022, 21.07.2017, 15:20 Uhr	getestet mit Readout-Board 005, 24.07.2017, 14:50 Uhr			getestet mit Cookie-Board 003-50, 20.07.2017, 15:15 Uhr	getestet mit Cookie-Board 003-50, 21.07.2017, 15:00 Uhr	
Cookie-Board	Spannung in mV	Spannung in mV	Spannung in mV	gemessene Temperatur	Readout-Board	Spannung in mV	Spannung in mV	gemessene Temperatur
003-50	892			26,09	003-	901		24,45
004-50	888			26,82	004-	901		24,45
005-50	891			26,28	005-	901		24,45
006-50	893			25,91	006-	901		24,45
007-50		888		26,82	007-	900		24,64
008-50	894			25,73	008-	901		24,45
009-25			895	25,55	009-	901		24,45
010-25			896	25,37	010-	901		24,45
011-25			892	26,09	011-		895	25,55
012-25			889	26,64	012-		897	25,18
013-25			891	26,28	013-		895	25,55
014-25			901	24,45	014-	900		24,64
015-25			896	25,37	015-	900		24,64
016-25			896	25,37	016-		890	26,46
017-					017-	900		24,64
018-					018-	900		24,64
019-					019-	899		24,82
020-					020-	899		24,82
021-					021-	898		25,00
022-					022-		888	26,82
023-					023-	897		25,18
024-					024-	896		25,37
025-					025-	896		25,37
026-					026-	895		25,55
027-					027-	895		25,55
028-					028-	895		25,55
029-					029-	895		25,55

Example of one test protocol : Foregoing readout board functional tests sensor for each IceScint detector

Readout-Board	Spannung einstellen hvc.setReferenceVoltage(50)	LG mean in mV	LG sdev µV	MG mean in mV	MG sdev in mV	HG mean in mV	HG sdev in mV	Bild	Pins für Temperatursensor
003-	✓	94,186	578	486,01	2,89	978,06	5,30	ARM5.png	✓
004-	✓	95,016	584	482,85	1,70	987,25	5,59	ARM6.png	✓
005-	✓	94,856	614	485,81	2,84	989,71	5,12	ARM7.png	✓
006-	✓	94,796	622	485,10	2,69	980,45	5,20	ARM8.png	✓
007-	✓	95,014	597	488,59	2,83	990,27	4,85	ARM9.png	✓
008-	✓	94,297	583	482,33	1,02	980,24	5,88	ARM10.png	✓
009-	✓	95,084	553	489,75	2,77	993,57	1,71	ARM11.png	✓
010-	✓	94,004	608	483,54	1,77	981,73	5,50	ARM12.png	✓
011-	✓	93,082	226	482,00	0,97	970,31	3,79	ARM29.png	✓
012-	✓	94,346	492	485,28	2,87	979,61	4,91	ARM30.png	✓
013-	✓	93,818	576	482,85	2,21	980,42	4,69	ARM31.png	✓
014-	✓	94,682	598	483,73	2,03	981,34	5,49	ARM13.png	✓
015-	✓	94,865	601	483,91	2,24	983,77	5,35	ARM14.png	✓
016-	✓	95,142	520	491,95	2,86	979,12	3,78	ARM32.png	✓
017-	✓	94,610	570	481,63	0,89	983,94	5,60	ARM16.png	✓
018-	✓	95,310	495	483,64	2,20	977,91	5,37	ARM17.png	✓
019-	✓	94,618	593	482,48	1,61	971,64	4,66	ARM18.png	✓
020-	✓	94,599	580	482,28	1,85	972,75	5,08	ARM19.png	✓
021-	✓	94,716	592	486,01	2,84	983,82	5,10	ARM20.png	✓
022-	✓	94,083	573	484,28	2,34	972,18	5,14	ARM33.png	✓
023-	✓	95,133	556	484,98	2,59	987,31	5,67	ARM22.png	✓
024-	✓	95,357	463	483,61	2,22	977,81	5,50	ARM23.png	✓
025-	✓	94,769	596	483,12	1,65	984,59	5,49	ARM24.png	✓
026-	✓	95,316	478	483,09	1,89	973,78	5,44	ARM25.png	✓
027-	✓	95,056	545	483,94	2,19	994,87	2,47	ARM26.png	✓
028-	✓	95,098	560	485,29	2,64	973,09	5,39	ARM27.png	✓
029-	✓	94,996	571	484,23	2,20	985,06	5,56	ARM28.png	✓

Puls: Freq 100Hz, Width 300ns, High 100mV, mean: 98,721mV, sdev: 358 µV

Bill of Materials and instructions for the installation of the IceARM electronics into the first IceScint detectors

Anzahl für 23 Detektoren		Anzahl für einen Detektor	ø	Länge		
soll	ist					
184	≈90	8	M4	12	Schraube	GP- und Readout-Board an 3D-Druck-Halterung
46	46	2	M4	20	Senkkopf-Schraube	3D-Druck-Halterung des GP- und Readout-Boards an Brett*
46	0	2	M4	40	Senkkopf-Schraube	3D-Druck-Halterung des Cookies an Brett**
46	46	2	M3	25	Schraube	Sub-D9-Stecker von Readout-Board zu Adapter-Board
46	46	2	M3	16 (15)	Schraube	Sub-D9-Stecker von Readout-Board zu GP-Board
46	46	2	M3	8	Schraube	Sub-D9-Stecker von GP-Board zu Adapter-Board
46	46	2	M3	6	Schraube	Sub-D9-Stecker von GP-Board zu Militärstecker
46	46	2	M3	40	Schraube	3D-Druck-Halterung des Cookies an Adapter-Board***
276	300	12	M4		Mutter	8 für GP- und Readout-Board an 3D-Druck-Halterung, 2 für 3D-Druck-Halterung des GP- und Readout-Boards an Brett*, 2 für 3D-Druck-Halterung des Cookies an Brett**
184	200	8	M3		Mutter	4 für 3D-Druck-Halterung des Cookies an Adapter-Board***, 2 für Sub-D9-Stecker von Readout-Board zu Adapter-Board, 2 für Sub-D9-Stecker von Readout-Board zu GP-Board
322	≈322	14	M4		Scheibe	8 für GP- und Readout-Board an 3D-Druck-Halterung, 2 für 3D-Druck-Halterung des GP- und Readout-Boards an Brett*, 4 für 3D-Druck-Halterung des Cookies an Brett**
92	≈92	4	M3		Scheibe	2 für Sub-D9-Stecker von Readout-Board zu Adapter-Board, 2 für Sub-D9-Stecker von Readout-Board zu GP-Board
92	≈92	4	M4		Sprengring	2 für 3D-Druck-Halterung der Boards an Brett*, 2 für 3D-Druck-Halterung des Cookies an Brett**

Anmerkungen:

* von unten: Schraube, Holzbrett, 3D-Druck-Halterung der Boards, Scheibe, Sprengring, Mutter

** von unten: Schraube, Holzbrett, 3D-Druck-Halterung des Cookies (Unterteil), 2 Scheiben, 3D-Druck-Halterung des Cookies (Oberteil), Sprengring, Mutter

*** Schraube, 3D-Druck-Halterung des Cookies (Unterteil), Mutter, Adapter-Board, Mutter

Appendix D

```python
#ComPro.py : RS285 Interface with the readout board and the SiPM at the cookie board

#!/usr/bin/env python3

import serial
import sys
#import exceptions
import itertools


class CommandParsingException(Exception):
    def __init__(self, message):
        self.message = message

    def __str__(self):
        return self.message


class ErrorResponseException(Exception):
    def __init__(self, code):
        self.code = code
        self.message = HighVoltageChip._errorCodes[code]

    def __str__(self):
        return "Error ({0}): {1}".format(self.code, self.message)


class HighVoltageChip:
    """
    Interface class to Hamamatsu C11204-02 Power Supply.

    The following functions are available:

     * getOutputVoltage()
     * getOutputCurrent()
     * getTemperature()
     * getStatus()
     * setHighVoltageOutput(bool on)
     * setTemperatureCompensationMode(bool enabled)
     * resetPowersupply()
     * setReferenceVoltage(real voltage)
     * getMonitoringInfo()
     * getTemperatureCorrectionFactor(self)
     * setTemperatureCorrectionFactor(self, real dT1_s, real dT2_s, real dT1, real dT2, real Tb)    #Neu
     * setOverCurrentProtection(bool on)
     * setOutputVoltageControlFunction(bool on)
     * readPowerFunction()

     So far, temperature compensation coefficients cannot be set :-(
     """

    _dataSizes = {
        # the response data size in bytes for each command
        "hxx": 4,
        "hpo": 20,
        "hst": 24,
        "hrt": 24,
        "hof": 0,
        "hon": 0,
        "hcm": 0,
        "hre": 0,
        "hbv": 0,
        "hgt": 4,
        "hgv": 4,
        "hgc": 4,
        "hgs": 4,
        "hsc": 0,        #NEU
        "hrc": 4        #NEU
    }
    _errorCodes = {
        1: "UART Communication Error",
        2: "Timeout Error",
        3: "Syntax Error",
        4: "Checksum Error",
        5: "Command Error",
        6: "Parameter Error",
        7: "Parameter Size Error"
    }
    _voltageConversionFactor = 1.812e-3
    _currentConversionFactor = 4.98e-3
    _firstCoefficientConversionFactor = 5.225e-2
    _secondCoefficientConversionFactor = 1.507e-3

    @classmethod
    def _temperatureConversionFunction(cls, x):
        return (x * 1.907e-5 - 1.035) / (-5.5e-3)

    @classmethod
    def _reversetemperatureConversionFunction(cls, y):
        return (1.035 - 5.5e-3 * y) / (1.907e-5)

    @classmethod
    def _commandResponseSize(cls, cmd):
        return 8 + cls._dataSizes[cmd]

    @classmethod
    def _dataToHex(cls, data):
        out = []
        for offset in range(0, len(data), 4):
            num = data[offset:(offset+4)]
            out.append(int(num, base=16))
        return out

    @classmethod
    def _intToBytes(cls, value):
        return "{0:04x}".format(value).encode("ASCII")

    def __init__(self, deviceFile="/dev/tty.UC-232AC", baud=38400): # 38400, 9600
        """
        Open serial channel via device file to Hamamatsu bridge.
        """
        self._port = serial.Serial(deviceFile, baud , parity=serial.PARITY_EVEN) # NEU!!
        #self._port.open()

    def __del(self):
        self._port.close()

    def _sendCommand(self, cmd, data):
        if isinstance(data, str):
            data = data.encode("ASCII")
        elif isinstance(data, list):
            data = b''.join(HighVoltageChip._intToBytes(v) for v in data)
        elif isinstance(data, int):
            data = HighVoltageChip._intToBytes(data)
        if not isinstance(data, bytes):
            raise ValueError("data parameter cannot be converted to bytes, nor is it binary data")
        responseCmd = cmd.lower()
        cmd = bytes(cmd, "ASCII")
        cmdLine = b'\x02' + cmd + data + b'\x03'
        check = "{0:02x}".format(sum(cmdLine) & 0xff).upper().encode("ASCII")
        cmdLine += check + b'\x0D'
        #print(cmdLine)
        self._port.write(cmdLine)

    def _getResponse(self):
        response = b""
        state = 0
        while True:
            b = self._port.read(1)
```

```
            response += b
            if state == 0 and b == b"\x02":
                state = 1
            if state == 1 and b == b"\x03":
                state = 2
            if state == 2 and b == b"\x0D":
                break
        if(response[0] != 0x02 or
           response[-1] != 0x0D or
           response[-4] != 0x03):
            raise CommandParsingException("Frame bytes did not match")
        try:
            cmd = response[1:4].decode("ASCII")
            if len(response) != HighVoltageChip._commandResponseSize(cmd):
                raise CommandParsingException("Expected data size dos not match
                received data size")
            data = response[4:-4]
            assert(len(data) == HighVoltageChip._dataSizes[cmd])
            checkReceived = int(response[-3:-1], base=16)
            checkCalculated = sum(response[:-3]) & 0xff
            if checkCalculated != checkReceived:
                raise CommandParsingException("Checksum mismatch")
            return cmd, HighVoltageChip._dataToHex(data)
        except IndexError:
            raise CommandParsingException("Unexpected end of data")

    def getOutputVoltage(self):
        "Query the voltage currently on supply output."
        self._sendCommand("HGV", b"")
        cmd, data = self._getResponse()
        if cmd == "hxx":
            raise ErrorResponseException(data[0])
        assert(cmd == "hgv")
        return data[0]*HighVoltageChip._voltageConversionFactor

    def getOutputCurrent(self):
        "Query the measured output current."
        self._sendCommand("HGC", b"")
        cmd, data = self._getResponse()
        if cmd == "hxx":
            raise ErrorResponseException(data[0])
        assert(cmd == "hgc")
        return data[0]*HighVoltageChip._currentConversionFactor

    def getTemperature(self):
        "Query the measured output voltage."
        self._sendCommand("HGT", b"")
        cmd, data = self._getResponse()
        if cmd == "hxx":
            raise ErrorResponseException(data[0])
        assert(cmd == "hgt")
        return HighVoltageChip._temperatureConversionFunction(data[0])

#Neu:
    def getTemperatureCorrectionFactor(self):
        self._sendCommand("HRT", b"")
        cmd, data = self._getResponse()
        if cmd == "hxx":
            raise ErrorResponseException(data[0])
        assert(cmd == "hrt")
        dT1_sec = data[0]*HighVoltageChip._secondCoefficientConversionFactor
        dT2_sec = data[1]*HighVoltageChip._secondCoefficientConversionFactor
        dT1 = data[2]*HighVoltageChip._firstCoefficientConversionFactor
        dT2 = data[3]*HighVoltageChip._firstCoefficientConversionFactor
        vb = data[4]*HighVoltageChip._voltageConversionFactor
        tb = HighVoltageChip._temperatureConversionFunction(data[5])
        return {
                "dT1_sec" : dT1_sec,
                "dT2_sec" : dT2_sec,
                "dT1" : dT1,
                "dT2" : dT2,
                "Vb" : vb,
                "Tb" : tb
                }

    def setTemperatureCorrectionFactor(self, dT1_s, dT2_s, dT1, dT2, tb):
        "Set the Temperature Correction Factors dT1_sec, dT2_sec, dT1, dT2 and
        Reference Temperature Tb"

        #Get Reference Voltage from getTemperatureCorrectionFactor
        vRef = int(getTemperatureCorrectionFactor(self).get(Vb) / HighVoltageChip.
        _voltageConversionFactor)

        #Define mins and maxs of TCFactors
        dTs_max = 0xfc18 * HighVoltageChip._secondCoefficientConversionFactor
        dTs_min = 0x03e8 * HighVoltageChip._secondCoefficientConversionFactor
        dT_max = 0xfff * HighVoltageChip._firstCoefficientConversionFactor
        tb_min = HighVoltageChip._temperatureConversionFunction(0x0000)
        tb_max = HighVoltageChip._temperatureConversionFunction(0xffff)

        if not 0 <= dT1 <= dT_max:
            raise ValueError("dT1 must be in range 0V - {0}V".format(dT_max))

        if not 0 <= dT2 <= dT_max:
            raise ValueError("dT2 must be in range 0V - {0}V".format(dT_max))

        if not dTs_min <= dT1_s <= dTs_max:
            raise ValueError("dT1_s must be in range {0}V - {1}V".format(dTs_min,
            dTs_max))

        if not dTs_min <= dT2_s <= dTs_max:
            raise ValueError("dT2_s must be in range {0}V - {1}V".format(dTs_min,
            dTs_max))

        if not tb_min <= tb <= tb_max:
            raise ValueError("Tb must be in range {0}V - {1}V".format(tb_min, tb_max))


        # Define values for sending to the Power Supply
        value_dT1_s = int(dT1_s / HighVoltageChip._secondCoefficientConversionFactor)
        value_dT2_s = int(dT2_s / HighVoltageChip._secondCoefficientConversionFactor)
        value_dT1 = int(dT1 / HighVoltageChip._firstCoefficientConversionFactor)
        value_dT2 = int(dT2 / HighVoltageChip._firstCoefficientConversionFactor)
        value_tb = int(HighVoltageChip._reversetemperatureConversionFunction(tb))
        value_vb = vRef

        #Send Command
        self._sendCommand("HST", value_dT1_s, value_dT2_s, value_dT1, value_dT2,
        value_vb, value_tb)
        cmd, data = self._getResponse()
        if cmd == "hxx":
            raise ErrorResponseException(data[0])
        assert(cmd == "hst")
#/Neu

    def getStatus(self):
        "Get a dictionary with module status flags."
        self._sendCommand("HGS", b"")
        cmd, data = self._getResponse()
        if cmd == "hxx":
            raise ErrorResponseException(data[0])
        assert(cmd == "hgs")
        status = data[0]
        high_voltage = (status & 1) != 0
        overcurrent_protection = (status & 2) != 0
        current_in_specification = (status & 4) == 0
        sensor_connected = (status & 8) == 0
        sensor_in_specification = (status & 16) == 0
        temp_conv_ef = (status & 64) == 0
        return {
            "high_voltage_on": high_voltage,
            "overcurrent_protection": overcurrent_protection,
```

```
            "current_in_specification": current_in_specification,
            "sensor_connected": sensor_connected,
            "sensor_in_specification": sensor_in_specification,
            "temperature_conversion_effective": temp_conv_ef
        }

    def setHighVoltageOutput(self, on):
        "Switch the high voltage output on and off."
        if on:
            self._sendCommand("HON", b"")
            cmd, data = self._getResponse()
            if cmd == "hxx":
                raise ErrorResponseException(data[0])
            assert(cmd == "hon")
        else:
            self._sendCommand("HOF", b"")
            cmd, data = self._getResponse()
            if cmd == "hxx":
                raise ErrorResponseException(data[0])
            assert(cmd == "hof")

    def setTemperatureCompensationMode(self, enabled):
        "Enable and disable temperature compensation mode."
        if enabled:
            self._sendCommand("HCM", b"\x31")
            cmd, data = self._getResponse()
            if cmd == "hxx":
                raise ErrorResponseException(data[0])
            assert(cmd == "hcm")
        else:
            self._sendCommand("HCM", b"\x30")
            cmd, data = self._getResponse()
            if cmd == "hxx":
                raise ErrorResponseException(data[0])
            assert(cmd == "hcm")

#        self._sendCommand("HCM", b"\x01" if enabled else b"\x00")
        # cmd, data = self._getResponse()
        # if cmd == "hxx":
        #     raise ErrorResponseException(data[0])
        # assert(cmd == "hcm")



    def resetPowersupply(self):
        "Reset power supply to default settings."
        self._sendCommand("HRE", b"")
        cmd, data = self._getResponse()
        if cmd == "hxx":
            raise ErrorResponseException(data[0])
        assert(cmd == "hre")

    def setReferenceVoltage(self, voltage):
        "Set the reference voltage."
        max_v = 0xffff * HighVoltageChip._voltageConversionFactor
        if not 0 <= voltage <= max_v:
            raise ValueError("Reference voltage must be in range 0V - {0}V"
                              .format(max_v))
        value = int(voltage / HighVoltageChip._voltageConversionFactor)
        self._sendCommand("HBV", value)
        cmd, data = self._getResponse()
        if cmd == "hxx":
            raise ErrorResponseException(data[0])
        assert(cmd == "hbv")

    def getMonitoringInfo(self):
        "Get all measured and set parameters."
        self._sendCommand("HPO", b"")
        cmd, data = self._getResponse()
        if cmd == "hxx":
            raise ErrorResponseException(data[0])
```

```
        assert(cmd == "hpo")
        status = data[0]
        vo_set = data[1]*HighVoltageChip._voltageConversionFactor
        vo_mon = data[2]*HighVoltageChip._voltageConversionFactor
        io_mon = data[3]*HighVoltageChip._currentConversionFactor
        T_mon = HighVoltageChip._temperatureConversionFunction(data[4])
        return {"status": status, "vo_set": vo_set, "vo_mon": vo_mon,
                "io_mon": io_mon, "T_mon": T_mon
                }
#Neu:
    def readPowerFunction(self):
        "Get status of Over-Current-Protection-Function and
        Output-Voltage-Control-Function"
        self._sendCommand("HSC", b"")
        cmd, data = self._getResponse()
        if cmd == "hxx":
            raise ErrorResponseException(data[0])
        assert(cmd == "hsc")
        status = data[0]
        if status == 3:
            statusOCP = "Automatic Restoration"
            statusOVC = "Effectiveness"
        elif status == 1:
            statusOCP = "Automatic Restoration"
            statusOVC = "Invalid"
        elif status == 2:
            statusOCP = "Not in use"
            statusOVC = "Effectiveness"
        elif status == 0:
            statusOCP = "Not in use"
            statusOVC = "Invalide"
        else:
            statusOCP = "Error in Response Data"
            statusOVC = "Error in Response Data"
        return {
            "Over Current Protection Function" : statusOCP,
            "Output Voltage Control Function" : statusOVC
            }

    def setOverCurrentProtection(self, on):
        "Set Over Current Protection Function"
        rPF = readPowerFunction(self)            #Looks whether Output Voltage
        Controle is set or not
        if rPF.get("Output Voltage Control Function") == "Effectiveness":
            if on:
                self._sendCommand("HSC", 3)
                cmd, data = self._getResponse()
                if cmd == "hxx":
                    raise ErrorResponseException(data[0])
                assert(cmd == "hsc")
            else:
                self._sendCommand("HSC", 2)
                cmd, data = self._getResponse()
                if cmd == "hxx":
                    raise ErrorResponseException(data[0])
                assert(cmd == "hsc")
        elif rPF.get("Output Voltage Control Function") == "Invalide":
            if on:
                self._sendCommand("HSC", 1)
                cmd, data = self._getResponse()
                if cmd == "hxx":
                    raise ErrorResponseException(data[0])
                assert(cmd == "hsc")
            else:
                self._sendCommand("HSC", 0)
                cmd, data = self._getResponse()
                if cmd == "hxx":
                    raise ErrorResponseException(data[0])
                assert(cmd == "hsc")
        else:
            return {"Not able to get Output-Voltage-Control-Function Status"}
```

```

    def setOutputVoltageControlFunction(self, on):
        "Set Output Voltage Control Function"
        rPF = readPowerFunction(self)                    # Looks whether Over
        Current Protection is set or not
        if rPF.get("Over Current Protection Function") == "Automatic Restoration":
            if on:
                self._sendCommand("HSC", 3)
                cmd, data = self._getResponse()
                if cmd == "hxx":
                    raise ErrorResponseException(data[0])
                assert(cmd == "hsc")
            else:
                self._sendCommand("HSC", 1)
                cmd, data = self._getResponse()
                if cmd == "hxx":
                    raise ErrorResponseException(data[0])
                assert(cmd == "hsc")
        elif rPF.get("Over Current Protection Function") == "Not in use":
            if on:
                self._sendCommand("HSC", 2)
                cmd, data = self._getResponse()
                if cmd == "hxx":
                    raise ErrorResponseException(data[0])
                assert(cmd == "hsc")
            else:
                self._sendCommand("HSC", 0)
                cmd, data = self._getResponse()
                if cmd == "hxx":
                    raise ErrorResponseException(data[0])
                assert(cmd == "hsc")
        else:
            return {"Not able to get Over-Current-Protection-Function Status"}
#/Neu


    def help(self):
        "Displays a help message."
        print(help(HighVoltageChip))

if __name__ == "__main__":
    try:
        deviceFile = sys.argv[1]
    except IndexError:
        deviceFile = "/dev/ttyACM0"
    hvc = HighVoltageChip(deviceFile)
    #print(hvc.getMonitoringInfo()["vo_mon"])
    #hvc.setReferenceVoltage(65.0)
    #print(hvc.getMonitoringInfo()["vo_mon"])
    import code
    code.interact("Interactive Powersupply Control\nUse 'hvc' object for access,
    hvc.help() shows functions", local={"hvc": hvc})

```

Appendix E

Muon tower measurements of the IceScint detectors 001-023

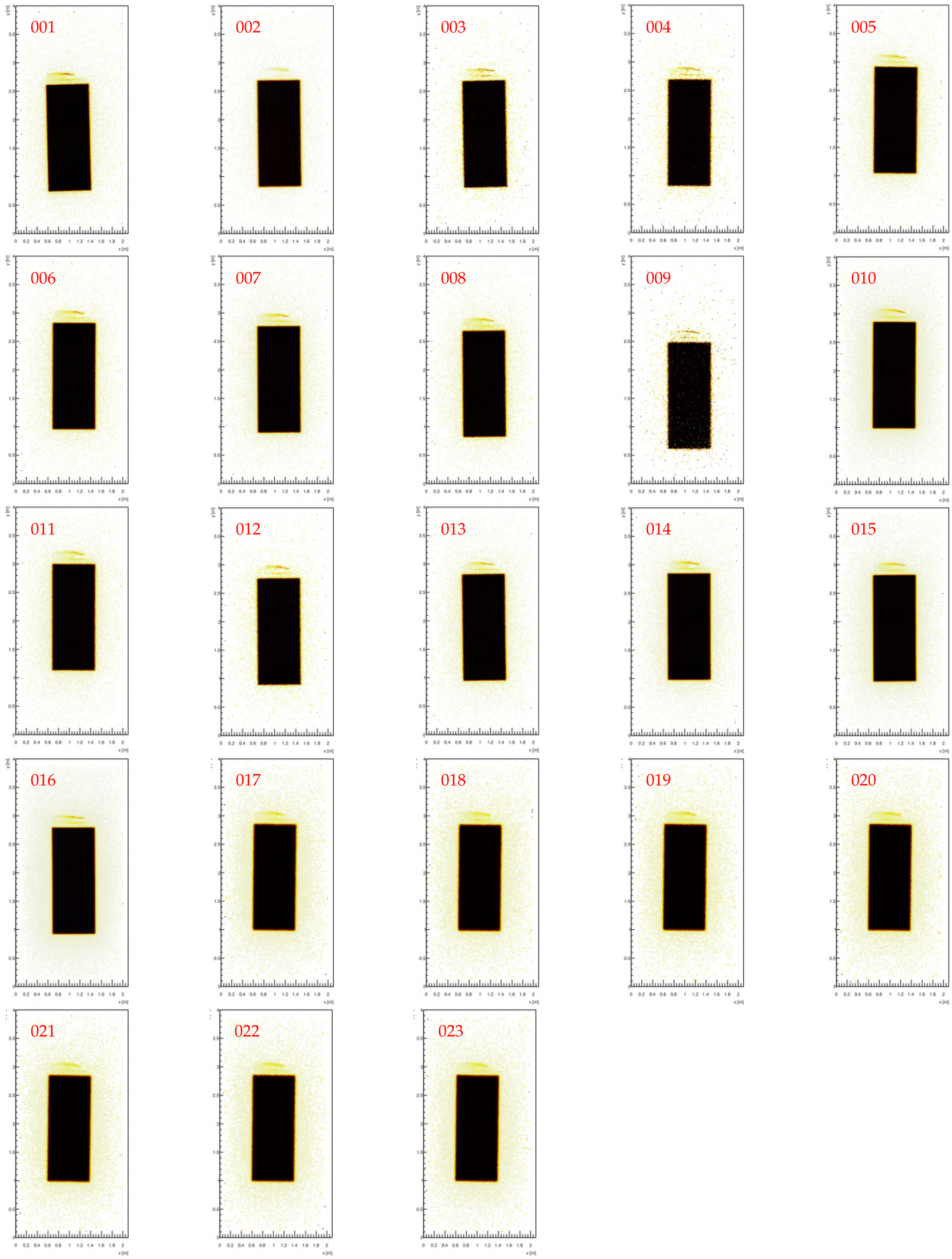

Figure 1: Efficiency, defined as the probability to see “light” (even with a very small number of photons or PE).

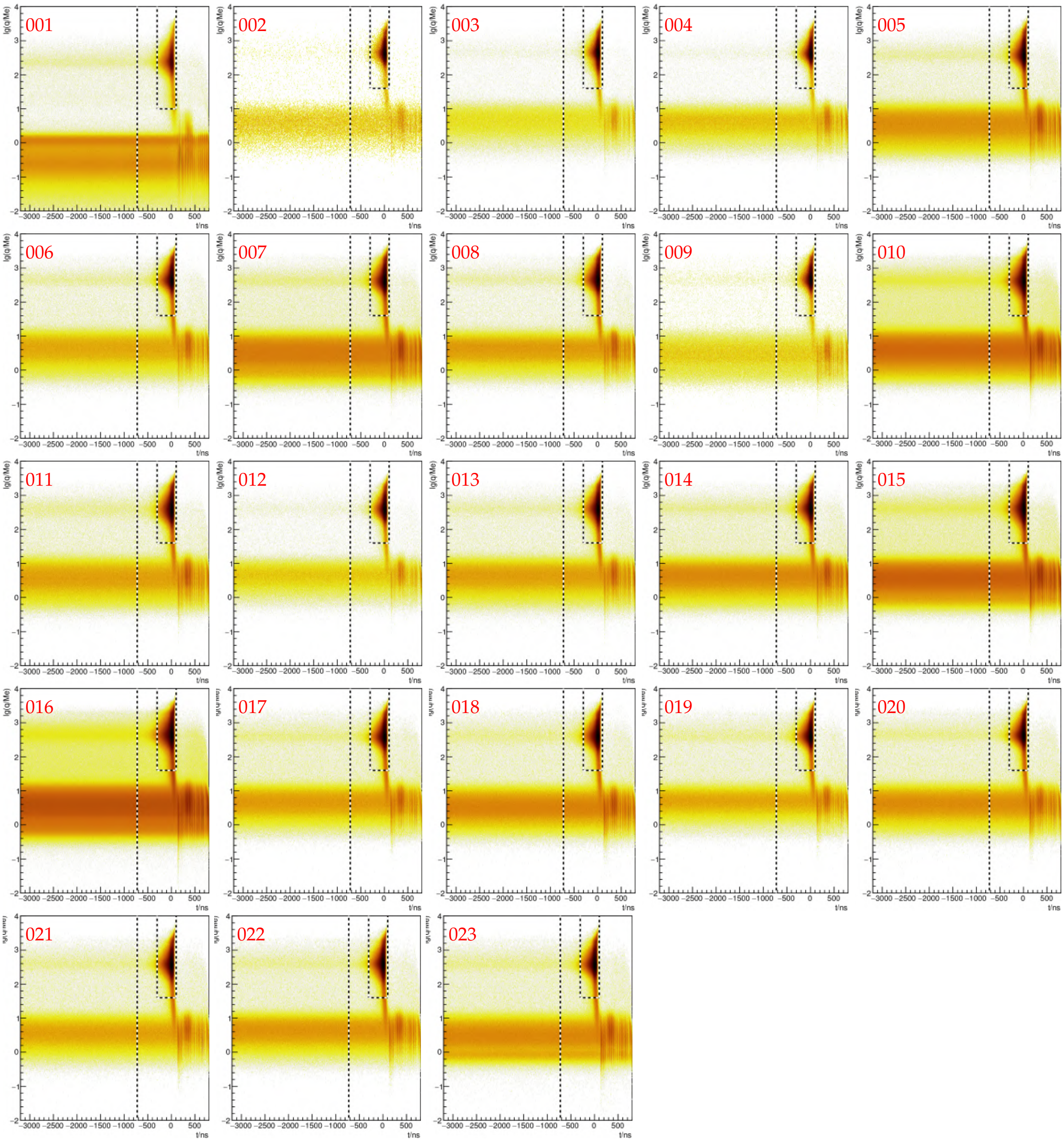

Figure 2: Pulse arrival times (x-axis) and $\lg(q/\mathrm{Me})$ (y-axis) vs. the muon trigger (at $t = 0$).

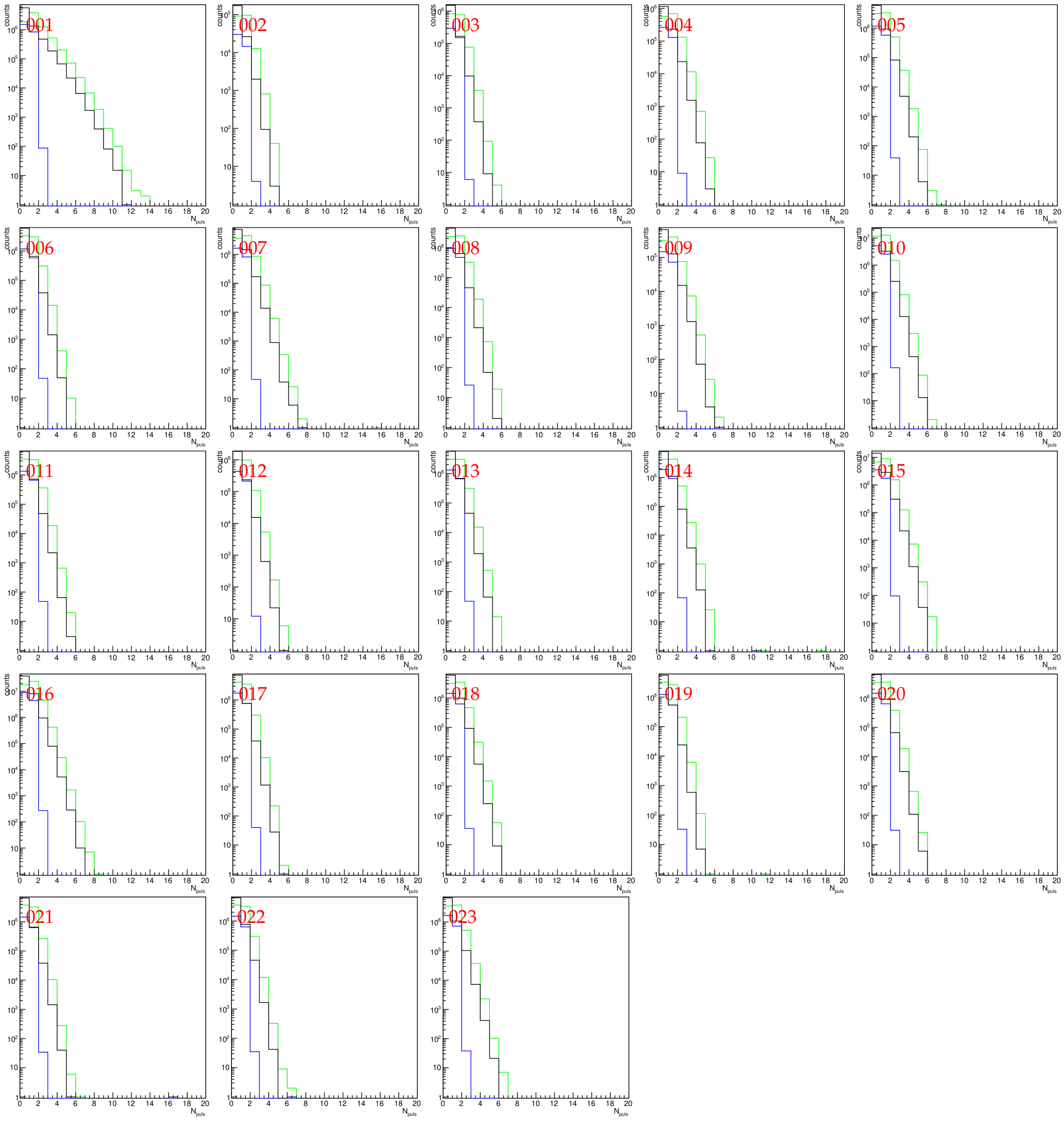

Figure 3: Histogram of number of pulses per trace. Increased tail means light leakage or electronic noise. Detector 001 is an example of such a strange behavior.

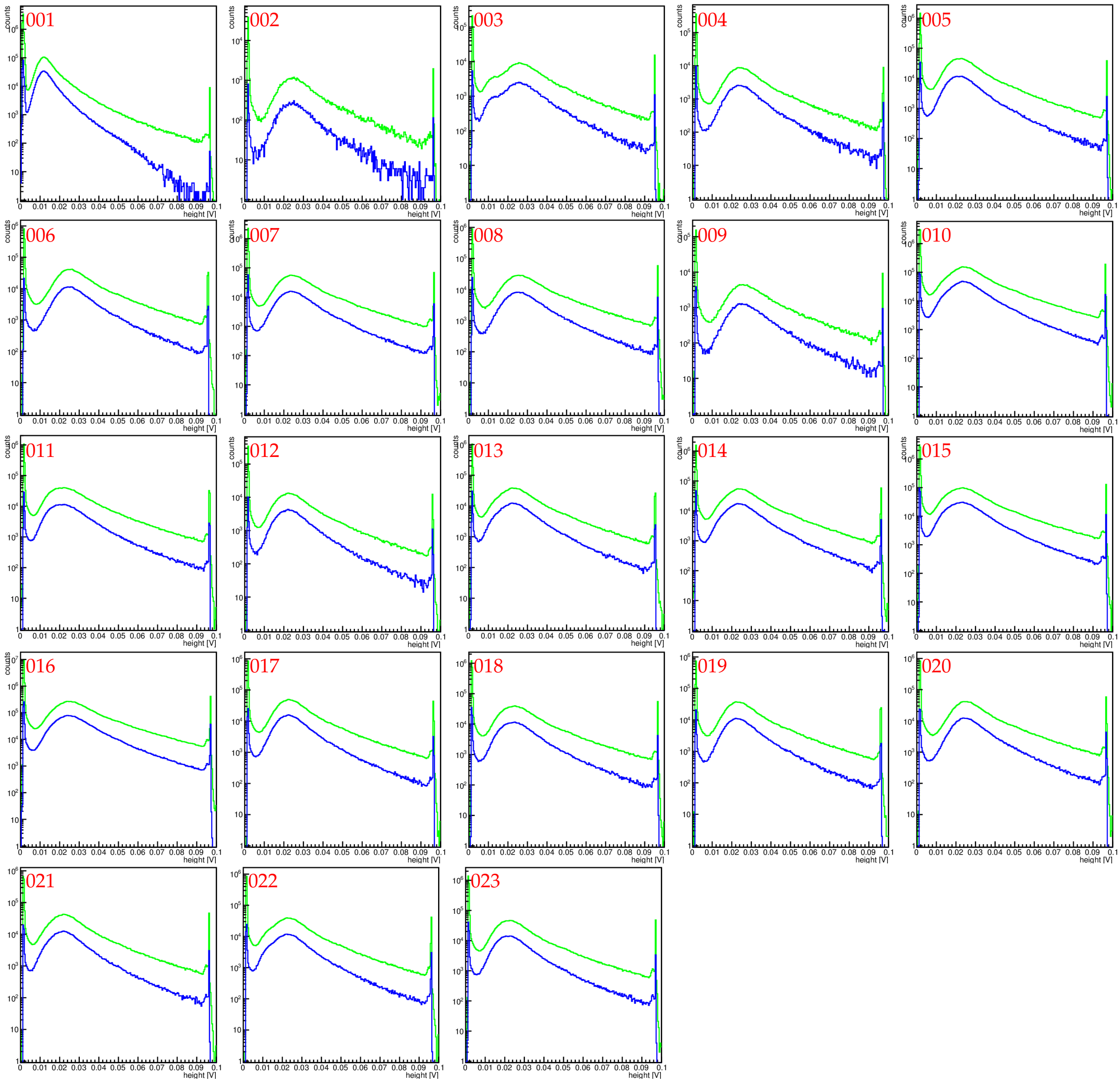

Figure 4: Pulse height (peak) histogram. Note that detector 002 was measured in the high-gain channel only with a low statistics.

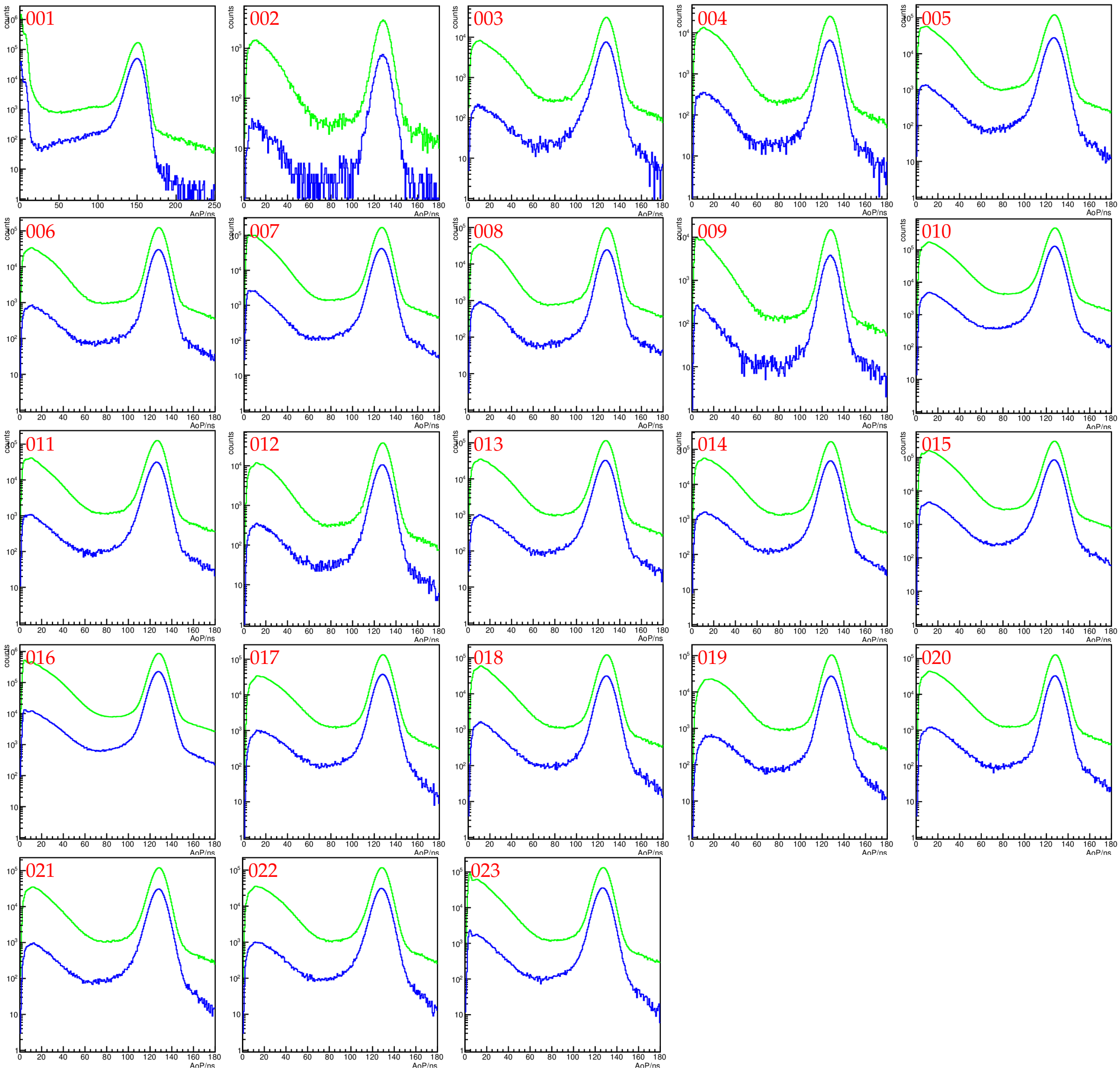

Figure 5: Area-over-peak (AoP). Pulses are affectively 130 ns long. Note that detector 002 was measured in the high-gain channel only with a low statistics.

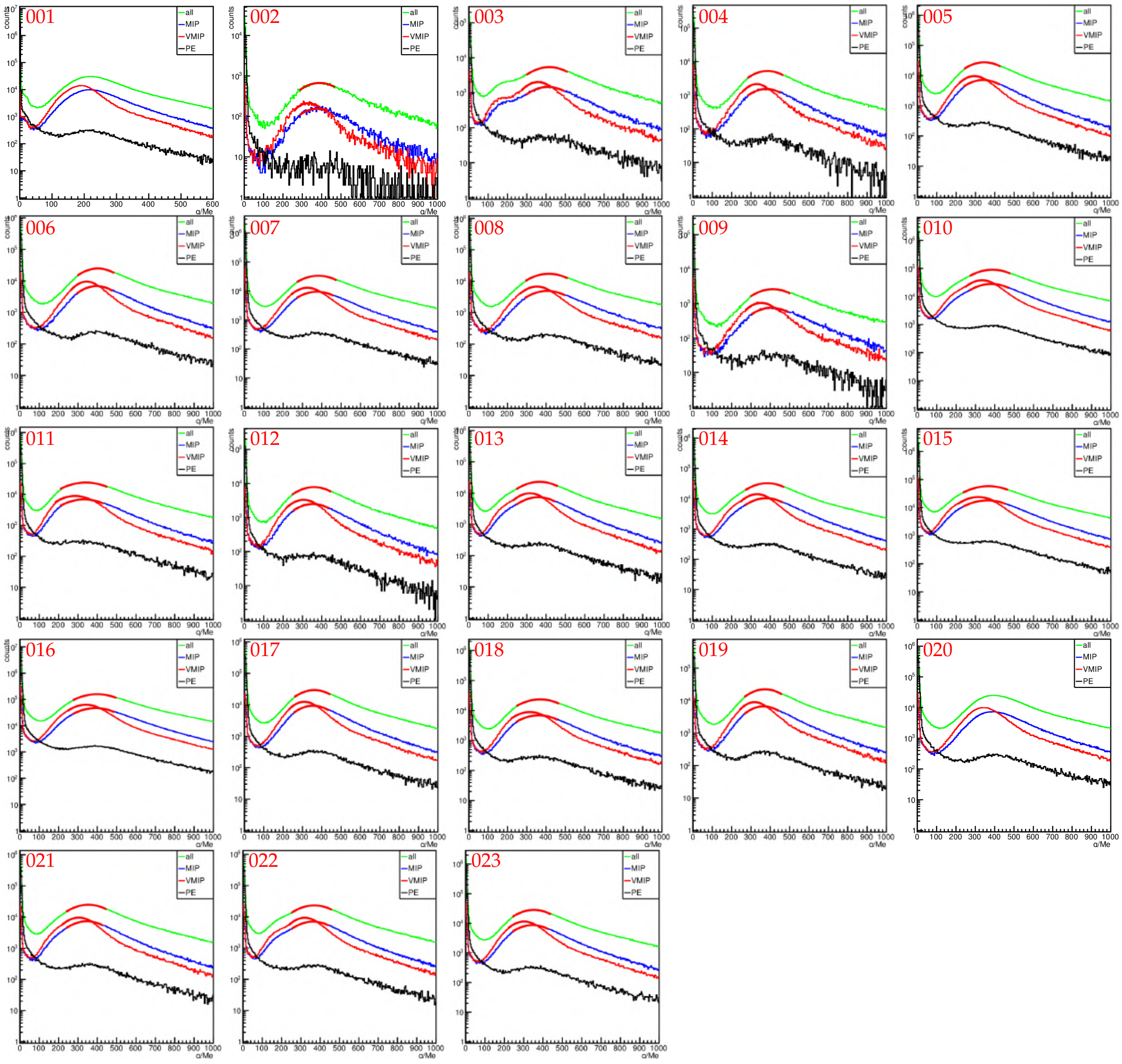

Figure 6: Charge histogram. Note that the detector 002 was measured in the high-gain channel only with a low statistics. Also note the double-bump structure for detector 003.

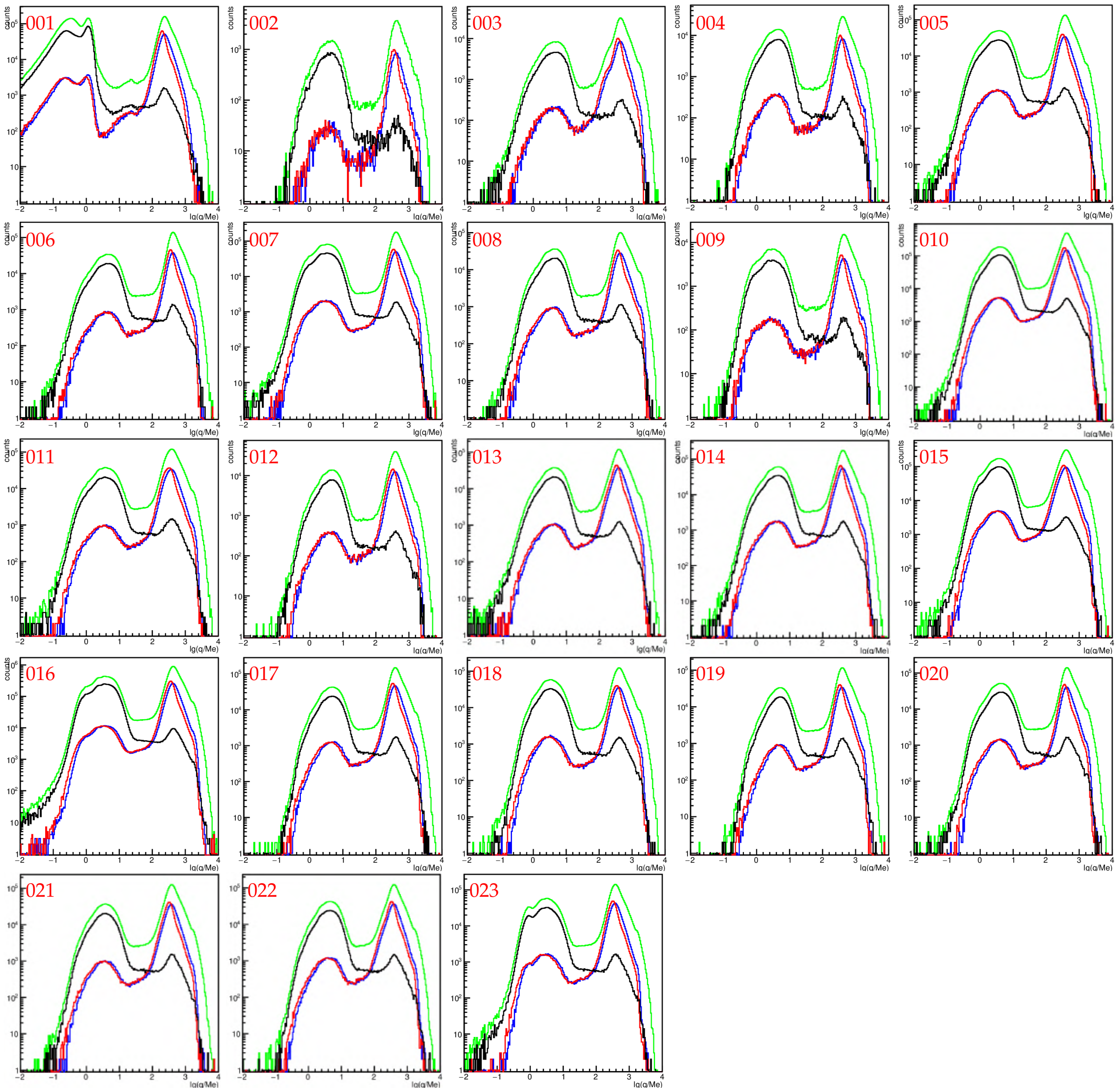

Figure 7: Histogram of the logarithm of the charge, $\lg(q/\text{Me})$.

Figure 8: Mean vertical-equivalent charge $\langle q \rangle$ over the detector.

Figure 9: Mean logarithm of vertical-equivalent charge $\langle \lg(q/\mathrm{Me}) \rangle$ over the detector.

Figure 10: Mean AoP over the detector.

Figure 11: Projection of the mean log-charge along the *x*-axis.

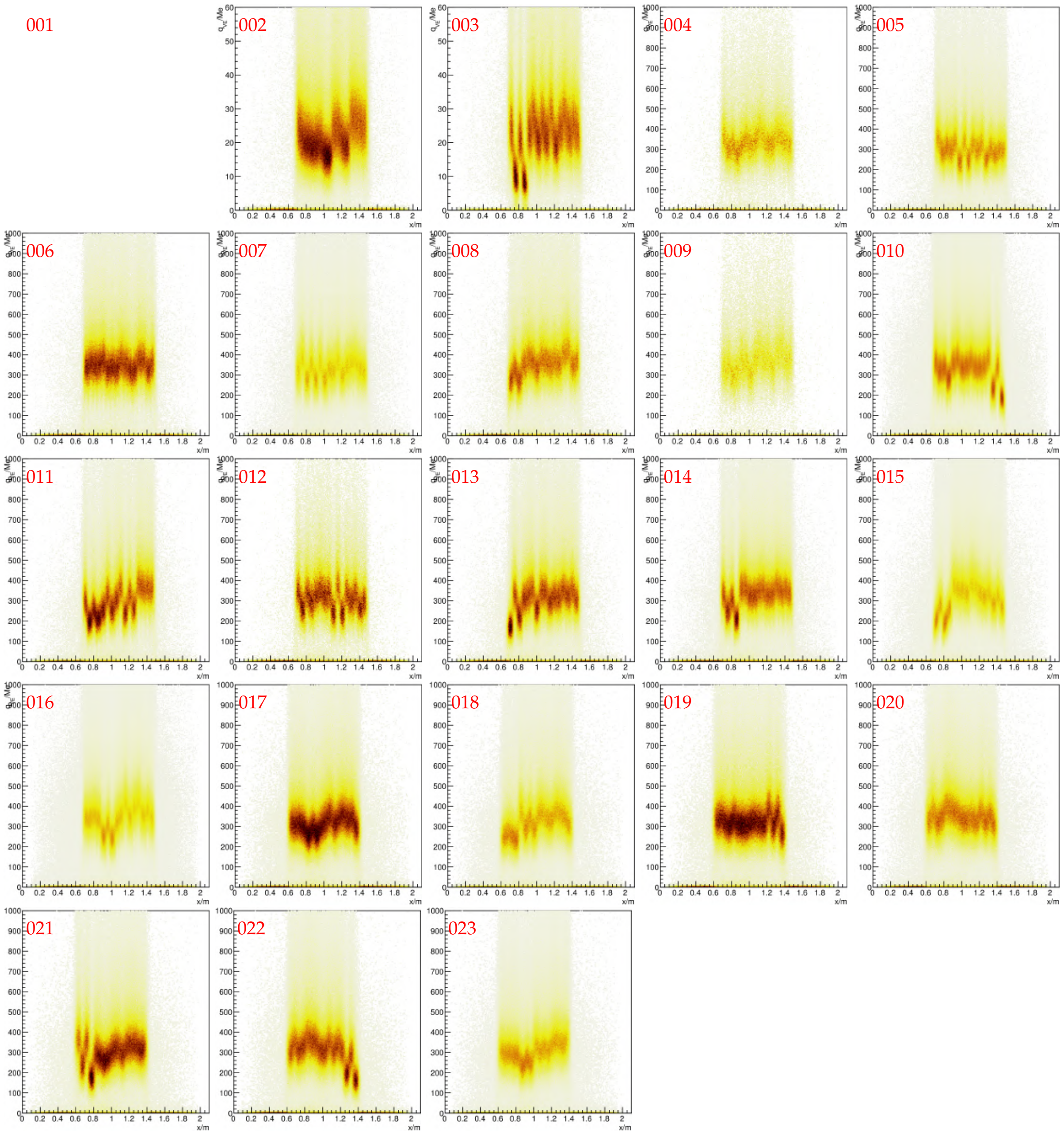

Figure 12: Projection of the mean charge along the *x*-axis.

Figure 13: Projection of the mean log-charge along the y-axis.

Appendix F

Muon tower PE/MIP results and SPOCK SiPM gain results for each detector

Time	Detector	Cookie Board	Gain	V_Bias+3V	MIP (all, Me)	PE per MIP	Gain SPOCK *10^5
07.08.2017, 09:42	002-25	9	High Gain	56,56	389,70	41,19	5,17
07.08.2017, 10:42	003-25	10	High Gain	56,58	416,00	45,56	4,99
07.08.2017, 16:00	004-25	11	High Gain	56,76	385,47	39,52	5,33
08.08.2017	005-25	12	High Gain	56,45	345,83	36,62	5,16
08.08.2017	006-25	13	High Gain	56,84	402,94	42,59	5,17
09.08.2017	007-25	14	High Gain	56,64	382,59	40,13	5,21
10.08.2017	008-25	15	High Gain	56,89	414,33	42,72	5,30
11.08.2017	009-25	16	High Gain	56.61	413,41	42,38	5,33
06.09.2017	010-25	17	High Gain	56,70	374,03	39,08	5,23
11.08.2017	011-25	18	High Gain	56,75	341,08	35,57	5,24
16.08.2017	012-25	19	High Gain	56,58	359,71	37,30	5,27
14.08.2017	013-25	20	High Gain	56,75	366,52	38,00	5,27
17.08.2017	014-25	21	High Gain	56,83	384,73	40,74	5,16
2. Run: 04.09.2017	015-25	22	High Gain	56,40	367,70	38,94	5,16
18.08.2017	016-25	23	High Gain	56,64	399,34	41,97	5,20
18.08.2017	017-25	24	High Gain	56,52	361,62	38,00	5,28
21.08.2017	018-25	25	High Gain	56,70	369,26	38,80	5,20
21.08.2017	019-25	26	High Gain	56,32	372,74	39,17	5,23
22.08.2017	020-25	27	High Gain	56,51	394,84	41,49	5,15
22.08.2017	021-25	28	High Gain	56,40	354,14	37,22	5,12
23.08.2017	022-25	29	High Gain	56,52	369,49	38,83	5,10
23.08.2017	023-25	30	High Gain	56,53	352,81	37,08	5,20

Notes SPOCK measurements:

Room temperature and a light source wavelength of 423 nm

Notes muon tower measurements:

010-25: Strange signal behaviour in first run due to new power supply of muon tower

015-25: Second Run: Changed PWR cable GPB->ARM

Appendix G

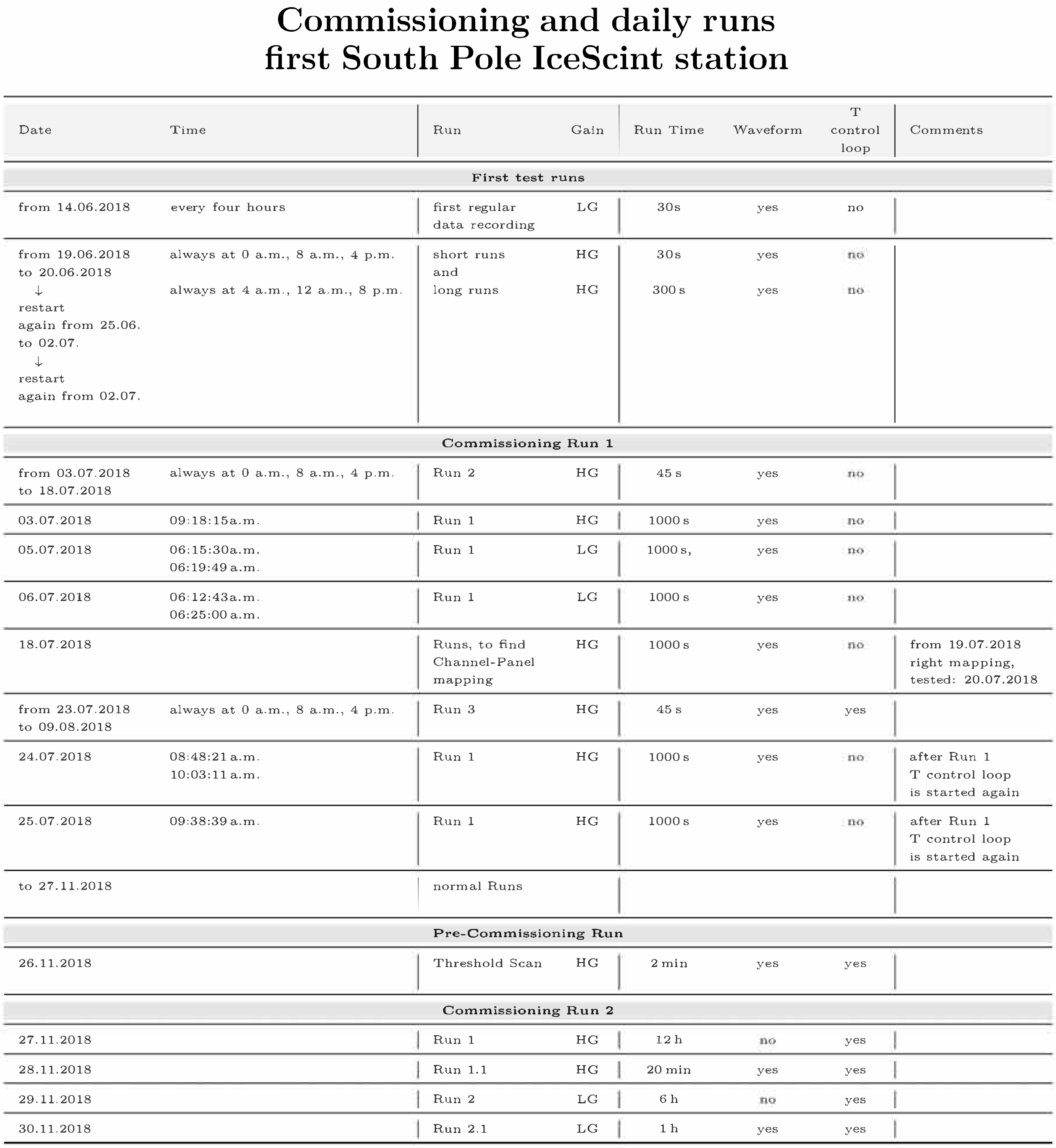

Commissioning and daily runs first South Pole IceScint station

Date	Time	Run	Gain	Run Time	Waveform	T control loop	Comments
First test runs							
from 14.06.2018	every four hours	first regular data recording	LG	30s	yes	no	
from 19.06.2018 to 20.06.2018 ↓ restart again from 25.06. to 02.07. ↓ restart again from 02.07.	always at 0 a.m., 8 a.m., 4 p.m. always at 4 a.m., 12 a.m., 8 p.m.	short runs and long runs	HG HG	30s 300 s	yes yes	no no	
Commissioning Run 1							
from 03.07.2018 to 18.07.2018	always at 0 a.m., 8 a.m., 4 p.m.	Run 2	HG	45 s	yes	no	
03.07.2018	09:18:15a.m.	Run 1	HG	1000 s	yes	no	
05.07.2018	06:15:30a.m. 06:19:49 a.m.	Run 1	LG	1000 s,	yes	no	
06.07.2018	06:12:43a.m. 06:25:00 a.m.	Run 1	LG	1000 s	yes	no	
18.07.2018		Runs, to find Channel-Panel mapping	HG	1000 s	yes	no	from 19.07.2018 right mapping, tested: 20.07.2018
from 23.07.2018 to 09.08.2018	always at 0 a.m., 8 a.m., 4 p.m.	Run 3	HG	45 s	yes	yes	
24.07.2018	08:48:21 a.m. 10:03:11 a.m.	Run 1	HG	1000 s	yes	no	after Run 1 T control loop is started again
25.07.2018	09:38:39 a.m.	Run 1	HG	1000 s	yes	no	after Run 1 T control loop is started again
to 27.11.2018		normal Runs					
Pre-Commissioning Run							
26.11.2018		Threshold Scan	HG	2 min	yes	yes	
Commissioning Run 2							
27.11.2018		Run 1	HG	12 h	no	yes	
28.11.2018		Run 1.1	HG	20 min	yes	yes	
29.11.2018		Run 2	LG	6 h	no	yes	
30.11.2018		Run 2.1	LG	1 h	yes	yes	

Appendix H

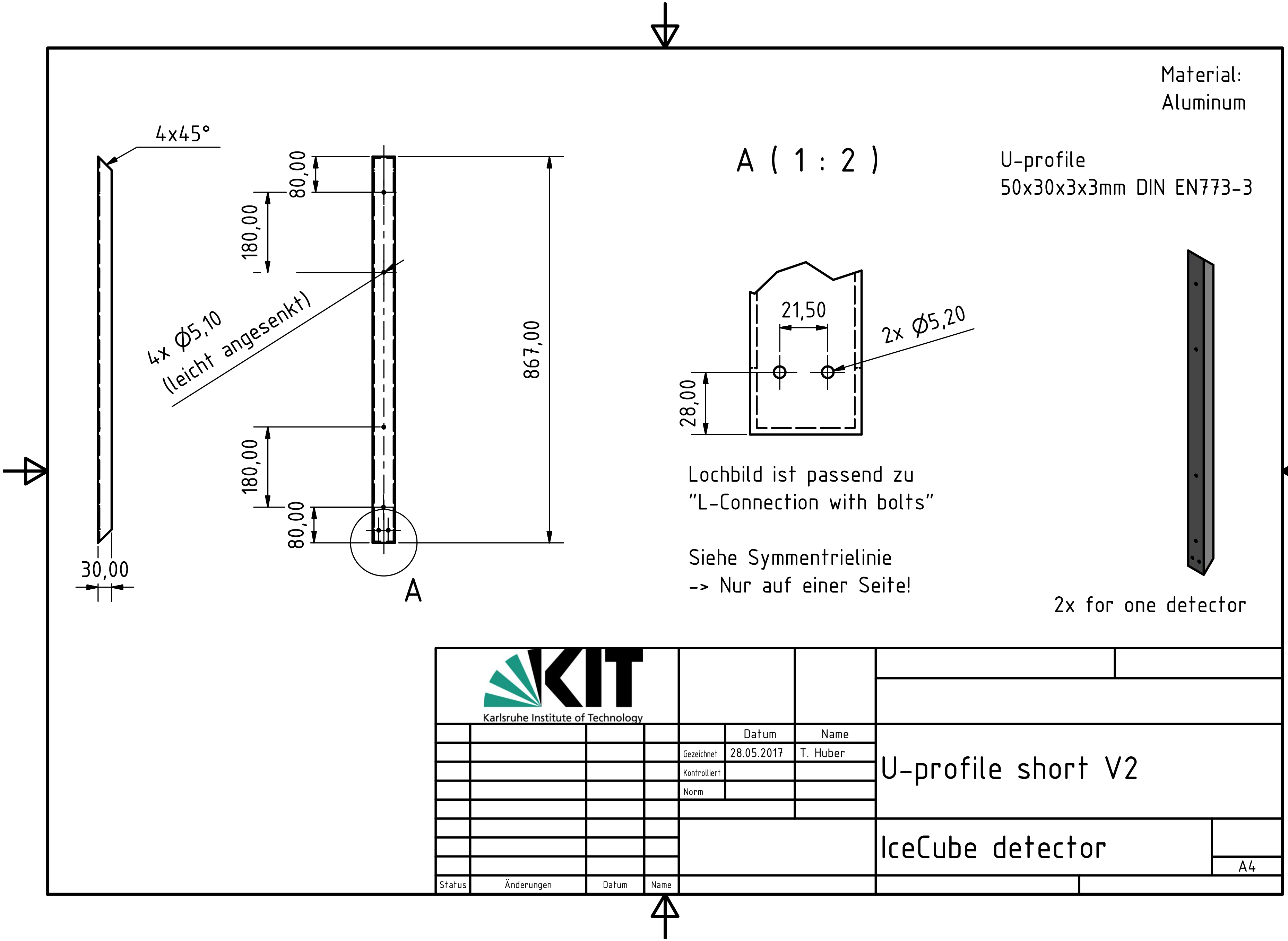
Material:
Aluminum
U-profile
50x30x3x3mm DIN EN773-3
4x45°
80,00
180,00
4x Ø5,10
(leicht angesenkt)
867,00
180,00
80,00
30,00
A
A (1 : 2)
21,50
2x Ø5,20
28,00
Lochbild ist passend zu
"L-Connection with bolts"
Siehe Symmentrielinie
-> Nur auf einer Seite!
2x for one detector
KIT
Karlsruhe Institute of Technology
Datum
Name
Gezeichnet
28.05.2017
T. Huber
Kontrolliert
Norm
U-profile short V2
IceCube detector
A4
Status
Änderungen
Datum
Name

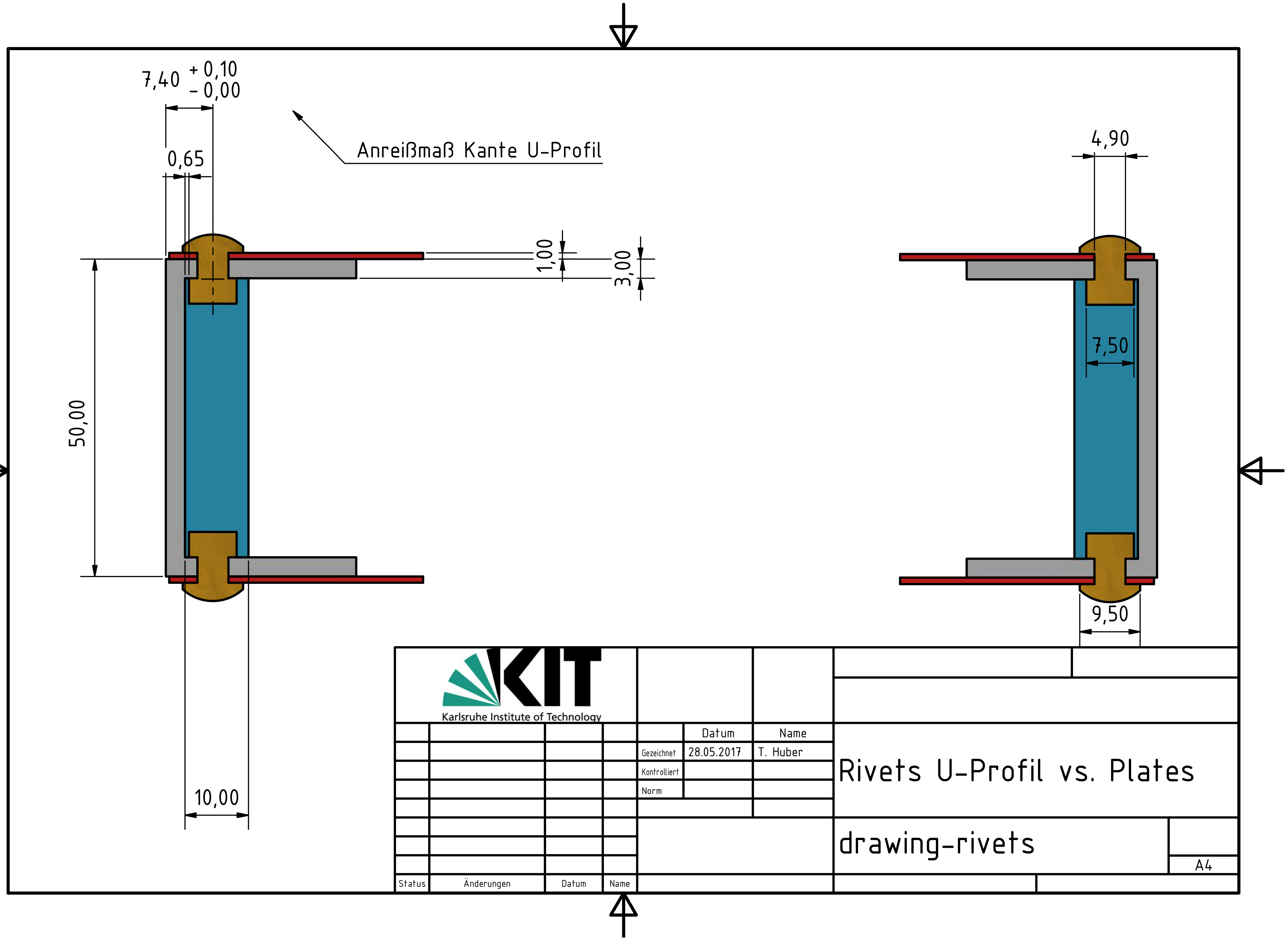

Rivets U-Profil vs. Plates

drawing-rivets

	Datum	Name
Gezeichnet	28.05.2017	T. Huber
Kontrolliert		
Norm		

Appenix I

Selection CAD IceScint detectors 2017

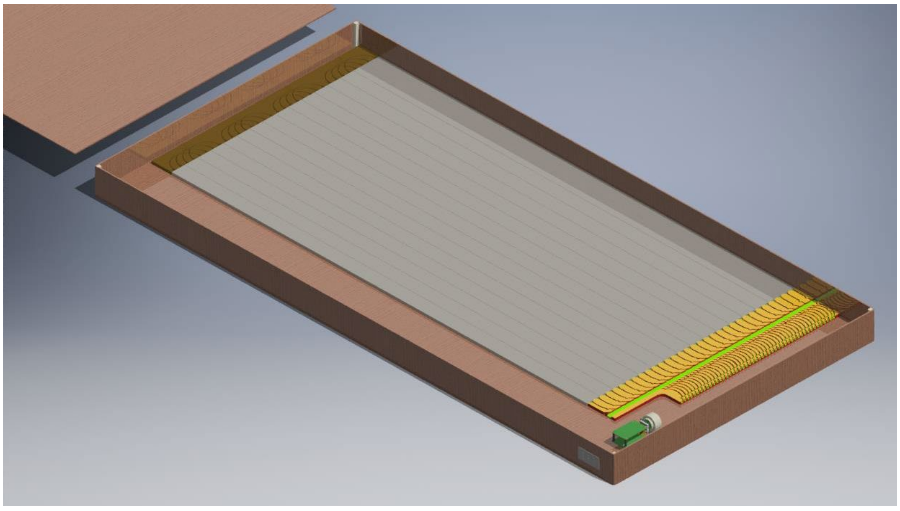

IceScint prototype detector

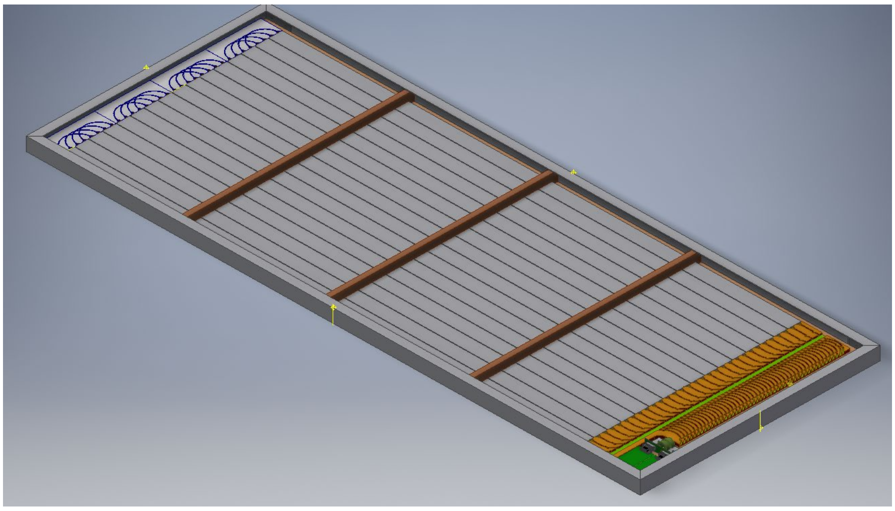

IceScint detector as deployed January 2018

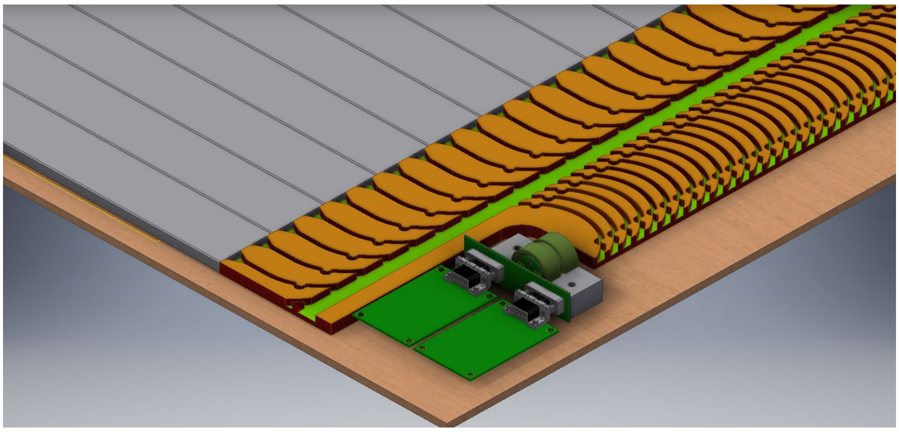

Zoom into the routing, optical coupling and IceARM placement

Detector 006-25

Date of install: **08.08.2017**

Kuraray fibers:	
Serial:	K16021519
Length of 1 fiber:	5.5 m
Sum of all fibers:	88 m

Fermilab bars:		Comments on bars:
Bar #1	RD14380B	
Bar #2	RD14390B	3mm gap
Bar #3	RD14351B	
Bar #4	RD14361B	
Bar #5	RD14371B	
Bar #6	RD14400B	
Bar #7	RD14381B	
Bar #8	RD14352B	
Bar #9	RD14362B	
Bar #10	RD14372B	
Bar #11	RD14382B	
Bar #12	RD14401B	
Bar #13	RD14538B	
Bar #14	RD14528B	
Bar #15	RD14539B	
Bar #16	RD14540B	
Routing:	Schmidt u. Bolz	

Links and location:	
Picture ARM:	https://goo.gl/zpLnuA
Muon Tower:	soon
Function tests:	soon
SiPM characterization:	soon
Location:	Shipped to South Pole

Comments on detector:

Cookie:	
Glued:	Huber
Melt:	Bolz u. Huber
Date:	07.08.17

Analog Readout Module:	
Cookie board	013-25
Adapter board	007
Readout board	007
GP board	007

Appendix K

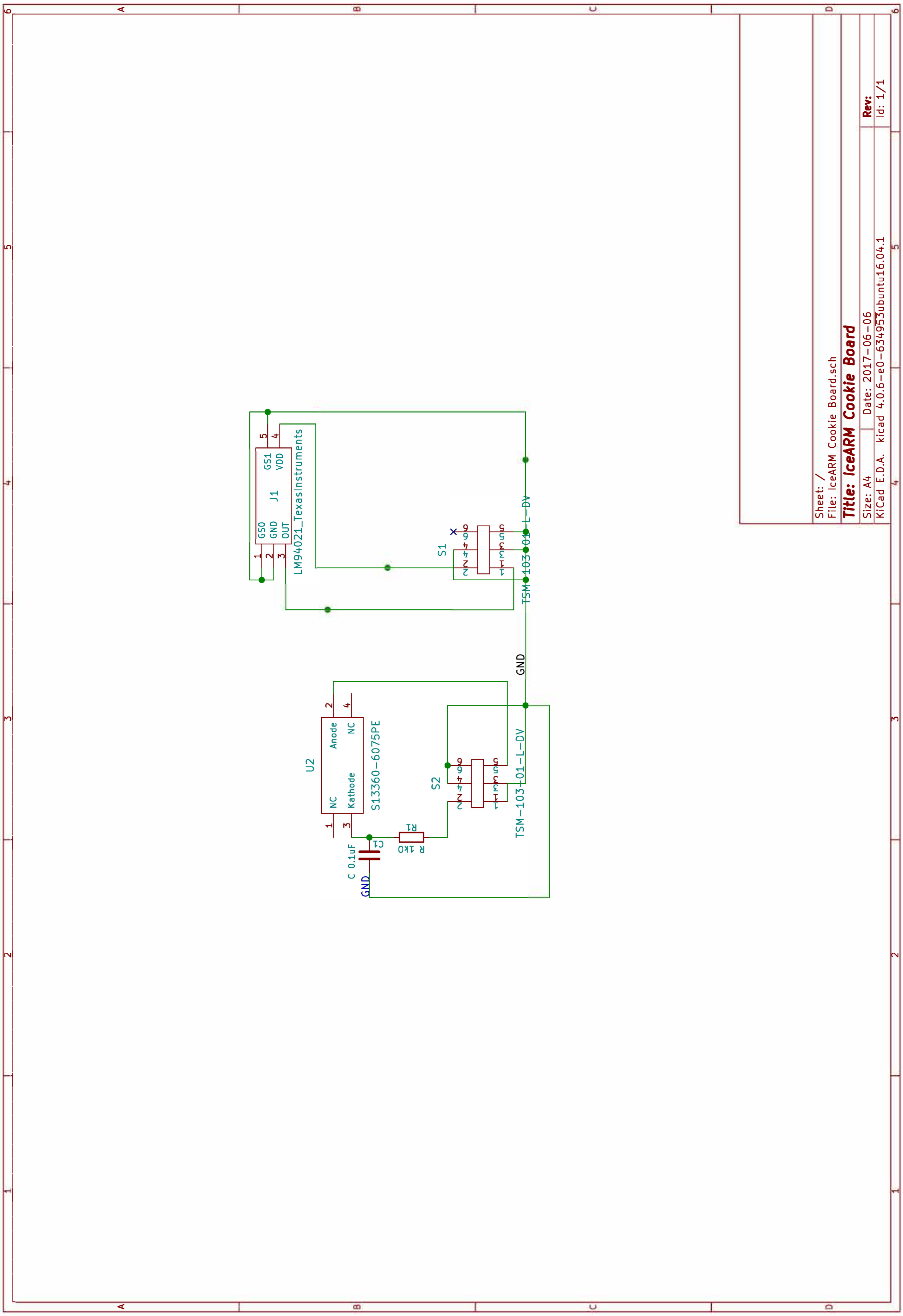
J1
LM94021_TexasInstruments
GS1
VDD
GS0
GND
OUT
1
2
3
4
5
S1
TSM-103-01-L-DV
1
2
3
4
5
6
GND
U2
S13360-6075PE
Anode
NC
NC
Kathode
1
2
3
4
S2
TSM-103-01-L-DV
C1
C 0.1uF
R1
R 1kΩ
GND
Sheet: /
File: IceARM Cookie Board.sch
Title: IceARM Cookie Board
Size: A4
Date: 2017-06-06
Rev:
KiCad E.D.A. kicad 4.0.6-e0-634953ubuntu16.04.1
Id: 1/1
A
B
C
D
1
2
3
4
5
6

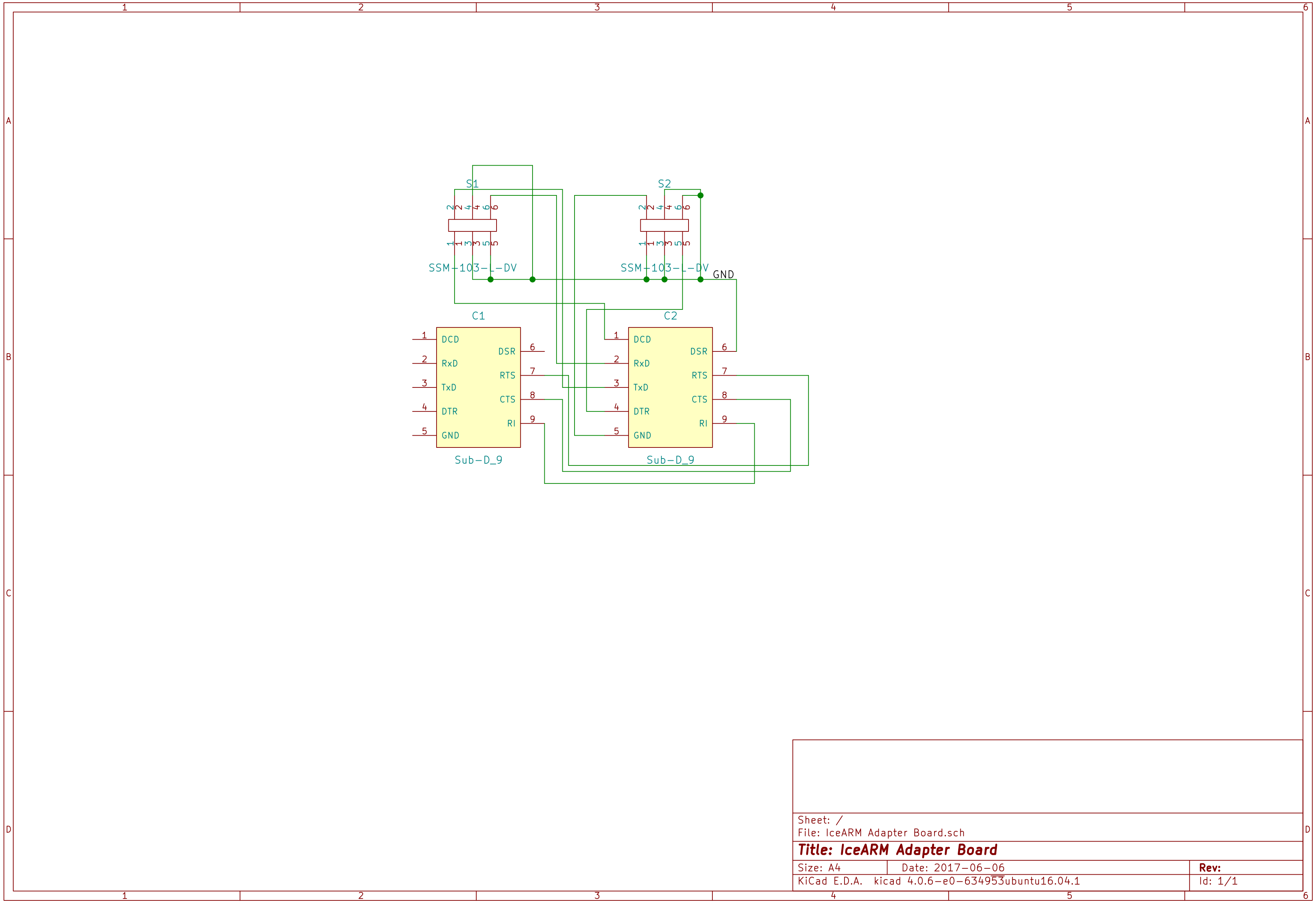
S1
SSM-103-L-DV
S2
SSM-103-L-DV
GND
C1
DCD
RxD
TxD
DTR
GND
DSR
RTS
CTS
RI
Sub-D_9
C2
DCD
RxD
TxD
DTR
GND
DSR
RTS
CTS
RI
Sub-D_9
Sheet: /
File: IceARM Adapter Board.sch
Title: IceARM Adapter Board
Size: A4
Date: 2017-06-06
Rev:
KiCad E.D.A. kicad 4.0.6-e0-634953ubuntu16.04.1
Id: 1/1

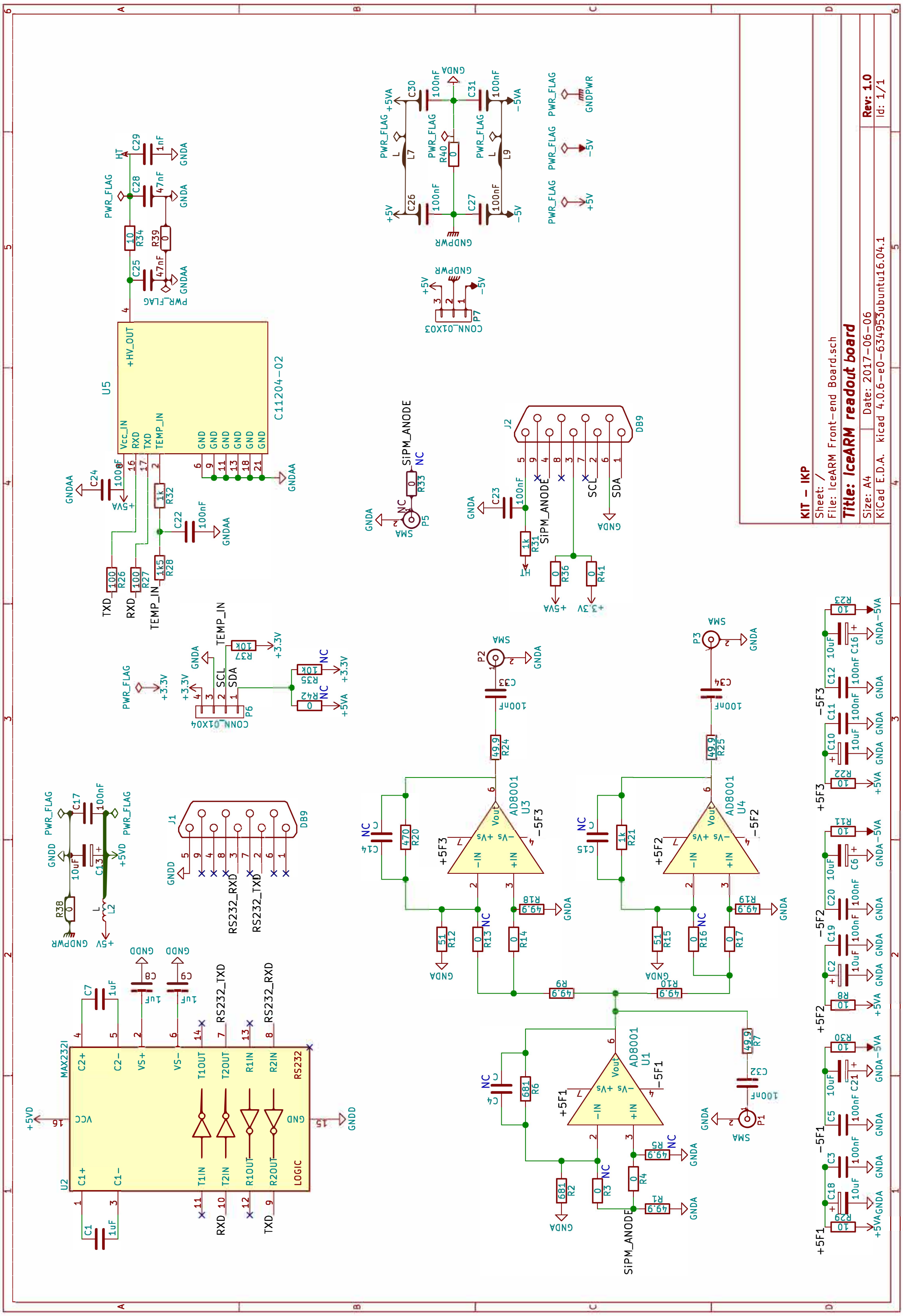
KIT – IKP
Sheet: /
File: IceARM Front-end Board.sch
Title: IceARM readout board
Size: A4
Date: 2017-06-06
Rev: 1.0
KiCad E.D.A. kicad 4.0.6-e0-6349~53~ubuntu16.04.1
Id: 1/1
U5
C11204-02
+HV_OUT
Vcc_IN
RXD
TXD
TEMP_IN
GND
U2
MAX232I
RS232
LOGIC
U1
U3
U4
AD8001
Vout
-IN
+IN
+Vs
-Vs
J1
J2
DB9
P1
P2
P3
P5
SMA
P6
CONN_01X04
P7
CONN_01X03
SiPM_ANODE
RS232_RXD
RS232_TXD
TEMP_IN
SCL
SDA
TXD
RXD
HT
PWR_FLAG
GNDPWR
GNDA
GNDAA
GNDD
+5VA
-5VA
+5VD
+3.3V
+5V
-5V
+5F1
-5F1
+5F2
-5F2
+5F3
-5F3
NC

Appendix L

People involved in IceScint (incomplete)

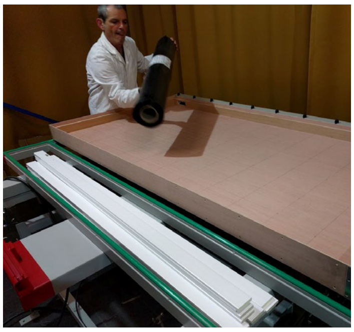


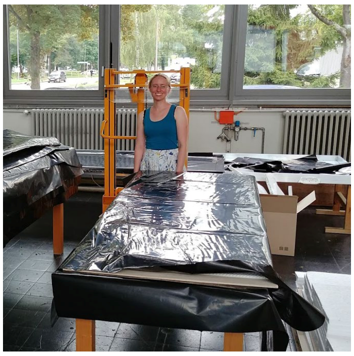



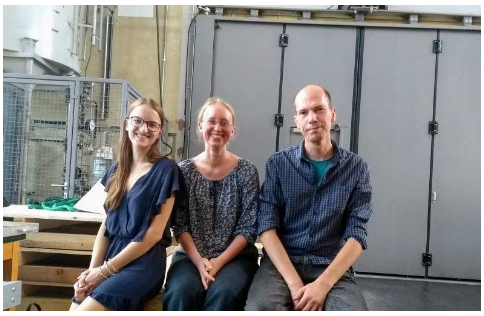
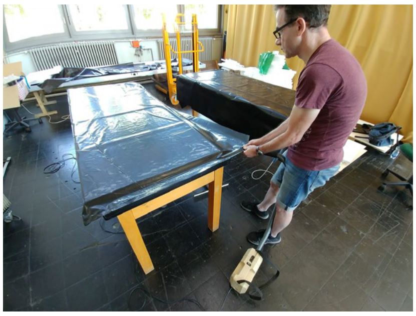



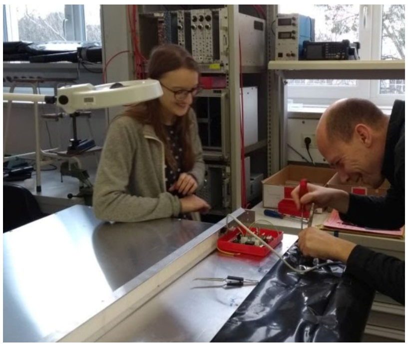

South Pole Travel and Deployment